



City Research Online

City, University of London Institutional Repository

Citation: Aboukhedr, M. (2019). Two-Phase Flow Simulation in Porous Media Geometries Reconstructed from micro CT Data : Application to Fluid Transport at Low Capillary Numbers. (Unpublished Doctoral thesis, City, University of London)

This is the accepted version of the paper.

This version of the publication may differ from the final published version.

Permanent repository link: <https://openaccess.city.ac.uk/id/eprint/23465/>

Link to published version:

Copyright: City Research Online aims to make research outputs of City, University of London available to a wider audience. Copyright and Moral Rights remain with the author(s) and/or copyright holders. URLs from City Research Online may be freely distributed and linked to.

Reuse: Copies of full items can be used for personal research or study, educational, or not-for-profit purposes without prior permission or charge. Provided that the authors, title and full bibliographic details are credited, a hyperlink and/or URL is given for the original metadata page and the content is not changed in any way.

City Research Online:

<http://openaccess.city.ac.uk/>

publications@city.ac.uk

Two-Phase Flow Simulation in Porous Media Geometries Reconstructed from micro CT Data : Application to Fluid Transport at Low Capillary Numbers

Mahmoud Salah Aboukhedr

Doctor of Philosophy



City University Of London

Department of Mechanical Engineering & Aeronautics

School of Mathematics, Computer Science & Engineering

January 2019

Contents

Contents	iii
List of Figures	vii
List of Tables	xvii
List of Nomenclature	xix
Acknowledgements	xxi
Declaration	xxv
Abstract	xxvii
Contribution	xxix
1 Introduction & Literature Review	1
1.1 Background	2
1.2 Two-phase Flow Through Complex Porous Structures	4
1.2.1 Droplet Impacting on Porous Media	6
1.2.2 Capillary Flow Through Porous Media	10
1.2.3 Challenges in Modelling the Pore-scale Effect for Multiphase Flow Transportation	12
1.3 Numerical Challenges	15
1.3.1 Multiphase Flow Solvers - An Overview	15
1.3.2 Numerical Surface Tension Force Modelling Using VoF Method	19
1.3.3 Wetting Behaviour	21
1.4 Motivation of the Study	27
1.5 Thesis Synopsis	29

2	Numerical Method	31
2.1	Governing Equations	32
2.1.1	Mass and Momentum Conservation	32
2.2	Finite Volume Method	34
2.2.1	Advection of the Indicator Function Using Adaptive Compression Scheme (Implicit)	36
2.2.2	Smoothing Scheme (Explicit)	39
2.2.3	Sharpening Scheme (Explicit)	40
2.2.4	Capillary Pressure Jump Modelling	41
2.2.5	Filtering Numerical Errors	42
2.3	Dynamic Contact Angle Model Implementation	44
2.4	Algorithm Implementation	46
2.4.1	Solution of the Momentum Equation	46
2.5	Concluding Remarks	49
3	Validation of the Numerical Method	51
3.1	Introduction	52
3.2	Stationary Droplet	53
3.2.1	Single Droplet	53
3.2.2	Multiple Droplets	60
3.3	Rayleigh-Taylor Instability with Surface Tension	62
3.3.1	Numerical Setup	62
3.3.2	Qualitative Description	64
3.3.3	Quantitative Results and Discussion	68
3.3.4	Self-similarity Solution	75
3.4	Notched Disc in Rotating Flow	77
3.5	Circle in a Vortex Field	82
3.6	Bubble Formation at T-junction	86
3.7	Droplet Impinging on a Solid Surface	92
3.8	Concluding Remarks	96
4	Two-Phase Flow Behaviour Inside Porous Structures Using Micro-CT porous media	97
4.1	Introduction	98

4.2	Porous Model Reconstruction and Meshing	100
4.2.1	3D Surface Generation Based on Micro-CT Images	100
4.2.2	Volume Mesh Generation	103
4.3	Extracting the Correct Numerical Simulation Parameters to Estimate Porous Media Macroscopic Properties	105
4.4	Investigating Different Flow Proprieties on Various Porosities	108
4.4.1	Case Setup and Imposed Conditions for Primary Water Injection	108
4.4.2	Primary Water Injection Using Different Wetting Conditions for Different Capillary Numbers	111
4.4.3	Effect of Porosity During Primary Water Injection Using Dy- namic Wetting Conditions	120
4.4.4	Effect of Surface Tension on Oil Drainage Behaviour	127
4.5	Concluding Remarks	129
5	Drop Impact on Micro-CT Porous Media	131
5.1	Introduction	132
5.2	Case Setup	134
5.2.1	Numerical Setup	134
5.3	Results and Discussion	139
5.3.1	Validation of the Numerical Method	141
5.3.2	Influence of Porous Wettability on Droplet Spreading	144
5.3.3	Influence of Porous Wettability on Droplet Penetration	154
5.3.4	Effect of Varying the Reynolds Re and Weber We Numbers at Fixed Porosity	158
5.4	Multiple Droplet Impacting Porous Medium	163
5.5	Concluding Remarks	169
6	Conclusions and Future work	171
6.1	Conclusions	172
6.2	Recommendations and Future Work	176
6.2.1	Numerical Aspects	176
6.2.2	Application Aspect	176
A	Complementary Simulations - Appendix A	179
A.1	Introduction	180

A.2 Droplet Impinging on a Porous Surface Using Darcy Model	180
A.3 Droplet Impinging on a Porous Surface Using 2D Porous Media Geometry	182
A.4 Flow and Transport in Porous media - Complimentary Studies	186
A.4.1 Secondary Water Injection for Water/Oil Mixed Porous Reservoir	186
A.5 Using Dynamic Grid Refinement	191

Bibliography	195
---------------------	------------

List of Figures

1.1	Outcomes of droplet impact on various substrates. (a) deposition: on rough glass ($D_0 = 1.7$ mm, $U = 1.8$ m/s); (b) prompt splash: water droplet on rough PE ($D_0 = 2.4$ mm, $U = 3.1$ m/s); (c) corona splash: isopropanol on light rough ceramic ($D_0 = 1.7$ mm, $U = 2.51$ m/s); (d) receding breakup: water on porous stainless steel ($D_0 = 2.4$ mm, $U = 3.44$ m/s); (e) partial rebound: water on porous bronze ($D_0 = 2.44$ mm, $U = 2.44$ m/s); (f) rebound: water on porous PTFE ($D_0 = 2.44$ mm, $U = 1.86$ m/s) [1]	8
1.2	Schematic of droplet impingement against porous substrates [2], where D_0 is the droplet diameter before impact and U_i is the droplet velocity before impact	9
1.3	Schematic to represent the quantities in Youngs equation and constant contact angle	22
1.4	Schematic representing the advancing (a) and receding (b) contact angle during droplet movement	23
1.5	Wetting of different fluids: A hydrophobic surface and a hydrophilic surface	23
2.1	Discretisation of the solution domain [3]	34
2.2	Parameters in finite volume discretisation [3]	35
2.3	Schematic to represent the adaptive compression C_{adp} selection criteria	39
2.4	A two-dimensional schematic of the steps in reconstructing the interface: (a) the indicator function α , (b) the sharp indicator function, α_{sh} , used to mark mixed-faces and their corner points (shown as filled black squares), and (c) linear reconstruction of the interface (dashed line), where $\alpha_{sh} = 0.5$	41

2.5	Schematic representation of the velocity dependence of the contact angle (a), schematic representation of viscous bending in different scales for an advancing scenario (b) [4]	44
3.1	Computational domain for modelling static droplet, (left) initial condition a cube of size $D_0 = 30 \mu\text{m}$, and (right) static shape of droplet. Mesh size $R/\delta x = 15$ at $t = 0.0025$ s.	54
3.2	(a)Evolution of maximum velocity during droplet relaxation using the standard <i>interFoam</i> solver with two different interface compression ($C_{compr.}$). (b) values Snapshot of the interface shape after the relaxation of the oil droplet using the standard <i>interFoam</i> . Velocity vectors near to the interface for different interface compression values are presented.	56
3.3	Effect of varying model coefficients described in table 3.1 and 3.2 on parasitic currents, all figures are showing velocity vector field at $t = 0.0024$ sec. Figures are coloured with indicator function α_{Sharp}) as yellow shows oil phase inside the droplet and bright blue shows water outside the droplet	58
3.4	Effect of varying models coefficients presented in Table 3.1 and 3.2 on maximum parasitic currents over period of time	59
3.5	Computational domain showing two static droplets , (left) initial condition a cube of size $D_0 = 20 \mu\text{m}$ each, and (right) static shape of droplet as two boxes.	60
3.6	Effect of combined flux filtering and smoothing in the presence of sharpening model on the interaction of parasitic velocity field. All figures are showing the velocity field at $t = 0.0024$ sec on the indicator function α_{Sharp} isocontour = 0.5	61
3.7	Computation domain for the simulation of the RTI.	64
3.8	Volume fractions predicted by <i>RCLSFoam</i> and <i>interPore</i> for the Rayleigh–Taylor instability with 60×224 mesh elements.	69
3.9	Interface (0.5 iso-contour of both indicator functions) predicted by both solvers for the Rayleigh–Taylor instability with 60×224 mesh elements, velocity field and velocity vectors overlaying the interface contour. . . .	70
3.10	Volume fractions predicted by both solvers for the Rayleigh–Taylor instability with 128×512 mesh elements.	71

3.11	Amplitude growth for the Rayleigh–Taylor instability in the 60×224 computational domain compared to the theoretically predicted growth rates of <i>RCLSFoam</i> (Case1) and <i>interPore</i> (Case 2).	73
3.12	Indicator functions smeared over cell count and y -location at $t = 0$ (<i>top row</i>) and $t = 0.2s$ (<i>bottom row</i>) for two mesh sizes: 60×224 and 128×512 mesh elements.	74
3.13	Theoretically predicted self-similar solution for the Rayleigh–Taylor instability against our numerically predicted solutions.	75
3.14	Schematic representation of two dimensional Zalesak’s Disk benchmark test case described at [5].	77
3.15	Zalesaks disk after one revolution. Iso-contours for indicator function alpha ($\alpha = 0.1, 0.5$ and 0.9) are plotted for the standard <i>interFoam</i> using different compression values, together with the reference shape.	78
3.16	Zalesaks disk after one revolution. Iso-contours of indicator function alpha sharp ($\alpha_{Sh} = 0.1, 0.5$ and 0.9) are plotted for the adaptive <i>interPore</i> solver using different sharpening coefficients, together with the reference shape.	79
3.17	Comparison between the used framework and available method reviewed by Gopala and van Wachem [6]. (a) is showing <i>interPore</i> adaptive compressive scheme, (b) is showing the compressive interface capturing scheme for arbitrary meshes (CICSAM), (c) is showing piecewise linear interface construction (PLIC) and (d) is showing flux-corrected transport FCT. All presented in mesh a domain of 200 by 200	80
3.18	Representation the initial configuration of the shearing flow test with the value of the color function is one inside the circle and zero outside	82
3.19	Circle in a vortex field after one revolution. Iso-contours for indicator function alpha ($\alpha = 0.1, 0.5$ and 0.9) is plotted for the standard <i>interFoam</i> using different compression values, together with the reference shape.	83
3.20	Circle in a vortex field after one revolution. Iso-contours of indicator function alpha sharp ($\alpha_{Sh} = 0.1, 0.5$ and 0.9) is plotted for the adaptive <i>interPore</i> solver using different sharpening coefficients, together with the reference shape.	84
3.21	Geometrical model boundaries and overall dimensions	86

3.22	Contact angle at injection tube measured from experimental images . . .	87
3.23	Slug flow in (left) experiments and (right) numerical simulations. $U_L = 0.318$ m/s and $U_G = 0.242$ m/s. Time (ms) is indicated in the upper right corner. Stream lines are coloured with velocity magnitude in all the figures.	88
3.24	Bubble flow in (left) experiments and (right) numerical simulations. $U_L = 0.531$ m/s and $U_G = 0.068$ m/s. Time (ms) is indicated in the upper right corner. Stream lines are coloured with velocity magnitude in all the figures.	89
3.25	Time evolution of the shape of the droplet: (left) numerical simulation vs. (right) experimental results [7].	92
3.26	Time evolution of the droplet diameter. Results from the standard (blue line) and the modified (black line) solver are compared with experimental data (red dots) from [7]	93
3.27	Velocity magnitude contour of the water droplet impact on stainless steel predicted by the standard VoF methodology of OpenFOAM (left) and our suggested framework (right). Both snapshots are taken at $T=4.5$ ms	94
3.28	Droplet spreading on solid surface with different droplet conditions, all data was compared with experimental and numerical results from [8]	95
4.1	Porous media reconstruction steps using RETOMO	101
4.2	Volume mesh building process starting from surface mesh	102
4.3	A visualization of the pore space for the Berea Sandstone B1, and the initial condition for the indicator function (alpha) with the prescribed boundary conditions	109
4.4	Plots of the capillary pressure in both phases (first row) and the computed effective permeability curves, showing the effect of surface wetting conditions at a constant injection rate	112
4.5	Cross section showing the water phase in blue and oil phase in yellow, when comparing Cases BM1, BM2 and BM3. The red circles are used to highlight the trapped oil droplets.	113
4.6	A 3D visualization for the oil residuals for Cases BM1, BM3 and BM3 at time = 0.0155s	114

4.7	Plots of the capillary pressure in both phases (first row) and the computed effective permeability curves, showing the effect of the capillary number	115
4.8	Cross section showing the water phase in blue and the oil phase in yellow for comparison of Cases BM3 and BM4	116
4.9	A 3D visualisation for the oil residuals for Cases BM3 at time = 0.0155s and Case BM4 at time = 0.041s	117
4.10	Plots of the capillary pressure in both phases and the computed effective permeability curves, showing the effect of varying the imposed contact angle	117
4.11	Cross section showing the water phase in blue and oil phase in yellow when comparing Cases AM1 and AM2	119
4.12	A visualisation of the indicator function (α_{Sh}): blue represents the water phase and yellow the oil phase, after 0.02 secs of water injection, for a capillary number of 8×10^{-5} ; a) presents BM1, b) presents BM2, c) presents AM1, and d) presents AM2	120
4.13	Plots of the capillary pressure and saturation curves for both phases and the computed effective permeability curves, showing the effect of varying porosity across Cases AM1, SM1 and B2M1	122
4.14	Cross section showing the water phase in blue and oil phase in yellow, when comparing cases AM1, SM1 & B2M1	124
4.15	A 3D visualisation for the oil residuals for Cases SM1, AM1 and B2M1 at time = 0.05 secs	125
4.16	Plots of the capillary pressure and saturation curves for both phases and the computed effective permeability curves, showing the effect of varying porosity between Cases BM1 and BM5	127
4.17	Cross section showing the water phase in blue and oil phase in yellow, when comparing Cases BM1 and BM5	128
5.1	Numerical model for Berea and carbonate porous media. (a and d) represent the original Mico CT for the two different porous media [9]; (b and c) represent the computational mesh for the Berea sandstone; (e and f) represent the carbonate	135

5.2	Representation of hybrid grid transformation from conformal mesh (at the box region) to conformal Hexa denominated mesh (at the porous region)	136
5.3	Three-dimensional computational domain, mesh and boundary conditions	137
5.4	3D simulated profile (a), 2D Top plan-view profile (b) and Calculated spreading radius (r) in red (c)	139
5.5	Droplet penetration Iso- surface	140
5.6	Comparison of droplet impacts for $D_0 = 2.0mm$ and $V_i = 1.0m/s$ on Berea stone (numerical) and Meule stone (experimental). (a) is a normalised wetted zone width r/R evolution for water droplets at $We = 28.5$. Developed solver at wetting conditions of $\theta_A = 125^\circ$ and $\theta_R = 25^\circ$ at the porous surface and porous media; standard solver <i>interFoam</i> at the same wetting conditions for the porous surface and porous media; the plot also includes the spreading predictions using the Darcy simulation and power law. (b) snapshots of droplet impact on porous materials at time = 1 ms. (c) droplet spreading using the developed and standard codes	143
5.7	Early stage snapshot of the droplet spreading and penetration for Berea porous media at $T = 0.0025s$. A velocity vector field is plotted on a slice passing by the middle of the porous structure. A constant impact velocity of 0.5 m/s and an initial droplet radius of 1 mm was used to simulate the influence of the contact angle presented in Table 5.3 . . .	145
5.8	Normalised radius r/R with different surface and pore contact angles vs. normalised time t/τ Berea sandstone. A constant impact velocity of 0.5 m/s and an initial droplet radius of 1 (mm) was used to simulate the influence of the contact angle, as presented in Table 5.3. Experimental spreading curves for Savonnières rock (porosity of 26.6 %) can be found in [10, 11]	147

5.9	The early stage of capillary imbibition of pores after droplet impacting on solid surfaces for Berea sandstone. Seven cases are presented at different time steps using the top and side view. The figures show the wetting conditions ranges from fully hydrophobic to fully hydrophilic using alpha contour. A constant impact velocity of 0.5 m/s and an initial droplet radius of 1 mm was used to simulate the influence of the contact angle presented in Table 5.3	148
5.10	Early stage snapshot for droplet spreading and penetration for porous carbonate media at $T = 0.0025s$. A velocity vector field is plotted on a slice passing by the middle of the porous structure. A constant impact velocity of 0.5 m/s and an initial droplet radius of 1 mm were used to simulate the influence of the contact angle, as presented in Table 5.3 . .	150
5.11	Normalised radius r/R with different surface and pore contact angles vs. normalised time t/τ for porous carbonate media . A constant impact velocity of 0.5 m/s and an initial droplet radius of 1 mm were used to simulate the influence of the contact angle, as presented in Table 5.3 . .	151
5.12	The early stage of capillary imbibition of pores after droplet impacting on solid surfaces. Four views are provided at each of five-time steps. The figures show two different wetting condition ranges from fully hydrophobic to fully hydrophilic. A constant impact velocity of 0.5 m/s and an initial droplet radius of 1 mm were used to simulate the influence of the contact angle, as presented in Table 5.3	152
5.13	The volume of liquid penetration during droplet impacting on porous media. On the left-hand side, the carbonate model is presented, while on the right-hand side is the Berea model. A constant impact velocity of 0.5 m/s and an initial droplet radius of 1 mm were used to simulate the influence of the contact angle presented in Table 5.3	155
5.14	(a) droplet height with respect to time when penetrating the Berea porous structure; (b) and penetrating the carbonate porous structure. A constant impact velocity of 0.5 m/s and an initial droplet radius of 1 mm was used to simulate the influence of the contact angle, as presented in Table 5.3. On the left ,the non-dimensional droplet height is plotted with respect to time, while on the right, some inductive results for the droplet shape are shown	156

5.15	The early stage of droplet spreading on a Berea sandstone porous structure. a, b and c present different droplet conditions, while figure (d) summarises the effect of these conditions on penetration at constant imposed wettability	160
5.16	Effect of capillary pressure on droplet presentation behaviour for different droplet sizes or impact velocity by imposing constant wettability conditions	161
5.17	Mapping penetration with respect to Reynolds and Weber numbers; snap shots are presented for $T = 0.005s$	161
5.18	Effect of surface tension on droplet spreading and penetration, with an impact velocity of 0.5 m/s and a constant contact angle of $\theta_A = 125^\circ$, where $\theta_R = 25^\circ$	162
5.19	Schematic for multi droplets set-up: distance (a) represents the distance from porous edge; (b) is the distance between droplets; (c) is the distance from the centre; and R represents the droplet radius	163
5.20	Alpha iso-surface for 3D droplet with constant impact velocity for the three cases of 0.5 m/s and constant contact angle of $\theta_A = 125^\circ$ and $\theta_R = 25^\circ$	165
5.21	The early stage of droplet spreading on the Berea porous structure. On the left of each figure, is a diagonal cross-section presenting capillary pressure and the velocity vector, whilst on the right-hand side an alpha iso-surface for as 3D droplet is illustrated. There is a constant impact velocity for three cases of 0.5 m/s and constant contact angle of $\theta_A = 125^\circ$ and $\theta_R = 25^\circ$	166
5.22	Multi-droplet presentation for porous media; on the left is the total volume penetration with respect to time; on the right is 3D VoF representation for the droplet penetration pattern	167
A.1	Time evolution of the droplet shape when impacting on a ceramic porous medium ($K=1.04 \times 10^{-12}$,). Numerical simulations of the indicator function and velocity magnitude are compared with the photographs obtained by Chandra and Avedisian [12]	181
A.2	Time evolution of the shape of the impinging droplet obtained by numerical simulation for different permeability values. The white colour shows the indicator function	181

A.3	Schematic of the numerical grid. Picture (a) corresponds to the 2D slice (wedge) used in the calculation and picture (b) shows a schematic of the 3D rotation of this slice that results in a domain filled with toroidal items.	183
A.4	Time evolution of the shape of the impinging droplet: (a) $We = 62$ and (b) $We = 6$	184
A.5	Experimental picture of a water droplet impinging on $120 \mu m$ glass beads [13] (left) compared with numerical simulation of the Sandstone [14]. Both samples have the same porosity and permeability.	184
A.6	Snapshot at $t = 73$ msec of drop with $We=6$ into a porous stones geometry: numerical simulations of the indicator function (iso-surface of $\alpha = 0.5$) (right) and capillary pressure field (left) are presented.	185
A.7	Cross section showing water phase in blue and oil phase in yellow comparing case BM5 & BM6, showing the effect of capillary number on oil saturation at secondary injection	188
A.8	Plots of the capillary pressure and phase saturation (on the left), and also the computed effective permeability curves (on the right) for oil removal at secondary water injection process	189
A.9	Comparison between dynamic refinement effect (on the left) and no refinement method	191
A.10	Comparison between spreading on porous media (carbonated rock) using dynamic grid refinement Case 19 and without dynamic refinement Case 1 the graph showing 5% deviation while spreading. spreading conditions are impact velocity of 0.5 (m/s) and Droplet radius ($R = 1$ mm) with assumptions constant contact angle of $\theta_A = 125^\circ, \theta_R = 25^\circ$	192
A.11	Comparison between dynamic refinement effect (on the left) and experiments by [10] showing the bubble formation during impact.	193

List of Tables

3.1	Control parameters used in studying the static droplet. In these test cases C_{sh} and C_{comp} are set to zero	54
3.2	Control parameters used in studying the static droplet. In these test cases C_{sh} and C_{comp} are not set to zero	54
3.3	Reduction in predicted capillary pressure and parasitic currents compared to the standard <i>interFoam</i>	60
3.4	Table of numerical parameters for the Raleigh-Taylor simulation for two different mesh sizes.	64
3.5	Inlet velocities for liquid and gas, dimensionless numbers and regime expected	86
3.6	Fluid physical properties	87
3.7	Error in Bubble generation frequency	90
4.1	Summary of the rock properties and mesh quality used in this study . .	104
4.2	Fluid Properties	108
4.3	Case set up for wetting conditions and average flow rate: the surface tension, σ , used in all the simulations is constant and equal to 0.024 (kg/s^2), except in the BM5 case, which has a value of 0.0221 (kg/s^2) .	110
5.1	Properties of water droplets and impact conditions for the drop test . .	134
5.2	Properties of porous stones and mesh quality	136
5.3	Imposed contact angle for a porous media surface (using the Kistler dynamic contact angle model) with different assumptions concerning the contact angle of the pore surfaces (varying from fully hydrophilic to fully hydrophobic) at an impact velocity of 0.5 m/s and droplet radius of $R = 1$ mm	137

5.4 Imposed conditions for Berea porous media surface (using Kistler, dynamic contact angle model) with assumptions of constant contact angle of $\theta_A = 125^\circ, \theta_R = 25^\circ$ at different impact velocity, droplet radius and surface tensions 158

5.5 Imposed conditions for Berea porous media surface (using the Kistler dynamic contact angle model) with the assumption of a constant contact angle of $\theta_A = 125^\circ$ and $\theta_R = 25^\circ$ at different impact velocities and different droplet radii 164

A.1 Wetting Conditions for secondary water injection simulation 187

List of Nomenclature

A list is provided for all the nomenclature used in the upcoming chapters.

K	Permibility
u	Velocity
p	Pressure
p_c	Capillary pressure
p_d	Dynamic pressure
f	External forces
f_g	Gravitational forces
f_s	Surface tension force
ρ	Density
μ	Dynamic viscosity
$u_{r,f}$	Relative velocity at cell faces
σ	Surface tension
ϕ_f	Volumetric flux
ϕ_c	Compression volumetric flux
ϕ	Capillary flux
$\phi_{threshold}$	Threshold volumetric flux
V_i	Volume per grid cell
S_f	Outward-pointing face area
κ	Interface curvature
κ_f	Filtered interface curvature calculated based on smooth function α_{smooth}
$\kappa_{s,i+1}$	Smooth interface curvature calculated based on smooth function κ_f
κ_{final}	Weighted interface curvature calculated based on smooth function $\kappa_{s,i}$
η_s	Normal vector to the interface
δ_s	Dirac delta function
α	Volume fraction
α_{smooth}	Volume fraction using Laplacian formulation
α_{sh}	Sharp inductor function
$C_{compr.}$	Constant interface compression coefficient
C_{adp}	Adaptive interface compression
C_{sh}	Sharpening coefficient
U_f	filtering coefficient
$\langle \eta_s \rangle_f$	Face centred normal vector
$\langle \nabla \alpha \rangle_f$	Volume fraction interpolated from cell centre to face centre
δ_n	Small value
ε	A small value = $1e^{-8}$

Acknowledgements

Looking back at the day when I received my Ph.D. acceptance letter, I wonder, if I understood the magnitude of involvement in doing Ph.D. degree. I started my Ph.D. being very naive and with a very little understanding of what is happening around me. In fact, my brain for the first couple of weeks could not cope with the magnitude of the project. I kept telling myself "In four years you have to come up with a state-of-the-art solution to your Ph.D. problem," which of course seemed to be impossible with my limited knowledge back then. Nevertheless, I was blessed by being surrounded by people who believed in me, believed in my abilities, and supported me all the way since day one. Many unfortunate events let me down during the long Ph.D. journey, yet my belief in God and the firm belief that everything happens for a reason made me stronger -I guess-. Today, I am submitting my thesis not just to prove a strong understanding of my scientific background and to present my findings, but I have the feeling that this thesis is proof of overcoming all the struggles I had in the past. During my Ph.D. I have learned a lot, not just on the scientific level, but also on the professional level, and for that, I would like to express my most sincere gratitude to both my supervisors, Dr. K. Vogiatzaki and Prof. M. Gavaises for their continuous help and support during my Ph.D. project.

It is very difficult to express how much I value Dr. K. Vogiatzakis supervision, guidance, support and belief in my work. During the first two and a half years, Dr. K. Vogiatzaki dedicated almost all her time to my Ph.D. project and supported my ideas. She was very patient during my learning process and understood the challenges I had during the project. Her faith in my work along with the constant optimistic encouragement empowered my learning abilities and was strongly reflected in my work. Apart from the supervisor/student relationship, and beyond the professional aspect, I will always remember her as an excellent close friend who always helped me during

my tough times and understood my difficult situation no matter what. I was very fortunate and thankful to have Dr. Konstantina's great support and helpful selfless advice during my career decision even after my Ph.D. project. My gratitude also goes to Prof. M. Gavaises, who supervised my Ph.D. project. Prof. M. Gavaises valuable discussions and his knowledge helped me during my thesis period. Prof. M. Gavaises trust in my scientific background at the early binging of the project strongly influenced my work. For that, I would like to express my appreciation for his support, guidance and patience during the study. I am also grateful to the City University of London for funding this research project, where I had a great chance to learn and achieve my passion in such big institution. Also, I would like to thank my scientific collaborates from Cambridge University Dr. C. Bilger, Prof. RS. Cant for the amazing work published in the journal of Computational Physics, and for the effort described in Chapter 5. Also I would like to deeply thank Dr. A. Georgoula and Prof. M. Marengo for the collaboration with University of Brighton and for the work and effort described in Chapter 3 Chapter 5 and published in the journal of Computers and Fluids. During this collaboration we were able to publish 5 papers with a good impact factor journals and conformances. I would like to send my full gratitude to Dr. A. Georgoula for sharing with me his knowledge and time at the start of my Ph.D., as working with Tasos gave me the confidence to continue with my work and helped me a lot during paper publishing process. Also, I would also like to thank BETA CAE systems, for supporting my Ph.D. by using their software through the university academic licence. I want to express my gratitude and recognition to all those anonymous persons around the world who generously share their knowledge, giving their time and effort to the OpenFOAM community without expecting any reward.

I wish to express my full gratitude to Dr. N. Mitroglou who assisted me since day one, his never-ending support during my Ph.D. and after the Ph.D. period will never be forgotten. Dr. N. Mitroglous support and help in solving many technical issues did not just save a significant amount of time for me, but also helped me in learning new tools and techniques. Nicholas Mitroglou will always be like an older brother to me, and I am very fortunate and grateful for having him as a close friend. Also, I would like to thank Dr. H. Kassem for his support and the hours of useful discussions and specially for reviewing my long thesis. Hassan's guidance and experience during the last period of my thesis revision helped me alot and gave me lots of confidence. Hassan

is the OpenFOAM wizard, and I learned a lot from his selfless tips. Hassan Kassem's friendship was not just limited to my Ph.D. but turned out to be a lifetime friendship, and for that am very grateful. Also, I would love to express my deepest gratitude and admiration to my close friend Mr. Mohamed Nady, who may never understand the magnitude of his anonymous support. Nady's endless support and care for my family and me is worthless, and for him I am thankful.

All my special thoughts go to my lifetime partner, friend and wife Issra, who supported me despite my difficult situations. Her moral support during my Ph.D.'s tough periods and through my father's sickness meant a lot to me. Together we passed the most difficult times in our life, and for that I am grateful. I assume, without her support and belief in me; it would not be even possible to get the degree. I know she sacrificed a lot during the last tough 5 years, and it is my life promise to make it up for her. No words can express my love for her, but I am simply thankful for her presence in my life, and I could not ask for more.

I would also express my special gratitude to my family, without my father, my mother and my younger brothers support I would not be even here today. The unconditional support and the amount of trust, belief and love I received from my parents was my only reason to work harder. Even during the hardest period of my father's sickness, they supported me to be strong and focused. I would also like to thank my younger brother for his support and motivation. Dad, Mom and Magdy, I hope I made you proud by getting my Ph.D. degree.

I dedicate this thesis to my father-in-law who passed away during my thesis writing up period and supported me all the way. He always believed in me as his son, and I know he was waiting for that day to come back home with my PhD degree. I send my prayers to you, and I know God loves you, so May God have mercy on your soul, and hopefully, I made you proud.

*Finally, I thank God for giving me all the help, strength and
determination to complete my Ph.D.*

Declaration

I declare that this thesis was composed by myself, that the work contained herein is my own except where explicitly stated otherwise in the text, and that this work has not been submitted for any other degree or professional qualification except as specified. Some parts of this work have been published as following;

- **Aboukhdr, M.**, A. Georgoulas, M. Marengo, M. Gavaises, and K. Vogiatzaki. "Effect of contact angle hysteresis on droplet impacting onto micro-CT reconstructed porous media at low Weber numbers." *Journal of Colloid and Interface Science* (2019) Under Review.
- **Aboukhdr, M.**, A. Georgoulas, M. Marengo, M. Gavaises, and K. Vogiatzaki. "Simulation of micro-flow dynamics at low capillary numbers using adaptive interface compression." *Computers & Fluids* (2018).
- Bilger, C., **Aboukhdr M.**, Vogiatzaki K., & Cant RS. "Evaluation of two-phase flow solvers using Level Set and Volume of Fluid methods." *Journal of Computational Physics* 345 (2017): 665-686.
- **Aboukhdr, M.**, Vogiatzaki, K., Mitroglou, N., Georgoulas, A., & Marengo, M. (2017). Simulation of droplet spreading on micro-CT reconstructed 3D real porous media using the volume-of-fluid method. *ILASSEurope 2017, Conference on Liquid Atomization and Spray Systems*, 28. doi:10.4995
- **Aboukhdr M.**, Georgoulas A., Gavaises M., Marengo M. & Vogiatzaki K. (2016) Numerical investigation of droplet spreading on porous and non-porous surfaces, 27th Annual Conference on Liquid Atomization and Spray Systems-ILASS, Brighton, UK.

- **Aboukhedr M.**, Georgoulas A., Gavaises M., & Vogiatzaki K. (2016). A novel framework for modelling micro-droplet interface dynamics at low capillary numbers. PMPM and UK InterPore Joint Annual Meeting
- **Aboukhedr M.**, Vogiatzaki K., Mitroglou N. & Gavaises M. (2015) A numerical simulation of single and two-phase flow in porous media; a pore-scale observation of effective microscopic forces, 6th BETA CAE International Conference, At Greece, 6.
- **Aboukhedr M.**, Vogiatzaki K. & Gavaises M. (2015) Direct numerical simulation of pressure drop in micro channels with various pillars arrangements, 7th International Conference on Porous Media & Annual Meeting Italy

Abstract

Liquid flow penetrating into porous media, such as rocks, metal foam, soil, and drug delivery, are often simulated as a single phase or multiphase continuum using Darcy's law. Darcy's law considered being the most used model of many approaches for simulating the flow through porous media, where the Darcy model assumes a simple proportional relationship between the instantaneous discharge rate through a porous medium, the viscosity of the fluid, and the pressure drop over a given distance. The law was formulated based on the results of experiments on the flow of water through beds of sand. It also forms the scientific basis of fluid permeability used in the earth sciences, particularly in hydrogeology. The underlying assumption with the Darcy method is that the microscopic concept of the liquid flow in any porous material will involve the use of the microscopic velocities associated with the actual paths of the liquid. However, in practice, it is challenging to measure the real microscopic velocities and for this reason, the average value of the real velocities is accepted. By averaging the steady-state Stokes equation this leads to Darcys law, which was introduced as an empirical relationship to describe flow in sand filters, as discovered by Darcy in 1856 and this served as a starting point for numerous practical applications and as a constant challenge for theoreticians.

While the original conditions studied by Darcy are found in many practical situations, its extensions to more general cases that are especially designed for theoretical analysis are widely used to represent situations in which experiments are difficult to perform. While this form of Darcy's law is used with great frequency, it is difficult to get experimental verification of the obvious terms representation of Darcy's law. For example, the Darcy velocity, which is defined as a volume-average of the flow field, does not represent the real velocity inside the porous media, but rather, the volume of fluid flowing per unit area of the porous medium, including both solids and voids. Also, the pressure gradient does not represent the microscopic pore-level quantity, but rather, is defined over a representative elementary volume medium.

To explore Darcy assumptions and to understand the controlling pore-scale mechanisms, a numerical framework has been developed that involves using a reconstructed real porous medium to present a detailed numerical domain for multiphase flow simulations. For the numerical multiphase flow methodology the Volume-of-Fluid (VoF) method combined with additional sharpening, smoothing and filtering algorithms is used as a basis for interface capturing. These algorithms help in the minimisation of the parasitic currents presented in flow simulations. The framework is implemented within a finite volume code (OpenFOAM) using a limited Multidimensional Universal Limiter with Explicit Solution (MULES) implicit formulation. This framework allows for more substantial time steps at low capillary numbers to be utilised compared to the standard solver. In addition, a novel adaptive interface compression scheme is introduced. This allows for dynamic estimation of the compressive velocity only at

the areas of interest and thus, has the advantage of avoiding the use of a priori defined compression coefficient parameters. The adaptive method increases the numerical accuracy and reduces the sensitivity of the methodology to tuning parameters. The accuracy and stability of the proposed model are verified against different benchmark test cases. Moreover, the numerical results are compared against analytical solutions as well as available experimental data and this reveals improved predictions relative to the standard VoF solver.

This thesis is focused on two different applications that involve porous media: first, flow and transport inside a porous structure, where the presented simulations results show the importance of liquid front invasion. Also, the salience of phase wettability on the residual phase using different wetting dynamic conditions is demonstrated. The results for simulations relating the pore-scale physics, thereby obtaining permeability values are presented. The overall results provide a detailed pore-scale analysis of multiphase flow, serving as a foundation for large-scale modelling and flow prediction. The second application is droplet impact on porous structures and the penetration physics on porous media. The work is focused on droplet spreading and absorption during the early stages of impact. Using the developed framework, the droplet penetrating the porous media is also studied. In addition, simulations of the penetration of different sizes of droplets with different fluid properties in the pore network with different porosities are performed to characterise the effect of the Re and We numbers on the penetration behaviour. The capability to estimate the key features of the flow dynamics has been investigated. For example, in order to relate the microscopic effects to the macroscopic ones, it is important to focus on the maximum spreading, while considering the influence of liquid properties, and wetting behaviour with relation to porous media properties such as porosity. Some conclusions regarding the relation between porosity and porous wall wetting conditions have been drawn using the developed numerical framework for studying the liquid spreading onto porous media. Also, in the thesis, the influence of the porous structure wetting behaviour, the morphology of porous surfaces and the effects of porosity on droplet penetration and spreading are presented. Using the proposed developed solver, a direct relation between penetration volume and the imposed dynamic contact angle was found. This would appear to contradict the expected behaviour in vertical liquid penetration that is obtained using the macroscopic multiphase Darcy's law.

The goals of this research have been achieved by deploying the complex flow physics using the two described applications and by showing the importance of the developed framework in relation to a wide range of applications. This provides evidence for the effectiveness of studying multiphase flows at the microscale level using interface tracking methods.

The Present Contribution

This study is aimed at simulating the flow inside porous media at low capillary numbers, which is induced either by pressure drop or by the impact of liquid droplets. Thesis contribution is presented in the following two sections:

Thesis Novelty

A numerical two-phase flow solver available within the OpenFOAM open source package is modified and extended to include the following new methods that have been developed as part of this study.

1. A new adaptive compression scheme is presented in Section 2.2.1, which allows for dynamic estimation of the compressive value only within the areas of interest (typically the diffused interface) and this has the advantage of avoiding the use of a priori defined parameters for the areas where this is applied. The adaptive method is found to increase the numerical accuracy and to reduce the sensitivity of the methodology to tuning parameters, as shown in Sections 3.4, 3.5 and 3.6.
2. The previous model was coupled with additional sharpening and smoothing algorithms for interface capturing, as presented in Sections 2.2.2 and 2.2.3. This coupling helps to minimise the parasitic currents present in low capillary number simulations, when viscous forces and surface tension dominate inertial forces, as presented in Section 3.6.
3. As a result of the numerical unbalance when modelling the movement of a closed interface, it is difficult to maintain the zero-net capillary force while modelling the movement of this interface. By using the calculated forces from the mentioned models in items 1 and 2 the capillary force then used to filter the capillary fluxes using a thresholding scheme mentioned in Section 3.17d to maintain a zero-net capillary force, while modelling the movement of the interface.

4. A coupling between the capillary pressure and the Navier-Stokes equations is added to improve the efficiency of the numerical method for low capillary number flows, as presented in Section 2.2.4. The new solver implementation is able accurately and efficiently to decrease the computational cost for this type of simulation by eliminating the spurious current problem present in the standard VoF formulation.

Flow and transport in porous structures

By using the new developed numerical framework, two-phase flow simulations through porous media have been performed. That is, the mechanisms dominating the flow development in two areas of physical and technological interest have been investigated as follows.

- First, the flow transport mechanics inside numerically reconstructed porous materials have been simulated, with the porous geometry being obtained from CT data.
1. Two-phase flow simulations for drainage on porous media at different capillary numbers have been executed and their residual non-wetting phase saturations computed. Also, prediction of droplet snap-off and droplet trapping during the drainage process have been achieved.
 2. These aforementioned physical phenomena were also tested using different wetting conditions, by using the Kistler model at the porous walls. Introducing the dynamic wetting model at pore scale allows for predicting the different drainage regimes for the same capillary number.
 3. Using the mentioned wetting conditions, the relations between the forces active at the sub-pore scale for different flow scenarios and capillary pressure drops have been effectively identified. These relations have been found to provide an explicit method for upscaling the numerical simulation results and calculating the relative permeability curves.
- The second scenario investigated was with regards to the impact of liquid droplets on the surface of porous media, simulations of which have not been presented

before in the literature. Using the described developed code the following have been achieved.

1. Two-phase flow simulations for drainage on porous media at different capillary numbers have been presented and their residual non-wetting phase saturations have been recruited. Also, prediction of droplet snap-off and droplet trapping during the drainage process has been achieved.
2. These aforementioned physical phenomena were also tested using different wetting conditions, by using the Kistler model at the porous walls. Introducing the dynamic wetting model to the pore scale has allowed for the prediction of different drainage regimes for the same capillary number.
3. Using the mentioned wetting conditions, the relations between the forces active at the sub-pore scale for different flow scenarios and capillary pressure drops have been successfully uncovered. These relations have been found to provide an explicit method for upscaling the numerical simulation results and calculating the relative permeability curves.

Chapter 1

Introduction & Literature Review

1.1 Background

Flows of two or more phases through "narrow passages", such as micro-channels or pore-scales, the dimensions of which are less than a millimetre and greater than a micrometer, are commonly used/presented in a wide range of geological processes and industrial areas. Flow physics is different to its macroscopic counterparts in important aspects, such as: (i) the small size of the geometries, which create molecular effects, such as wall slip or wettability; and (ii) the amplifications magnitudes of certain ordinary continuum effects associated with strain rate and shear stress. Such flows are present in various natural formations (rocks and human organs) as well as man-made applications (micro-conductors, microemulsions). Thus, micro-scale flows attract the interest of various disciplines including the cosmetic, pharmaceutical, biomedical and petroleum engineering industries.

Among all these applications, flow transport inside porous media and droplets impinging onto porous structures at low capillary numbers ($Ca = \frac{\mu V}{\sigma}$), where V is the Darcy velocity, μ is dynamic viscosity and σ is the interfacial tension, has attracted the interest of both the theoretical and experimental research [15–17]. The capillary number indicates the magnitude of viscous forces, represented by fluid viscosity multiplied by its velocity, in relation to forces due to surface or interfacial tension. In enhanced oil recovery operations, capillary number is an important number to consider. Where the value of capillary number is higher, viscous forces dominate and the effect of interfacial tension between fluids in the rock pores is reduced, thereby augmenting recovery. In typical reservoir conditions, capillary number varies from 10^{-8} to 10^{-2} . Effective permeability to water is described in the following section. Also, understanding the dynamics of immiscible fluids in micro-devices can facilitate the creation of monodisperse emulsions. Droplets of the same size moving with low velocities through microchannel networks are used as micro-reactors to study very fast chemical kinetics [18]. Another example is how low Ca flow dynamics in micro-scale porous media can be seen in trapped oil blobs in porous reservoirs. Understanding the trapping flow dynamics at the pore scale level can be a key to minimising the trapping of a non-wetting phase and enhancing the recovery systems of hydrocarbons [19]. Moreover, the interpenetration of the liquid-vapour interface into porous media is widely seen in practical applications, such as the flow through the wick structure inside heat pipes, which uses capillaries to move the liquid working fluid from the condenser back to the evaporator section.

The term multiphase also covers a wide range of flow patterns and regimes, such as immiscible two-phase flow in porous media. Inside porous media, solid-fluid tortuosity interaction can affect the flow behaviour of immiscible fluids. Immiscible fluids co-existing in a porous medium are labelled as the (a) wetting phase and (b) non-wetting phase, where the former refers to the fluid with a higher affinity to wet the porous surface. Immiscible flows are classified into two groups: (a) *drainage*, in which a wetting phase is displaced by a non-wetting one; and (b) *imbibition*, in which a wetting phase displaces a non-wetting one. The imbibition process is further divided into two flow patterns, namely co-current, with both phases flowing in the same direction, and counter-current flow, in which the two phases flow in opposite directions. The variety of these combinations and the inherent complexity of pore-scale displacement through the irregular geometry of natural porous media makes the prediction of two-phase flow in many processes a challenging task.

Accurate prediction of the behaviour of multiphase flow is of vital importance in many engineering fields. As an example, in the petroleum industry, the economic value of a reservoir is determined by the amount of oil that it can produce. It is affected by both the field scale behaviour of fluid flow present in the porous media as well as the pore-scale behaviour of the flow. Knowing the latter, gives a better understanding of the macroscopic (core-scale) properties of porous media, such as relative permeability and capillary pressure curves. These macroscopic properties, which are used in field-scale simulations of flow through porous media, are conventionally obtained from laboratory experiments or by history matching to field observations. However, both of these two approaches are costly and time-consuming. Moreover, they may give answers that are non-unique or unrepresentative of the field as a whole. Further, it is difficult to perform experiments on pore-scale behaviours and to extrapolate to the macroscopic level.

Nevertheless, similar approaches are taken into account to study the effect of porous media using a numerical approximation, such as Darcy models, to establish the link between the microscopic and macroscopic without the need for a high level of complexity. In this chapter, the literature on flow dynamics inside porous media and its interlinking with droplet impacting porous structures will be summarised. Then, there will be discussion on the numerical challenges with respect to creeping flows. Finally, the research objectives are presented.

1.2 Two-phase Flow Through Complex Porous Structures

Capillary flow and penetration of liquid into porous structures can be linked to many applications. For example, the liquid absorbed into a permeable fabric [20], the spontaneous imbibition during oil recovery and two-phase fluid transport in fuel cell applications, which is an essential industrial application for penetration into porous material [21, 22]. There have been several studies on the impact and penetration of a liquid droplet in simplified geometries, such as capillary tubes. For example, Delbos et al. [23] experimentally investigated the penetration of a capillary tube using the kinetic energy of an impacting droplet. Moreover, Delbos et al. [23] focused on a single capillary tube with either a hydrophilic or hydrophobic surface. In the presented experiment [23], the impact of a liquid drop on a single hole, with a diameter of the same order of magnitude size was evaluated. Different regimes for penetration based on the hydrophobicity of the surface were predicted based on the wetting conditions. These studies presented detailed experimental investigation of the phenomenon of penetration concentrated on the effect of varying droplet size rather than pore size using non-realistic porous structures, their authors did not take into account geometrical complexity.

A porous medium is a structure containing pores (voids). The pores are typically filled with a fluid (liquid or gas). The porous medium is usually a solid, but structures like foams are often also usefully analyzed using concept of porous media. A porous medium is most often characterized by its porosity. Other properties of the medium (e.g., permeability) can sometimes be derived from the respective properties of its constituents (solid matrix and fluid) and the media porosity and pores structure, but such a derivation is usually complex. Even the concept of porosity is only straightforward for a porous structures.

Often both the solid matrix and the pore network (also known as the pore space) are continuous, so as to form two interpenetrating continua such as in a sponge. However, there is also a concept of closed porosity and effective porosity, i.e., the pore space accessible to flow. Many natural substances such as rocks (such as petroleum reservoirs), biological tissues (such as bones), and man-made materials such as cements and ceramics can be considered as porous media. Fluid flow through porous media is a subject of most common interest and has emerged a separate field of study.

Large-scale flow through porous media is described by defining the macroscopic

pressure and flow rates over a representative elementary volume (REV), where the REV-scale is that above which the heterogeneities at smaller scales do not affect these macroscopic properties. The Darcy equation is then used to relate the flow rate to the macroscopic pressure drop (Δp), which for single-phase flow through a one-dimensional porous medium with a length of (Δx) is as follows. Darcy found that flow rate was proportional to pressure gradient. Darcys equation for calculating volumetric flow rate q for linear, horizontal, single-phase flow is

$$q = -\frac{KA}{\mu} \frac{\Delta p}{\Delta x} \quad (1.1)$$

where q is volumetric flow rate, K is permeability, A is cross-sectional area, p is pressure, μ fluid viscosity, Δx is length of porous sample. The movement of a single-phase fluid through a porous medium depends on cross sectional area A that is normal to the direction of fluid flow, pressure difference Δp across the length Δx of the flow path, and viscosity μ of the flowing fluid. The minus sign indicates that the direction of fluid flow is opposite to the direction of increasing pressure: the fluid flows from high pressure to low pressure in a horizontal (gravity-free) system. The proportionality constant K in Eq. 1.1 is permeability. If we rearrange Eq. 1.1 and perform a dimensional analysis, we see that permeability has dimensions of area (L^2), where L is a unit of length. The areal unit (L^2) is physically related to the cross-sectional area of pore throats in rock. A pore throat is the opening that connects two pores. The size of a pore throat depends on grain size and distribution. For a given grain distribution, the cross-sectional area of a pore throat will increase as grain size increases. Relatively large pore throats imply relatively large values of L^2 and correspond to relatively large values of permeability. Permeability typically ranges from 1 md ($1.0 \times 10^{-15} m^2$) to 1 Darcy (1000 md or $10^{-12} m^2$) for commercially successful oil and gas fields. Permeability can be much less than 1 md in unconventional reservoirs such as tight gas and shale gas reservoirs. Advances in well stimulation technology and increases in oil and gas prices have improved the economics of low-permeability reservoirs.

Evaluation of the influence of different parameters on liquid penetration, including Darcy number $Da = (\frac{K}{r^2})$, where K is the permeability and r is the porous media grain size was chartrised by Reis et al. [24] showing the ratio of the flow momentum to dissipation by the porous matrix. In fluid dynamics of flow through porous media, the

Darcy number represents the relative effect of the permeability of the medium versus its cross-sectional area. Smaller values of Darcy number show that the flow resistance of the substrate is significant, since the space available for the fluid to flow into is smaller, and the penetrated liquid occupies a larger overall volume of the substrate. Many models had been developed to replace the geometrical complexity using the generic definition of the Darcy Law [25, 26]. In the study of droplet impact/flow in porous structures, several parameters need to be also considered, such as the spreading diameter, contact angle and penetration depth. These parameters cannot be modelled using the traditional Darcy law due to various reasons. The next section will briefly review the common literature on the droplet impacting dynamics and capillary penetration effect, and its importance to flow inside porous media.

1.2.1 Droplet Impacting on Porous Media

Droplet impact on porous media is one of the most evolving fields of study due to its complexity. Droplet penetration and spreading occur in many important applications, such as printing using inkjets, where an ink droplet is deposited on the surface of porous paper and in the spray coating of porous surfaces. In nature, it happens with rainfall on soil and wetting by rain droplets carried by the wind affecting a buildings porous structure. Recently, several attempts have been made to enhance spray cooling performance by coating surfaces with small particles [27], or by constructing microstructures [28, 29] on the target surfaces. According to [28], the cooling performance could be significantly improved by employing such artificial surfaces, because not only the liquid-solid interfacial area is enlarged, but also, the contact between the surface and the droplets is maintained longer. Different droplet dynamics during the first impact may affect building materials, which becomes an important issue when, for example, maintaining old or historical buildings by adding insulation. Not only is droplet impact dynamics on porous surfaces vital for durability assessment, but also drop impact on surfaces is every day and found everywhere phenomenon with essential applications. In sum, the phenomenon of droplet impact and spread can be found in natural, agricultural and industrial processes, such as microchip production, microfluidic applications, analysis of DNA microarrays, and spontaneous imbibition that is of particular importance to oil recovery from fractured reservoirs [21].

Regardless of the importance of impact and penetration behaviour given the criti-

cal role it plays in different applications and the impacts of a liquid droplets on solid surfaces as well as liquid penetration through porous media having been studied extensively individually, there have been very few studies on their combined effects. A comprehensive explanation of drop physics on porous media is challenging given their complex structure in terms of surface roughness and absorption by capillary force.

When a droplet falls on a non-porous solid material, it spreads in a radial direction to the maximum spreading diameter, which is considered to be the advancing phase. Then, the droplet retracts in what is known as the receding phase and after several oscillations reaches an equilibrium shape on the top of the surface. Based on the wetting conditions and the droplet spread, it may splash and break up into small droplets or it may bounce off the surface [30, 31].

The maximum spreading diameter and the final outcome of the droplet impact depend on the droplets impact velocity, size and liquid along with surface properties, including surface tension, surface roughness and wettability [32]. Other effects, such as bubble formation during the impact [33] as well as hydrophobic and hydrophilic surface effects [4, 32, 34, 35] have also been considered in the literature. The impact of droplets on porous media is determined by a combination of droplet impact on a solid non-porous surface and capillary penetration of the liquid into the media. Droplet behaviour on impact is driven by different contact phenomena, including: (1) droplet related characteristics, like droplet size, impact velocity and incident angle; (2) surface related characteristics such as dynamic spreading, wetting behaviour and porosity; as well as (3) evaporation from the droplet surface and wetted surface.

As abovementioned, studies focused on droplet impact and penetration into real porous materials are limited [10, 11]. Most of these have been focused on the imbibition of liquid due to capillary pressure difference. For example, there has been prior research on liquid droplet impact on a single hole in terms of the scale of droplet size, and penetration behaviour based on the hydrophobicity of the surface. Yue and Renardy [36] proposed a model for the penetration of a non-wetting liquid droplet into a porous medium, with the droplet being considered to be approaching an exposed pore along the axis of symmetry. Four penetration regimes were identified based on the static contact angle and initial droplet radius. Studying penetration on a single hole, which characterises the porous structure, neglects the effects of inertia and capillary complexity. However, this work has revealed different possible scenarios for spreading regimes: (1) penetration without spreading; (2) penetration with spreading;

(3) penetration with spreading that relies on the initial contact velocity; and (4) non-penetration with spreading. Chandra and Avedisian [12] studied the dynamic aspect (deformation and spreading on a surface) of an n-heptane droplet impingement onto a porous ceramic surface with different surface temperatures. Droplets impacting on these surfaces may undergo very different outcomes, such as deposition, spreading, splashing or rebound, as shown in Fig. 1.1 [1]. The outcome of droplet impact depends on the impact conditions (impact velocity, drop size, the angle of impact, cross air flow, liquid and air temperature), properties of the liquid (density, viscosity, surface tension), as well as the geometry of the surface wettability, i.e. roughness. Research on the effects of these parameters in studying droplet impact is constantly evolving. The understanding of spreading is crucial regarding the determination of the outcome of droplet impact and its deposition on surfaces due to capillarity penetration.

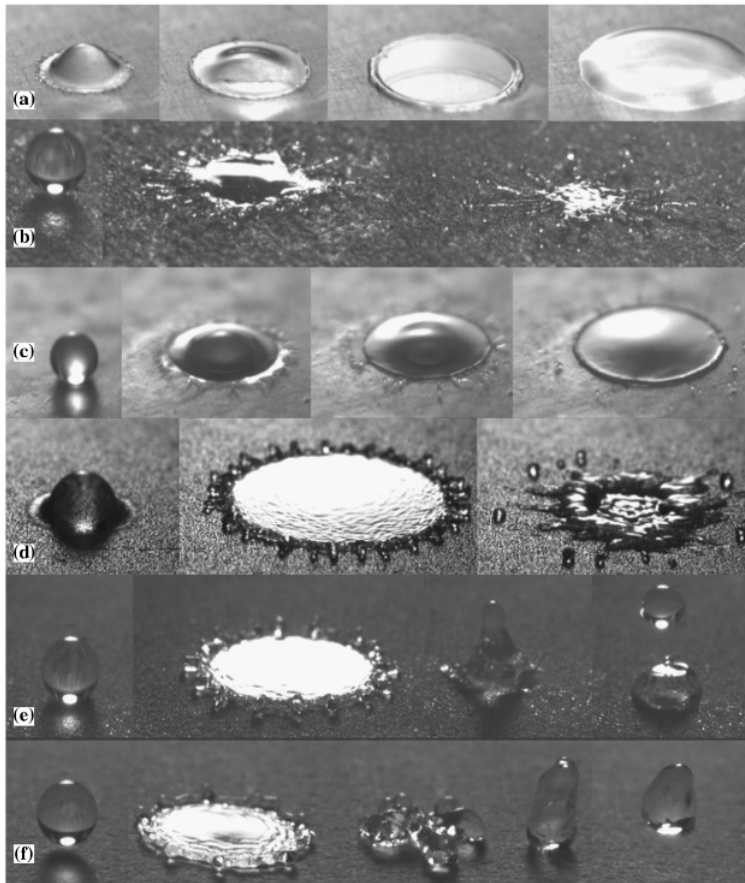


Figure 1.1: Outcomes of droplet impact on various substrates. (a) deposition: on rough glass ($D_0 = 1.7$ mm, $U = 1.8$ m/s); (b) prompt splash: water droplet on rough PE ($D_0 = 2.4$ mm, $U = 3.1$ m/s); (c) corona splash: isopropanol on light rough ceramic ($D_0 = 1.7$ mm, $U = 2.51$ m/s); (d) receding breakup: water on porous stainless steel ($D_0 = 2.4$ mm, $U = 3.44$ m/s); (e) partial rebound: water on porous bronze ($D_0 = 2.44$ mm, $U = 2.44$ m/s); (f) rebound: water on porous PTFE ($D_0 = 2.44$ mm, $U = 1.86$ m/s) [1]

In general, the literature survey on droplet behaviour impacting on a porous surface

can be summarised as shown in Fig. 1.2. When the droplet is impinging against the surface of the porous surface, it permeates into the porous medium while also spreading along the surface. The spreading and the permeation motions co-occur from the instant of the droplet impact to the maximum spreading state and then, the remaining liquid on the surface is simply permeated into the substrate with minimum receding motion at a pinpoint on the surface.

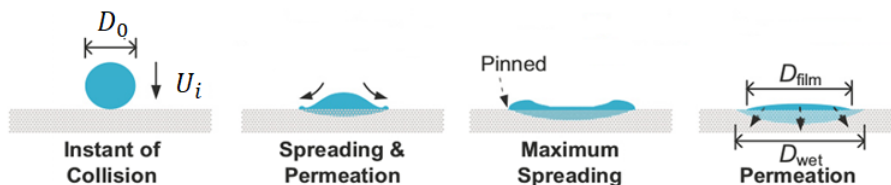


Figure 1.2: Schematic of droplet impingement against porous substrates [2], where D_0 is the droplet diameter before impact and U_i is the droplet velocity before impact

The spreading process can be considered as being a balance of the kinetic $e_k = \rho D_0^3 U_i^2$, capillary $e_\sigma = \sigma D_0^2$ and viscous energies, where ρ is the fluid density, σ the fluid surface tension, D_0 the initial droplet diameter and U_i is the impact velocity. To compare different conditions, two dimensionless numbers are used: Weber number $We = \rho U_i^2 D_0 / \sigma$, where it represents the ratio between the inertial and capillary forces (kinetic and capillary energies), and Reynolds number $Re = \rho U_i D_0 / \mu$, where it represents the ratio between the inertial and viscous forces (kinetic and viscous energies). The maximum droplet spreading diameter is often reported as the maximum spreading ratio D_{max}/D_0 , where D_{max} is the maximum spreading diameter. After a droplet impacts on a porous medium, it spreads over the porous surface and is absorbed into porous media by capillarity. The spreading of the impacting droplet over the porous surface is governed by the same factors as mentioned before, while its absorption into porous media is dependent on the properties of the liquid and the porous medium, such as porosity, pore size and connectivity as well as wettability in the pore [37, 38]. Once the inertia of the droplet impact is dissipated, the capillary absorption of the deposited droplet into the porous medium continues until the liquid is depleted from the surface. The absorbed liquid is further redistributed and also evaporates through the surface of the porous medium. Reis et al. [24] performed implicit numerical simulations of droplet impact on porous media with the VoF method. The implicit numerical model was developed to resolve the shape of the impacting droplet on the surface and the liquid content distribution in the porous medium. Using this numerical methodology they performed a parametric study for impact condition, permeability, porosity, pore

size and wettability, using a black box approach for the porous structures. The simulated liquid content in the porous medium was compared with Magnetic Resonance Imaging (MRI) after full absorption. It was found that they could be predict similar shapes, but not with a great deal of accuracy.

More recently, droplet impact on granular media has been studied. Marston et al. [39] studied the maximum droplet spreading diameter on packed glass beads for different liquids. Zhao et al. [40] measured the maximum depth and showed that the maximum spreading for water droplets impacting on dry glass bead granular media scales with the effective Weber number defined by the maximum crater depth. Whilst several studies have involved investigating drop impact on porous media, the influence of such media on spreading is still unknown due to the presence of simultaneous phenomena occurring, especially spreading and absorption. One of the main reasons for the unclear characterisation of these phenomena is the lack of knowledge of the contact line behaviour on porous and rough surfaces. There is a clear need to properly quantify droplet spreading on porous media. As most of the experimental results document only the exterior geometry of the droplet during spreading, numerical studies are needed to identify flow and pressure fields within the droplet during penetration inside the porous structures. The typical process of spreading and penetration occurs in micro or milliseconds over a micro or millimetre length. The currently available experimental methods do not allow yet for the examination of all the aspects of droplet physics on porous media with sufficient spatial, temporal resolution and information inside them. There is, indeed, a great need for numerical studies, that will enable the capturing of the hydrodynamics of penetration on a complex porous surface and the liquid mass migration inside porous media. The questions that still await a comprehensive explanation are

- how the impinging droplet spreads over the porous media.
- how the water is absorbed into porous media from the impacting droplet.
- and what are the mechanisms of water distribution inside porous media.

1.2.2 Capillary Flow Through Porous Media

Apart from the impacting behaviour, the capillary effect has a significant influence on the two-phase flow of liquids into the porous structure. The capillary penetration of

the liquid into the pore spaces is mainly due to pressure gradients in the pore network or interfacial pressure differences. The simplest model of liquid flow into capillaries is that of cylindrical capillary tubes. Hamraoui and Nylander [41] studied the mechanism of capillary rise into an infinite cylindrical capillary tube by accounting for all the dynamic and physical forces applied to the meniscus of the liquid in capillary tubes, which include: surface tension force, inertia force, gravity force and that due to liquid viscosity. The equilibrium of these forces leads to the Lucas-Washburn equation:

$$\rho\pi r^2 \frac{\partial}{\partial t} \left(h(t) \frac{\partial h(t)}{\partial t} \right) = 2\pi r \sigma \cos(\theta) - \pi r^2 \rho g h(t) - 8\pi \mu \frac{\partial}{\partial t} \left(h(t) \frac{\partial h(t)}{\partial t} \right) \quad (1.2)$$

where, σ is the surface tension, ρ and μ are liquid density and dynamic viscosity, respectively, $h(t)$ is the penetration of liquid into the capillary tube over time of t and r is the capillary radius. The analytical solution using Eq. (1.2) shows that the liquid imbibition into a capillary tube changes proportionally to \sqrt{t} without considering droplet impingement momentum or additional forces. Experimental studies of droplet impact onto capillary holes represent a trend of penetration with a stronger effect on inertia due to consideration of the momentum of impact. Regarding the parametric studies on the effect of each governing parameter in Eq. (1.2), it has been shown that penetration into a capillary depends on its diameter and the contact angle rather than physical properties (viscosity and surface tension). Also, the value of the contact angle, which is dependent on the surface and liquid, can either drive or oppose capillary penetration [42]. The dynamics of the capillary rise of liquid into the capillary tube can also be derived using a momentum balance for the liquid inside the tube. Capillary forces must be balanced by inertial viscous and hydrostatic forces:

A divergence from the experimental investigations was found due to the effect of a thin air layer, which may affect the capillary penetration. Based on the theoretical understanding of the capillary effect, the impact of droplets on a porous structure may or may not penetrate through a capillary gap depending on the droplet velocity, fluid properties, contact angle and geometrical parameters of the gap. However, it is evident that capillary penetration increases with a reduction in viscosity and with large surface tension [43]. Davis and Hocking [44] studied spreading and imbibition of deposited droplets on porous media and predicted their depletion time. Also, Davis and Hocking [44] elaborated upon an analytical model that considered the contact line

slip on the surface using the lubrication approximation. Clarke et al. [45] showed the absorption of droplet impingement into microporous filter membranes by measuring the volume of deposited droplets remaining on the surface and proposed an analytical model using the Lucas-Washburn equation derived from Darcys law.

Markicevic and Navaz [46] showed the transition numerically between fully and partially saturated moisture content during droplet absorption. Markicevic and Navaz [46] developed a capillary network model based on the micro-force balance, with the same formulation applied to primary and secondary infiltrations. However, most of the previous studies were focused on absorption mass and depletion time to understand absorption behaviour as they had no accessible information on liquid transport inside porous media. For a better understanding of the absorption process inside porous media, the direct observation of the liquid content redistribution in them is required and this has been studied with non-destructive techniques. Reis et al. [47] used an MRI measurement to investigate the evaporation of the droplets in glass bead substrates. The results showed that the general shape of liquid redistributed within the porous media resembles a half spheroid and compared with the implicit numerical simulation with less matching results than expected. For these previous experimental studies, low temporal and spatial resolutions were used to capture the absorption process of a droplet in a porous medium in sufficient detail.

1.2.3 Challenges in Modelling the Pore-scale Effect for Multiphase Flow Transportation

The pore structure representation is one of the crucial aspects when studying the effect on fluid flow physical behaviour at pore scale. As aforementioned, it is a quite challenging task, especially for numerical studies, due to the geometrical complexity associated with porous structures. The wide range of scales is one additional challenge to understanding the geometrical complexity. Various methods have been developed to generate a three-dimensional (3D) representation of complex pore space, such as porous rock structures. One commonly used approach is the direct imaging reconstruction, which produces 3D images mapping the interior structure of the rock sample, such as non-destructive X-ray micro-tomography (micro-CT). Micro-CT technology provides a direct way to image the pore space with a high resolution volumetric (3D) representation of structures.

These high-resolution 3D images of a pore space provide the opportunity to simulate two-phase flow directly onto real porous media. In addition, they allow for studying of the mechanisms that control the flow patterns at the pore level and relating them to the macroscopic properties of the porous media, which are conventionally expressed in terms of the porosity, permeability, relative permeability curves and capillary pressure curves. From the above considerations, it is clear that the development of a framework that can model with considerable detail and with sufficient accuracy the dynamics of flow onto the micro-CT images of the pore space in particular, two-phase flow would be greatly beneficial. Such a framework exists in the form of pore-scale simulation of fluid flow and associated phenomena, using computational fluid dynamics (CFD).

However, modelling multiphase flow in porous media is a challenging task, as it concerns forces acting at different scales in the flow domain. Liquid viscosity is responsible for the dissipation of energy of the fluid system at larger scales. Moreover, the interfacial tension between two fluids governs the shape and movement of one phase with respect to the solid boundaries at the pore scale. Finally, wall adhesion forces are active at the nanoscale thickness of the contact lines, controlling the contact angle and contact line dynamics.

In many transport problems in porous media, capillary forces are more significant at the pore scale than viscous ones. For example, typical capillary numbers in petroleum reservoirs are in the range ($Ca = 10^{-10}$ to 10^{-5}) Lake [48]. As a result, if any small numerical error is introduced due to the incorrect capillary forces calculation, a huge numerical instability will be triggered, which may affect the numerical method up to a point where it is unusable. Moreover, the numerical method should be able to handle complex interface motion and complex solid boundaries encountered in flow through porous media.

Also, in this study, finding a method that can be used in multiphase flow simulation of micro-CT images of porous rocks, which may contain millions of grid cells in practical simulation time is one objective. To summarise, pore-scale simulations of multiphase fluid flow in porous structures present a challenging problem compared to single-phase flow simulations for three main reasons found in the literature: (1) it is very challenging to have a fast, robust, and accurate multiphase solver to predict the complex dynamics of multi-fluid interfaces; (2) the behaviour of multiphase fluids with large density, viscosity, and compressibility ratios is difficult to compute accurately at very low capillary numbers even with many exciting robust methods; and (3) the

behaviour at the solid-fluid contact lines and its association with that of the dynamic contact angles is inherently complex and sensitive to small length-scale that influence the wetting behaviour and/or surface tension. This been said, it is important to add that in some applications, the flow driven by surface tension gradients may be necessary for which natural surfactants are present or synthetic surfactants are used for the application. In the rest of this chapter, an overview of the numerical challenges is presented.

1.3 Numerical Challenges

The representation of complex interface movement in real multiphase flows requires robust and efficient numerical techniques.

Attempts to simulate various multiphase flows have resulted in a range of different numerical approaches. Among them, implicit interface-capturing methods, such as Volume of Fluid (VoF) and Level-Set (LS), have attracted significant attention for simulating flows involving extensive topological changes [49–54]. Tryggvason et al. [55] gave a comprehensive review of the subject.

The VoF method has become a contemporary standard in commercial and open-source CFD software, e.g. Weller et al. [56], Popinet [57]. On the other hand, LS methods are still used mainly within more specialised in-house research codes. These interface-capturing methods, despite being successful for many problems, have a number of well-known but still inadequately addressed numerical deficiencies, which limit their accuracy [5, 58, 59].

The most important of these is in relation to the accurate representation of the sharp interface regarding its location and its advection, while guaranteeing mass conservation, as well as, the representation of the effect of the surface tension forces. Amongst other things, this requires the accurate computation of the interface normal and curvature, using the underlying liquid volume fraction or level set field.

1.3.1 Multiphase Flow Solvers - An Overview

In the VoF method [60] a volume fraction field α is used to discriminate between the fluids in the domain. When $\alpha = 1$, the cell is entirely filled with fluid one and when $\alpha = 0$, the cell is filled with fluid two. The interface is located in the cells where α lies between 0 and 1.

Two major VoF methods are commonly used for interface representation: (a) the compressive method and (b) the geometric method. Both capture the discrete volume fraction of each phase and transport is based on the underlying fluid. On the one hand, the compressive interface method discretises the partial differential equation in a way to describe the transport of the volume fraction of each phase using algebraic differencing schemes, as mentioned in [61, 62]. However, the temporal and spatial discretisation require higher-order schemes and careful tuning to keep the interface sharp, and without distortion. Otherwise, it may suffer from excessive diffusion of the

interface region, which also affects the calculation of the interface curvature and the normal interface vectors. On the other hand, when using the geometric method, an explicit representation of the interface is advected, reconstructed from the VoF volume fraction field. The piecewise linear method so-called (PLIC) is the most developed reconstruction technique found in the literature [63, 64]. In fact, geometric methods advect the interface very accurately. However, the main drawback is their complexity for 3D applications, in particular, when used in conjunction with an unstructured mesh [65].

Park et al. [66] and Gopala and van Wachem [6] showed the compressive VoF method capabilities of an advecting sharp interface. Yet, the difficulty in using the compressive VoF methods is to retain the shape and sharpness of the interface. The VoF methods are based on a discontinuous α function to facilitate the calculation of the properties of each phase and to make it possible to present an accurate numerical scheme for solving the colour transport equation. However, the accuracy of the calculated interface curvature depends on determining the derivative of the introduced colour function, which is considered to be difficult from a numerical point of view, and can lead to numerical instabilities [67].

It should be stressed that the local force unbalances between the capillary pressure and the surface tension forces can create non-physical velocity spurious currents, which are commonly small in absolute value in inertia dominated flows, but become very problematic in capillary dominated flows. The numerical challenges relating to the advection of the interface in the context of VoF have been well-documented by Tryggvason et al. [55]. Intrinsic to the method is numerical diffusion of the interface at a rate that is highly dependent on the mesh size [62]. The numerical diffusion can be reduced by using a geometrical reconstruction coupled with a geometrical approximation of the VoF advection, as discussed by Roenby et al. [68]. Alternatively, using a compressive algorithm, the convective term of the VoF advection equation can be discretised using a compressive differencing scheme designed to preserve the interface sharpness, examples of which include: (Compressive Interface Capturing Scheme for Arbitrary Meshes) CICSAM by Ubbink and Issa [62]; HRIC by Muzaferija and Peric [69]; and the compressive model available within OpenFOAM [56]. Compression schemes do not require any geometrical reconstruction of the interface and extension to three dimensions as well as unstructured meshes is straightforward. However, compression schemes are not always sufficient to eliminate numerical diffusion, and additional treatment is needed

[70].

Various remedies that still leave room for development have been suggested, which can be summarised as follows: (i) ensuring an accurate balance between pressure gradient and surface tension forces, as Francois et al. [49] reported that the most important consideration for modelling surface tension-driven flows is the formulation for surface curvature. Francois et al. [49] have introduced a cell-centred framework and demonstrated that this algorithm can achieve an exact balance of surface tension and pressure gradient using structured mesh. Moreover, Francois et al. [49] and [51] discussed the origin of spurious currents within the proposed balanced-force flow algorithms, highlighting the deficiencies introduced when estimating interface curvature. (ii) sharp representation of the interface, with accurate curvature estimation and introduction of a so-called compression velocity to damp diffusion. Ubbink and Issa [62] introduced the compressive discretisation scheme so-called CICSAM that makes a use of the normalised variable diagram concept proposed by Leonard [71], where the scheme is based on the concept of no diffusion of the interface being allowed. Popinet [72] generalised a height-function and CSF formulations to an adaptive quad/octree discretisation to allow for refinement along the interface for the case of the capillary breakup of a three-dimensional liquid jet. Moreover, Popinet [72] discussed the long-standing problem of parasitic currents around a stationary droplet in contrast to the recent study of Francois et al. [49], where the issue was shown to be solved by a combination of the appropriate implementation of a balanced-force CSF approach and height-function curvature estimation. (iii) implicit or semi-implicit treatment of surface tension. Denner and van Wachem [73] reviewed the time-step requirements associated with resolving the dynamics of the equations governing capillary waves, to determine whether explicit and implicit treatments of surface tension have different time-step requirements, with respect to the (1) dispersion of capillary waves, and (2) the formulation of a stable time-step criterion for the propagation of capillary waves based on established numerical principles. A fully-coupled numerical framework with an implicit coupling of the governing equations and interface advection along with an implicit treatment of surface tension, was used by [73] to study the temporal resolution of capillary waves with an explicit and implicit treatment of surface tension.

The LS method was first developed by Osher and Sethian [74]. After being initially used in the context of multiphase incompressible flows by Sussman et al. [75], it has matured into a promising numerical technique for accurate simulation of multiphase

flows, as shown by Losasso et al. [76]. Instead of using a continuous volume fraction variable, LS relies on a signed distance function ϕ to distinguish between the two fluids in a mixture. The function has a positive value in one fluid and a negative value in the other, while it takes the value $\phi = 0$ at the interface. The interface is advected by solving a transport equation for ϕ that is reinitialised periodically to recover the distancing property [77]. The LS approach inherently offers a sharp representation of the interface and accurate representation of the interfacial quantities, such as the interface normal and curvature, as needed for computing accurate surface tension forces. However, as opposed to VoF approaches, mass conservation is not embedded in the formulation. It has been shown by Sussman et al. [75] that mass is lost due to the re-distancing procedure that may involve artificial displacement of the interface [78]. Moreover, the initialisation procedure increases the computational cost.

The numerical challenge of representing the surface tension force at the phase interface is present in both methods. Surface tension is commonly represented as a source term in the momentum equation, calculated using the Continuous Surface Force (CSF) model of Brackbill et al. [53]. The calculation involves an approximation of the interface curvature from the gradients of either the VoF or LS function, as well as the calculation of the normal to the interface and since the interface is a discontinuous function the calculation of derivatives is problematic. For VoF methods that suffer from diffusion, it is difficult to achieve an accurate representation of interface curvature. For LS methods that provide a sharp interface, the effect of the volumetric surface force is confined to a narrow region around the interface and the calculation of the normal normal can be numerically unstable. These numerical effects are known to generate non-physical vertical flows at the interface, i.e. the spurious currents discussed earlier [49, 51, 61]. Various methods have been developed to minimise these, such as (i) improvement of the curvature computation, (ii) achievement of a discrete balance between the surface tension and pressure gradient and (iii) the use of an adaptive time integration scheme to tackle the numerical stiffness induced by surface tension. One promising approach relies on minimal energy considerations and can eliminate spurious currents to machine precision. Alternatively, it is proposed to use consistent volume fluxes in the Navier-Stokes equations either in a VoF framework [79] or in the LS framework [80] using geometric arguments.

It should be noted that, the generation of spurious currents is not usually considered of great importance for inertia-dominated flows. However, it is detrimental in

the computation of capillary flows and surface tension dominated ones, for example, in hydrodynamic flows involving atomisation and pore-scale modelling. More recently, it was shown that spurious currents also affect droplet collision with surfaces by preventing the transition to the recoil phase [81]. Moreover, for flows with large density ratios, the interfacial force imbalance is massive, and thus, the generation of spurious currents is more likely [55, 80].

Hybrid methods have been proposed to combine the advantage of the VoF method regarding mass conservation even on coarse meshes and the LS method in terms of accuracy of the interface contour as well as a smoothly differentiable field for the calculation of the surface tension forces. A fully coupled CLSVOF method was proposed by Sussman and Puckett [82] and has been implemented by a number of researchers since. It has been applied to Cartesian orthogonal meshes, successfully tested by Ménard et al. [83, 84] on diesel jet atomisation, and utilised by Yokoi [85] on the problem of droplet splashing and on Rayleigh-Taylor instability. A recent development by Arienti and Sussman [86] has reformulated the CLSVOF method to adaptive Cartesian meshes. Also, in some other recent works, CLSVOF has been applied to unstructured meshes [87, 88]. A large number of methods have been developed for simulating multiphase flows at macro-scale, including the well-known Level Sets (LS) [89] and Volume of Fluid (VoF) methods [53]. The extension of these methods to the micro-scale is not always straightforward. For example, the main weakness of the LS methods is that they do not preserve mass. As a result of the mass conservation problem, poorly resolved regions of the flow are typically susceptible to mass loss behaviour and loss of signed distance property due to advection errors. Various modifications have been suggested focusing on solving the conservation issues [90], extending the method to high Reynolds numbers [75] and unstructured meshes [91, 92]. While using a re-initialisation procedure as discussed by [77] is a solution to the mass conservation issue, it increases the computational cost and creates an artificial interface displacement that may affect mass conservation (see the review by Russo and Smereka [78] for details).

1.3.2 Numerical Surface Tension Force Modelling Using VoF Method

At the micro-scale, interfacial tension is considered as a body force and a review of interfacial forces at these scales is given in [93]. According to [93], the multiphase

flow can be described quite accurately by the incompressible Navier-Stokes equations consisting of the momentum conservation equation. For most applications, a numerical solution using these equations on a traditional grid-based method is the preferred approach. This is due to its superior numerical efficiency and its ability to simulate fluid flow with very large density and viscosity ratios. However, as mentioned in the previous subsection, the application of well known multiphase fluid flow methods in pore-scale systems, such as fractured and porous media with small characteristic length scales, has been inhibited by two difficulties. First, the challenge of tracking the complex dynamics of fluid-fluid interfaces. Second, the need for a contact line/contact angle model that can be coupled with the CFD simulation.

One approach to include the effects of surface tension in the model - often referred as a continuous surface tension force model [53] - is to replace the pressure jump at the interface by a body force integrated across the interface that acts only on the fluid near the interface. The sharp interface is replaced by a smooth function, which varies from 0 to 1, as the distance from the interface width. The capillary force is then approximated in terms of a body force per unit volume acting on the fluid and given by:

$$\int_V f dV = \int_S \int_{-W/2}^{W/2} \delta\sigma(\nabla \cdot n) n dndS \quad (1.3)$$

where, Brackbill et al. [53] introduced the Continuous Surface Force (CSF) method, in which the capillary force is acting on a narrow thickness of $[-W/2$ and $W/2]$ around the interface, n is a parametrised coordinate normal to the interface surface S , and δ is the Dirac delta function, which acts as step function at zero. The integrated surface tension force is then evaluated using the indicator function in each element of the computational grid. Using the two-phase fluid approach, the volume fractions are not sufficient to determine the direction and position of the interface in the grid cell. So, an interface reconstruction algorithm based on the volume fractions in neighbouring cells is needed.

Hence, the orientation of the interface segment that cuts the grid cell is determined from the volume fraction gradient, treating it as if it were a continuous function. Then, using this function the unit vector normal to the interface is obtained from the equation below:

$$n = \frac{\nabla\alpha}{|\nabla\alpha|} \quad (1.4)$$

where, α is the volume fraction, and n defines the orientation of the interface as the normal to it. In liquid-gas simulations, for example, the indicator function is given a value of (1) in the liquid phase and (0) in the gas phase. Using this method, n points into the liquid phase. The value of n , calculated using Eq. (1.4) in cell i containing part of the interface and the volume fraction, ϕ_i , in that cell should provide the correct information to specify the surface segment inside the grid cell. In the next simulation step, the interface is advected with the local velocity v .

To predict correctly the multiphase fluid flow behaviour, the curvature κ , calculated using Eq.(1.5) on the fluid interface, is required to calculate the pressure jump caused by surface tension ($\Delta P = \sigma\kappa$).

$$\kappa = \nabla \cdot n \tag{1.5}$$

In the VoF method, the surface tension is expressed as a body force that acts on the fluid domain in the cells close by the interface, as Eq. (1.6):

$$F = \sigma\kappa\nabla\alpha \tag{1.6}$$

where, the gradient of the indicator function is a non zero value and these body forces can be simplified as mentioned by [53]. Yet, the contact line adhesion due to surface wetting is not modelled using the surface tension force. The next subsection will present the implantation of different wetting models as found in the literature.

1.3.3 Wetting Behaviour

Accurate modelling of multiphase fluid flow in porous systems depends on an accurate prescription for the behaviour of the macroscopic contact angle. Modelling the wetting behaviour depends mainly on the sharp interface velocity adjacent to solid surfaces. Moreover, the physical wetting behaviour and the dynamics of the fluid-solid contact line, also depends on the correct modelling of the fluid-fluid-solid contact line at mesoscale, where scales between the atomic and continuum scales are essential to the interface motion. According to the literature on modelling contact angles, [94, 95],

it is common to use a simple thermodynamic model to predict the angle between the fluid interface and the solid surface measured with respect to one fluid phase, when the interface between two fluids contacts can be described to be a smooth solid

surface. The theoretical description of the contact line from the consideration of a thermodynamic equilibrium can be defined using Youngs equation [96]:

$$\cos\theta_C = \frac{(\Gamma_{SF^1} - \Gamma_{SF^2})}{\Gamma_{F^1F^2}} \quad (1.7)$$

where, Γ_{SF^1} is *solid – fluid¹* interfacial energy, Γ_{SF^2} is *solid – fluid²* interfacial energy, $\Gamma_{F^1F^2}$ is *fluid¹ – fluid²* interfacial energy (i.e. the surface tension), and θ_C is the equilibrium contact angle, as seen in Fig. 1.3. Equation 1.7 can also be understood as the balance of three surface tensions, as originally described by Young [96], but it has also been derived using the principle of minimizing the total free energy of the system. The latter thermodynamic derivation relies on interpreting $\Gamma_{SF^1}, \Gamma_{SF^2}, \Gamma_{F^1F^2}$ as scalar thermodynamic surface energies, instead of tension vectors. In reality, the equilibrium contact angle given by Eq. (1.7) is rarely observed. For example, If *fluid¹* slowly displaces *fluid²* at the surface of the solid, an ”advancing” contact angle, θ_a^1 , is measured, and if *fluid²* slowly displaces *fluid¹*, a receding contact angle, θ_r^1 , is measured. In general, $\theta_a^1 > \theta_C > \theta_r^1$, as seen in Fig. 1.4.

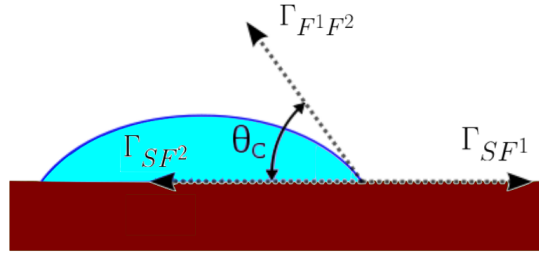


Figure 1.3: Schematic to represent the quantities in Youngs equation and constant contact angle

If the fluid-fluid interface is not moving, the contact angle can take a range of time-dependent values, while if it is, the advancing and receding contact angles will depend on the velocity at which the fluid-fluid contact line advances or recedes across the solid surface. A liquid with an ”equilibrium” contact angle (measured in that liquid) is said to be wetting or ”hydrophilic”, when $\theta_C \leq 90^\circ$, and if, $\theta_C \geq 90^\circ$, the liquid is non-wetting or ”hydrophobic”, as demonstrated in Fig.1.5. It is well known that the classical continuum hydrodynamics model, based on the no-slip boundary condition at fluid-solid interfaces, cannot be applied at the contact line due to the strain rate divergence at the contact line [32].

A variety of approaches have been proposed to resolve dynamic contact angle behaviour. Most of the proposed models in the literature relate contact line velocity to the dynamic contact angle. Both values should be imposed as a slip boundary condition

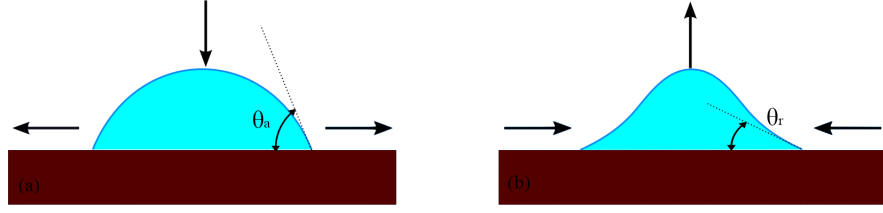


Figure 1.4: Schematic representing the advancing (a) and receding (b) contact angle during droplet movement

on the wall of interest. Common practice suggested is using maximum and minimum advancing and receding contact angles from experimental histories, while the challenging part is defining the contact line velocity near to the wall. In the simplest possible contact angle model, a given fixed value for equilibrium contact angles is imposed as a boundary condition when the contact line spreads or recoils.

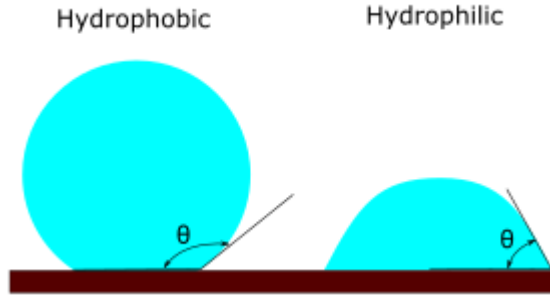


Figure 1.5: Wetting of different fluids: A hydrophobic surface and a hydrophilic surface

The theoretical and experimental studies on dynamic contact wetting have produced a number of dynamic contact angle models, including hydrodynamic [97], experimental [98] and hybrid models [4]. Various dynamic contact models are presented in this subsection and while the contact angle methods are not within the scope of this thesis, the work of Malgarinos et al. [8] presents a significant review regarding contact angle modelling methods. In order to study the contact angle one can refer to the work of Cox [30], which gives an essential relationship between the contact line velocity and the dynamic contact angle based on the flow capillary number, as follows:

$$Ca = \left(\ln(\eta^{-1}) - \frac{C_1}{f(\theta_D)} + \frac{C_2}{f(\theta_S)} \right)^{-1} [H(\theta_D) - H(\theta_S)] + O\left(\frac{1}{\ln(\omega^{-1})}\right)^{-1} \quad (1.8)$$

where, θ_D is the dynamic contact angle, θ_S is the static contact angle, C_1 and C_2

are constants associated with the outer flow and with the wall slip, whilst ω is a small dimensionless parameter associated with the micro-region of the contact line, $f(\cdot)$ and $H(\cdot)$ are functions obtained by Moffatt [99].

The existing empirical dynamic contact angle models are considered as simplifications of the Eq. (1.8). The most used dynamic contact angle model for a low capillary number is given by Hoffman-Voinov-Tanners law [35]:

$$\theta_D^3 - \theta_S^3 = 9 Ca \ln\left(\frac{L}{L_m}\right) \quad (1.9)$$

where, L is the macroscopic length scale and L_m is microscopic length scale. In the treatment of [100], L_m is the distance from the solid at which the solution is truncated. In Cox [30] analysis, it defines the scale of the inner region where slip is important. However, it was defined in [4] that L can take the value of 10 micrometre, which is the approximate distance from the wetting line at which the contact angle can be measured, and L_m can take one nanometre, i.e. the order of molecular size. In which case, $\ln(L/L_m)$ is estimated to be of the order of 10. Experimental values vary widely, though values of about 10 are often found, especially for liquids that completely wet the solid. Much larger values have sometimes been reported, such as by Petrov et al. [101], for non-wetting liquids, especially at low Ca , where it might have been anticipated that the model would be most effective. Jiang et al. [102] discussed a correlation of the dynamic contact angle and its effect on capillary rise, which depends on the contact line velocity. This model was expressed as:

$$\cos(\theta_D) = \cos(\theta_S) - (1 + \cos(\theta_S))\tanh(4.9Ca^{0.702}) \quad (1.10)$$

In both of the previous methods, the dynamic contact angle θ_D increases with flow velocity and asymptotically reaches 180° for high capillary numbers. Several additional empirical correlations, as presented by Petrov et al. [101], are obtained using the experimental data for solid bars dipped a pool at low capillary numbers that range between ($0.002 < Ca < 0.02$).

An empirical correlation for the dynamic contact angle given by Kistler [34] has been proven to be well adapted and modelled as:

$$f_{Hoff} = \arccos\left\{1 - 2\tanh\left[5.16\left(\frac{x}{1 + 1.31x^{0.99}}\right)^{0.706}\right]\right\} \quad (1.11)$$

where, $f_{Hoff}(x)$ is the "Hoffman's" function, which is defined as:

$$\cos\theta_D = 1 - 2\tanh\left[5.16\left(\frac{Ca + f_{Hoff}^{-1}}{1 + 1.31(Ca + f_{Hoff}^{-1})^{0.99}}\right)^{0.706}\right] \quad (1.12)$$

$$(f_{Hoff}^{-1})^{0.706} = \frac{1}{5.16}\left(1 + 1.31(f_{Hoff}^{-1})^{0.99}\right)^{0.706} \tanh^{-1}\left(\frac{1 - \cos\theta_S}{2}\right) \quad (1.13)$$

Also, Eqs. 1.11 and 1.12 can be simplified to be:

$$\theta_D = f_{Hoff}[Ca + f_{Hoff}^{-1}\theta_S] \quad (1.14)$$

[35] deduced a universal function from a systematic study of dynamic contact angles in glass capillary tubes for a wide range of capillary numbers ($4 \times 10^{-5} < Ca < 36$). In the rest of the thesis, the Kistler model will be implemented and also used for predicting the interface behaviour near to the solid surface.

Finally, Shikhmurzaev [103] recently proposed a modelling method to track the moving contact line and the dynamic contact angle. Shikhmurzaev [103] continuum hydrodynamics treatment not just accommodates dissipation through standard hydrodynamic channels, but also, exploits non-equilibrium thermodynamics. It includes dissipation due to the interfacial transformation process occurring as the wetting line moves across the solid surface. One consequence of this approach is that the microscopic dynamic contact angle is coupled directly with the flow and it is not an independent value. For this reason, analytical expressions can be obtained for certain simplifying conditions, which successfully describe the experimental results found in the literature. Full descriptions of Shikhmurzaevs mathematical model, the associated analysis and comparisons with experiments can be found in [104]. However, it is not within the scope of this thesis to compare between different contact angle models, but despite this, a small comparison between the models is presented in Appendix A.

All the previous discussed typical hydrodynamic and empirical models attribute the changes in the experimentally observed dynamic contact angle to the viscous bending of the two-phase interface within a mesoscopic region. Kistler and Shikhmurzaevs approaches, in particular, try to model the physical movement of the contact line observed in experiments. This challenge is equally divided between modelling dynamic the contact angle (at microscopic length scale) and the apparent contact angle (at

macroscopic length scale) within the inner region near the triple line point. In the next chapter, the dynamic contact angle using the Kistler model will be discussed in detail.

1.4 Motivation of the Study

The motivation of this thesis is to devise a novel framework and solutions for the long-standing problem of multiphase flows in porous structures by improving the understanding of droplet penetration on porous media as well as the related flow inside the porous structures. Due to the complexity of porous media, modern micro computer tomography was drawn upon to reconstruct numerical porous geometry and study the flow characteristics inside porous structures, as well as, the droplet penetration after impact on natural porous stone. A modified multiphase numerical method that is based on the volume of fluid approach and implemented in the OpenFOAM toolkit for CFD simulation was used, which it was believed would enrich the current state-of-the-art.

The results of this work are important for a wide range of applications, for which developing a better understanding of flow physics for liquid transport in porous structures and the control of droplet penetration is of prominent importance. This study is aimed at understanding the flow physics inside porous media that accompanies fluid penetration through porous structures at low capillary numbers and droplet impact, spreading, and absorption on a porous structure, in general. The specific objectives of this work are: firstly, to develop an accurate numerical two-phase flow framework based on the Volume of Fluid method for the study of the microscale flows and its applications for low capillary numbers, such as flow inside porous media and droplets impacting on porous media. Secondly, the aim is to build up an adequate computational meshing framework to reconstruct complex porous structures based on microtopography data found in the open literature. Thirdly, there is the purpose of characterising the flow regimes inside porous media based on the microscopic understanding and proposing a better macroscopic model. Finally, understanding the penetration and impacting process of liquid droplets for different liquids and porous structures, during absorption, is another study objective.

This thesis focuses in depth on the following points:

1. Tackling the numerical challenges posed by two-phase flow simulations when using sharp interface tracking methodologies;
2. Developing and validating the needed modifications to simulate flow in complex porous structures accurately;
3. Understanding the effect of wetting conditions on two-phase transport, such as

water injection inside porous media and studying the effect of varying wetting conditions on permeability for different porosity values;

4. Examining droplet impact on phenomena on porous media focusing on the droplet hydrodynamics inside the porous structures. Based on the knowledge of droplet impact on an impermeable surface, the dynamics of such impact on porous media will be investigated. Specifically, this is achieved by focusing on the influence of their wetting behaviour, the morphology of porous media as well as the effects of permeability and porosity;
5. Liquid droplet mass transfer into porous media will be analysed numerically in terms of inertia-driven penetration and capillary absorption in order to extract a macroscopic understanding towards the phenomena of droplet impact on porous media.

1.5 Thesis Synapsis

The thesis is composed of six chapters. Chapter 2 presents the mathematical model and the governing equations for multiphase flows at pore scale when considering low capillary numbers and the numerical solution of these equations.

Chapter 3 presents six different numerical validation test cases using the developed numerical methodology, with the results being compared against their analytic solutions. The goal of this chapter is to validate the accuracy of the proposed numerical method and to consider its advantages and the disadvantages.

Chapter 4 presents the reconstruction processes of complex porous structures and the framework developed to generate different computational models based on porous rock CT-scans. Also, the numerical results on modelling two-phase flow through porous geometries are provided. In addition, pore-scale phenomena occurring in two-phase flow through porous media are studied and the effect of different wetting conditions using the modified VoF method.

Chapter 5 presents the numerical results of a droplet impacting on porous structures using the modified VoF methods, with the dynamic contact angle model and adaptive grid refinement. The droplet dynamics during impact on porous media is studied using a number of porous natural stones, as it was possible to model the spreading on the porous material. Maximum spreading and dynamic contact angle at low impact velocity are also addressed in detail. Moreover, the full absorption process of impinging droplets on natural porous stones is investigated. The study has been extended to explore droplet spreading and penetration in porous stones for different wetting conditions, and also, the effect of having multiple droplets impacting on a single porous structure.

Finally, in Chapter 6, a summary of the main conclusions of this thesis and presenting the perspectives. Moreover, the achievements of this study are discussed, followed by some recommendations for future work being proposed. These include, but not limited to, applications and extensions for the presented numerical method, for improvement is needed, for example, regarding adaptive mesh refinement. Also, some suggestions for future work to extend the numerical investigations of the wetting effect under different flow rates for flow transport inside porous media are made.

Chapter 2

Numerical Method

2.1 Governing Equations

2.1.1 Mass and Momentum Conservation

The method presented in this section is implemented within the open source CFD toolkit OpenFOAM [105]. An incompressible and isothermal two-phase flow with constant phase densities ρ_1 and ρ_2 and viscosities μ_1 and μ_2 are considered. The two phases are treated as one fluid. A single set of equations is solved in the entire computational domain. The volume fraction, α of each phase within a cell is defined by an additional transport equation. The formulation for the conservation of mass and momentum for the phase mixture is given by the following equations:

$$\nabla \cdot \mathbf{u} = 0 \quad (2.1)$$

$$\rho \left(\frac{\partial \mathbf{u}}{\partial t} + (\mathbf{u} \cdot \nabla) \mathbf{u} \right) = -\nabla p + \mu \nabla^2 \mathbf{u} + \mathbf{f} \quad (2.2)$$

where \mathbf{u} is the fluid velocity, p is the pressure and ρ is the density. The pressure-velocity coupling is handled using the Pressure-Implicit with Splitting Operators (PISO) method of [106, 107]. μ is the dynamic viscosity. The term $\mathbf{f} = \mathbf{f}_g + \mathbf{f}_s$ corresponds to all the external forces, i.e., $\mathbf{f}_g = \rho \mathbf{g}$ is the gravitational force and \mathbf{f}_s represents the capillary forces for the case of constant surface tension coefficient σ . The global properties are weighted averages of the phase properties through the volume fraction value that is calculated in each cell:

$$\rho = \rho_1 + (\rho_2 - \rho_1)\alpha \quad (2.3)$$

$$\mu = \mu_1 + (\mu_2 - \mu_1)\alpha \quad (2.4)$$

The sharp interface α represents a discontinuous change of the properties of the two fluids. The surface tension force must balance the jump in the stress tensor along the fluid interface. At each time step, the dynamics of the interface are determined by the Young-Laplace balance condition as;

$$\Delta P_{exact} = \sigma \kappa \quad (2.5)$$

accounting for a constant surface tension coefficient σ along the interface. The term

κ represents the interface curvature. The term on the right-hand side of Eq. (2.5) is effectively the source term in the Navier–Stokes equations for the singular capillary force, that is only present at the interface. In the proposed numerical method, the Continuum Surface Force (CSF) description of Brackbill et al. [53] is used to represent the surface tension forces in the following form:

$$f_s = \sigma \kappa \delta_s \quad (2.6)$$

where the term κ represents the interface curvature, δ_s is a delta function concentrated on the interface, and η_s is the normal vector to the interface α is calculated by the following equation:

$$\eta_s = \frac{\nabla \alpha}{|\nabla \alpha|} \quad (2.7)$$

where δ_s and κ_f are terms associated with the artificially smoothed and sharpened indicator function fields that will be discussed in details in the following section. In the VoF method, the indicator function α represents the volume fraction of one of the fluid phases in each computational cell. The indicator function evolves spatially and temporally according to an advection transport equation of the following general form:

$$\frac{\partial \alpha}{\partial t} + \nabla \cdot (\alpha \mathbf{u}) = 0 \quad (2.8)$$

Ideally, the interface between the two phases should be massless since it represents a sharp discontinuity. However, within VoF formulation the numerical diffusion of Eq. (2.8) results in values of α that vary between 0 and 1. In section 2.2.2 the concept of interface smoothing is introduced where α and κ are reformulated.

The framework described above reflects the generalised framework of VoF methods that have been used in an extensive range of two-phase flow problems with various adjustments and different degrees of success. In the following sub-sections, an enhanced version of this basic framework is presented; its validity is demonstrated through a range of benchmark cases that address some numerically challenging problems reported in the relevant literature.

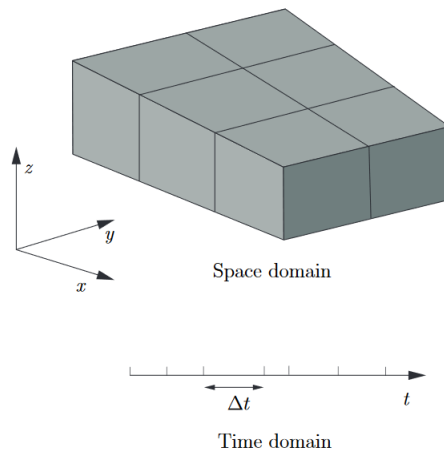


Figure 2.1: Discretisation of the solution domain [3]

2.2 Finite Volume Method

This section presents the application of the finite volume method for the discretisation of partial differential equations (PDEs) presented in the previous section. In the finite volume discretisation, the solution domain is subdivided into small discrete non overlapped volume covering all the space domain as demonstrated in Fig. 2.1. The continuum variables represented in the previous section are then replaced by discretised volume average variables at specified locations in the space and time domain. A typical cell is shown in Fig. 2.2. Almost all the dependent variables and other properties are principally stored at the cell centroid P although some other may be stored on faces or vertices. The cell is bounded by a set of flat faces, given the generic label f . In OpenFOAM, there is no limitation on the number of faces bounding each cell, nor any restriction on the alignment of each face. OpenFOAM code offers greater freedom in mesh generation and manipulation in particular when the geometry of the domain is complex or changes over time, due to the use of "arbitrarily unstructured to differentiate faces from meshes in which the cell faces have a prescribed alignment, typically with the coordinate axis. There are two types of cell face; (i) internal faces, where that connect two cells (and it can never be more than two). For each internal face, OpenFOAM designates one adjoining cell to be the face owner and the other to be the neighbour. (ii) Boundary faces where faces belonging to one cell since they coincide with the boundary of the domain. These faces simply have an owner cell.

By using OpenFOAM code, all primary variables (velocities, pressures and indicator function) are defined at the centre of elementary volumes and used as volume field values. If the values of such variables are needed at face centres, they can be

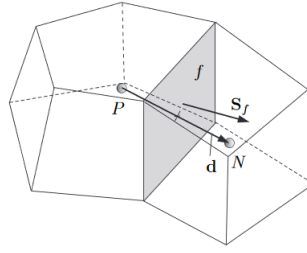


Figure 2.2: Parameters in finite volume discretisation [3]

interpolated from the cell-centred field. For the internal faces, the face field ϕ_f can be evaluated using a variety of schemes such as; (i) second-order accurate unbounded Central differencing (CD) which defined as following:

$$\phi_f = f\phi_P + (1 - f)\phi_N \quad (2.9)$$

$$f = \frac{\text{Distance between f and cell center N}}{\text{Distance between cell centers P and N}} \quad (2.10)$$

or (ii) using the upwind differencing (UD) which determines the direction of flow and expressed as following :

$$\phi_f = \begin{cases} \phi_P & \text{for } f \geq 0 \\ \phi_N & \text{for } f < 0 \end{cases} \quad (2.11)$$

or (iii) the blended differencing (BD) schemes which combine UD and CD in an attempt to preserve boundedness with reasonable accuracy as shown in Eq. (2.12). The blended differencing scheme was used in all of our simulations to maintain fast and accurate results.

$$\phi_f = (1 - \gamma)(\phi_f)_{UD} + \gamma(\phi_f)_{CD} \quad (2.12)$$

where γ is the blending coefficient, however OpenFOAM also offers other well-known schemes such as van Leer. The choice of γ in blended differencing in discretisation of the advection term has a significant effect on the boundedness, accuracy and convergence of the numerical method for parameters annotations; where the cell in needed will be identified by subscript P, and its neighbours by N as shown in Fig. 2.2. In the discretisation of all differential operators other than the advection terms, we use blended differencing in this study. If the values of field variable are known at the cell

centres, the results of the interpolation will be a new collocated variable defined at the centre of faces. In this case, the variable is called a face-field. In the case interpolation is required for a variable which is a function of primary variables, the results of interpolation, for each face, will be the function of primary field variables. These functions will be linearised and used to form a matrix of coefficients.

In general, equation discretisation converts the PDEs into sets of algebraic equations. This set of algebraic equations will be solved using appropriate numerical methods to obtain a solution for the set of unknown variables ϕ . As stated previously, we have used the OpenFOAM finite volume library for discretisation of the differential operators. The multidimensional universal limiter for explicit solution (MULES) solver developed by OpenFOAM was used to implicitly solve the discretised equation for advection of the indicator function α . A geometric-algebraic multi-grid (GAMG) solver implemented in OpenFOAM is used for solving the discretised capillary pressure equation. Also, the dynamic pressure equation which will be presented in the next sections.

2.2.1 Advection of the Indicator Function Using Adaptive Compression Scheme (Implicit)

To deal with the problem of numerical diffusion of α , an extra compression term is used in order to limit the convection term of Eq. (2.8) and consequently the thickness of the interface. Its numerical significance is that it acts in such a way that the local flow steepens the gradient of the phase indicator function. The model for the compression term makes use of the two-fluid Eulerian approach, where phase fraction equations are solved separately for each individual phase, assuming that the contributions of two fluids velocities for the free surface are proportional to the corresponding phase fraction. These phase velocities (u_1 and u_2) relate with the global velocity of the one fluid approach u as:

$$u = \alpha u_1 + (1 - \alpha) u_2 \quad (2.13)$$

Replacing the above equation to Eq. (2.8) one gets:

$$\frac{\partial \alpha}{\partial t} + \nabla \cdot \left\{ \left(\alpha u_1 + (1 - \alpha) u_2 \right) \alpha \right\} = 0 \quad (2.14)$$

Considering a relative velocity between the two phases ($u_r = u_1 - u_2$) which arises from the density and viscosity changes across the interface, the above equation can be written in terms of the velocity of the fluid:

$$\frac{\partial \alpha}{\partial t} + \nabla \cdot (u_1 \alpha) - \underbrace{\nabla \cdot \left\{ u_{r,f} \alpha \left((1 - \alpha) \right) \right\}}_{\text{compression term}} = 0 \quad (2.15)$$

It should be noticed that in the above equation, $\nabla \cdot (u_1 \alpha)$ term contain the unknown velocity u_1 instead of u (where u represent domain velocity) creating an inconsistency with the basic concept of the one fluid approach. However, since the compression term - in reality - is active only at the interface that continuity imposes $u_1 = u_2 = u$ and thus u_1 by u can be replaced. The discretisation of the compression term in Eq. (2.15) is not based directly on the calculation of the relative velocity u_r at cell faces from Eq. (2.13) since u_1 and u_2 are unknown. It is instead formulated based on the maximum velocity magnitude at the interface region and its direction, which is determined from the gradient of the phase fraction:

$$u_{r,f} = \min \left(C_{compr} \frac{|\phi_f|}{|S_f|}, \max \left[\frac{|\phi_f|}{|S_f|} \right] \right) \left(\langle \eta_s \rangle_f \right) \quad (2.16)$$

where the term ϕ_f is the volumetric flux and S_f is the outward-pointing face area vector and $\langle \eta_s \rangle_f$ is the face centred interface normal vector. $\langle \rangle_f$ is used to denote interpolation from cell centres to face centres using a linear interpolation scheme, and defined as the following:

$$\langle \eta_s \rangle_f = \frac{\langle \nabla \alpha \rangle_f}{|\langle \nabla \alpha \rangle_f + \delta_n|} \cdot S_f \quad (2.17)$$

and

$$\delta_n = \frac{\epsilon}{\left(\frac{\sum_N V_i}{N} \right)^{1/3}} \quad (2.18)$$

where δ_n is a small number to ensure that the denominator never becomes zero, ϵ is a small value set to be 10^{-8} , N is the number of computational cells, for each grid volume element V_i .

The compressive term is taken into consideration only at the interface region, and it is calculated in the normal direction to the interface. The maximum operation in Eq. (2.16) is performed over the entire domain, while the minimum operation is done locally on each face. The constant ($C_{compr.}$) is a user-specified value, which serves as a tuning

parameter. Depending on its value, different levels of compression result are calculated. For example, there is no compression for $C = 0$ while there is moderate compression with $C \leq 1$ and enhanced compression for $C \geq 1$. In most of the simulations presented here, ($C_{compr.}$) is taken as unity after initial trial simulations. Values higher than unity, in this case, may lead to non-physical results. Generally, this compression factor can take values from zero (no compression) up to four (maximum compression) as suggested in the literature; the selected values are case specific. To overcome the need for a-priori tuning, in the present numerical framework a new adaptive algorithm has been implemented. That is based on the idea of introducing a dynamic one C_{adp} instead of a constant value for $C_{compr.}$ through the following relation:

$$C_{adp} = \left| -\frac{u_n \cdot \nabla \alpha}{|u_n| |\nabla \alpha|} \right| \quad (2.19)$$

$$\phi_c = \max\left(C_{adp}, C_{compr.}\right) \frac{|\phi_f|}{|S_f|} \quad (2.20)$$

where ϕ_c is the compression volumetric flux calculated, u_n represents each phase velocity normal to the interface velocity. It is expressed as:

$$u_n = (U \cdot n_s) * (n_s) * |\alpha - 0.01| * |0.99 - \alpha| \quad (2.21)$$

The concept of using u_n is shown in Fig. 2.3. When the interface profile becomes diffusive (wide) C_{adp} value will increase accordingly in the zone of interest. When the profile is already sharp and additional compression is not necessary C_{adp} will go to zero. Note that the compression term in Eq. (2.15) is only valid for the cells at the interface. However, to solve Eq. (2.19), a wider region of α is required. Therefore, the facial cell field is extrapolated to a wider region using the expression (near interface) in Eq. (2.21) as $(|\alpha - 0.01| * |0.99 - \alpha|)$. The new calculated, adaptive compression coefficient ϕ_c then substitutes the original $C_{compr.} \frac{|\phi_f|}{|S_f|}$ and Eq. (2.16) can be rewritten as:

$$u_{r,f} = \min\left(\phi_c, \max\left[\frac{|\phi_f|}{|S_f|}\right]\right) \langle \eta_s \rangle_f \quad (2.22)$$

The new equation yet still has a user-defined value $C_{compr.}$ to give the user the choices in cases where the adaptive coefficient is not sufficient. Therefore, the new transport equation works in an adaptive manner without any user-defined parameters

as it can be seen in Eq. (2.22)

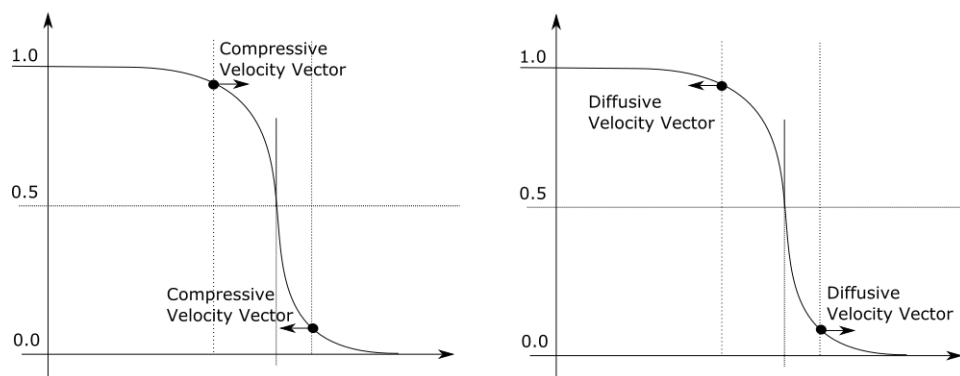


Figure 2.3: Schematic to represent the adaptive compression C_{adp} selection criteria

2.2.2 Smoothing Scheme (Explicit)

By solving the transport equation for the volume fraction Eq. (2.15), the value of (α) at the cell is updated. In order to proceed with the calculation of the interface surface, scalar fields for the calculation of η_s and κ , linear extrapolation from the cell centres are used. At this stage, the value of α sharply changes over a thin region as a result of the compression step. This abrupt change of the indicator function creates errors in calculating the normal vectors and the curvature, which will be used to evaluate the interfacial forces. The miscalculations induce non-physical parasitic currents in the interfacial region. A commonly followed approach in the literature to suppress these artefacts is to compute the interface curvature from a smoothed function α_{smooth} , which is calculated by the smoother proposed by Lafaurie et al. [61] and applied in OpenFOAM by Georgoulas et al. [108] and Raeini et al. [109]. The indicator function is artificially smoothed by interpolating it from cell centres to face centres and then back to the cell centres recursively using the following equation:

$$\alpha_{i+1} = 0.5\langle(\alpha_i)_{c \rightarrow f}\rangle_{f \rightarrow c} - 0.5\alpha_i \quad (2.23)$$

Initial trial simulations indicated that the recursive interpolation between the cell and face centres can be repeated up to three times, in order to prevent decoupling of the indicator function from the smoothed function. After smoothing is implemented, the interface normal vectors in the vicinity of the interface, are filtered using a Laplacian formulation. Equation (2.24) in Georgoulas et al. [108] is used to transform the VoF

function (α_{i+1}) to a smoother function (α_{smooth}) :

$$\alpha_{smooth} = \frac{\sum_{f=1}^n (\alpha_{i+1})_f S_f}{\sum_{f=1}^n S_f} \quad (2.24)$$

where the subscript denotes the face index (f) and (n) the times that the procedure are repeated in order to get a smoothed field. The value at the face centre is calculated using linear interpolation. It should be stressed that smoothing tends to level out high curvature regions and should, therefore, be applied only up to the level that is strictly necessary to suppress parasitic currents sufficiently. After calculating the (α_{smooth}) , the interface normal vectors are computed using 2.7, and the interface curvature at the cell centres can be obtained by $\kappa_f = -\nabla \cdot (\eta_s)$. Then in order to model the motion of the interfaces more accurately, an additional smoothing operation is performed to the curvature. The interface curvature in the direction normal to the interface is calculated, recursively for two iterations:

$$\begin{aligned} \kappa_{s,i+1} = & 2\sqrt{\alpha_{smooth}(1 - \alpha_{smooth})}\kappa_f + (1 - 2\sqrt{\alpha_{smooth}(1 - \alpha_{smooth})}) * \\ & \frac{\left\langle \left\langle \kappa_{s,i} \sqrt{\alpha_{smooth}(1 - \alpha_{smooth})} \right\rangle_{c \rightarrow f} \right\rangle_{f \rightarrow c}}{\left\langle \left\langle \sqrt{\alpha_{smooth}(1 - \alpha_{smooth})} \right\rangle_{c \rightarrow f} \right\rangle_{f \rightarrow c}} \end{aligned} \quad (2.25)$$

This additional smoothing procedure diffuses the variable κ_f away from the interface. Finally, the interface curvature at the face centres κ_{final} is calculated using a weighted interpolation method that is suggested by Renardy and Renardy [51]:

$$\kappa_{final} = \frac{\left\langle \kappa_{s,i} \sqrt{\alpha_{smooth}(1 - \alpha_{smooth})} \right\rangle}{\left\langle \sqrt{\alpha_{smooth}(1 - \alpha_{smooth})} \right\rangle} \quad (2.26)$$

where the interface curvature κ_{final} is obtained at face centres.

2.2.3 Sharpening Scheme (Explicit)

Recalling Eq. (2.6), the surface tension forces are calculated at the face centres based on the following equation:

$$f_s = (\sigma \kappa \delta_s)_f \dot{\eta}_s = \sigma \kappa_{final} \delta_{sf} \quad (2.27)$$

In order to control the sharpness of the surface tension forces, the delta δ_s is calculated from a sharpened indicator function α_{sh} as $\delta_s = \nabla_f^\perp \alpha_{sh}$, where ∇_f^\perp denotes

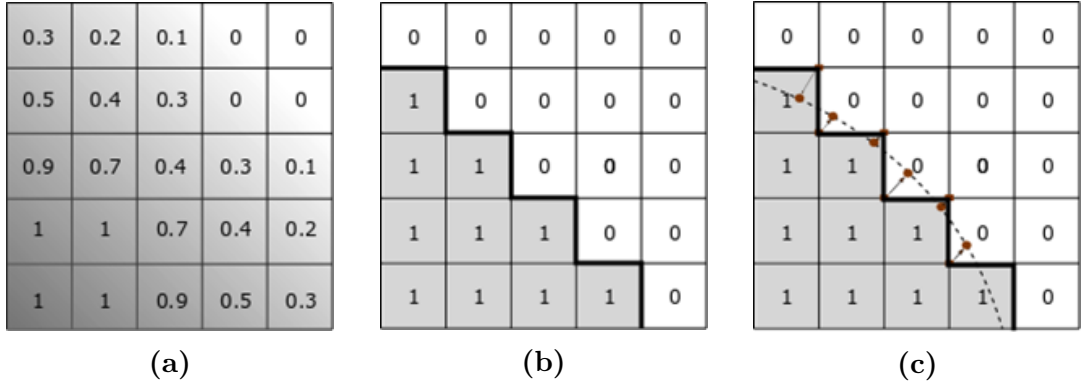


Figure 2.4: A two-dimensional schematic of the steps in reconstructing the interface: (a) the indicator function α , (b) the sharp indicator function, α_{sh} , used to mark mixed-faces and their corner points (shown as filled black squares), and (c) linear reconstruction of the interface (dashed line), where $\alpha_{sh}=0.5$.

the gradient normal to the face f . In Eq. (2.27) the surface tension force term is non-zero only at the faces across which the indicator function α_{sh} has values. The α_{sh} represents a modified indicator function, which is obtained by curtailing the original indicator function α as follows;

$$\alpha_{sh} = \frac{1}{1 - C_{sh}} \left[\min \left(\max \left(\alpha, 1 - \frac{C_{sh}}{2} \right), 1 - \frac{C_{sh}}{2} \right) - \frac{C_{sh}}{2} \right] \quad (2.28)$$

where C_{sh} is the sharpening coefficient. From Eq. (2.28) one can notice that as the sharpening coefficient (C_{sh}) value increases, the unphysical interface diffusion decreases (i.e., it limits the effect of unphysical values at the interface, by imposing a restriction on alpha - α - as demonstrated). A zero value of C_{sh} will lead to the original CSF formulation, while as C_{sh} value increases the interface becomes sharper. As expected, the continuous - α - approach has a smooth (and diffused) transition across the interface. Whereas the sharp - α_{sh} - approach has a more abrupt transition with larger extremes. At high values of C_{sh} (0.5 to 0.9), Eq. (2.28) limits the indicator function - α - where values between (0 to 0.4) are summed to zero and values between (0.6 to 1) are summed to be one. This implementation introduces a sharper approach of the surface tension forces as discussed by Aboukhedr et al. [110]. Values in the range of (0.5) C_{sh} were observed to give the best results for most of our test cases.

2.2.4 Capillary Pressure Jump Modelling

In order to avoid difficulties associated with the discretisation of capillary force f_c a rearrangement of the terms on the right hand side of the momentum equation is conducted following the work of Raeini et al. [109], where Eq. (2.2) is rewritten in

terms of the microscopic capillary pressure p_c :

$$\frac{D}{Dt}(\rho u) - \nabla \cdot T = -\nabla p_d + f', \quad (2.29)$$

$$f' = \rho g + f_s - \nabla p_c \quad (2.30)$$

where dynamic pressure $p_d = p - p_c$, this approach includes the effect of capillary forces explicitly in the Navier-Stokes equations and allows for the filtering of the numerical errors related to the inaccurate calculation of capillary forces. Considering a static fluid configuration for a two-phase flow. The stress tensor reduces to the form $(n \cdot \tau \cdot n = -p)$, and the normal stress balance is assumed to have the form of $(p_c = \sigma \nabla \cdot n)$ [111]. Then, the pressure jump across the interface is balanced by the curvature force at the interface.

$$\nabla \cdot \nabla p_c = \nabla \cdot f_s \quad (2.31)$$

Assuming that pressure jumps can sustain normal stress jumps across a fluid interface, they do not contribute to the tangential stress jump. Consequently, tangential surface stresses can only be balanced by viscous stresses. Therefore, one can apply a boundary condition of:

$$\frac{\delta p_c}{\delta n_s} = 0 \quad (2.32)$$

where n_s is the normal direction to the boundaries. By including this set of equations to the Navier-Stokes equations, one can have a better balancing of momentum. Hence filtering the numerical errors related to inaccurate calculations of the surface tension forces.

2.2.5 Filtering Numerical Errors

As a result of the numerical unbalance discussed in the previous sections when modelling the movement of a closed interface, it is difficult to maintain the zero-net capillary force while modelling the movement of the interface. Hence it is difficult to decrease the errors in the calculation of capillary forces to zero $\oint f_s \cdot A_s = 0$ where A_s is the interface vector area. Raeini et al. [109] proposed a solution to filter the non-physical fluxes

generated due to the inconsistent calculation of capillary forces based on a user-defined cut-off. The cut-off uses a thresholding scheme, aiming at filtering the capillary fluxes ($\phi = |S_f|(f_s - \nabla_f^\perp p_c)$) and eliminate the problems related to the violation of the zero net capillary force constraint on a closed interface. The proposed filtering procedure explicitly sets the capillary fluxes to zero when their magnitude is of the order of the numerical errors. The filter starts from setting an error threshold as;

$$\phi_{threshold} = U_f |f_s|_{avg} |S_f| \quad (2.33)$$

where $\phi_{threshold}$ is the threshold value below which capillary fluxes are set to zero and $|f_s|_{avg}$ is the average value of capillary forces over all faces. The filtering coefficient U_f is used to eliminate the errors in the capillary fluxes. Different values for the U_f coefficient is used for different test cases, in which capillary fluxes are set to zero. After selecting the threshold, the capillary flux is filtered as:

$$\phi_{filter} = |S_f|(f - \nabla_f^\perp p_c) - \max(\min(|S_f|(f - \nabla_f^\perp p_c), \phi_{threshold}), -\phi_{threshold}) \quad (2.34)$$

Using this filtering method, numerical errors in capillary forces causing instabilities or introducing significant errors in the velocity field are prevented. By using the aforementioned filtering technique, the problem stiffness is found to be reduced by eliminating the high-frequency capillary waves when the capillary forces are close to equilibrium with capillary pressure. Consequently, it allows larger time-steps to be used when modelling interface motion at low capillary numbers.

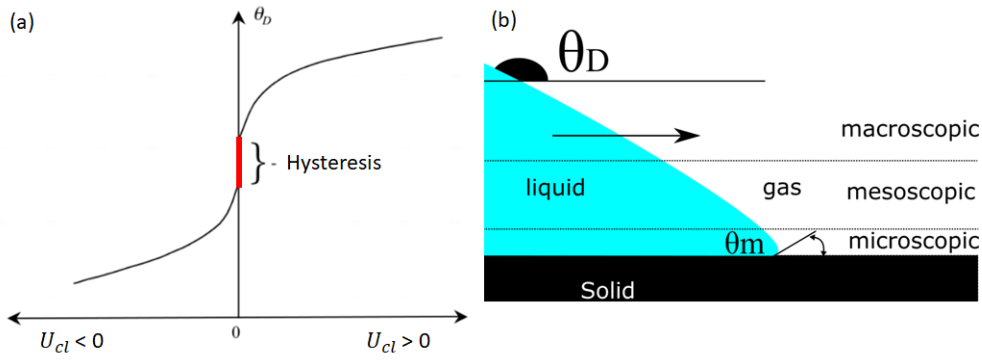


Figure 2.5: Schematic representation of the velocity dependence of the contact angle (a), schematic representation of viscous bending in different scales for an advancing scenario (b) [4]

2.3 Dynamic Contact Angle Model Implementation

The main parameters used to characterize the dynamics of contact line movement are the fluid-solid relative velocity U_{cl} , at which the liquid moves across the solid, and the dynamic contact angle θ_D . The dynamic contact angle represents the key to boundary condition definition for any wetting process. Since solid surfaces are often rough, the equilibrium contact angles may not be represented by single-valued, but will depend on whether the interface has been advanced or recessed, a phenomenon is known as contact angle hysteresis. In forced wetting applications, the fluid contact line is made to move by an external force, where a relationship is expected between θ_D and U_{cl} for a given system under a given set of conditions. It is generally noticed that the contact angle behaviour depends on both the speed and direction of displacement. This is shown schematically in Fig. 2.5 for a system that also exhibits contact angle hysteresis, and is demonstrated in the schematic of Fig. 2.5. The presence of hysteresis at such creeping velocity (red line at zero velocity), which represents a modelling challenge.

Due to the fact that the observed dynamic contact angle is velocity-dependent, therefore it will differ from its equilibrium value. The hydrodynamic theory in wetting conditions, emphasises energy dissipation due to viscous flow within the wedge of liquid near the moving contact line. Although various methods had been proposed to model wetting behaviour, the basic methodology remains the same: where changes in the macroscopic dynamic contact angle are attributed to viscous bending of the two-phase interface within a mesoscopic region at a scale below that of observation but greater than the molecular scale. The microscopic angle θ_m is assumed to be governed by short-range intermolecular forces and to retain its static value θ_S as illustrated in Fig. 2.5.

To implement empirical correlation given by Kistler Eq. (1.14, 1.11) in our multi-phase simulation with the presence of solids, the fluid-solid contact angle model must be coupled with the VoF simulation. The coupling can be done by imposing the contact line model according to the following equation:

$$\hat{n} = \hat{n}_n \cos \theta + \hat{n}_t \sin \theta \quad (2.35)$$

where θ is a prescribed value of the contact angle at the wall as a boundary condition and varied based on the model implementation, \hat{n} is the unit vector normal to the interface, \hat{n}_n is the unit vector normal to the solid-fluid interface pointing into the solid, and \hat{n}_t is the unit vector tangent to the solid-fluid interface pointing toward phase one [112]. In our simulations, the smoothed indicator function α_{smooth} is then used to obtain the interface normal vectors at the centre of cells. The calculation of the contact line velocity is based on the actual velocity calculated at each computational cell, in the close region of the triple-phase contact point, from which the velocity component parallel to the wall and based on the velocity capillary number is calculated:

$$\vec{U}_{cl} = (U_{cell} \cdot \hat{n}_t) \frac{\hat{n}_t}{|\hat{n}_t|} \quad (2.36)$$

$$Ca = \frac{\mu U_{cl}}{\sigma} \quad (2.37)$$

where μ is the dynamic viscosity of liquid, U_{cl} is the contact line velocity and σ surface tension. Based on the relevant experimental data.

$$\theta_D = \begin{cases} \theta_A & \text{if } U_{cl} \geq 0 \\ \theta_R & \text{if } U_{cl} < 0 \end{cases} \quad (2.38)$$

In order to consider the effect of hysteresis see (Fig. 2.5) in the numerical model, the equilibrium contact angle θ_S in Eq. (1.14) is replaced by either the advancing contact angle or the receding contact angle depending on the sign of the velocity vector at the contact line, where advancing θ_A and receding θ_R contact angles are system properties and should be imposed as in Eq. (2.38)

2.4 Algorithm Implementation

The modelling approach for VoF compression scheme has been implemented using the OpenFOAM finite volume library [56], which is based on the VoF-based solver InterFOAM [113]. No geometric interface reconstruction or tracking is performed in InterFoam; rather, a compressive velocity field is superimposed in the vicinity of the interface to counteract numerical diffusion as already discussed in Section 2.2.1. In the original VoF-based solver (InterFOAM), the time step is only adjusted to satisfy the Courant-Friedrichs-Lewy (CFL) condition. This imposes a limit on the time step by introducing a variable numerical timescale. In this work, a semi-implicit formulation is used for estimating the capillary forces, along with a Crank-Nicholson scheme for advection of the indicator function, in order to ensure the accuracy and stability of the numerical method when more substantial time steps are used. Initially, the indicator function is advected for half of the time step using the fluxes at the beginning of each time step. Then the equations for the advection of the indicator function for the second half of the time step are solved iteratively in two loops). The discretised phase fraction Eq. (2.15) is then solved for a user-defined number of sub-cycles (typically 2 to 3) using the multidimensional universal limiter with clear solution MULES solver. Once the updated phase field is obtained, the algorithm enters in the pressure-velocity correction loop.

2.4.1 Solution of the Momentum Equation

The solution of the momentum equation coupled with the surface tension models is applied by constructing an assumed velocity field and then correcting it using the Pressure Implicit with Splitting of Operators (PISO) implicit pressure correction procedure to time advance the pressure p and velocity fields. The PISO iteration procedure in OpenFOAM is indexed by m , where m corresponding to the number of steps at the presented time level t^n for n time step. First, we consider the discrete version of the left-hand side of Eq. (2.2) accounting only for the temporal, viscous and advective terms, which yields an explicit expression for the predicted velocity field \mathbb{U}_P^r as:

$$\frac{(\rho_P^{n+1}\mathbb{U}_P^r) - (\rho\mathbb{U})_P^n}{\Delta t} + \sum (\rho_f\phi_f)^n\mathbb{U}_f^r \quad (2.39)$$

Before describing the advection and viscous terms, the velocity corresponding to a

given face f needs to be defined, which can be obtained using Eq. (2.40). With respect to the viscous term, the surface gradient operator ∇_f^\perp acting on \mathbb{U} is given by:

$$(\nabla_f^\perp \mathbb{U}^r) = \Theta(f) \frac{\mathbb{U}_N^m - \mathbb{U}_P^r}{|cellsize|} \quad (2.40)$$

where $\Theta(f)$ is 1 if P is the owner for face f and N is the neighbour, and -1 if N is the owner for face f and P is the neighbour. The momentum equation, after discretisation and linearization can be written as a function of U_P^r , but due to the issues with collocated variable arrangement observed in the case of high-density ratio flows it is solved by interpolating U_P^r to the cell faces as:

$$\left(\mathbb{U}_P^r\right)_f = \left(\frac{\widehat{\mathbb{H}}_u}{A_p}\right)_f + \left(\frac{(\sigma k \alpha_{sh})^{n+1}}{A_p}\right)_f - \left(\frac{(g \cdot x \nabla \rho)^{n+1}}{A_p}\right)_f \quad (2.41)$$

where $\widehat{\mathbb{A}}_u$ represents the diagonal entries in the discretised form of the momentum equation, and $\widehat{\mathbb{H}}_u$ can be expressed as:

$$\widehat{\mathbb{H}}_u = \sum \mathbb{A}_N \mathbb{U}_N^m + \mathbb{B}_P^n \quad (2.42)$$

$$\mathbb{A}_N = -0.5(\rho_f \phi_f)^n [1 - \Theta(f) S(f) (1 - \alpha)] + \mu_f^{n+1} \Theta(f) \frac{|S_f|}{cellsize} \quad (2.43)$$

$$\mathbb{B}_P^n = \frac{(\rho \mathbb{U})_P^n}{\nabla t} + \nabla \mathbb{U}_P^n \cdot \nabla \mu_P^{n+1} \quad (2.44)$$

and,

$$S(f) = \begin{cases} 1 & \text{for } S(f) \geq 0 \\ -1 & \text{for } S(f) < 0 \end{cases} \quad (2.45)$$

The associated volume flux $\phi_f = \mathbb{U}_P^r \cdot S_f$ is obtained by performing an inner product with face surface area, where it completes the predictor step, then the pressure contribution in terms of a flux as is derived from the discretization of the incompressibility condition and momentum conservation, Eq. (2.41):

$$\left(-\frac{\nabla p}{A_p}\right)_f \cdot S_f = \frac{-1}{A_p} (\nabla_f^\perp p^{m+1}) |S_f| \quad (2.46)$$

Then the associated volume flux $\phi_f = \mathbb{U}_P^r \cdot S_f$ will treat p implicitly in iterative way

as follows :

$$\phi_f^{m+1} = \phi_f^r + \frac{1}{A_{p_f}} (\nabla_f^\perp p^{m+1}) |S_f| \quad (2.47)$$

To determine the unknown pressure field p^{m+1} mass conservation for an incompressible medium has been imposed, and results in a linear system for p^{m+1} , and can be solved using the preconditioned conjugate gradient (PCG) method. Besides PCG, OpenFOAM provides various other options such as preconditioned biconjugate gradient, generalised geometricalgebraic multi-grid and smoothSolver, which uses a smoother for convergence. Finally, the cell centred velocity fields \mathbb{U}_p^{m+1} are obtained by reconstructing the face velocity flux, which will mark the end of a single PISO iteration loop. The next PISO iteration is performed by changing the superscript m to $m+1$ and updating $\widehat{\mathbb{H}}_u$ with the velocity. In the simulations, a five PISO iteration levels (i.e. $M = 5$) were used. At the end of the iteration procedure, the values corresponding to the M th iteration are assigned to the new time step ($n + 1$), which marks the end of the solution procedure for the t_{n+1} time level.

2.5 Concluding Remarks

This chapter illustrated the numerical framework developed to solve the two-phase flow problems at low capillary numbers applications. The two-phase flow framework solver is developed using OpenFOAM platform as it provides open source capabilities to implement new models on existing libraries. The proposed framework is developed for modelling two-phase flow for the micron scale models at creeping flow rates, where the capillary forces play an important role. To improve the numerical model stability and to decrease the required computational resources, a new adaptive compression scheme is introduced, allowing for dynamic estimation of the compressive value only at the areas of interest. The adaptive method is found to increase the numerical accuracy and to reduce the sensitivity of the methodology to tuning parameters. The previous model is coupled with additional sharpening and smoothing algorithms for the interface capturing. Coupling the adaptive compression scheme with the sharpening and smoothing algorithms helped in minimising the parasitic currents present in low capillary number simulations when viscous forces and surface tension dominate inertial forces. A coupling between the capillary pressure and the Navier-Stokes equations is added to improve the efficiency of the numerical method for low capillary number flows as mentioned. The capillary pressure equation was solved separately from the dynamic pressure. This allowed to filter the capillary forces to avoid numerical errors and instabilities. Finally this chapter presents an implicit formulation for capillary forces, which alleviates the capillary time-step constraint and allows larger time-steps for long-term prediction of two-phase flow at low capillary numbers. The new solver implementation is able to accurately and efficiently decrease the computational cost for this type of simulation by eliminating the spurious current problem present in the standard VoF formulation as shown in the next chapter.

Chapter 3

Validation of the Numerical Method

3.1 Introduction

In the following sections, numerical simulations are presented for a range of benchmark cases that assess the performance of the proposed model. As a first benchmark case, a stationary single droplet and a pair of droplets (in the absence of gravity) have been considered. The convergence of velocity and capillary pressure to the theoretical solution is demonstrated. This test case assesses the performance of solvers in terms of spurious currents suppression. Then two other cases, commonly used in the literature, namely the Notched disc in rotating flow Zalesak [114] and the Circle in a vortex field Roenby et al. [68], Rider and Kothe [115] are examined. Moreover, a systematic comparative study for the Level Set and VoF numerical methods on the Rayleigh-Taylor instability problem, is used to stress the important advantages and disadvantages of the two methods presented. Finally, a more indicative example of flows through narrow passages is considered. This includes the generation of millimetric size bubbles in a T-junction. For the T-junction case, the prediction of any non-smoothed and diffused interface is accompanied by the development of spurious velocities resulting in unphysical results in comparison with the available experimental data. Calculations with the standard VoF-based solver of OpenFOAM *interFoam* are also included for completeness.

3.2 Stationary Droplet

3.2.1 Single Droplet

When an immiscible cubic 'droplet' fluid is immersed in a fluid domain (in the absence of gravity), surface tension will force the formation of the spherical equilibrium shape. The force balance between surface tension and capillary pressure should converge to an exact solution of zero velocity field. The corresponding pressure field should jump from a constant value p_0 outside the droplet to a value $p_0 + 2\sigma/R$ inside the droplet. Modelling the relaxation process of an oil droplet ($D_0 = 30 \mu m$) in water at static equilibrium serves as an initial demonstration case for testing the suggested methodology. The fluid properties of the background phase (water) density $\rho_1 = 998 \text{ kg/m}^3$, and the viscosity $\nu_1 = 1.004e - 6 \text{ m}^2/s$, while the droplet phase (oil) density $\rho_2 = 806.6 \text{ kg/m}^3$, and the viscosity $\nu_2 = 2.1e - 6 \text{ m}^2/s$, and surface tension $= 0.02 \text{ kg/s}^2$. These values result to ($\Delta Pc = \frac{2\sigma}{R} = 2666 Pa$). The calculation set up includes a single cubic fluid element located at the centre of the computational domain, and it is allowed to relax to a static spherical shape as shown in Fig. 3.1. It has been shown in the literature [116] that under these conditions and depending on the accuracy of the interface tracking/capturing scheme, non-physical vortex-like velocities may develop in the vicinity of the interface and can result in its destabilization. Tables 3.1 and 3.2 demonstrate the different controlling parameters that have been tested. The main testing parameters shown in the Table are: (i) the flux filtering percentage U_f as presented in Eq. (2.33), (ii) the number of smoothing loops n as presented in Eq. (2.24), (iii) the sharpening coefficient C_{sh} as presented in Eq. (2.28) and finally (iv) the compression coefficient $C_{compr.}$ as presented in Eq. (2.16). Each series of test cases is designed to examine the effect of the mentioned models on parasitic currents and pressure jump calculation accuracy. Cases (S) examine the effect of smoothing loops number in the absence of interface sharpening and filtering. Cases (A) are designed to study the effect of error filtering percentage in the absence of smoothing loops and interface sharpening. Cases (B) examine the combined effect of filtering and smoothing in the absence of interface sharpening, while cases (SE) and (SF) are designed to test the combined effect of smoothing and filtering in the presence of interface sharpening and interface compression, respectively. The adaptive compression scheme introduced in the previous section is not considered in this section.

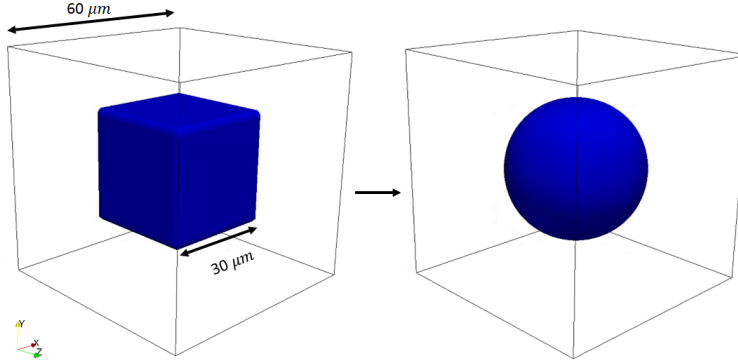


Figure 3.1: Computational domain for modelling static droplet, (left) initial condition a cube of size $D_0 = 30 \mu\text{m}$, and (right) static shape of droplet. Mesh size $R/\delta x = 15$ at $t = 0.0025 \text{ s}$.

Table 3.1: Control parameters used in studying the static droplet. In these test cases C_{sh} and C_{comp} are set to zero

Case	$U_f\%$	n Eq. (2.24)	Case	$U_f\%$	n	Case	$U_f\%$	n
S1	0	2	A1	0.01	0	B1	0.05	2
S2	0	5	A2	0.05	0	B2	0.05	5
S3	0	10	A3	0.1	0	B3	0.05	10
S4	0	20	A4	0.2	0	B4	0.05	20

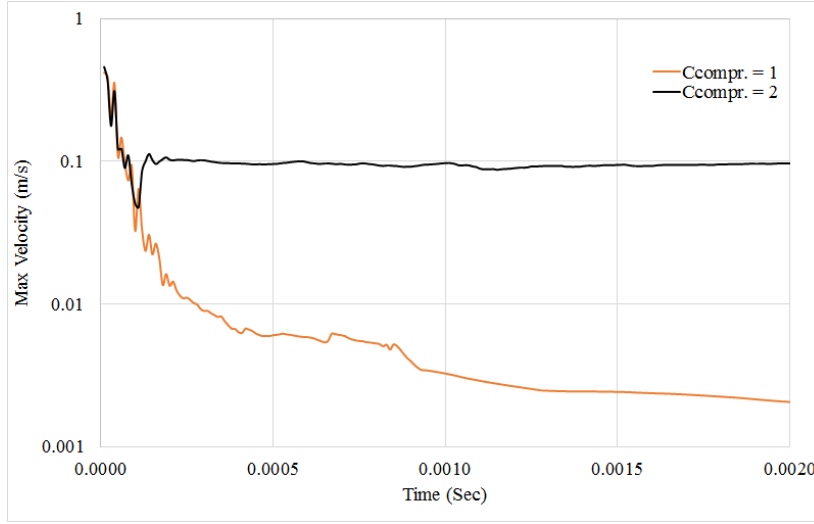
The maximum velocity magnitude in the computational domain is presented as a function of various numerical parameters. If inertial and viscous terms balance in the momentum equation then parasitic velocities should be zero. However, the CSF technique introduces an unbalance by replacing the surface force with a volume force which acts over the small region surrounding the continuous phase interface. The surface force suggested by Brackbill et al. [53] includes a density correction as $1/We \frac{\rho}{\langle \rho \rangle} \kappa n$ for modelling systems where the phases have unequal density. Where ρ is the local density and $\langle \rho \rangle$ is the average non-dimensional density of the two phases. Including these two variables does not affect the total magnitude of the force applied, but weights the force more towards regions of higher density. This tends to produce more uniform fluid accelerations across the width of the interface region. Such a force is irrotational

Table 3.2: Control parameters used in studying the static droplet. In these test cases C_{sh} and C_{comp} are not set to zero

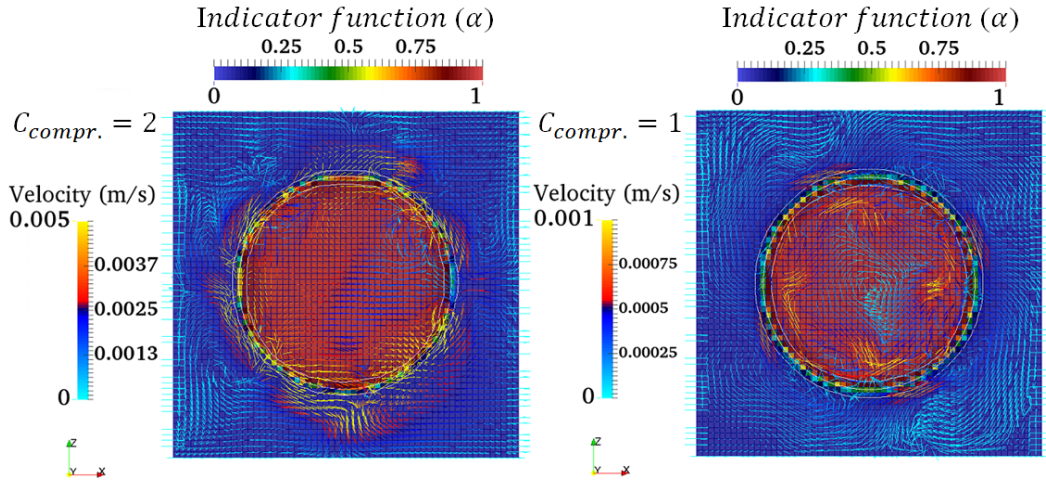
Case	$U_f\%$	n	C_{sh} Eq. (2.28)	C_{comp}	Case	$U_f\%$	n	C_{sh}	C_{comp}
SE1	0.05	10	0.1	0	SF1	0.05	10	0.5	0.5
SE2	0.05	10	0.5	0	SF2	0.05	10	0.5	1
SE3	0.05	5	0.1	0	SF3	0.05	10	0.5	2
SE4	0.05	5	0.5	0	SF4	0.05	10	0.5	3

and so can be represented as the gradient of a scalar field. Referring to the momentum equation 2.2, the surface tension force has to be precisely balanced by the pressure gradient term, with all velocity dependent terms, and thus velocities, being zero. The commonly used VoF numerical implementation of this system differs from this ideal implementation of α , which when discretised represents the volume fraction integrated over the dimensions of a computational mesh cell and varies by a small amount in the radial direction. This results in n -(the normal to the interface) not being precisely directed in the radial direction, κ value varying slightly and the full interface volume force having a rotational component. The rotational component of the surface tension force cannot be balanced by the irrotational pressure gradient term. So it must be balanced instead by one or more of the three other velocity dependent terms. As these velocity terms (inertial transient, inertial advection and viscous) all require non-zero velocities if they themselves are to be non-zero, spurious currents develop. Looking into the parasitic velocity magnitude for the standard *interFoam* solver during the relaxation period Fig. 3.2a, parasitic velocities are high and depend on the compression level. As the value of $C_{compr.}$ increases, the maximum velocity also increases. This might appear to be counter-intuitive since increased compression should result in sharper interfaces and thus, in a more accurate calculation of the curvature κ and the normal vectors. However numerically, this is not the case since the sharper the interface, the more numerical challenging becomes the calculation of derivatives. Fig. 3.2a indicates this paradox while Fig. 3.2b presents a graphical explanation. It can be seen that as $C_{compr.}$ increases then vortex-like structures develop randomly around the interface that prevents the droplet from relaxing to equilibrium.

Testing the smoothing effect presented in Eq. (2.23, 2.24 and 2.25) using the modified solver *interPore* by varying the number of smoothing loops (n); as shown in cases (S1,S2,S3,S4) of Table 3.1 is also performed in the present sub-section. The mentioned setup in cases (S1,S2,S3,S4) is used to investigate the effect of smoothing loops on the parasitic currents, isolated from the other examined controlling parameters. It is evident from Fig. 3.3e that by increasing the number of smoothing loops, the magnitude of the parasitic currents decreases. However, it should be pointed out that this reduction of parasitic currents comes at the cost of a corresponding increase in the interface region thickness. Increasing the smoothing loops to 20, the interface thickness increases almost 4 times (6 cells) and parasitic currents tend to develop again and increase by time at a certain point after the relaxation of the droplet. The effect of varying the



(a) Spurious currents with relation to interface compression



(b) 2D representation for spurious currents vector field

Figure 3.2: (a) Evolution of maximum velocity during droplet relaxation using the standard *interFoam* solver with two different interface compression ($C_{compr.}$). (b) values Snapshot of the interface shape after the relaxation of the oil droplet using the standard *interFoam*. Velocity vectors near to the interface for different interface compression values are presented.

coefficient U_f for filtering the capillary forces parallel to the interface see Eq. (2.34) is revealed from cases A1 to A4 of Table 3.1. A decrease of the parasitic currents due to the wrong flux filtering near to the interface can be noticed. In the absence of smoothing loops and just changing the filter value U_f , a significant decrease of the parasitic currents is observed as shown in Fig. 3.3b. Moreover, an optimum decrease in parasitic currents using a value of $U_f = 0.05$ is observed Table 3.1. The decrease of parasitic currents magnitude, in this case, is a combination of the interface treatment of Eq. (2.23) and the flux filtering without any smoothing loops being performed. Looking at Fig. 3.3b one can observe the asymmetric distribution of the velocity vector field with almost zero velocity inside the droplet. By examining the isolated filtering and smoothing models, the suggested framework drastically reduces the spurious velocities,

by almost four orders of magnitude, over a relatively long period. Cases B1 to B3 of Table 3.1 reveal the effect of combining both techniques (smoothing and flux filtering) for damping the parasitic currents; one of the parameters has kept constant - in this case, U_f . Comparing cases (B2) presented in Figs. 3.3c with the previously presented cases (S and A), a major improvement in velocity reduction can be seen. In Fig. 3.4 (B) a reduction of almost four orders of magnitude has been achieved, when compared with the standard solver.

By examining the individual filtering and smoothing effects, it has been demonstrated that the suggested model drastically reduces the maximum velocity field (see Tables 3.3). Selecting the best combination of smoothing and the filtering coefficient ($5 < n < 10$ and $U_f = 0.05$), the effect of the sharpening model Eq. (2.28) is examined next. In Table 3.2 cases (SE1 to SE4), the C_{sh} has been varied. Looking at Fig. 3.3a, a great reduction in the interface thickness can be seen, reaching almost one grid cell. By combining the effect of sharpening, filtering and smoothing techniques, the same order of magnitude for parasitic currents has been achieved, with a significant decrease in interface thickness. It has also been found that in SF1 case specifically, a very good balance in the velocity vector field with zero velocity inside the droplet Fig. 3.4 has been achieved.

As mentioned before, the literature review has revealed the negative effect of increasing the value of compression coefficient, since as the value of $C_{compr.}$ increases the magnitude of parasitic currents also increases. Using the same droplet test case, the effect of increasing the $C_{compr.}$ value on the parasitic current is demonstrated; but this time after applying the smoothing and flux filter models. It should be noted, the aforementioned adaptive compression model is not tested in this case yet, as it will be tested in the next section. In Table 3.2 cases (SF1 to SF4), the cases using the best combination of the previously mentioned smoothing and filter values coefficient are used with different compression values. The overall maximum velocity values are higher compared to those achieved using no compression; nevertheless, these are still lower than those achieved using the standard solver. A swirling behaviour around the external diagonal direction of the droplet had been noticed as shown in Fig. 3.3b and 3.3c. The observed small swirling velocity confirms that the unbalanced surface tension force may increase parasitic currents at one specific location due to this swirling behaviour around the droplet interface. At the same time, the effects of the smoothing and the filtering can have a positive effect on smoothing these swirling velocities. The

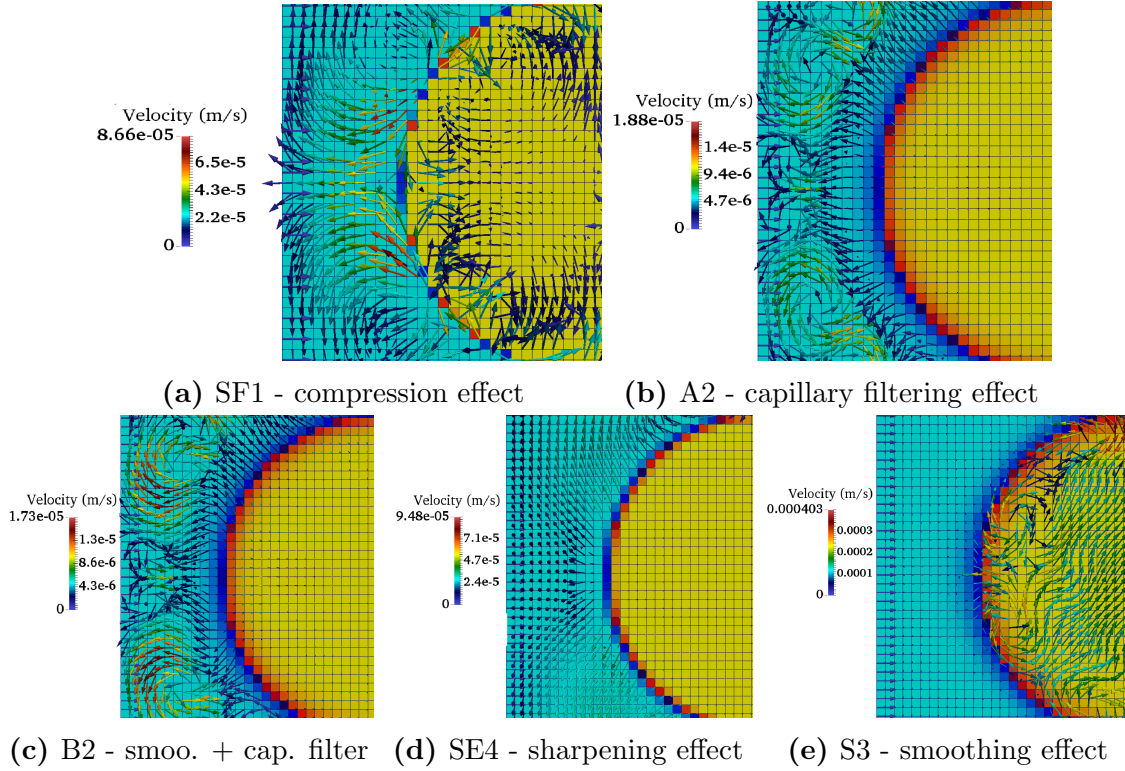


Figure 3.3: Effect of varying model coefficients described in table 3.1 and 3.2 on parasitic currents, all figures are showing velocity vector field at $t = 0.0024$ sec. Figures are coloured with indicator function α_{Sharp} as yellow shows oil phase inside the droplet and bright blue shows water outside the droplet

behaviour of the droplet, when different parameters are considered, is vital in assessing the impact that the parasitic currents have on the results. Similar simulations but with varying domain sizes (not included in this study) showed that when the parasitic currents were inertia-driven at the deformation phase, they spread further across the computational domain. Depending on the nature of the simulation being considered, this may mean that inertia-driven parasitic currents have a greater impact on the results. Quantifying this effect would be difficult, as an integral measure of the parasitic currents – such as the total kinetic energy within the domain for example – would be dependent on additional geometrical factors, such as the domain size and interfacial area. While the structure of the velocity field is changing with time, one can conclude that the parasitic currents are dominated by unbalanced inertia term. The assessment of the effect of different parameters on the maximum velocity can also be presented in the percentage of divergence from the standard solver results as illustrated by Eq. (3.1):

$$E_{parasitic} = \frac{\min(U)}{\min(U)_{C_\alpha=2}} \quad (3.1)$$

where $E_{parasitic}$ represents the error calculated by the $\min(U)$ to be the minimum ve-

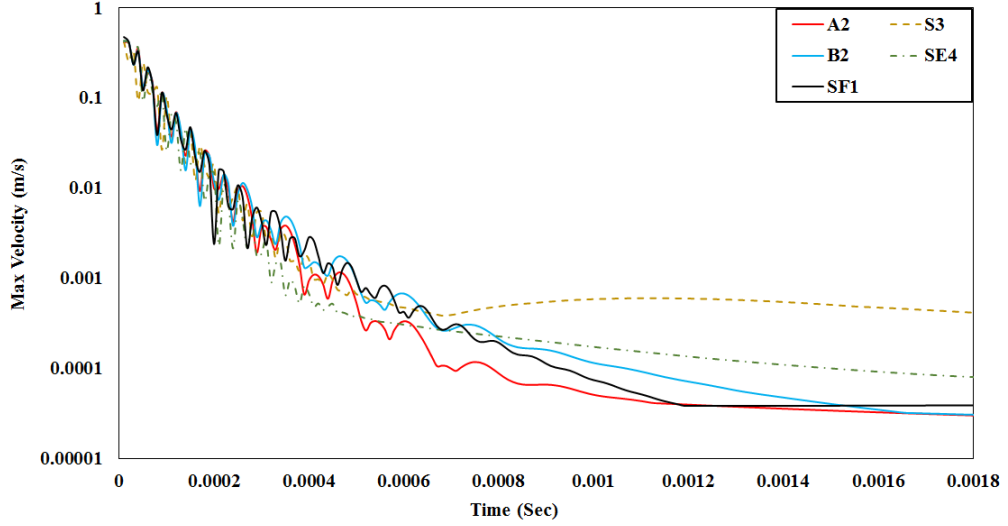


Figure 3.4: Effect of varying models coefficients presented in Table 3.1 and 3.2 on maximum parasitic currents over period of time

locity in the domain achieved using *interPore* and $\min(U)_{C_\alpha=2}$ to be minimum velocity using standard solver at $C_{compr.} = 2$ during the droplet relaxation over a long time interval. Table 3.3 shows that the magnitude of parasitic currents decreases to minimal in case (B2) where compression and sharpening are null; one can also achieve the same level of reduction in parasitic currents after applying sharpening, as in case (SE3) and with only a slight further increase by adding compression as in case (SF1). Table 3.3 shows numerically predicted pressure difference between the relaxed spherical droplet and the ambient liquid along the droplet diameter axis for each of the 20 simulated cases, in comparison with the theoretical value predicted from the Laplace equation (see [117] for more details). The results are presented in terms of the errors in predicted capillary pressure, $Error_{Pc}$, defined as follows:

$$Error_{Pc} = \frac{Pc - Pc_{theoretical}}{Pc_{theoretical}} / \left(\frac{P - P_{theoretical}}{P_{theoretical}} \right)_{interFoam_{c_{\alpha}=2}} \quad (3.2)$$

where Pc is the calculated capillary pressure using the developed solver, and the P is the calculated capillary pressure using the standard solver at compression values equals to two. The $Error_{Pc}$ presents the deviation of the calculated capillary pressure using the developed solver and the standard solver with respect to the theoretical capillary pressure. Equation 3.2 shows the reduction in error between the developed solver and the standard solver using compression ($C_{compr.} = 2$). In all the presented cases, reduction in predicting the capillary pressure by 40 % can be seen.

Table 3.3: Reduction in predicted capillary pressure and parasitic currents compared to the standard *interFoam*

<i>Smooth</i>	S1	S2	S3	S4
$Error_{pc}\%$	41.43	40.57	39.64	33.38
$E_{parasitic}$	0.0051	0.0053	0.0080	0.0112
<i>Filter</i>	A1	A2	A3	A4
$Error_{pc}\%$	45.55	45.51	45.51	45.63
$E_{parasitic}$	0.0031	0.0006	0.0011	0.0014
<i>Filter</i>	B1	B2	B3	B4
$Error_{pc}\%$	44.36	43.39	42.20	40.91
$E_{parasitic}$	0.0005	0.0006	0.0013	0.0032
<i>Sharp</i>	SE1	SE2	SE3	SE4
$Error_{pc}\%$	43.04	45.14	43.97	46.11
$E_{parasitic}$	0.0008	0.0024	0.0007	0.0015
<i>Sharp</i>	SF1	SF2	SF3	SF4
$Error_{pc}\%$	49.79	50.20	50.12	49.95
$E_{parasitic}$	0.0008	0.0045	0.0057	0.0067

3.2.2 Multiple Droplets

This section will discuss the effect of parasitic current interaction for the case of two stagnant droplets that undergo the same relaxation process. The same droplet properties as in the previous test case have been used. To the authors best knowledge, this test case has not been presented before in the literature. When two droplets are found in the same domain in close proximity, the parasitic currents may interact resulting in artificial movement of the droplets and eventually merging. Figure 3.6 shows the veloc-

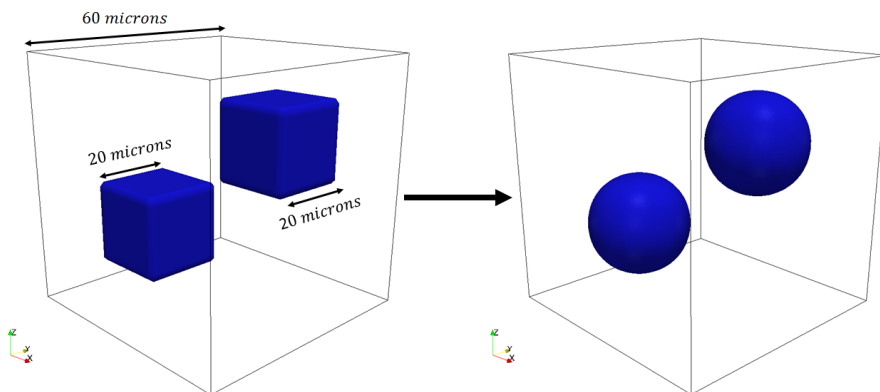


Figure 3.5: Computational domain showing two static droplets , (left) initial condition a cube of size $D_0 = 20 \mu\text{m}$ each, and (right) static shape of droplet as two boxes.

ity magnitude on the droplet represented by the 0.5 liquid volume fraction iso-surface. The same set of parameters is utilised as in (A2, B2, SE3 and SF1) cases mentioned in Tables 3.1 and 3.2. One can notice in Fig. 3.6a to Fig. 3.6c that the two droplets

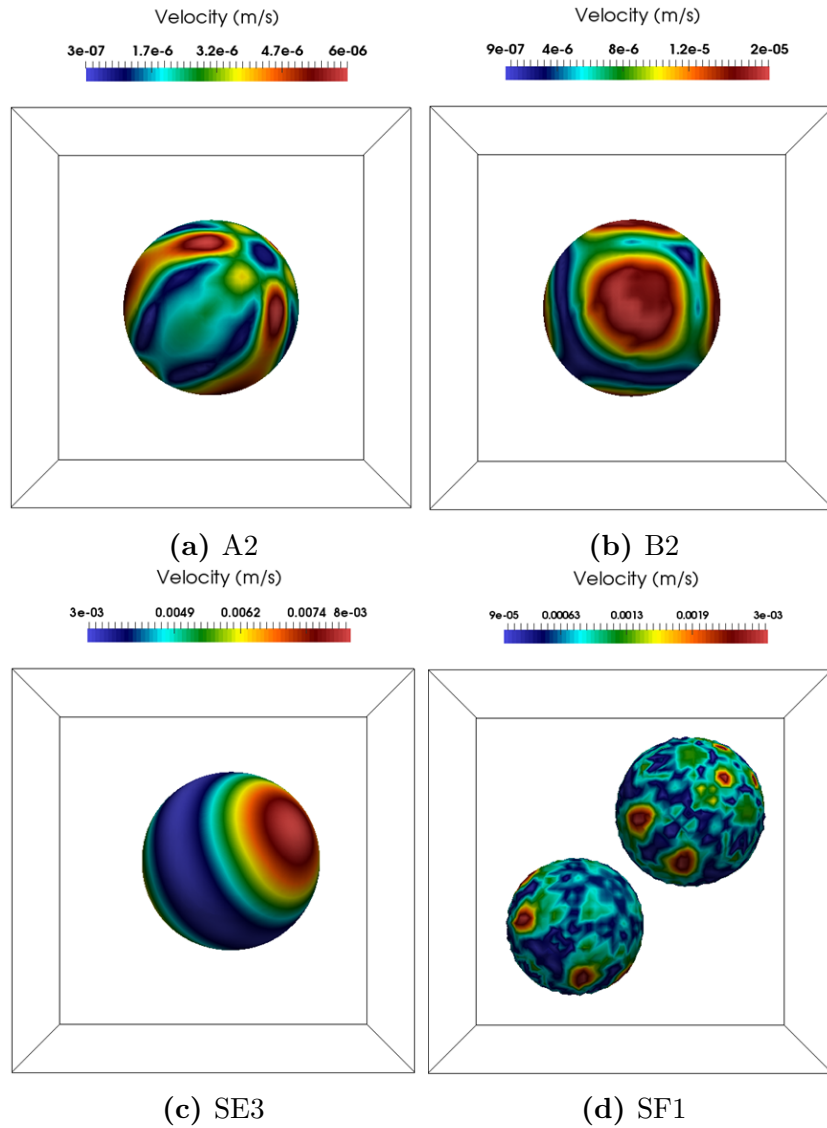


Figure 3.6: Effect of combined flux filtering and smoothing in the presence of sharpening model on the interaction of parasitic velocity field. All figures are showing the velocity field at $t = 0.0024$ sec on the indicator function α_{Sharp} isocontour = 0.5

have merged into one big droplet located at the centre of the computational domain.

In contrast Fig. 3.6d shows that the two droplets remain in their initial position as they should. This can be considered as a demonstration that optimising compression for one case does not necessarily mean that can offer optimum results for other similar cases and the solver should automatically adapt the needed compression. Hence, in the next sections that consider cases with higher deformation of the interface, the adaptive solver will be introduced.

3.3 Rayleigh-Taylor Instability with Surface Tension

The second test configuration consists of a Rayleigh–Taylor problem with homogeneous layers of a high-density fluid penetrating a low-density fluid under the influence of gravity alone. A hydrodynamically-unstable interface is formed between the stratified laminar immiscible fluid layers, initially at rest. The Rayleigh–Taylor instability (RTI) is of great fundamental interest in physics and fluid mechanics. For example, in geological flows, it can represent situations where water is suspended above the oil.

For the present unstable configuration, infinitesimally small perturbations of the interface will grow with time. Due to the continuous generation of vorticity that leads to a pattern of bubbles of light fluid penetrating the heavy fluid (upwards), and spikes of heavy fluid penetrating the light fluid (downwards). This process may lead to the formation of a mixing layer. The RTI was initially investigated by Lord Rayleigh in 1883 [118] and later theoretically studied by Taylor [119]. An overview of the subject has been given by Sharp [52]. In the following sections, the capability of the modified VoF solver *interPore* is evaluated along with the conservative LS method as implemented in the RCLS solver discussed by [120], for the modelling of a single “finger”, or “spike”, of the RTI with surface tension. The numerical demonstration of the RTI is a common test case when examining the numerical convergence and the capability of a solver to capture the interface physics in the presence of high-density ratio and surface tension [121–123]. We refer the reader to a previous study by Pringuey and Cant [124] that assessed the performance of *RCLSFoam* against *interFoam*. To the best of the authors knowledge, there has not been a systematic comparative study of state-of-the-art LS and VoF numerical methods on the RT problem, where the important advantages and disadvantages are presented. The comparison between the two well-known methods, will help the reader to understand the important difference between the two methods, and the advancements of modified VoF method compared to the theoretical results.

3.3.1 Numerical Setup

The two isothermal fluids are set at ambient temperature and pressure. The viscosities are assumed equal so that there is no jump in viscosity at the interface and thus no jump

in the velocity gradient, as viscosity controls the shear stress. The two adjacent fluids are initially quiescent, but the sharp horizontal density mismatch induces a density gradient (upwards) opposite to the pressure field and gravitational field (downwards). The interface is hydro-dynamically accelerated by the pressure gradient [52]. The gravitational forces act to destabilise the interface, while the surface tension forces act to stabilise it.

A chosen set of parameters is used in the comparison and validation of the RTI given in Popinet and Zaleski [122] and Puckett et al. [123] on a comparatively coarse mesh of 64×224 hexahedral elements and a finer one of 128×512 elements. The two-dimensional domain is $[-0.5, -2] \times [0.5, 2]$ m Fig. 3.7. The physical parameters for the fluids are $\rho_l = 0.1694 \text{ kgm}^{-3}$, $\mu_l = 3.13 \times 10^{-3} \text{ kgm}^{-1}\text{s}^{-1}$ and $\rho_h = 1.255 \text{ kgm}^{-3}$, $\mu_h = 3.13 \times 10^{-3} \text{ kgm}^{-1}\text{s}^{-1}$ (density ratio of 7.4), with a constant surface tension of $\sigma = 0.01 \text{ Nm}^{-1}$. The acceleration due to gravity is set as $g = (0, -9.8\text{ms}^{-2}, 0)$. An initial surface perturbation is applied with a wave number of 2π and wavelength of 1 m. The initial disturbance in the free surface is given by the expression:

$$y = -0.05 \cos(2\pi x). \quad (3.3)$$

For the phase fraction and level-set, a homogeneous Neumann boundary condition was set at the bottom boundary of the domain and symmetry conditions were set at both sides. The same boundary conditions were set for the relative pressure $p_d = p + \rho gh$, as defined in the framework of OpenFOAM. In multiphase flow dynamics, the time-step Δt must be small enough to resolve the propagation of the capillary waves that develop at the interface. The time-step was set initially as $\Delta t = 0.001\text{s}$, but it was allowed to adapt automatically at runtime, which assured a Courant number below 0.5 throughout the run. Finally, the boundary conditions for the velocity were set as no-slip walls for the top and bottom boundaries and symmetry planes at both sides. The chosen set of simulation parameters is summarised in Table 3.4.

Calculations with *RCLSfoam* were made on an Intel Xeon machine with 32GB main memory possessing one 2.4Ghz CPU with 8 cores. The simulations with *interPore* were carried out on an Intel Xeon machine with 64GB main memory possessing one 2.4Ghz CPU with 12 cores. The total execution time on a 128×512 grid for *RCLSfoam* was 3.6 CPU hours, while that for the *interPore* was 17 CPU hours to generate 1.5 seconds of outputted results. It is interesting to note that for this test case the disparity in

Table 3.4: Table of numerical parameters for the Raleigh-Taylor simulation for two different mesh sizes.

RCLS	interPore	60×224	128×512
$N_S = 5 \ \epsilon = 0.5\overline{\Delta x} \ , \ S = 10 \ U_f = 0.1$	$C_{\text{comp}} = 0 \ C_{sh} = 0.1$	Case 1	Case 4
$N_S = 5 \ \epsilon = 1.0\overline{\Delta x} \ , \ S = 10 \ U_f = 0.1$	$C_{\text{comp}} = 0 \ C_{sh} = 0.5$	Case 2	Case 5
$N_S = 5 \ \epsilon = 2.0\overline{\Delta x} \ , \ S = 10 \ U_f = 0.5$	$C_{\text{comp}} = 1 \ C_{sh} = 0.1$	Case 3	Case 6

computational cost between the two codes is reversed. Here *RCLSFoam* is more efficient at dealing with the rapidly-evolving interface, as well as the fast-changing velocity and field.

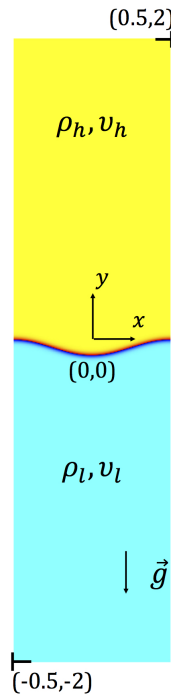


Figure 3.7: Computation domain for the simulation of the RTI.

3.3.2 Qualitative Description

Fig. 3.8 presents the relative performance of *RCLSFoam* with respect to *interPore*. This figure shows the interfacial history obtained by the two solvers on the same rectangular mesh of 60×224 cells, for eight different times in the interval $[0, 1.3]$ seconds. It can be seen that as time passes, the initial perturbation of the interface grows. The light fluid moves into the heavy fluid in the form of rising round bubbles on either side of the domain; while the heavy fluid sinks into the light fluid under gravity, between the bubbles, building up a central falling spike (Fig. 3.8-a (i) $t = 0.55$ s). A mushroom-shaped structure develops at $t = 0.7$ s. Then, the mushroom is stretched and filaments

start to detach forming isolated liquid structures (at $t = 0.95\text{s}$). Towards $t = 1.3\text{s}$, a settling process begins in which the denser fluid falls back down as droplets.

The complex phenomenology associated with the evolution of an RT unstable interface is reproduced reasonably well here by both solvers. The evolution of the instability compares well with the calculations presented in the literature [122, 125]. Indeed, the solutions predicted by both numerical approaches remain close to the reference solutions obtained with an accurate front tracking method [122]. The two numerical methods appear to provide the same interface topology for most of the simulation. Nevertheless, differences are evident in terms of interface thickness, penetration rate and secondary structure formation (filaments, droplets) as will be discussed Sections 3.3.2.1.

3.3.2.1 Interface Capture and Sharpness

The sharpness of the phase boundary between the two fluids is an indication of the numerical diffusion of the scheme used. Also, the amount of fine-scale structure is sensitive to how well the algorithm preserves the sharpness of the interface. The works of Popinet and Zaleski [122] and Puckett et al. [125] suggested that the correct capture of the thin ligaments has a strong influence on the overall simulation results in terms of penetration of the dense phase and opening of the mushroom cap. As can be seen in Fig. 3.8 both simulation methods are able to capture the thin liquid structures and maintain a sharply defined interface.

In the RCLS method, as the interface thickness parameter ϵ is increased from $0.5\overline{\Delta x}$ to $2\overline{\Delta x}$, the interface becomes smeared over an increasing number of cells (for more information about ϵ please check [?]; there is a loss of sharp numerical resolution of tiny secondary liquid structures Fig.3.8-a. The re-initialisation procedure integrated into *RCLSFoam* helps in capturing the formation of droplets correctly. The more diffused the interface, i.e., the bigger the interface thickness parameter ϵ , the less visible are the droplets (compare Case 1 to Case 3 in Fig. 3.8-a). In addition, the rate of high-density fluid penetration also decreases: for Case 3, at $t = 1.3\text{s}$ the mushroom tip does not yet touch the bottom wall (Fig. 3.8-a (iii)).

Attention is then turned to the solution obtained with the *interPore* solver Fig. 3.8-b. A higher interface sharpening coefficient C_{sh} with no numerical compression Fig. 3.8-b (ii)) is able to capture a sharper interfacial jump than with a lower C_{sh} . When

numerical compression is added (Fig. 3.8-b (iii)) the interface is even sharper. Overall the comparison of the interface predicted by the two solvers for the first four times ($t = 0.55, 0.70, 0.85, 0.95$ seconds) demonstrates the similar performance of both simulation methods. The *interPore* solver appears less sensitive to the tuning parameters than *RCLSFoam*, which is consistent with observations in the case of the static droplet. A disadvantage is while the VoF method is capable of reproducing the ligaments formed by the elongation of the mushroom sides when low compression is used these ligaments disappear as C_{sh} increases and compression is added. The RCLS method, on the other hand, seems to be better able to treat the small-scale inclusions of one phase into the other regardless of the ϵ parameter.

Indeed, for times beyond $t = 0.95$ s, i.e. at $t = 1.10$ s, $t = 1.20$ s, and $t = 1.30$ s, small differences in the solution can be perceived between the two methods Fig. 3.8: for *interPore* the interface sharpening algorithm with no compression is able to capture droplets up to a time of 0.95s. After that, filaments continue to detach from the mushroom but fragment into liquid structures can not be resolved, and these get diffused numerically (Case 1 and Case 2 in Fig. 3.8-b).

3.3.2.2 Stem Symmetry and Numerical Convection

With the *RCLSFoam* solver, the symmetry of the flow structure is well captured (Fig. 3.8-a. The interface obtained for the central stem is slightly asymmetrical in the case of *interPore* with added numerical compression (Case 3 in Fig. 3.8 (b)). This may be due to the compression scheme in OpenFOAM [56]. As a result, *interPore* does not fully recover the physical solution published in the literature [122, 125] after $t = 0.95$ s. On the other hand, the non-physical wiggles usually seen with VoF solvers [126] in the neck of the stem close to the mushroom-shaped structure have disappeared for all *interPore* runs, with compression factors $C = 0$ and with $C = 1$ Fig. 3.8-b.

3.3.2.3 Rate of Penetration of the Heavy Phase into the Light Phase

For both solvers, the dense phase penetrates the light phase at a rate that is in accordance with the simulations of Popinet and Zaleski [122]. As ϵ is increased from $0.5\overline{\Delta x}$ to $2\overline{\Delta x}$ in the RCLS formulation, the start of the instability is marginally delayed at $t = 0.7$ s; hence the rate of penetration of the spike is reduced overall. On the other hand, the penetration rate does not seem to be altered when varying the numerical

parameters of *interPore* Fig. 3.8-b.

3.3.2.4 Mushroom-Shaped Structure Development

Fig. 3.9 (ii) shows the distribution of the velocity field at a number of discrete time intervals, along with the corresponding interface contour Fig. 3.9 (i). The spike itself has a positive velocity downwards, consistent with the direction of acceleration it experiences from the pressure gradient. There is a stagnation point on the lower tip of the spike. Upstream of the mushroom cap, there is a low-velocity region. This location is consistent with a high-pressure region. The highest velocities are located on either side of the mushroom cap, extending along and at the tip of the ejected fluid ligaments. The light fluid is thus accelerated faster upwards than the spike and mushroom cap are accelerated downwards. There is evidence of interfacial shearing instabilities Fig. 3.9 (iii) associated with the formation of a mushroom-shaped structure. It is believed [52] that the Kelvin–Helmholtz instability is the reason for the development of the mushroom cap at the tip of the spike. It is characterised by the development of structures on the spike, arising mainly due to the velocity shear between the two fluid layers. Once the mushroom cap is formed, the effect of drag forces on the spike is increased.

As ϵ is increased from $0.5\overline{\Delta x}$ to $2\overline{\Delta x}$ in the RCLS numerical formulation, the mushroom cap becomes less open Fig. 3.8-a. With the modified VoF method *interPore*, a change in the sharpening coefficient does not seem to alter the openness of the mushroom cap, but adding numerical compression does make the cap more open (Fig. 3.8-b (iii)). At $t = 0.70\text{s}$, the roll-up of the edges of the mushroom cap under the shearing instability is predicted similarly by both solvers (Fig. 3.9 (iii)). At $t = 0.85\text{s}$ however, droplets have already detached from the two ligaments in the *interPore* solution (Fig. 3.9-b (i)), causing a noticeable difference in the development of the shearing instability compared to the RCLS formulation. In the latter, the mushroom cap is more open, and at the point of droplet separation from the two ligaments a strong upwards velocity is visible (Fig. 3.9-a (iii)).

3.3.2.5 Ligament Breakup into Droplets

For all the runs with the RCLS method, at $t = 0.95\text{s}$, the filaments elongated on either side of the mushroom have not yet fragmented into droplets, in accordance with Popinet and Zaleski [122]. This is true also for Case 1 and Case 3 simulated with the

interPore solver (Fig. 3.8-b (i and iii)). However, in *interPore* Case 2, at $t = 0.95\text{s}$, the two droplets have already detached from the end of the filaments (see Fig. 3.9-b (i)). This may be due to the extra sharpening employed in this solver in Case 2.

3.3.2.6 Mesh Refinement to 128×512 Cells

Fig. 3.10 presents the volume fractions and interface predicted by *RCLSFoam* and *interPore* on a refined mesh of 128×512 cells. The RCLS method with $\epsilon = 0.5\overline{\Delta x}$ is not particularly affected by mesh refinement: the interface is sharper but just as many liquid structures are resolved as with the previous coarser mesh Fig. 3.10-a. Hence it is possible to run the RCLS numerical scheme on coarser meshes without loss of physical accuracy, further highlighting the relevance of this capability. On the other hand, mesh refinement does slightly improve the performance of *interPore*, with extra droplet capture at later times (see Case 5 in Fig. 3.10-b versus Case 2 in (Fig. 3.8-b(ii)). This behaviour is expected. While LS methods provide interface sharpness inherently, VoF methods require additional treatment to limit diffusion, and mesh refinement acts as an additional sharpening treatment. When compression is added (Case 6 in Fig. 3.10-b), ligaments and ligament breakup are well resolved; however, numerical wiggles start forming along the stem and mushroom cap. There appears to be an optimal numerical set-up for the *interPore* solver, in which the traditional OpenFOAM numerical compression scheme is not used; but in which the interface sharpening algorithm provides good physical accuracy and resolution of the interface (Case 2 and Case 5). Similarly to the conservative level-set method with $\epsilon = 0.5\overline{\Delta x}$ (Case 1 and Case 4).

3.3.3 Quantitative Results and Discussion

The growth of an RTI can be described using a number of stages [52, 127] as follows. When the perturbation amplitudes η are small compared to their wavelength λ , the early stages in the growth of the instability can be analysed using the linearised equations of motion. The result is that small initial amplitude perturbations of wavelength λ increase in magnitude, exponentially with time [52].

Substantial deviations from the linear theory are observed when non-linear effects begin to appear. Their development is strongly influenced by three-dimensional effects such as the formation of well-known structures: spikes, bubbles and mushrooms.

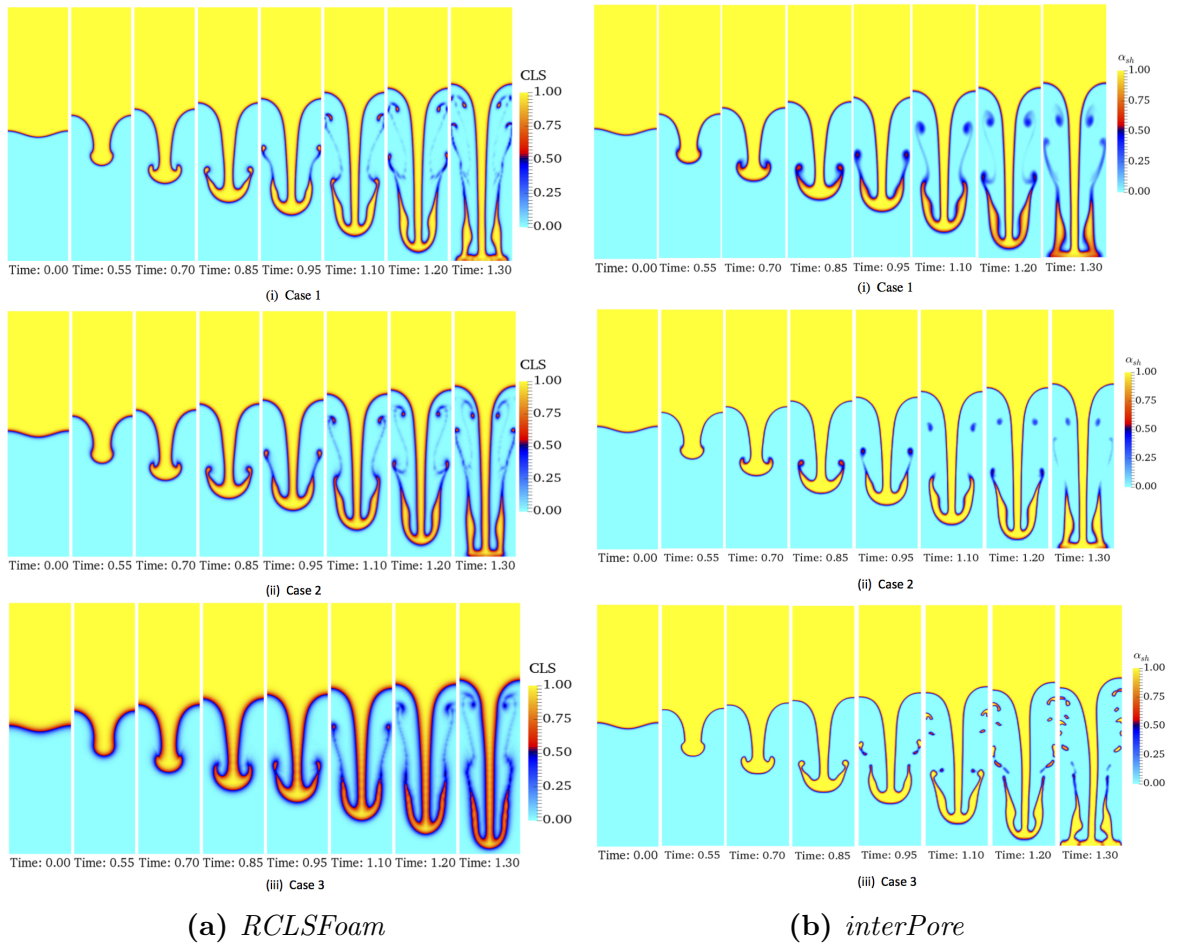


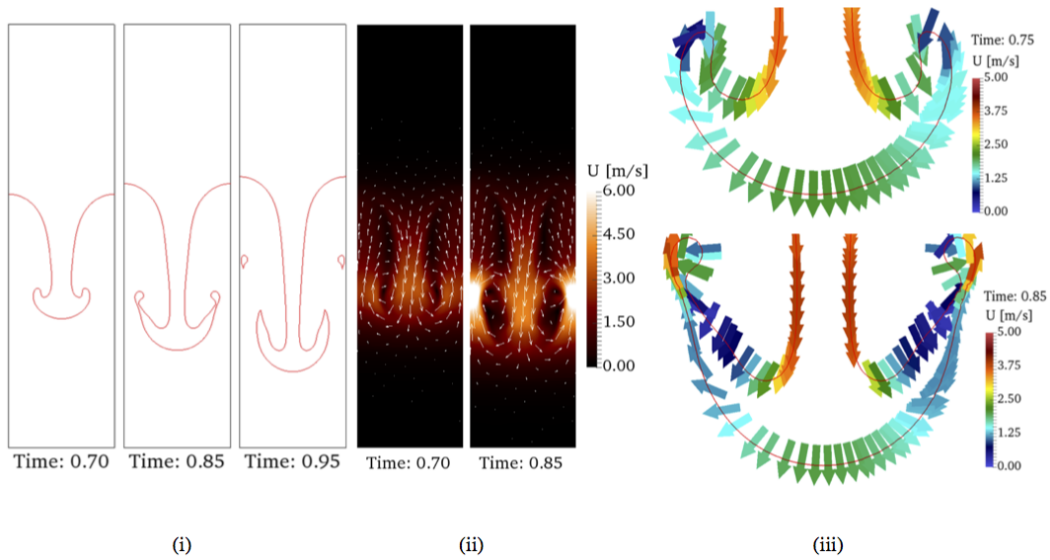
Figure 3.8: Volume fractions predicted by *RCLSfoam* and *interPore* for the Rayleigh–Taylor instability with 60×224 mesh elements.

At later times, spikes and bubbles develop their own mushroom-shaped structures at their tips, which eventually interact and merge. At this stage, non-linear effects can no longer be ignored. The system enters a regime of turbulent or chaotic mixing of the two fluids. In order to describe the aforementioned stages, a more quantitative description of the RTI is presented through the amplitude growth rate and the volume fraction profiles.

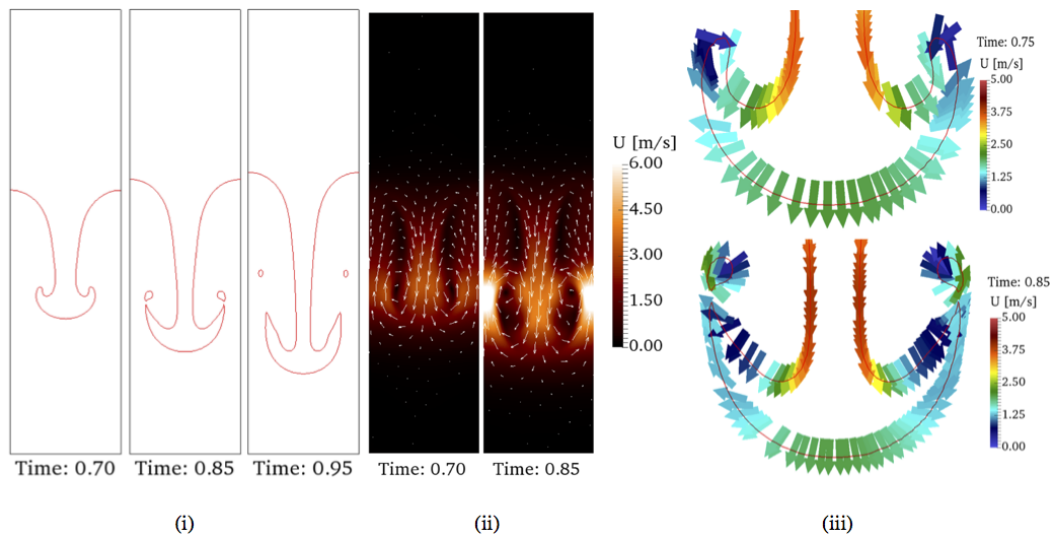
3.3.3.1 Amplitude Growth Rate

The initial growth rate of small amplitude perturbations can be affected by various physical properties including viscosity and surface tension. In linear theory, viscosity tends to reduce the growth rate appreciably, whereas surface tension stabilises wavelengths shorter than a critical wavelength.

The first stability analyses of Rayleigh [118] and Taylor [119] on RTI have been extended in various directions to include additional physical effects such as, for instance, surface tension and viscosity [52].

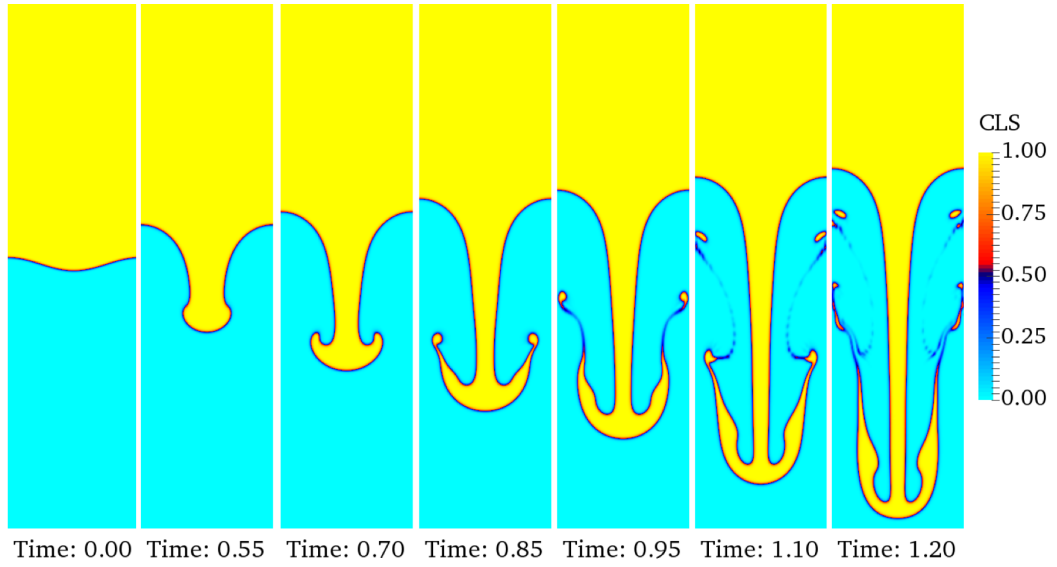


(a) *RCLSFoam*, Case 1

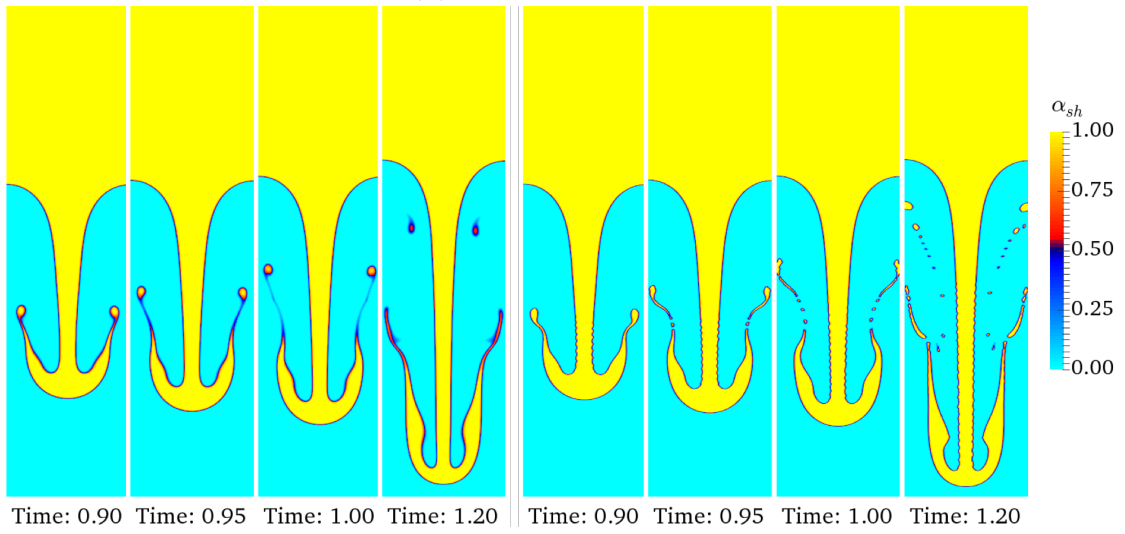


(b) *interPore*, Case 2

Figure 3.9: Interface (0.5 iso-contour of both indicator functions) predicted by both solvers for the Rayleigh–Taylor instability with 60×224 mesh elements, velocity field and velocity vectors overlaying the interface contour.



(a) *RCLSFoam*, Case 4



(b) *interPore*, Case 5 (left) and Case 6 (right)

Figure 3.10: Volume fractions predicted by both solvers for the Rayleigh–Taylor instability with 128×512 mesh elements.

The work of Chandrasekhar [128, Chapter 10] sought to extend the inviscid linear theory and has led to a rather complete understanding of RTI in incompressible viscous fluids, including the effects of surface tension.

At time t , a fluid element of cross section $dydx$ displaced at a distance $\eta(t)$ below $y = 0$, feels a downwards force due to gravity and a downward force from surface tension. The fluid element net downward acceleration in the $-y$ direction is a combination of the downward gravity force and the downward surface tension force:

$$g \frac{\rho_h - \rho_l}{\rho_h + \rho_l} - \frac{\sigma}{\rho_h + \rho_l} k^2. \quad (3.4)$$

The simple harmonic solution is given by:

$$\ddot{\eta} - \alpha^2(k)\eta = 0 \quad (3.5)$$

where

$$\alpha^2(k) = gk \frac{\rho_h - \rho_l}{\rho_h + \rho_l} - \frac{\sigma}{\rho_h + \rho_l} k^3. \quad (3.6)$$

Eq.(3.6) is the well-known dispersion equation for interfacial waves of wavenumber k when viscosity is neglected. As expected, the interface is now unstable, and the solution to Eq.(3.6) for fluids initially at rest is:

$$\eta(t) = \eta(0) \cosh(\alpha t) \quad (3.7)$$

where $\eta(0)$ is the perturbation amplitude at $t = 0$.

The interfacial wave amplitude grows like $e^{\alpha t}$. The description of the instability is, of course, valid only so long as the amplitude remains small. It is evident from Eq.(3.6) that surface tension can prevent the instability for sufficiently small wavelengths.

Chandrasekhar also applied normal mode analysis to the linearised Navier–Stokes equations to derive an implicit fourth-order ODE for the amplitude of the y -velocity component as a viscous eigenvalue problem that needs to be solved numerically. Fig. 3.11 shows the results of the linear stability analysis discussed above as well as some of the simulation results. The numerical solutions reproduce accurately the theoretical prediction of Chandrasekhar [128] at early times when the system is still behaving linearly. *RCLSFoam* (Case 1) and *interPore* (Case 2) perform equally well.

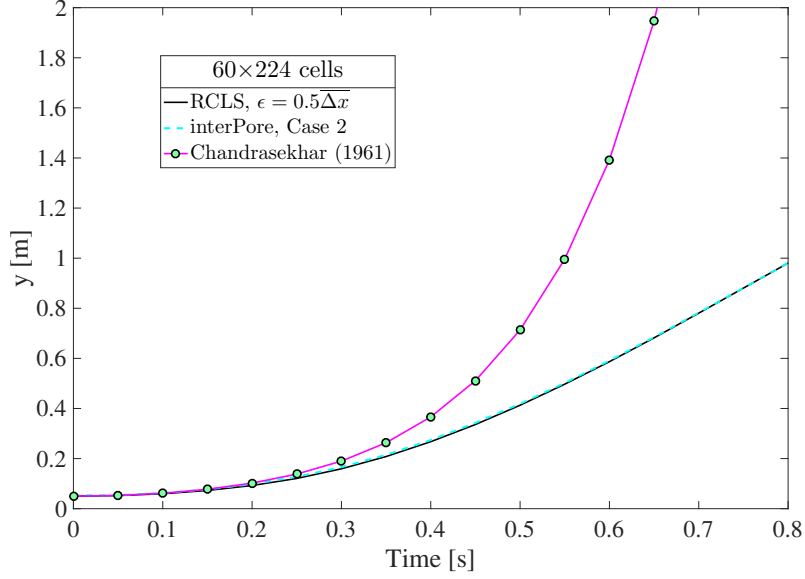


Figure 3.11: Amplitude growth for the Rayleigh–Taylor instability in the 60×224 computational domain compared to the theoretically predicted growth rates of *RCLSFoam* (Case1) and *interPore* (Case 2).

3.3.3.2 Volume Fraction Profiles

Fig. 3.12 shows volume fraction profiles along the y -direction centreline of the computational domain at two different times: $t = 0\text{s}$ and $t = 0.2\text{s}$ and for two different mesh resolutions. As ϵ is increased from $0.5\overline{\Delta x}$ to $2\overline{\Delta x}$ in the RCLS method, at $t = 0\text{s}$, the ψ field is initially smeared over a chosen number of cells. The number of cells within the interface thickness remains constant during the simulations. A change in mesh resolution does not change the diffusion of the interfacial thickness. In the modified VoF method with interface sharpening, however, the initialised interfacial jump happens over a single computational cell. The later development of the interface thickness over the course of a simulation is affected by the order of accuracy of the numerical scheme and the mesh resolution employed.

At $t = 0.2\text{s}$, and for the 60×224 mesh size, both solvers marginally under-predict the theoretical amplitude, at a liquid phase fraction of 0.5. As Chandrasekhar’s linear theory does not take into account viscosity, the authors postulate that this is the reason for the under-prediction of the perturbation amplitude compared to the estimated theoretical value (grey vertical line in Figure 3.12 *bottom-left*). The *interPore* solver shows a lower sensitivity to the numerical parameters (i.e., numerically-added sharpening or filtering or both). The *interPore* solver with high sharpening or compression (Case 2 and Case 3) predicts the same perturbation amplitude as the base case (Case 1), but the profiles are steeper.

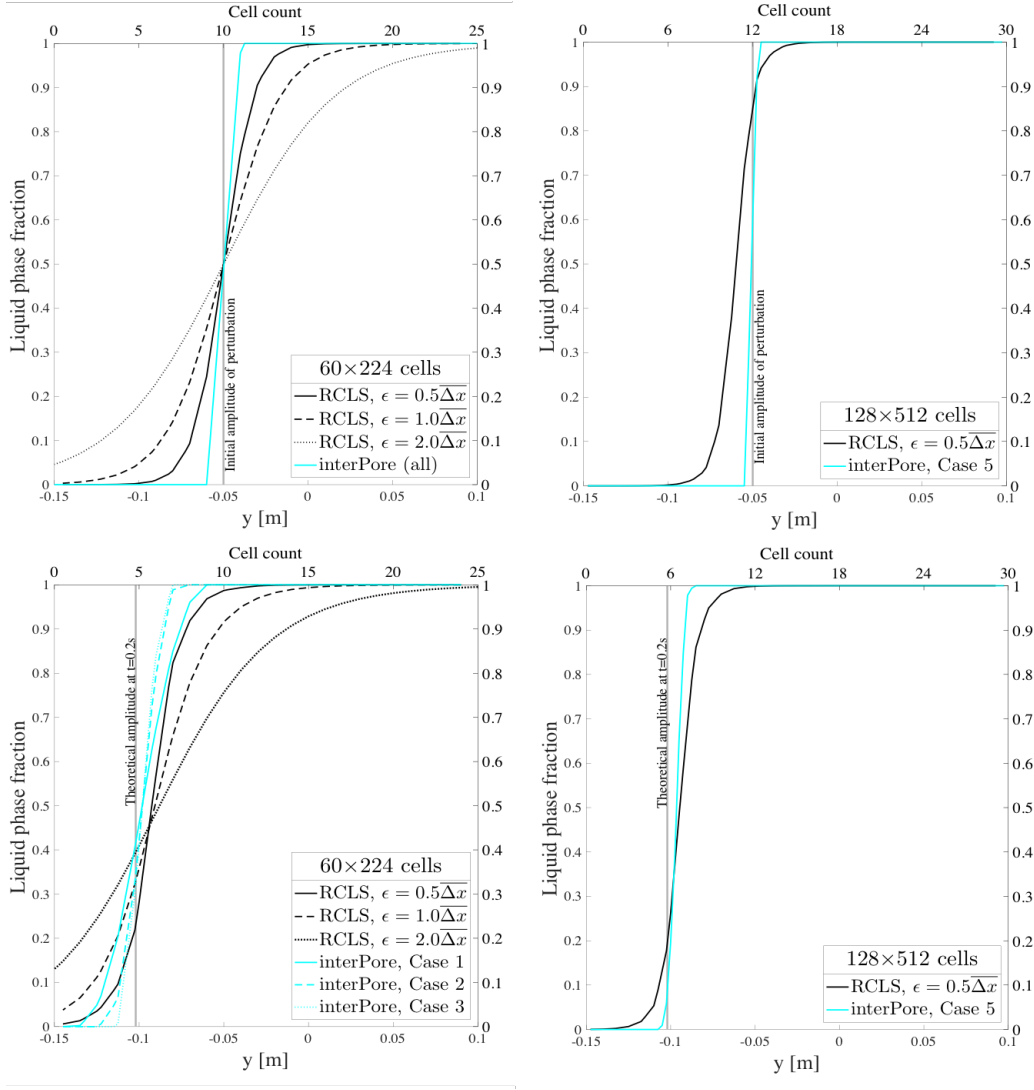


Figure 3.12: Indicator functions smeared over cell count and y -location at $t = 0$ (top row) and $t = 0.2s$ (bottom row) for two mesh sizes: 60×224 and 128×512 mesh elements.

Over the range of interface parameters ϵ tested for the RCLS method, as ϵ is increased the amplitude at the 0.5 iso-contour diminishes in magnitude, i.e., departs from the theoretical value, in accordance with a less sharply defined interface location. Indeed, the interface needs to have a minimal thickness, so that the gradient of ϕ and the interface normal are accurately calculated.

At $t = 0.2s$, and for the 128×512 cells, the 0.5 volume fraction iso-contour of the perturbation amplitude is slightly under-predicted for both solvers. Probably for the same reason described in the paragraph above.

For the VoF solver with interface sharpening *interPore*, a refined mesh does not change the calculated amplitude of the perturbation. *RCLSFoam* predicts an amplitude very slightly closer to the theoretical value.

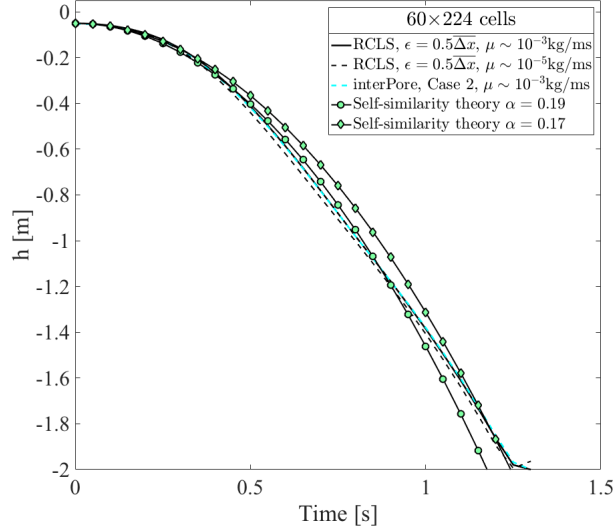


Figure 3.13: Theoretically predicted self-similar solution for the Rayleigh–Taylor instability against our numerically predicted solutions.

3.3.4 Self-similarity Solution

The RTI marks only the onset of a complex interpenetration process, leading ultimately to the growth of mixing regions between neighbouring fluids [129]. At later times, once the instability has become fully nonlinear, it is difficult to make quantitative comparisons. However, the flow may enter a self-similar growth phase [130]. In the present case, self-similarity can be described by the following equation:

$$\frac{dh}{dt} = 2\sqrt{\alpha Agh} \quad (3.8)$$

where h is the height of the mixing region and α is a dimensionless growth parameter [131]. The parameter α is the subject of extensive research [131–133]. The physically realisable solution to Eq.(3.8) is

$$h(t) = h(0) + \sqrt{\alpha Agh(0)}t + \alpha Agt^2 \quad (3.9)$$

taking $t = 0$ as the moment in time when the flow first achieves self-similarity. Then $h(0)$ corresponds to the thickness of the mixing region at that instant. The last term dominates the right-hand side of Eq.(3.9) and hence the mixing thickness becomes:

$$h(t) \sim \alpha Agt^2. \quad (3.10)$$

Fig. 3.13 shows the numerically calculated mixing height versus time, as well as the

predicted mixing height Eq.(3.10) for two different numerical values of the parameter α . It has been chosen here to compare what resulted through our previous results in the optimised runs for each solver in terms of numerical parameters Table 3.4.

For $t = 0.4-0.8$ s, both solvers present a similar behaviour, slightly under-predicting the two theoretical curves, while for $t \geq 0.9$ s, our numerical predictions fall in-between the two theoretical curves. It is argued that the system becomes self-similar from the very early stages of the instability. A numerical value of α between 0.19 and 0.17 appears to match very well with the numerical results; as viscosity is not taken into account by the model [131]. An additional case was run with *RCLSfoam* in which the dynamic viscosity was reduced artificially by two orders of magnitude. This reduction in viscosity does not result in a change of the amplitude growth of the instability Fig. 3.13.

3.4 Notched Disc in Rotating Flow

In addition to the previous test cases, the rotation test of the slotted disk, which is known as the Zalesak problem [114] has been tested. The Zalesaks circle disk is initially slotted at the centre (0.5,0,0.75) of a 2D unit square domain. The disk is subjected to a rotational movement under the influence of a rotational field that is defined by the following equations:

$$u(x) = -2\pi(x - x_0) \quad (3.11)$$

$$w(z) = 2\pi(z - z_0) \quad (3.12)$$

where $u(x)$, $w(z)$ are the imposed velocity components. By applying this velocity, one complete rotation of the disk is completed within $t = 1\text{sec}$. For all simulations performed for this test case, a fixed time-step has been used, keeping the Courant number equal to 0.5. The initial disk configuration used for the simulation is presented in Fig. 3.14. Three different mesh densities were used consisting of 64×64 , 200×200 and 400×400 cells, respectively.

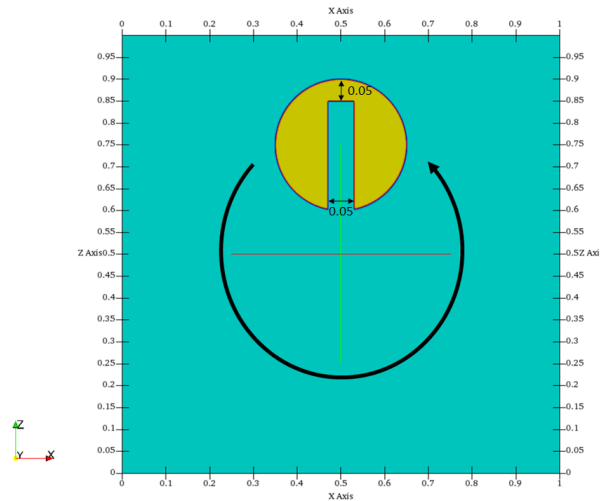


Figure 3.14: Schematic representation of two dimensional Zalesak's Disk benchmark test case described at [5].

Figures 3.15 and 3.16 show the comparison between the standard solver using different compression ($C_{compr.}$) values and the developed adaptive solver *interPore* with different sharpening (C_{sh}) values. In each plot, the exact initial and final interface shape are presented. In all the figures, the iso-contours values of indicator function α of (0.1, 0.5 and 0.9) after one revolution of the disk are shown. The reason for

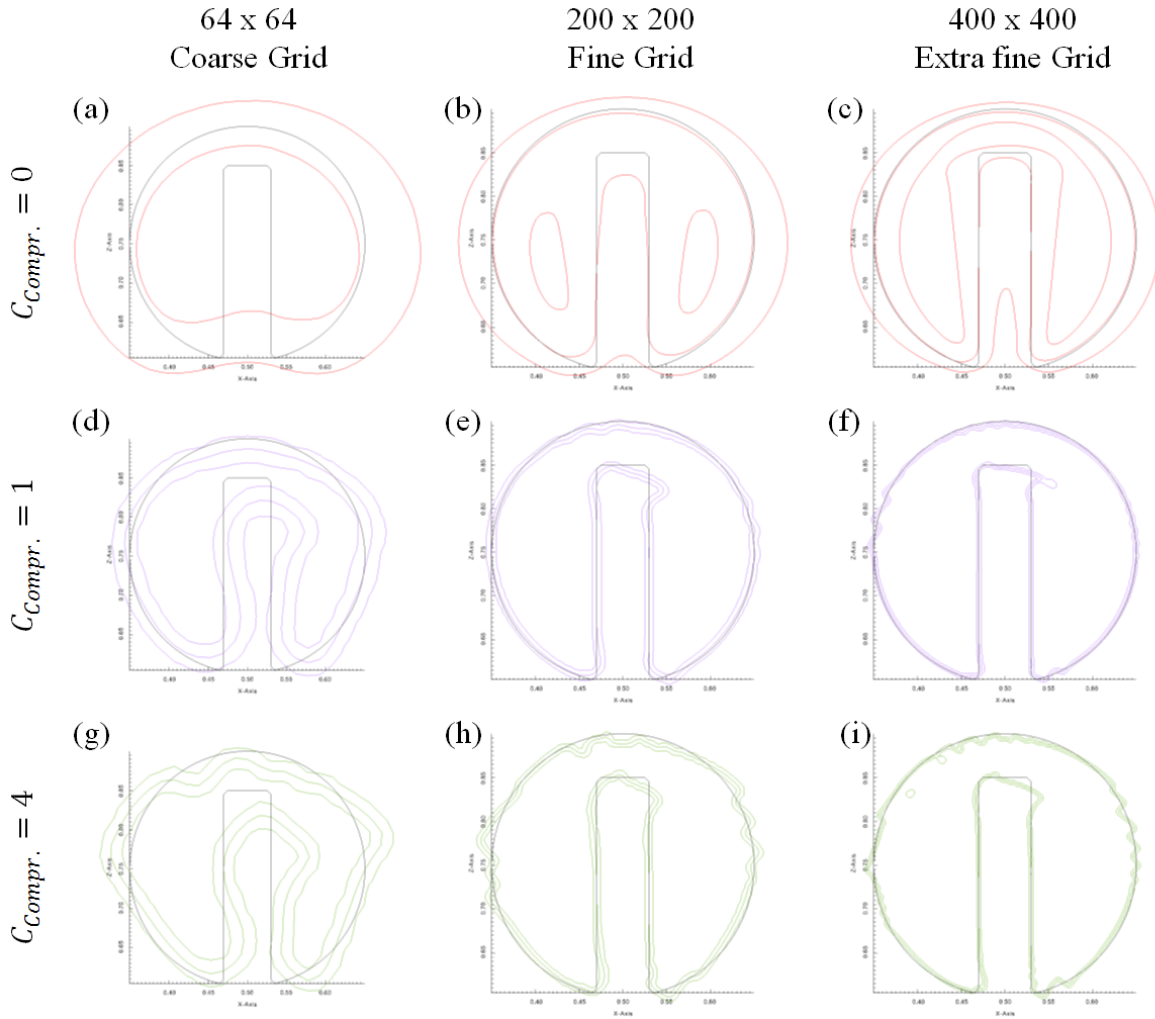


Figure 3.15: Zalesaks disk after one revolution. Iso-contours for indicator function alpha ($\alpha = 0.1, 0.5$ and 0.9) are plotted for the standard *interFoam* using different compression values, together with the reference shape.

presenting three contour lines is to better explore the effect of the adaptive compression model on both the interface diffusion and the overall disk shape. For the coarse mesh (64×64) neither using the standard *interFoam* with three compression values ($C_{compr.} = (0, 1$ and $4)$), nor the three values for C_{sh} , ($C_{sh} = 0.1, 0.5$ and 0.9) for the adaptive *interPore* solver, can provide a satisfactory interface representation. One can even notice that due to the large interface deformation and diffusion, the interface iso-contour of (0.9) at Fig. 3.15(a) has disappeared for the standard solver. Nevertheless, for the *interPore* cases, the modified solver can keep the main geometrical features as seen in Figs. 3.16-(a,d,g).

By using high compression as in Fig. 3.15-g, one can notice a reduction in the interface thickness, although a rather high deformation and corrugated shape of the final disk shape has been noticed. Comparing Fig. 3.15-g to Fig. 3.16-g one can notice the effectiveness of the adaptive model that preserves the geometrical outline of the

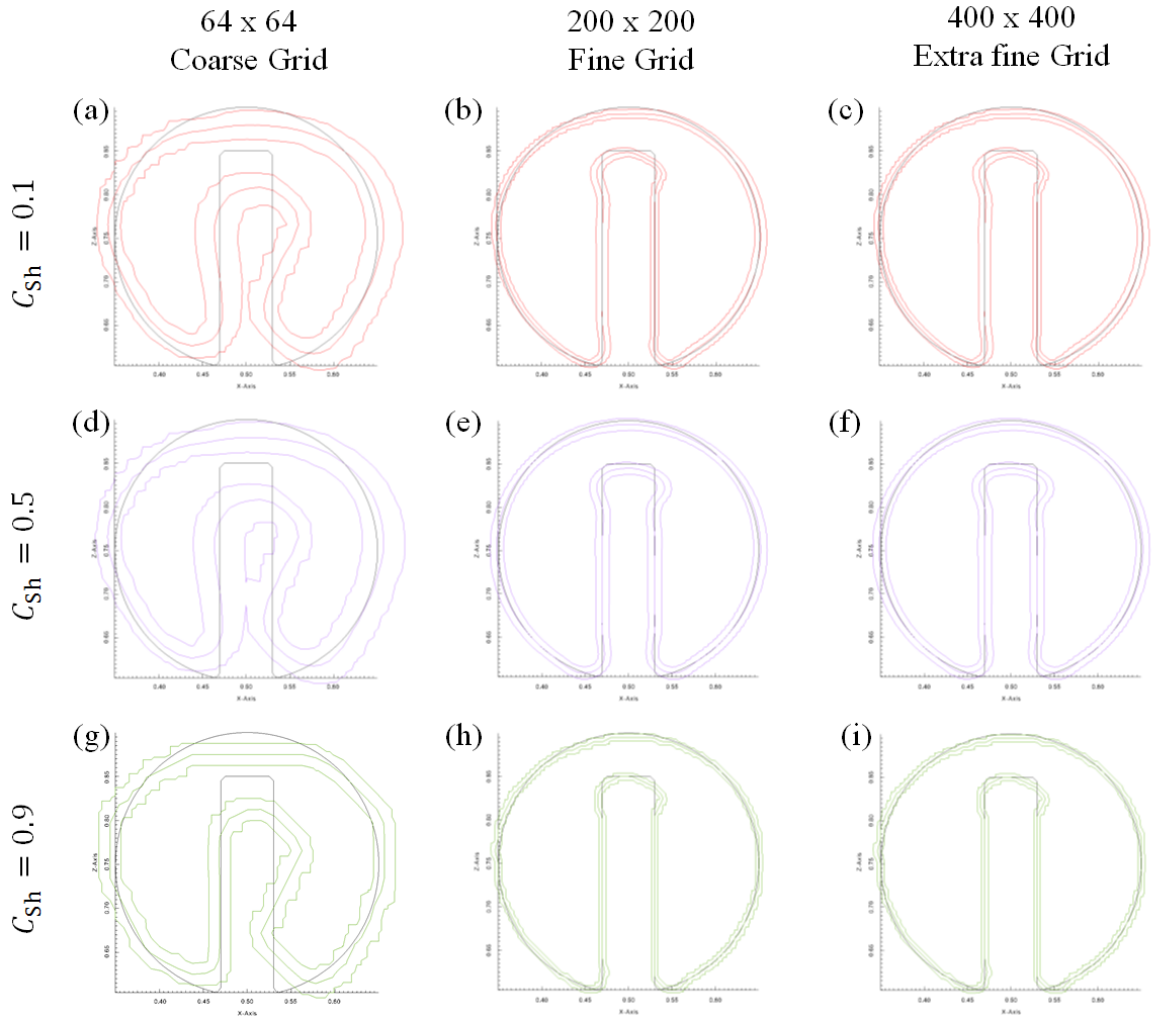


Figure 3.16: Zalesaks disk after one revolution. Iso-contours of indicator function alpha sharp ($\alpha_{Sh} = 0.1, 0.5$ and 0.9) are plotted for the adaptive *interPore* solver using different sharpening coefficients, together with the reference shape.

disk while the sharpening model decreases the interface thickness. Moving to a finer mesh (200×200) cells, high interface diffusion using the standard *interFoam* with no compression ($C_{compr.} = 0$ in Fig. 3.15-b) has been noticed. The higher grid resolution is not adequate to provide remedies to the previously mentioned deficiencies noticed in the coarser mesh using *interFoam*.

The highly diffusive interface using the standard *interFoam* also did not maintain the 0.9 iso-contour making two oval shapes at the sides. For higher compression values Fig. 3.15-(e,h) although the disk shape is preserved by the standard solver, the interface is significantly deformed near to the outer disk boundary. Use of the adaptive solver Fig. 3.16-(b,e,h) shows better consistency for the shape regardless of the imposed sharpening level. Moreover, the adaptive compression eliminates any irregular shapes compared to the standard solver. Figure 3.16-h clearly shows an excellent agreement with the original circular shape layout. This test case also demonstrates the role of the

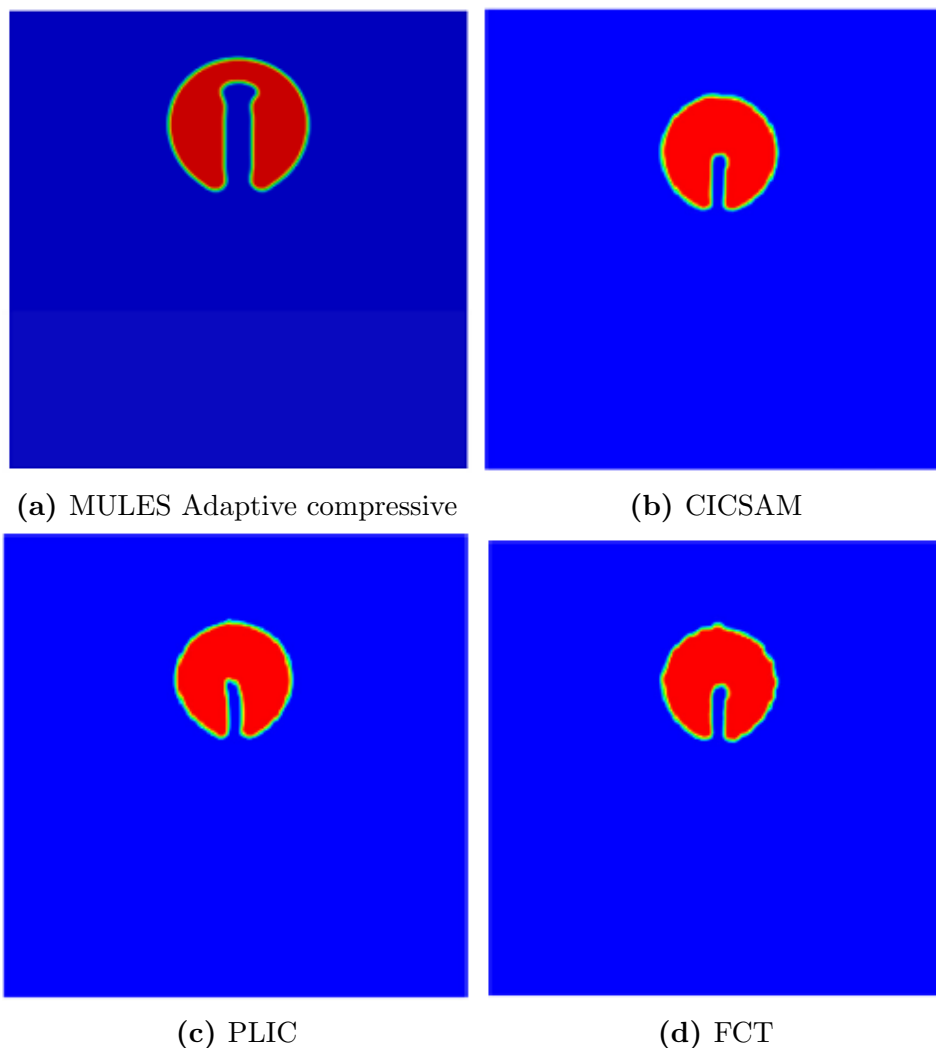


Figure 3.17: Comparison between the used framework and available method reviewed by Gopala and van Wachem [6]. (a) is showing *interPore* adaptive compressive scheme, (b) is showing the compressive interface capturing scheme for arbitrary meshes (CICSAM), (c) is showing piecewise linear interface construction (PLIC) and (d) is showing flux-corrected transport FCT. All presented in mesh a domain of 200 by 200

sharpening value C_{sh} which can help in controlling the interface diffusion depending on the case under consideration.

To examine the adaptive solver mesh dependency, the mesh has been doubled to 400×400 . Even for this fine grid resolution case, the standard solver gives inaccurate disk shape regardless of the compression value used, as none of them is adequate to balance the interface shape. A zero compression value using the standard *interFoam* preserves the characteristic shape for the first time (see Fig. 3.15-c, compared to Fig. 3.15-(a,b)). For the higher compression values as in Fig. 3.15-(f,i), high corrugated regions at the interface have been observed. Using the adaptive *interPore* solver a better disk shape representation has been obtained, regardless of the sharpening coefficient value C_{sh} (see Fig. 3.16-(c,f,i)). Moreover, by using the three different sharpening coefficient

C_{sh} a thickness of approximately 1-2 cells has been preserved. Also, the minimum difference between the fine and the extra fine grid in terms of interface thickness has been observed, and sharpening algorithm shows the perfect fit to the internal notch. These observations indicate that the adaptive compression is less sensitive to tuning parameters such as the sharpening see Eq. (2.28), which is not effective for coarse grid resolution.

For completeness, results included in [6] are also shown. In [6] various commonly used interface capturing methods have been presented for the same test case; these include the standard compression scheme used by OpenFOAM, the compressive interface capturing scheme for arbitrary meshes (CICSAM) employed by FLUENT commercial code, the piecewise linear interface construction (PLIC) and the flux-corrected transport (FCT)). In this test cases, the notched disk was a bit different than what is presented in the standard Zalesak [114] test case, yet it has the same overall characteristics. Looking to this comparison, one can relate and compare the overall behaviour for the different solvers as seen in Fig. 3.17. Nevertheless, one can detect the difference in geometrical layout between our test case and the test cases; the mesh was kept the same as in [6] (200×200) cells. By comparing the results from the developed solver to those reported in [6], it can be concluded that a good solution has been achieved.

3.5 Circle in a Vortex Field

In this section, the solver performance is tested in a vortex flow as presented by Rider and Kothe [115] and Roenby et al. [68]. The aim of this benchmark test is to verify the ability of the model to deal with severe interface stretching. The test case includes an initially static circular fluid disk with radius of $R = 0.15$ mm centred at $(0.5, 0, 0.75)$ in a unit square domain. The disk is subjected to the flow induced by a vortex as shown in Fig. 3.18. The axis of rotation is located in the centre of the field, and can be described by the following stream function:

$$u(x, z, t) = \cos((2\pi t)/T)(-\sin^2(\pi x) \sin(2\pi z), \sin(2\pi x) \sin^2(\pi z)) \quad (3.13)$$

where u is the field rotational velocity and T is the period of the flow during rotation. Due to the flow direction, the disc is stressed into a long thread until time $t = 4s$ forming a spiral shape. The interface thickness of the deformed disk shape, as well as the numerical diffusion of values located at the tail of the fluid body during its spiral motion, are of interest. The results presented in Fig. 3.19 and 3.20 are for three different grid sizes using the standard *interFoam* and the newly developed *interPore* solver. On each figure, the final interface shape is shown with three iso-contours values for the indicator function (α) of (0.1, 0.5 and 0.9) after one revolution of the disk ($t = 4$ s).

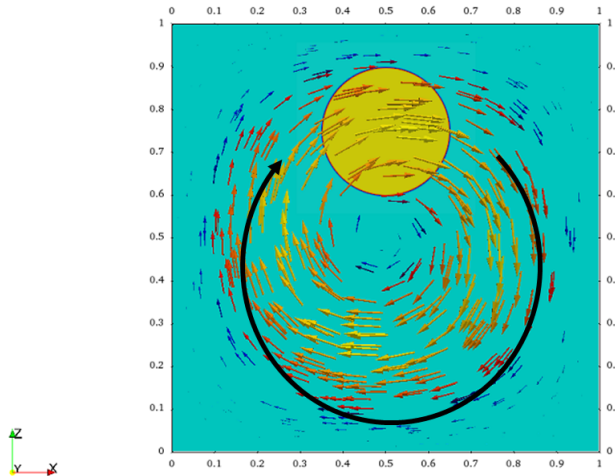


Figure 3.18: Representation the initial configuration of the shearing flow test with the value of the color function is one inside the circle and zero outside

The standard solver failed to capture the full spiral shape after the disk rotation using the coarse mesh (see Fig. 3.19(a,d,g)). Due to the very high diffusion and the absence of compression, iso-contours of 0.1 and 0.5 volume fraction have disappeared

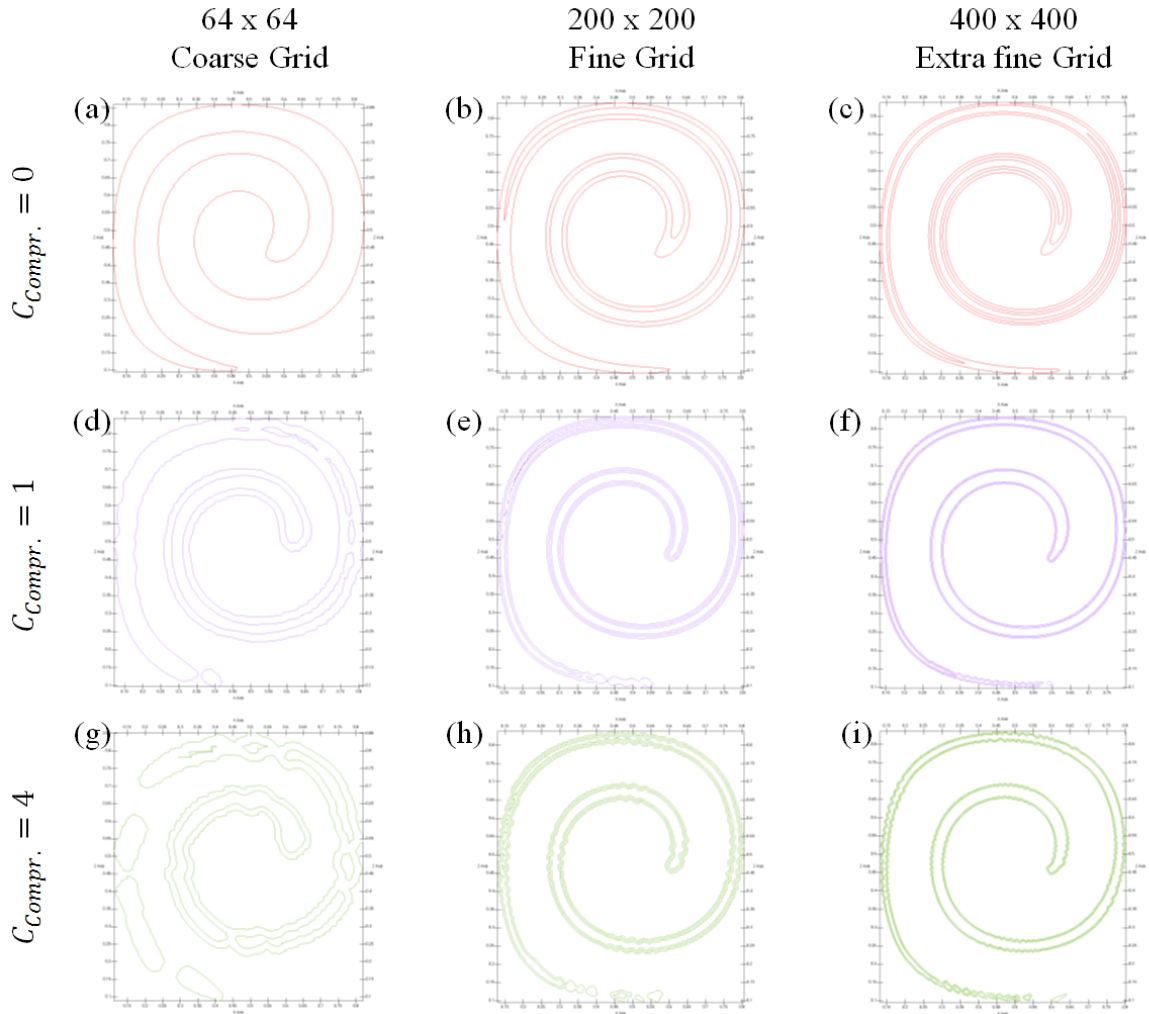


Figure 3.19: Circle in a vortex field after one revolution. Iso-contours for indicator function alpha ($\alpha = 0.1, 0.5$ and 0.9) is plotted for the standard *interFoam* using different compression values, together with the reference shape.

from the computational domain (see Fig. 3.19-a. Using the adaptive *interPore*, the results are problematic as well especially for the tail as presented in Fig. 3.20-(a,d,g). By using high sharpening value Fig. 3.19-(d,g) at low grid resolution to counter balance the numerical diffusion, tail snap-off at the spiral formation has been observed. Fragmentation or tail snapping off is evident in all figures.

Moving to a finer grid (200x200) the behaviour of the two solvers becomes similar although some differences can be noticed. The standard solver with no compression Fig. 3.19-b suffers from high diffusion as seen in the previous test cases where the (0.1) iso-contour disappears. As the compression value increases (see Fig. 3.19-(e,h)) the standard solver shows early fragmentation at the tail or non-smooth interface. In contrast, the adaptive solver agrees with the expected spiral shape using different sharpening coefficients. Nevertheless, with low sharpening value as shown in Fig. 3.20-b early fragmentation with the 0.1 iso-contours lines loss has been observed. Increasing

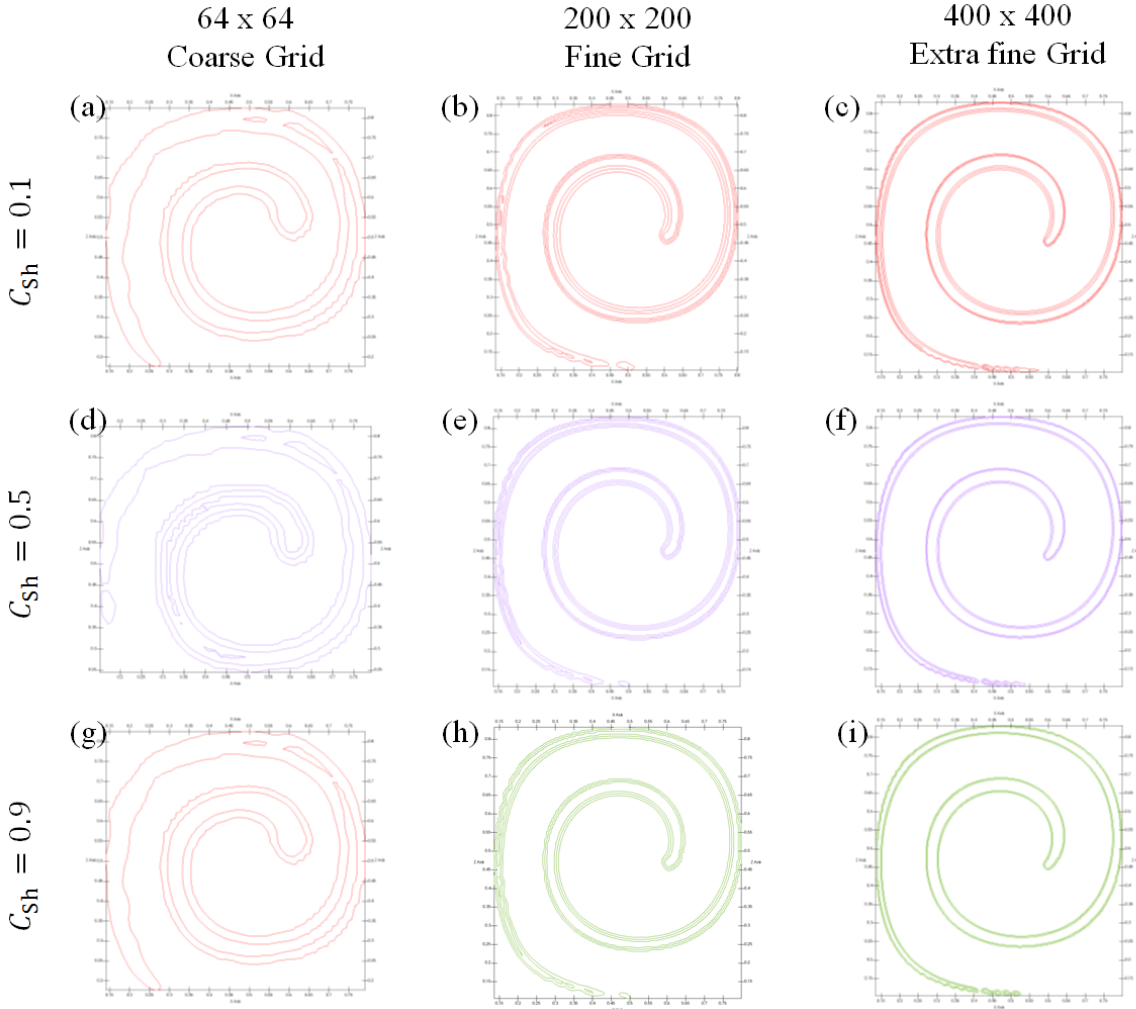


Figure 3.20: Circle in a vortex field after one revolution. Iso-contours of indicator function alpha sharp ($\alpha_{Sh} = 0.1, 0.5$ and 0.9) is plotted for the adaptive *interPore* solver using different sharpening coefficients, together with the reference shape.

α_{Sh} to values greater than 0.5 (see 3.20-(e,h)) provides an accurate spiral shape with minimum phase snapping at the tail. Good agreement using adaptive compression has been achieved in balancing the swirling tails compared to the wiggly interface appeared using the standard solver. One can notice that the smallest fragmentation at the spiral tale seems to be unavoidable by using any applied sharpening algorithm as also discussed by Sato and Ničeno [134] and Malgarinos et al. [135], especially at regions where the liquid body becomes very thin. Fragmentation happens when the local interface curvature becomes comparable to the cell size. At this point, the iso-contours are not able to represent the significant interface curvature inside the cell anymore. Iso-contours based on volume fraction advection leads to errors in the estimate of the fragmented droplet motion similar to those reported by Černe et al. [136] and Roenby et al. [68]. As a final sensitivity test, the grid size has been doubled (400x400), to examine the influence of the mesh size on the adaptive solver. Both solvers perform

better with this high-resolution grid. However, differences have been noticed as with the previous cases. As seen in Fig. 3.19-c the standard *interFoam* using zero compression coefficient gives a better interface representation with less diffusion and stable tail. By introducing compression (see Fig. 3.19-(f,i)) the spiral shape is maintained, although wiggly shapes emerge near the outer interface. Using the adaptive solver no significant change is noticed; by varying the sharpening value (C_{sh}): as seen in Fig. 3.20-(c,f,i), the results do not change. The results indicate that the balance between sharpening and compression is well achieved. Combining the developed solver with fine grid proves the proposed methodology independent of tuning parameters which is a very desirable feature within multiphase flows. Finally, it had been concluded that even by using medium quality mesh (i.e., 200x200) cells, the adaptive solver could provide satisfying results for a wide range of sharpening coefficients.

3.6 Bubble Formation at T-junction

The previous benchmark cases tested the suitability of the developed model to a range of idealised conditions. No significant topological changes occur, and wettability effect is not present. Thus, further validation against experimental data for the case of formation of bubbles in a T-junction has been performed. This is a test case that involves wetting conditions at the wall as well as complex fluid interface topological changes through the breakup and generation of bubbles. The focus is to test the accuracy of our adaptive model in estimating the correct bubble shape and frequency as presented in the experiment of Arias et al. [137]. Full wetting conditions ($\theta = 0^\circ$) at the main tube are used. Moreover, the contact angle imposed on the injection tube (see Fig. 3.22) has been taken from the corresponding flow images. A constant contact angle of $\theta = 25^\circ$ for the left wall and $\theta = 45^\circ$ for the right wall has been chosen to match the experiments. The connection between the two channels as well as the flow directions and geometrical representation are shown in Fig. 3.21.

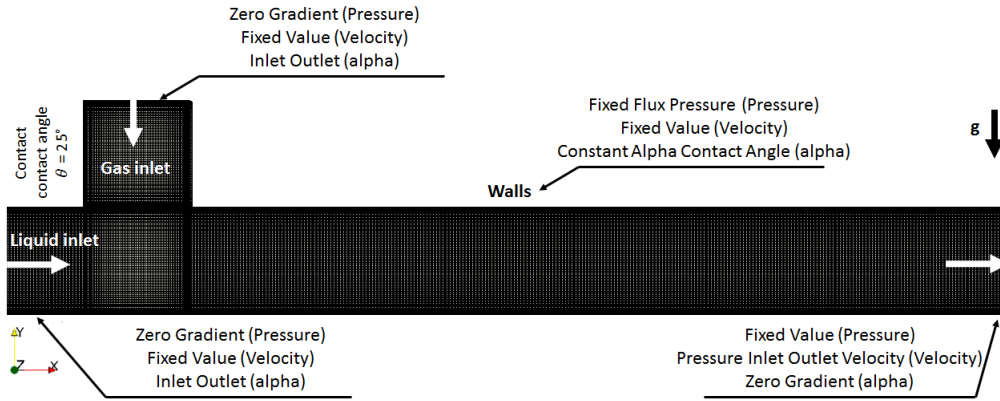


Figure 3.21: Geometrical model boundaries and overall dimensions

Two different operating conditions, summarised in Table 3.5, have been selected for presentation. The velocities selected for comparison with our numerical simulations are also shown in Table 3.5. The conditions used are carefully selected to simulate low capillary number and to show two different bubble size formation with fluid properties listed in Table .3.6. Benchmark 1:

Table 3.5: Inlet velocities for liquid and gas, dimensionless numbers and regime expected

Case	$U_g(m/s)$	$U_l(m/s)$	Max Re	Max We	<i>Exp.Regime</i>
Case 1	0.242	0.318	32	1.4	<i>Slug</i>
Case 2	0.068	0.531	53	3.92	<i>Bubble</i>

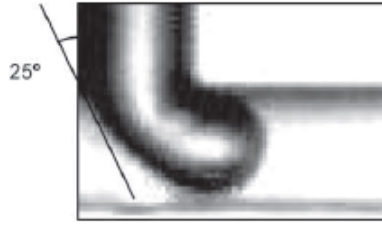


Figure 3.22: Contact angle at injection tube measured from experimental images

Table 3.6: Fluid physical properties

	$\rho(Kg/m^3)$	$\nu(m^2/s)$	$\sigma(N/m)$
Water properties at $25^\circ C$	1000	1.004×10^{-6}	0.07
Air properties at $25^\circ C$	1.2	8.333×10^{-6}	0.07

For this test case, the appearance of spurious numerical currents would create instability during the bubble formation process. These currents induce unphysical vortices at the interface, destabilising the simulations and strongly distorting the interface movement. Gravity acceleration constant was $9.8 m/s^2$, while the values of maximum Weber number ($\frac{\rho DU^2}{\sigma}$) and the maximum Reynolds number ($\frac{\rho DU}{\mu}$) were the same as in the experiments and shown in Table 3.5.

Comparison of the results from the developed solver and the standard solver *interFoam* using different compression values against the experiments are shown in Figs. 3.23 and 3.24. Depending on the inlet velocity imposed, one should expect to reproduce different bubbles formation.

Figure 3.23 presents the first bubble generation sequence as mentioned in Case 1, Table 3.5. Using the standard solver, the slug formation is achieved only when adjusting the compression coefficient to the value of two as seen in Fig. 3.23d. Even in this case though, the detached ligaments of the fluid appear to be more spherical than what the experiments indicate. Using the comparison value of one, the standard solver failed to predict the interface snap-off as seen in Fig. 3.23c. In contrast looking at Fig. 3.23b it is noticed that the results obtained by the new adaptive model agree very well with the experiments in terms both of slug formation and snap-off time as seen in Fig. 3.23a. The adaptive framework predicts the interface snap-off correctly and minimises the overall parasitic currents. Moreover, the standard solver shows a considerable increase in parasitic velocity near the interface that reaches eight orders of magnitude of the flow velocity. The new solver achieved low parasitic currents during the snap-off events while maintaining an accurate, sharp interface.

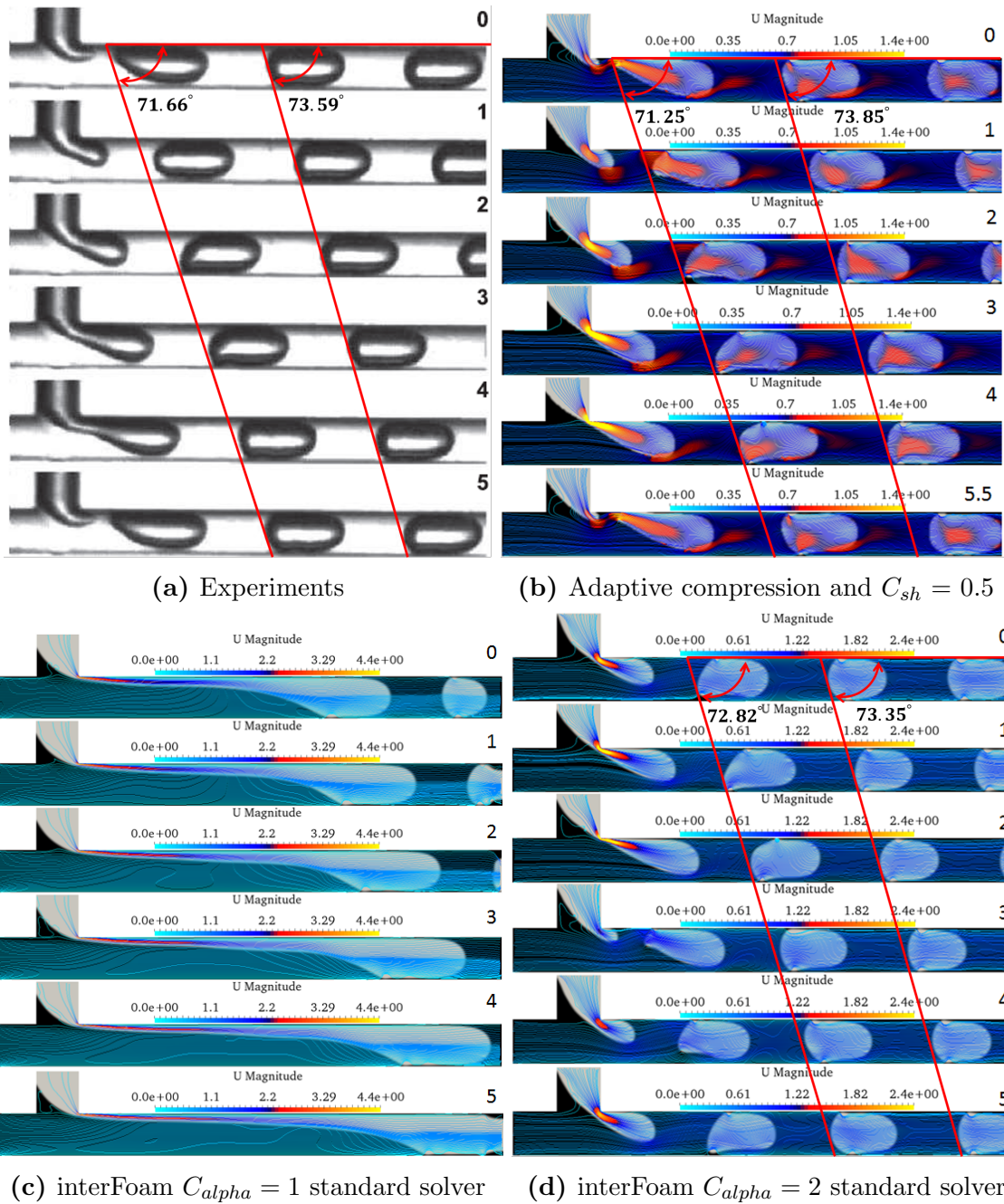


Figure 3.23: Slug flow in (left) experiments and (right) numerical simulations. $U_L = 0.318$ m/s and $U_G = 0.242$ m/s. Time (ms) is indicated in the upper right corner. Stream lines are coloured with velocity magnitude in all the figures.

Figure 3.24 presents bubble flow patterns obtained by imposing higher liquid velocity but lower gas velocity as in Case 2 Table 3.5 in comparison to the previous case. Good agreement regarding shape and patterns between experiments and all numerical simulations can be observed regardless of the solver used. It is worth mentioning though that, looking at Figs. 3.24c, 3.24d when the standard *interFoam* solver is used, bubbles are generated at different frequencies based on the compression coefficient value. By comparing the two figures to the experimental Fig. 3.24a one can also notice that the snap-off time is delayed compared to the experimental results. While in Fig. 3.24b

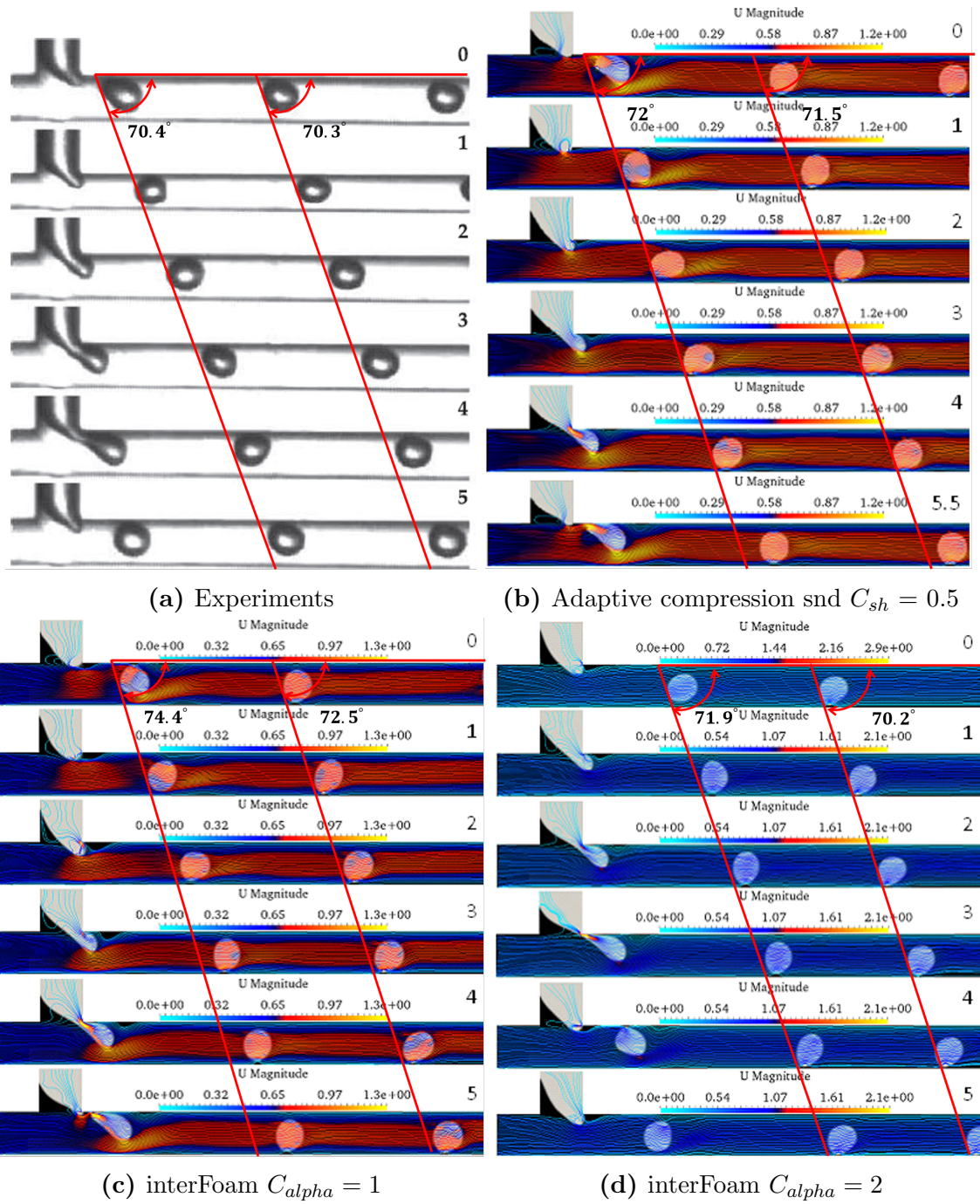


Figure 3.24: Bubble flow in (left) experiments and (right) numerical simulations. $U_L = 0.531$ m/s and $U_G = 0.068$ m/s. Time (ms) is indicated in the upper right corner. Stream lines are coloured with velocity magnitude in all the figures.

one can observe that using the developed adaptive solver, the snap-off time and the bubble generation frequency is matching well with the experiences. According to the experimental observations, bubble generation results from the breakup of a gas thread that develops after the T- junction. The explanation for the breakup is supported by the Plateau-Rayleigh instability as discussed by Ménétrier-Deremble and Tabeling [138] or by the effects of the flowing liquid from the tip of the thread to the neck where pinch-off occurs as presented by van Steijn et al. [139]. The surface tension has a sta-

bilising effect and opposes any deformation of the interface tending to create a bubble. The snapping events discussed by the previous literature are in agreement with the simulations presented here since no unnatural pinch-off has been observed using the developed solver. On the other hand, a long thread of gas generated using *interFoam* is clearly seen in Fig. 3.23c.

In order to understand the numerical accuracy, the angle of the dispatched droplet is measured. As seen in Fig. 3.23, the developed solver predicted almost precisely the same droplet sequence compared to the experiment. While the standard solver using a compression value of two produces close results to the experiments. The failure of predicting the correct droplet behaviour using the standard solver with compression value of one, show the importance of using the adaptive solver in predicting the proper compression. Similarly, in Fig. 3.24 judging by the measured angle for the droplet dispatched, one can notice the effect of numerical compression on the droplet behaviour compared to the experiments. Figure 3.24 shows some deviation at the first line of droplets compared to the experiments. However, the correct prediction using the developed solver when comparing the results to the standard solver.

Table 3.7: Error in Bubble generation frequency

	<i>Sim.frequency(Hz)</i>	<i>Error_f</i>
Case 1 <i>interPore</i>	190.47	4.7 %
Case 1 (<i>interFoam</i> $C_{alpha} = 1$)	210.53	5.2 %
Case 1 (<i>interFoam</i> $C_{alpha} = 2$)	No Bubble generation	100 %
Case 2 <i>interPore</i>	200.00	1.9 %
Case 2 (<i>interFoam</i> $C_{alpha} = 1$)	184.00	9.8 %
Case 2 (<i>interFoam</i> $C_{alpha} = 2$)	179.21	12.15 %

The previous section demonstrated a qualitative comparison using the standard solver and the developed solver against different variation of the control parameters. The validation has been extended to, quantitatively, compare the bubble generation frequency with experiments. To ensure regularity in the formation of bubbles, a train of bubbles is generated containing at least four of them. The generation frequency was estimated by measuring the time required to create the bubbles. The first bubble of each train, which was strongly dependent on the initial geometry, was not considered. The accuracy of the bubble generation frequency was quantified using the following

equation:

$$Error_f = \frac{Sim.freq - Exp.freq}{Exp.freq} \quad (3.14)$$

where the *Sim. freq* is the time calculated from the simulations in order to generate one bubble and *Exp. freq* is the time needed to produce one bubble in the actual experiment. Table 3.7 shows the error in the bubble frequency generation compared to the experimental data. For Case 1 although the qualitative results are very close between Fig. 3.23b and Fig. 3.23d, one can notice that the developed solver can achieve better accuracy in the in bubble generation frequency. In Case 2 the simulation data are qualitatively similar to the experimental results.

3.7 Droplet Impinging on a Solid Surface

As mentioned in the previous sections, different benchmark test cases are used in presenting work to test the developed solver different performance aspect with respect to experimental or theoretical data available. In this section, we present the developed solver results for the droplet impacting flat solver for different wetting conditions. The aim of this section is not to understand the droplet impacting solid surface, as it is a well-known topic. It aims at demonstrating the effect of parasitic current reduction on the spreading behaviour which will play a very important role in stimulating droplet impacting on porous media. The case of a water droplet ($D_0=2.05\text{mm}$) hitting a flat non-porous (stainless steel) surface is compared the experimental results presented by Pasandideh-Fard et al. [7]. The impact velocity of the droplet is set to be constant and equal to $U_0 = 1\text{m/s}$. Numerical results will be presented and compared with experiments in terms of photographic evidence and time evolution of the spreading factor. Figure 3.25 shows the time evolution of the shape of the droplet. Both computer-generated images and photographs are viewed from the same angle $\sim 30^\circ$ from the horizontal axis and at the same time after impact. In the spreading phase, the liquid spreads on the wall in a flat film (lamella) bounded by a rim. It reaches its maximum extent at approximately $T = 2.6\text{ms}$, after which surface tension and viscous forces have overcome inertia, so that fluid accumulated at the leading edge of the rim starts pulling back. In the preceding phase, (non-wetting of the wall) the thickness of the lamella decreases but the rim continues to grow. This behaviour is overall well reproduced by the simulation. Figure 3.26 shows the time evolution of the droplets spreading diameter. Results from the modified (black line) solver are compared with experimental data (red dots) and the standard solver in blue [7].

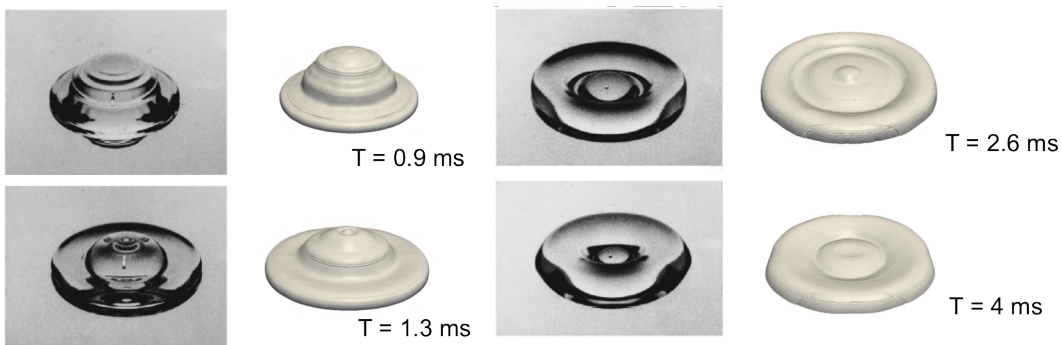


Figure 3.25: Time evolution of the shape of the droplet: (left) numerical simulation vs. (right) experimental results [7].

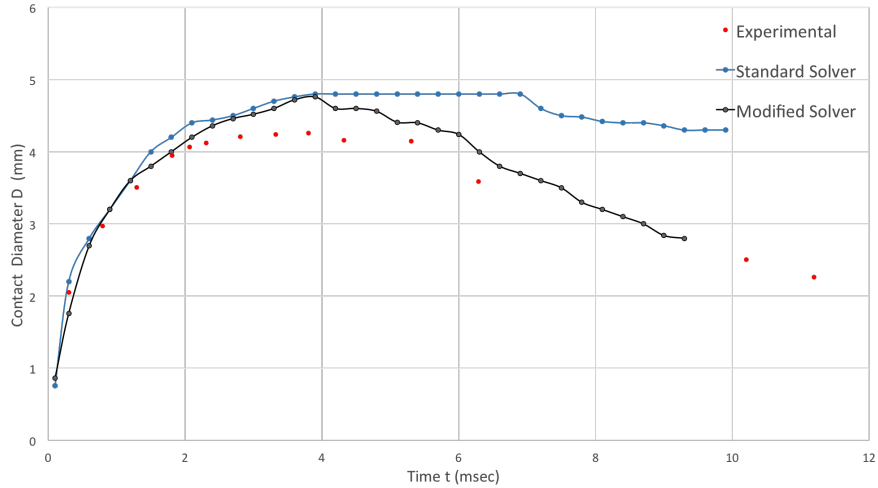


Figure 3.26: Time evolution of the droplet diameter. Results from the standard (blue line) and the modified (black line) solver are compared with experimental data (red dots) from [7]

It can be seen that the agreement is good although the droplet diameter at the recoil phase is slightly overpredicted meaning that the droplet recoils slower than expected. The difference is more pronounced at approximately 4ms. Looking at Fig. 3.25 at the snapshot of 4 ms, it seems that the rim size is underpredicted and the corresponding lamella is overpredicted. For completeness, the results are compared with the standard solver (blue line). The results show that at the inertia dominated phase (spreading up to 4 ms) both models have a similar performance as expected. However, in the recoil phase some pronounced differences are noticed.

It can be seen that the droplet recoils slower when the standard solver is used. Given that for both cases the same contact angle is used we believe this is was caused because of the interface velocity calculation especially close to the solid surface. To provide a better understanding of the previous point Fig. 3.27 is included. It shows the velocity magnitude contour of the water droplet predicted by the standard VoF methodology of OpenFOAM (left) and our suggested framework (right). Both snapshots are taken at $T=4.5$ ms presenting the recoiling phase as experiments predicted . As it is noticed the standard solver predicts much higher contact line velocities at the droplet edge (around the rim) not allowing the surface tension to overcome inertia and thus the recoil is delayed.

We extend our study to droplet impacting solid surface to compare our solver to the dynamic contact angle models found in literature. Fig. 3.28 presents four different cases for droplet impacting at different impact velocities and different imposed dynamic contact angle conditions. The aim of this comparison is to understand the solvers

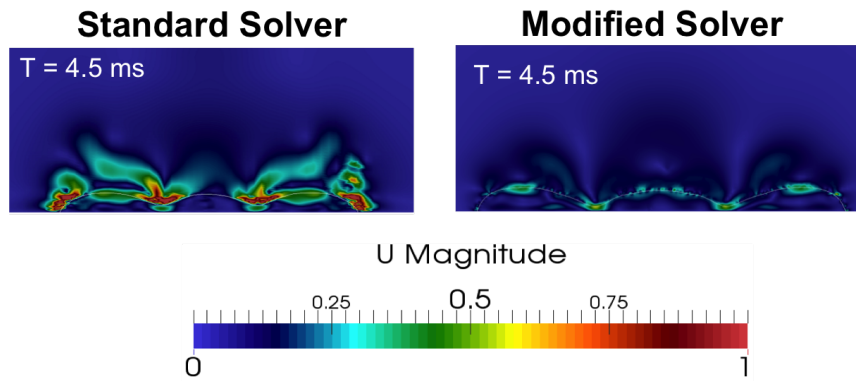
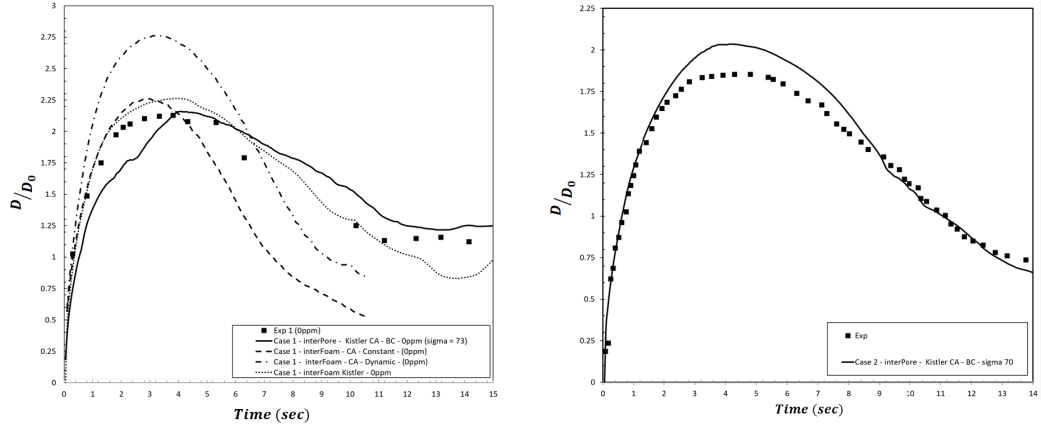


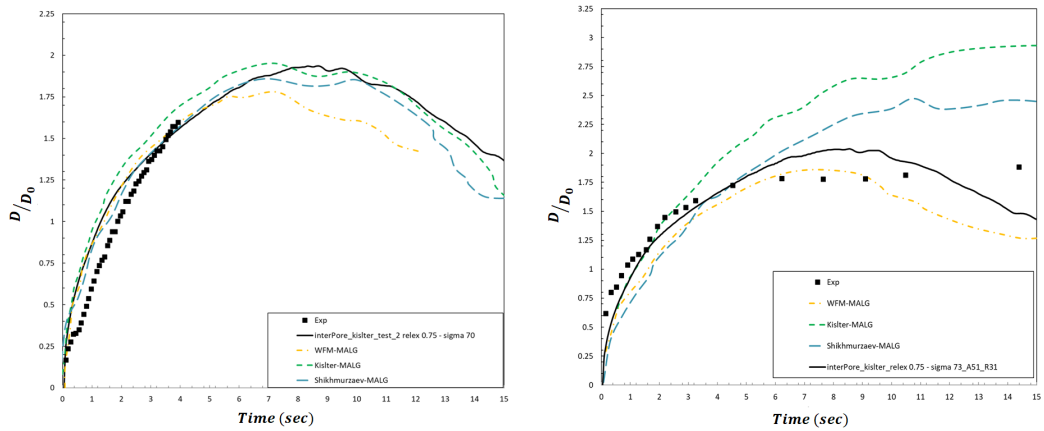
Figure 3.27: Velocity magnitude contour of the water droplet impact on stainless steel predicted by the standard VoF methodology of OpenFOAM (left) and our suggested framework (right). Both snapshots are taken at $T=4.5$ ms

behaviour at a low impact velocity and the effect of our solver modifications on the spreading behaviour.

In order to understand our code behaviour in conjunction with Kistler dynamic contact angle boundary condition, we performed a series of droplet impacts on a solid surface at low Weber number. Different spreading and recoiling behaviour were tested using droplet impacting at low Weber number to understand the effect of parasitic current in conjunction with the dynamic wetting condition assumption. The results presented in fig. 3.28 show a comparison between our developed code behaviour and the experimental data found in the literature. Also Fig. 3.28 compares our numerical data to similar numerical methods used to predict the droplet spreading and recoiling behaviour at the same operating conditions.



(a) Case 1; Impact velocity of 1 (m/s), (b) Case 2; Impact velocity of 1 (m/s), $We = 27$, Droplet diameter = 2 (mm) and $We = 32$, Droplet diameter = 2.28 (mm) dynamic contact angle of $\theta_A = 110^\circ, \theta_R =$ and dynamic contact angle of $\theta_A = 107^\circ, \theta_R = 77^\circ$



(c) Case 3; Impact velocity of 0.22 (m/s), (d) Case 4; Impact velocity of 0.08 (m/s), $We = 2$, Droplet diameter = 2.4 (mm) and $We = 0.2$, Droplet diameter = 2.3 (mm) dynamic contact angle of $\theta_A = 70^\circ, \theta_R =$ and dynamic contact angle of $\theta_A = 51^\circ, \theta_R = 31^\circ$

Figure 3.28: Droplet spreading on solid surface with different droplet conditions, all data was compared with experimental and numerical results from [8]

3.8 Concluding Remarks

This chapter verified the numerical framework by testing it against a wide range of two-phase benchmark cases. The static capillary pressure was predicted by solving the differential form of the Young-Laplace equation numerically for single and multiple droplets. The code was also tested using the Rayleigh Taylor problem with homogeneous layers of a high-density fluid penetrating a low-density fluid under the influence of gravity. This chapter also considered the validation of the solver performance using the vortex flow as presented by Rider and Kothe [115] and Roenby et al. [68] to verify the ability of the developed model in dealing with severe interface stretching. In addition to the vortex flow benchmark, the developed solver was also tested using the rotation test of the slotted disk, which is known as the Zalesak problem Zalesak [114] to determine the effect of adaptive compression method on sharp interface diffusion. Finally, an experimental flow in T-junction and droplet impacting a solid surface was used to validate our solver in real complex flow. By using the developed solver, the sharp interface during the break-up process for different operating conditions was predicted. In summary, based on the numerical results presented in this chapter, the numerical method is considered as a reliable and accurate method to solve the flow at the continuum scale of pores and throats of a microscale geometry. Especially at the low capillary numbers encountered in flow through porous media. Some more predictions using adaptive grid refinement can be found on Appendix A

Chapter 4

Two-Phase Flow Behaviour Inside Porous Structures Using Micro-CT porous media

4.1 Introduction

Flows of two or more phases through porous media, such as flow in porous rocks, are commonly presented in many types of geological processes. The predominant focus of flow physics is wettability and surface tension conditions. Understanding the flow dynamics inside porous media, and the effect of different wetting conditions can lead to technologies that enhance the removal of trapped oil residuals in porous reservoirs. Moreover, analysing the trapping physics using two-phase flow simulations at the pore scale level allows for testing different surfactant surface tension effects to minimise the trapping of an oil phase and enhancing the recovery systems of hydrocarbons. In two-phase flow with immiscible liquid-liquid contact porous media, each phase can be defined based on the physical wetting conditions, including a non wetting phase (such as water) or a wetting phase (such as oil). Inside porous media, the rock-fluid tortuosity interaction can affect the flow behaviour of the wetting and the non-wetting phases based on the flow dynamics. Due to the different flow combinations of water phase behaviour during the oil phase extraction process at the irregular geometry of natural porous media, the prediction of two-phase flow in many processes is a challenging task. Comprehending the micro-scale flow behaviour for a given porous media can also provide better understanding of the macroscopic properties of such media, including the relative permeability and capillary pressure curves. These two properties, which are extensively used in macro-scale simulations, are usually obtained from laboratory experiments, which are time-consuming and expensive. However, similar approaches are normally used to study the effect of porous media using a numerical approximation, such as Darcy models, to link between the microscopic and macroscopic without the need of high complexity porous structures. In the next two chapters, the flow dynamics inside porous media and droplet penetrating of porous structures will be considered in detail.

This chapter presents the simulation results of three different porous media based on micro-CT images. The porous media reconstruction process will be briefly discussed, first, then the simulation setup and the boundary and initial conditions will be listed. As mentioned before, the aim of this study is to investigate the effect of different flow conditions and extract the correct macroscopic properties description, i.e. capillary pressure and relative permeability. In order to estimate the capillary pressure and relative permeability, the approach used to up-scale the simulation results to obtain

the Darcy-scale properties is explained. Finally, the simulation results of two-phase flow on micro-CT images of Berea Sandstone (B1), Synthetic Silica (A1) and Sandstone 1 (S1) available in open source literature [140] will be presented. Using the developed method discussed in the previous section, where the importance of the direct numerical simulation is explained. The numerical model is also used to study the flow behaviour for the two-phase flow through porous media and potentially obtain the macroscopic scale properties. Moreover, it will be shown how using dynamic wetting conditions introduced by modelling the Kistler dynamic contact angle, will help in the development of the macroscopic theoretical models.

4.2 Porous Model Reconstruction and Meshing

For modelling the flow inside porous media, an accurate physical description of the pore structure should be presented numerically. The accuracy of the discretised domain, i.e. grid cells, which is reflected in the simulations computational cost, is considered to be one of the biggest challenges in modelling two-phase flow using micro-CT scanned images. In the next subsection, the porous reconstruction process and the numerical mesh build-up will be discussed.

4.2.1 3D Surface Generation Based on Micro-CT Images

This subsection discusses the procedures followed to extract a computational mesh from micro-CT scan data. As a non-destructive technique, X-ray micro-CT provides the necessary insight into opaque objects, eliminating the need for sectioning/partitioning. That is, micro-CT is a comprehensive tool for capturing internal rock structures due to the smooth classification/transition of rock versus void (air) materials. A micro-CT scanner uses X-rays that penetrate a 3D object and create density-based attenuated two-dimensional projections, which are collected at small angular steps, preferably, around 360 degrees. These projections are later synthesised using a variety of techniques. In addition, the complete volume of the object is reconstructed in terms of two-dimensional image slices. The computed stack of 2D slices usually shares a resolution of a few microns, and their pixel values are bound to material density-based attenuation.

Micro-CT images are usually found in the form of a 3D voxelized grey-scale stack of images. This is used as a base to be converted into binary images formed from zeros representing void spaces and ones representing the internal rock structure. The assembly of the used grayscale images or input cross sections is called a CT volume. The grayscale images can be found in the open literature of [9], and four different models have been used in these investigations. They are not much used without a proper segmentation process. Hence, it is absolutely necessary to implement a transition and conversion from grayscale images to an STL-like data format, where the surface mesh is generated and can be later improved to generate volume mesh.

In order to convert the CT images into surface geometry, several steps are needed. First, to generate the outer shell mesh, which describes the pore space structure, a scalar field or the voxelised matrix is generated from the grayscale micro-CT images.

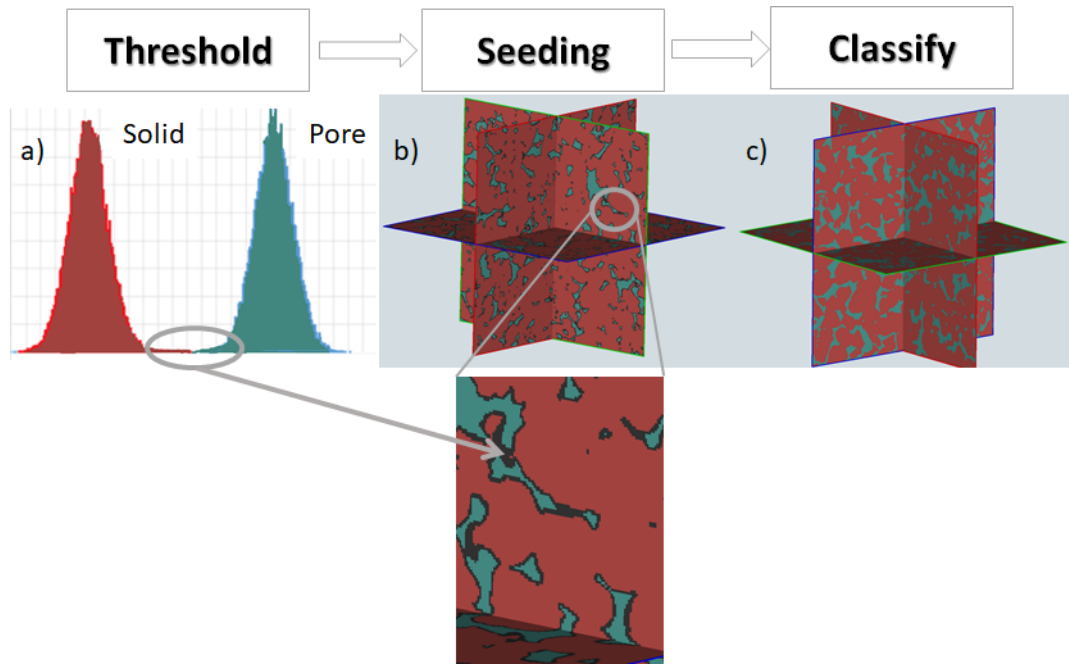


Figure 4.1: Porous media reconstruction steps using RETOMO

This scalar field contains only brightness information and is usually presented by the scaled indexed image that uses a grayscale colour-map. After assigning such a map with the corresponding values that represent each material based on the material histogram (in this case it ranges between zero and one), region growing algorithms are applied. The utilisation of these algorithms (a process known as seeding) is aimed at searching for the homogeneous regions inside the image based on connectivity and similar values among the image voxels. The seeding method operates by merging the nearby voxels that meet a given homogeneity criterion, which is set in prior to this using RETOMO [141]. The histogram region set-up is shown in Fig. 4.1-a and 4.2-b, starting from an initial set of points, known as seeds. This approach offers several advantages over conventional segmentation techniques in that it preserves a very sharp interface after region growing, as shown in Fig. 4.1-c. Also, instead of identifying boundaries, region growing algorithms always operate on closed regions in each step of the algorithm, thus avoiding further post-processing to recover the boundaries of disconnected objects.

In order to perform a proper segmentation after the previous seeding process to the closed substructures of the image and create a compact geometrical representation of the boundary surfaces the marching cube method is used. The marching cubes algorithm [142] is a well know method for constructing a triangular mesh that approximates the location of an iso-surface in volumetric data. It extracts the polygonal mesh of an iso-surface by taking eight neighbour locations at a time (thus forming an imag-

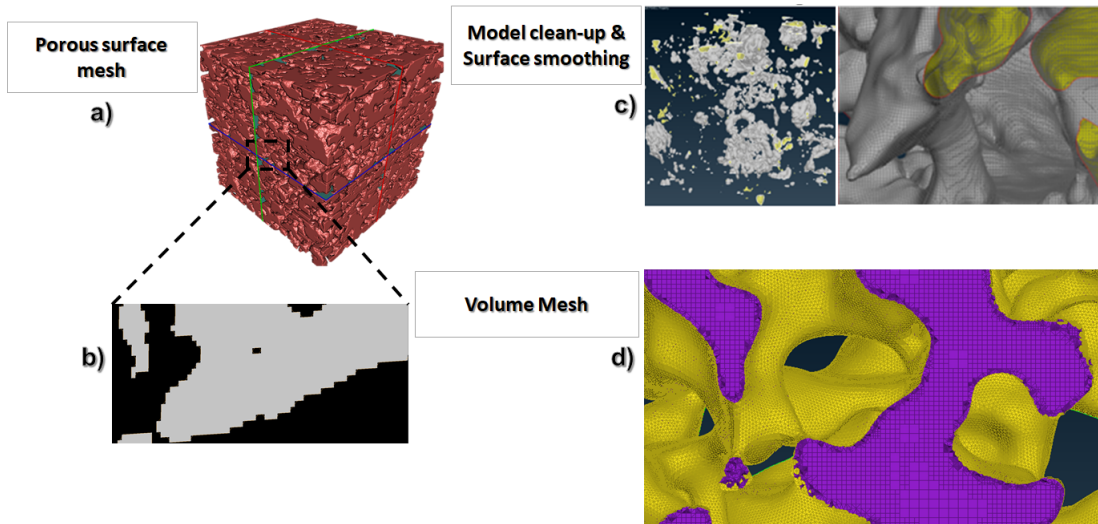


Figure 4.2: Volume mesh building process starting from surface mesh

inary cube). Then, it determines the polygon(s) needed to represent the part of the iso-surface that passes through this cube and the individual polygons are subsequently fused to the desired surface. In each of the boundary faces, two triangles are used in labelling their vertices in order to ensure a close and oriented mesh. The resulting surface will have step discontinuities since the triangles are perpendicular to each other, as seen in Fig. 4.2-a and 4.2-b. Then, the mesh is smoothed by applying a smoothing filter on each vertex. However, a smoothing strength is required as a user-defined parameter, which helps in avoiding undesirable effects on the surface topology, as seen in Fig. 4.2-c.

The results after iso-surface generation are smooth hole-free surfaces without irregularities, whilst preserving the main topological information of the detected components and avoiding the drawbacks of conventional approaches based on iso-surfaces. This algorithm developed by RETOMO [141] is fast and can usually detect well-defined boundaries. The aforementioned framework is a powerful method for tackling problematic segmentations, although the final reconstructions sometimes do not meet the required standards, as the model accuracy is based on the initial image voxel size. In other words, the main limitation of region-growing algorithms is the discrete voxels provided by the CT images, i.e. the finest resolution is the elemental voxel. Hence, the resulting surface models usually present discontinuous steps, which may need the extra step of smoothing over the feature lines. This extra smoothing is undertaken using the pre-processing tool ANSA before the volume mesh generation, as discussed in the next subsection.

4.2.2 Volume Mesh Generation

After iso-surface generation, pore space volume mesh is constructed. An ANSA pre-processor was used to perform the surface mesh improvements and the volume mesh generation after RETOMO iso-surface reconstruction process. The input format used to import the iso-surface models to ANSA was (.obj) type, where the surface mesh kept the connectivity information between the generated triangles, as seen in Fig. 4.2-a. After RETOMO iso-surface construction, it was important to ensure that the pores and throats representations of the rock were kept intact and connected. The generated surface mesh using RETOMO was of high quality; however, further mesh improvements were conducted in the ANSA pre-processor in order to control the surface mesh quality.

Three important steps were performed to improve and ensure the surface quality: (i) surface checks and fixes performed regarding element penetration, surface approximates and overlapping surface elements, without changing the geometrical topology of the porous structure. ii) smoothing the generated surface, if needed, whereby extra surface smoothing filter was applied while the surface mesh was reconstructed to make sure that all surface elements followed the surface quality criteria, as seen in Fig. 4.2-c. (iii) watertight checks were carried out after boundary conditions were assigned at the pore space boundaries and floating pores were removed, as shown in Fig. 4.2-c. The produced surface was then used to define the volume boundary of the flow domain, which was discretised using a hexahedrons dominant volume mesh, as seen in Fig. 4.2-d.

During the volume mesh operation, a coarse background of hexahedron mesh was generated at the spaces far away from the throats and approximates. Then, the number of refined rounds happens close to the surface boundary and self-approximates. The number of refinement levels is usually between two and three. This approach reduces the overall number of elements, whilst still providing an accurate definition for the porous topology. At the small flow passages and throats with small diameters, it is difficult to fit a uniform hexahedrons mesh. To get over this problem, an unstructured mesh is fitted in these regions using tetrahedrons or triangular prisms near to the boundaries. Creating an unstructured mesh for the pore space near to the small surface approximates, in general, and discretising them with a higher resolution, gives an accurate topological description. However, the hybrid mesh used may affect the results due to the non-orthogonality effect.

Table 4.1: Summary of the rock properties and mesh quality used in this study

	Berea sandstone (B1)	Synthetic Silica (A1)
Size (mm)	0.74 ³	1.11 ³
Average Porosity (Exp)	Unknown	42.9
Average Porosity (Num)	$\frac{1.28 \times 10^{-07}}{(7.4 \times 10^{-3})^3} \% = 37.3\%$	$\frac{5.7382 \times 10^{-10}}{(1.11 \times 10^{-3})^3} \% = 41.9\%$
Max aspect ratio	7.62	7.54
Number of cells	2,762,889	3,211,590
Max non-orthogonality (degrees)	62.13	69.68
Max skewness	3.81	16.46
	Sandstone 1 (S1)	Berea sandstone (B2)
Size (mm)	2.585 ³	2 ³
Average Porosity (Exp)	14.1%	18.5%
Average Porosity (Num)	$\frac{2.2958 \times 10^{-9}}{(2.585 \times 10^{-3})^3} \% = 13.29\%$	$\frac{1.6951 \times 10^{-9}}{(2.132 \times 10^{-3})^3} \% = 17.51\%$
Max aspect ratio	9.08	20.58
Number of cells	2,527,384	3,391,171
Max non-orthogonality (degrees)	64.99	64.94
Max skewness	6.94	4.87

The overall framework for volume mesh generation can be summarised as follows: (i) a surface defining the pore-solid boundary is created and improved by using the surface mesh exported from RETOMO surface elements. (ii) the surface can then be smoothed to create a smooth boundary between the pore and the solid. The smoothed generated surface should follow geometrical topology, without shrinking the volume of the pores. (iii) the mesh generation starts, first, with a coarse background hexahedron mesh. (iv) the next step is to refine the background mesh in the throats and narrow restrictions, using two or three levels in each direction. The refining criteria are based on the surface approximates, where the mesh is defined to be refined. The refinement criteria are based on the maximum distance between the two surface proximities. The distance and the angle of the proximities are defined based on the porous structure complexity. (v) finally, the mesh quality checks are performed, which include the orthogonality of the faces to the line connecting the neighbouring cell centres, the aspect ratio, the flatness of the faces, and element skewness. Four different porous structures were used in this study: a Berea Sandstone (B1, B2); Synthetic Silica (A1) and Sandstone 1 (S1) open source [140]. Table (4.1) summarises the porous media properties and the mesh size used in this study.

4.3 Extracting the Correct Numerical Simulation Parameters to Estimate Porous Media Macroscopic Properties

Fluid flow simulations are described using macroscopic properties, including pressure and flow rates. The macroscopic properties can be described in terms of some average properties over a representative elementary volume. The representative elementary volume scale is the scale above which the heterogeneities at smaller scales do not affect these macroscopic properties. The following subsections present brief definitions of these macroscopic properties. Also, the usage of the numerical results is assessed in terms of analysing the ability to obtain the macroscopic properties without considering the effect of gravity. Starting from the single-phase flow through porous media, Darcys law relates the fluid velocities to a macroscopic pressure drop where:

$$U = -\frac{K}{\mu} \frac{\Delta P}{\Delta x} \quad (4.1)$$

where, U is the Darcy velocity, K is the permeability and ΔP is the macroscopic pressure drop with a length of Δx . For the multiphase flow, Darcys law can be written as the relation between the flow rate of each phase to the gradient of a macroscopic pressure for that phase, as follows:

$$U_a = -\frac{K_a}{\mu_a} \frac{\Delta P_a}{\Delta x} \quad (4.2)$$

where, U_a is the Darcy fluid velocity, subscript a carries either water, oil or air, K_a is the phase permeability and $\frac{\Delta P_a}{\Delta x}$ is the gradient of macroscopic pressure for phase (a). Using the definition of the absolute permeability, the phase permeability can be defined as (i.e. the effective permeability of the phase) as follows:

$$K_a = -\frac{Q_a \mu_a}{\Delta P_a} \quad (4.3)$$

where, Q_a is the flow rate passing through a cross section and defined as $(\int u \cdot n_A \alpha dA)$

The rest of the chapter will demonstrate how forces are calculated using Navier-Stokes equations, which are related to the pressure drops used in the multiphase Darcy equations presented above. Accurate predictions using the direct simulation results,

will help in developing a better understanding to the unscaled models, which can be used for a broader range of flow patterns and flow regimes where the apparent relative permeability is dependent on the flow rate and flow properties. Using the direct numerical simulation results, the flow rate of fluid phases can be related to the pressure drop. Since the size of the flow domain is small and the pressure drop calculation can be very sensitive to the method deployed due to the small sample size used, it is not possible to calculate the pressure drops based on the difference between the pressures at the inlet and the outlet of the porous media. Instead, it is better to represent the link between the pressure drop and the different forces controlling the flow field. In theory, pressure can be defined at any point, while pressure gradient will be the factor that drives the fluid flow, yet it is not evident how pressure should be averaged in pore-scale models [143]. In this work, the definition of the pressure gradient calculated based on the rate of work done by the fluid in the pore space, was used. In a single-phase flow, it can be assumed that the work done on the fluid by the dynamic pressure drop is dissipated by the viscous force, neglecting the inertial terms effect at the pore space are negligible. The work done can be defined as:

$$\frac{dW_{Pd}}{dt} = -\Delta P Q \quad (4.4)$$

$$\frac{dW_{\mu}}{dt} = Q \int_V (\nabla \cdot (\mu \nabla u)) \cdot u dV \quad (4.5)$$

where, $\frac{dW_{\mu}}{dt}$ is the rate of dissipation of the energy in the fluid due to internal viscous forces. By equating the two equations shown in (4.4 and 4.5), the pressure drop in both phases can be calculated alternatively in the represented porous model. In the rest of this chapter, the pressure drop will be used as a reference to the work done on the fluid phases in the porous media divided by the flow rate, which can be written as:

$$\Delta P_{\mu} = Q \int_V (\nabla \cdot (\mu \nabla u)) \cdot u dV \quad (4.6)$$

where, Eq. (4.6) calculates the pressure drop as the energy loss in both phases due to viscous dissipation per unit flow rate of both phases. Using the aforementioned method, it is possible to define the macroscopic pressure drop per phase as:

$$\Delta P_a = \frac{1}{Q_a} \int_V (\nabla \cdot (\mu \nabla u)) \cdot u dV_a \quad (4.7)$$

Hence, ΔP_a can define the pressure drop in individual phases, which is used in the definition of the dynamic effective permeability per phase Eq. (4.3). Using the previous definitions, it is possible to relate to the dynamic pressure gradient and the capillary field using the Navier-Stokes equations. Similarly, the capillary pressure drop can be calculated as defined in Chapter 2, where the rate of work done on the fluid by the capillary field ($f_s \nabla p_c$), per unit flow rate is:

$$\Delta P_{c,a} = \frac{1}{Q_a} \int_V (f_s \nabla p_c) \cdot u dV_a \quad (4.8)$$

Looking at the capillary pressure formulation, it should be noted that the Darcy-scale flow potential in two-phase is the result of work done by the capillary field and the dynamic pressure gradient force that is equal to the work done by the viscous forces. In other words, for the energy to be conserved, the dynamic pressure for multiphase flow should be different from that used in the Navier-Stokes equations, ignoring the inertial force effect. One significant advantage of the mentioned approach in calculating pressure drops is that the Darcy equations will be strictly a statement of energy balance, which can help in studying the effect of the interfacial energy and the gravity potentials accurately.

4.4 Investigating Different Flow Properties on Various Porosities

This section presents different numerical results for water injection simulations (removing the oil phase) with different water surfactant properties, i.e. surface tension and wetting conditions on the micro-CT porous structures presented in the previous section. The size of the porous media and the mesh size are given in Table 4.1. To predict the behaviour for the oil removal process, the developed solver presented in the previous chapter was used. The solver numerical setup is similar to the T-junction test case discussed in Chapter 3. Using the newly developed solver *interPore*, it was possible too predict the oil transport by tracking the water oil interface. In all the simulations presented in this section, the flow is injected in the x-direction as seen in Fig. 4.3. it should be noted that the direction of the flow will drive the permeability results. Fluid properties for water and oil are presented in Table 4.2 and will be used for the rest of the simulation as constant values.

Table 4.2: Fluid Properties

Property	Density ρ (kg/m^3)	Kinematic Viscosity ν (m^2/s)
Water	998	1.004×10^{-6}
Oil	806	2.8×10^{-6}

4.4.1 Case Setup and Imposed Conditions for Primary Water Injection

In the primary drainage simulation for the oil phase, the water injection was used at the inlet in order to study the effect of imposed wetting conditions on the oil phase removal. During the primary drainage simulation, a zero-gradient boundary condition for the indicator function (α) for the inlet and an (inletOutlet) boundary condition for the outlet, with a fixed value of ($\alpha = 1$), was used. The dynamic Kistler Boundary Conditions (KBC) for the rest of the porous walls was imposed, while for the inlet velocity a constant flow rate was imposed, as shown in Fig. 4.3. A zero gradient boundary condition for the pressure at the inlet and a fixed value zero at the outlet were also used. Fig. 4.3 corresponds to the initial time step after using the (setField) function to set the pore volumes for the water phase into the pore space from the left

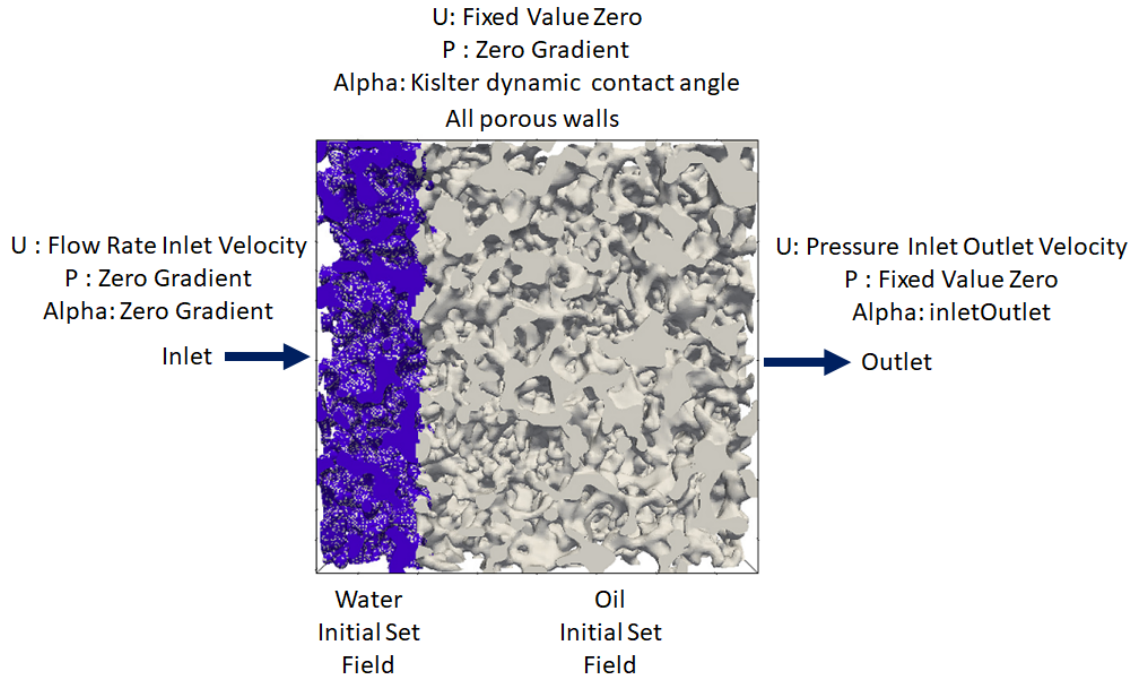


Figure 4.3: A visualization of the pore space for the Berea Sandstone B1, and the initial condition for the indicator function (alpha) with the prescribed boundary conditions

side. This means that before starting the simulation all the elements located at the first 10% of the domain are set to have a constant value of ($\alpha = 1$) so as to reduce the instability at the inlet boundary condition. Finally, the surrounding walls of the porous media are considered walls. Table 4.3 presents the case setup for the different wetting conditions that will be used in the rest of the chapter. Each wetting condition represents a different surface response for the water/oil interaction.

As reported in Table 4.3, the simulation results are presented at various injection flow rates that start from $1 \times 10^{-8} m^3/s$. Different representations for the dynamic contact angle have been simulated to demonstrate the effect of dynamic wetting conditions on the effective permeability and phase saturation. In the primary drainage simulations, since the current model does not capture wetting film flow when the film thickness is less than the grid element size, it was not possible to reach the maximum possible saturation of the water phase. A detailed analysis of the effect of fluid properties is beyond the scope of this research; however, the variation of surface tension forces is studied briefly. Also, this subsection will link the effect of the capillary number and wetting conditions to the trapped oil clusters during the drainage process.

It should be noted that the main disadvantage of simulations modelling using the VoF method, is its high computational cost. The simulation time has been found to depend on the boundary conditions, fluid properties and the capillary number. The

Table 4.3: Case set up for wetting conditions and average flow rate: the surface tension, σ , used in all the simulations is constant and equal to 0.024 (kg/s^2), except in the BM5 case, which has a value of 0.0221 (kg/s^2)

Model	Case	Injection flow rate (m^3/s)	Advancing Contact Angle	Receding Contact Angle	Average Capillary no.	Average Reynolds no.
B1	BM1	1×10^{-8}	120	65	2.05×10^{-3}	229
B1	BM2	1×10^{-8}	31	31	1.87×10^{-3}	208
B1	BM3	1×10^{-8}	8	6	1.72×10^{-3}	205
B1	BM4	1×10^{-9}	8	6	1.66×10^{-4}	20
B1	BM5	1×10^{-8}	120	65	2.07×10^{-3}	227
A1	AM1	1×10^{-8}	120	65	6.6×10^{-4}	74
A1	AM2	1×10^{-8}	31	31	5.9×10^{-4}	65
S1	SM1	1×10^{-8}	120	65	1.5×10^{-4}	6.71
B2	B2M1	1×10^{-8}	120	65	1.41×10^{-4}	6.27

resultant simulation shows that the run time increases significantly as the capillary number ($\frac{\nu U_{avg}}{\rho}$) value decreases to lower than (1×10^{-5}). Longer time was needed to run all the models after showing signs of saturation stability. On average, it was found that one simulation for water injection at a capillary number of (1×10^{-5}) may take around one week of computing and data analysis. Table 4.3 gives a full description of Reynolds number and capillary number calculated for each individual case setup for the oil drainage simulations.

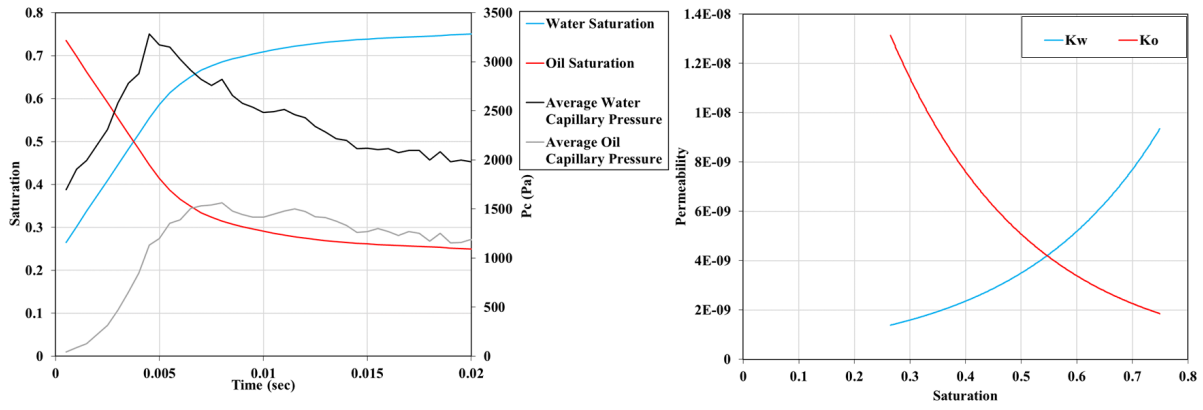
4.4.2 Primary Water Injection Using Different Wetting Conditions for Different Capillary Numbers

This subsection starts with a prediction of water injection behaviour for the Berea Sandstone (B1). In order to illustrate the fluid behaviour, a representation for capillary pressure, oil and water saturation and permeability for each case will be shown. Also, to present the water/oil phase interaction inside the porous structure, a cross section slice at the middle of each porous media was selected to represent the phase fraction and the oil clusters.

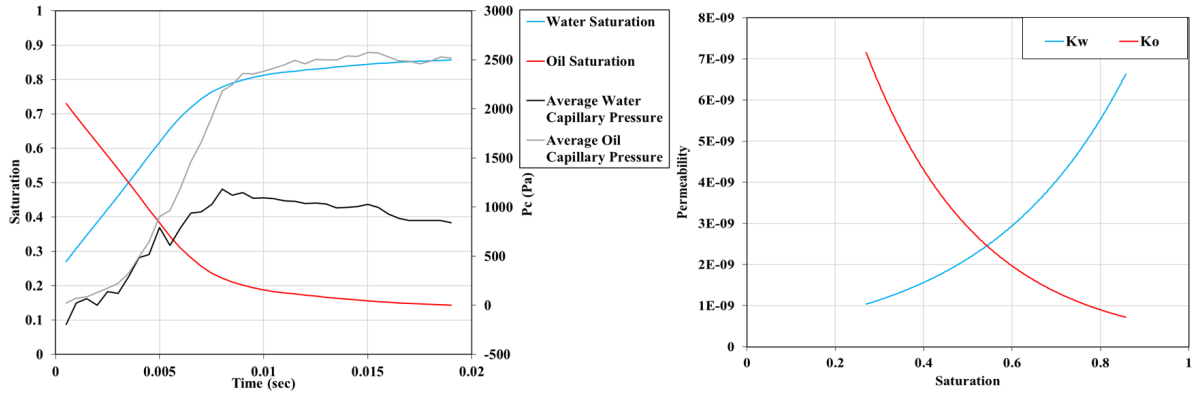
Three different different dynamic wetting conditions (BM1, BM2 and BM3), as shown in Fig. 4.4 where considered, where a comparison between the phase saturation at the beginning and the end of the water injection process at the same capillary number order of magnitude is provided. Comparing Fig. 4.4a, 4.4b and 4.4c, shows that the point of intersection between the two saturation lines is shifted to the left with respect to time in Case b and Case c. This shift presents the effect of intermediate and low wetting conditions values imposed on the oil drainage process. Also, as expected, a very high water capillary pressure is observed in Case when compared to the dynamic wetting low values of Case b and Case c. The difference in capillary pressures indicates the direct impact of intermediate and low contact angle values on the oil and water capillary pressure. The effect of the lower capillary pressure for water in Case b and Case c is reflected on the permeability plots on the right hand side of Fig. 4.4, which differ from Case a. Also, the permeability curves for Case b and Case c look almost exactly the same, thus indicating that a change in the wetting boundary condition does not affect the invasion capillary pressure.

Reflecting the previous saturation curve for the transport of the oil phase, the results presented in Fig. 4.5 show the size of the trapped oil phase. It was predicted that in case of a low dynamic contact angle value, the trapped droplets would be smaller compared to the high dynamic contact angle results (circled in red), due to the adhesion force present in the former case.

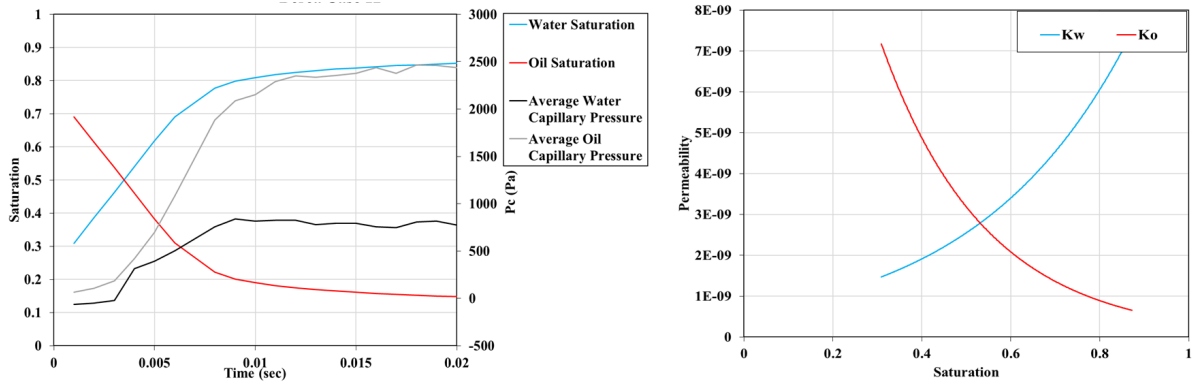
When investigating the 3D representation for Cases BM1, BM2 and BM3, as seen in Fig. 4.6, it is clear that the size of the trapped oil clusters is smaller in Case BM1, as mentioned before, compared to cases BM2 and BM3. Nevertheless, it presents a larger number of clusters than the other two cases. This observation shows the importance of the wetting condition on the oil cluster formation, where the contact angle force has



(a) Case BM1 ($\theta_A = 120^\circ, \theta_R = 65^\circ, ST = 0.024kg/s^2, Ca = 2.05 \times 10^{-3}$)



(b) Case BM2 ($\theta_A = 31^\circ, \theta_R = 31^\circ, ST = 0.024kg/s^2, Ca = 1.87 \times 10^{-3}$)

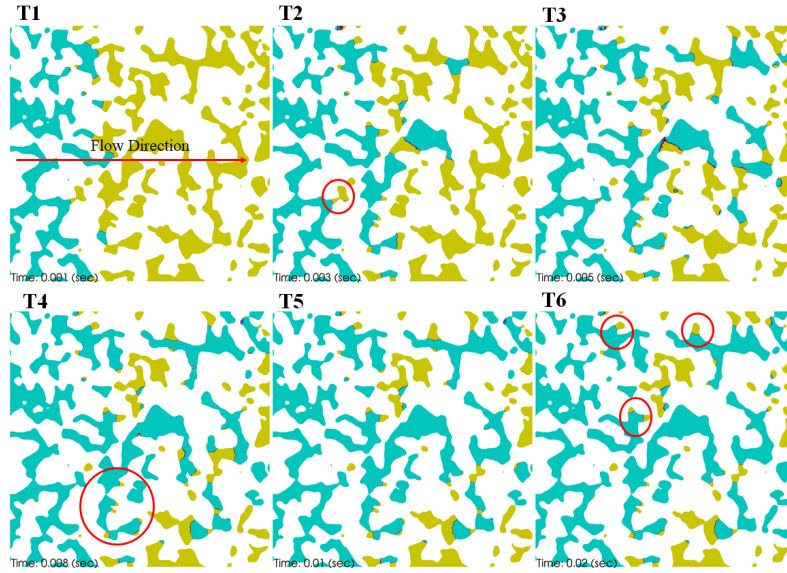


(c) Case BM3 ($\theta_A = 8^\circ, \theta_R = 6^\circ, ST = 0.024kg/s^2, Ca = 1.72 \times 10^{-3}$)

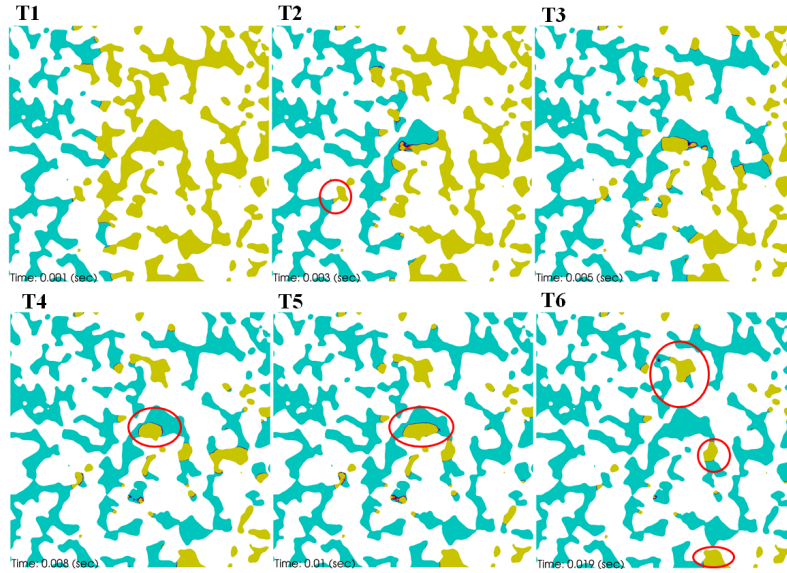
Figure 4.4: Plots of the capillary pressure in both phases (first row) and the computed effective permeability curves, showing the effect of surface wetting conditions at a constant injection rate

a big influence on the oil transport at the same porous structure and flow rate. Also, for the 3D representation a very small difference between Case BM2 and Case BM3 emerged due to the close contact angle value imposed.

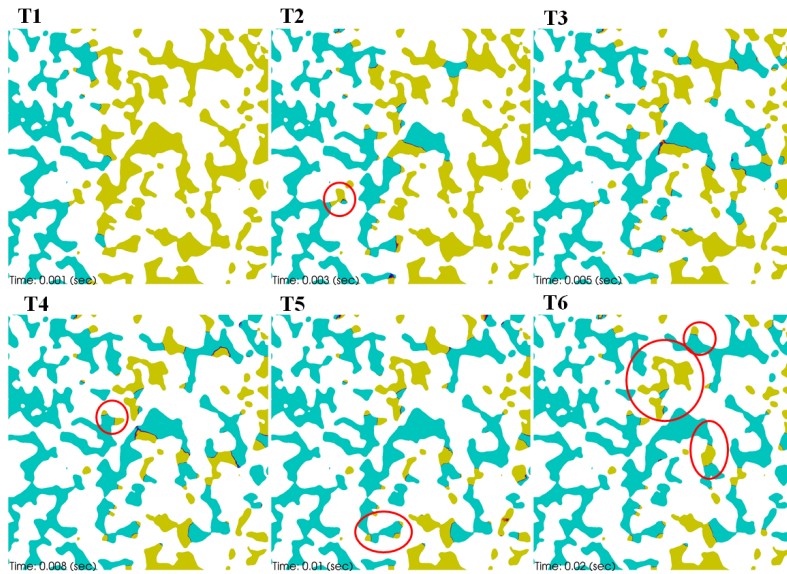
When considering the effect of the water injection flow rate on the oil transport, Cases BM3 and BM4 can be compared as they share the same wetting conditions. Comparing these two case, which represent a decrease in the injection flow rate, there is a significant change in the permeability curve, as shown in Fig. 4.7b. Due to the decrease in capillary pressure shown in Fig. 4.7a the flow behaviour noticed to be



(a) Case BM1 ($\theta_A = 120^\circ, \theta_R = 65^\circ, ST = 0.024kg/s^2, Ca = 2.05 \times 10^{-3}$)



(b) Case BM2 ($\theta_A = 31^\circ, \theta_R = 31^\circ, ST = 0.024kg/s^2, Ca = 1.87 \times 10^{-3}$)



(c) Case BM3 ($\theta_A = 8^\circ, \theta_R = 6^\circ, ST = 0.024kg/s^2, Ca = 1.72 \times 10^{-3}$)

Figure 4.5: Cross section showing the water phase in blue and oil phase in yellow, when comparing Cases BM1, BM2 and BM3. The red circles are used to highlight the trapped oil droplets.

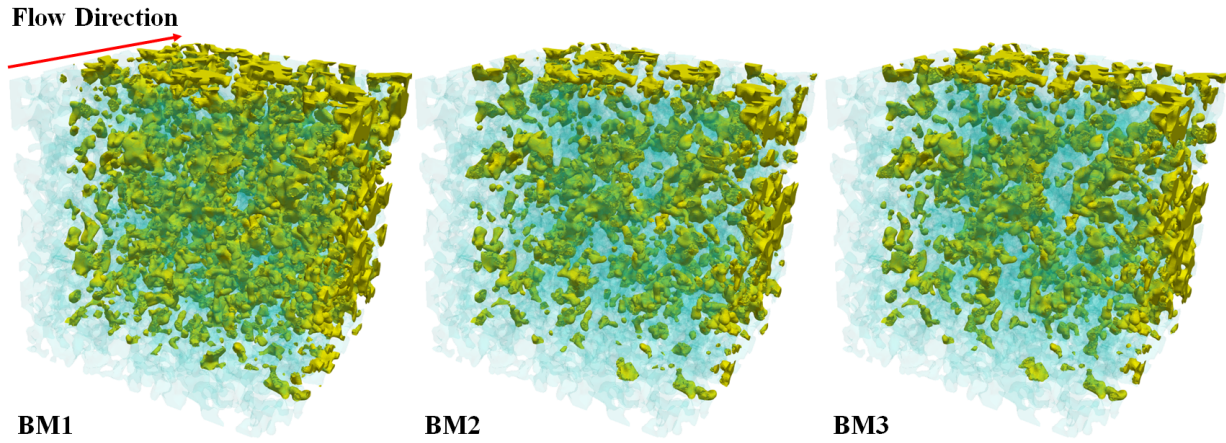


Figure 4.6: A 3D visualization for the oil residuals for Cases BM1, BM3 and BM3 at time = 0.0155s

changed as compared to Case BM3. The difference in behaviour can be noticed from the shifted intersection point for saturation curve (saturation curve in Case BM4 is shifted to the right with respect to time), which represents a different water invasion behaviour during oil removal. The shifted intersection was predictable because the lower injection flow rate, Nevertheless, the predicted capillary pressure indicates a change in the flow behaviour as compared to Case BM3. When considering the saturation curve on 2D slices presented in Fig. 4.8, it can be seen that the amount of trapped oil in Case BM4 is less than for Case BM3. The low velocity of the water phase effect seen in Case BM4 allows more time for the unconnected cluster formation to transport in the flow direction and to overcome the wall resistance. As a consequence, a higher permeability curve was obtained, as can be seen in Fig. 4.7b. Nevertheless, to get a more accurate prediction for Case BM4, more time should be allowed for the simulation at a lower capillary number.

Also, the behaviour for the trapped oil droplets in Case BM4 at the low capillary number shown in Fig. 4.8 is different to that of BM3. The differences are found to be due to the high capillary pressure developed during the slow water injection at a low contact angle value. The small difference between the average capillary pressure values for water and oil in BM4 shown in Fig. 4.7b has a significant impact on the permeability values. Also, for the case of a lower capillary number, as in Fig. 4.8, the size of the trapped oil phase cluster is similar to the higher capillary numbers imposed. Moreover, using the micro-scale simulation provided a direct link between the physical changes in the pore scale and its reflection in the macroscopic parameters.

Similar to the previous observation, using the 3D representation for the oil residuals

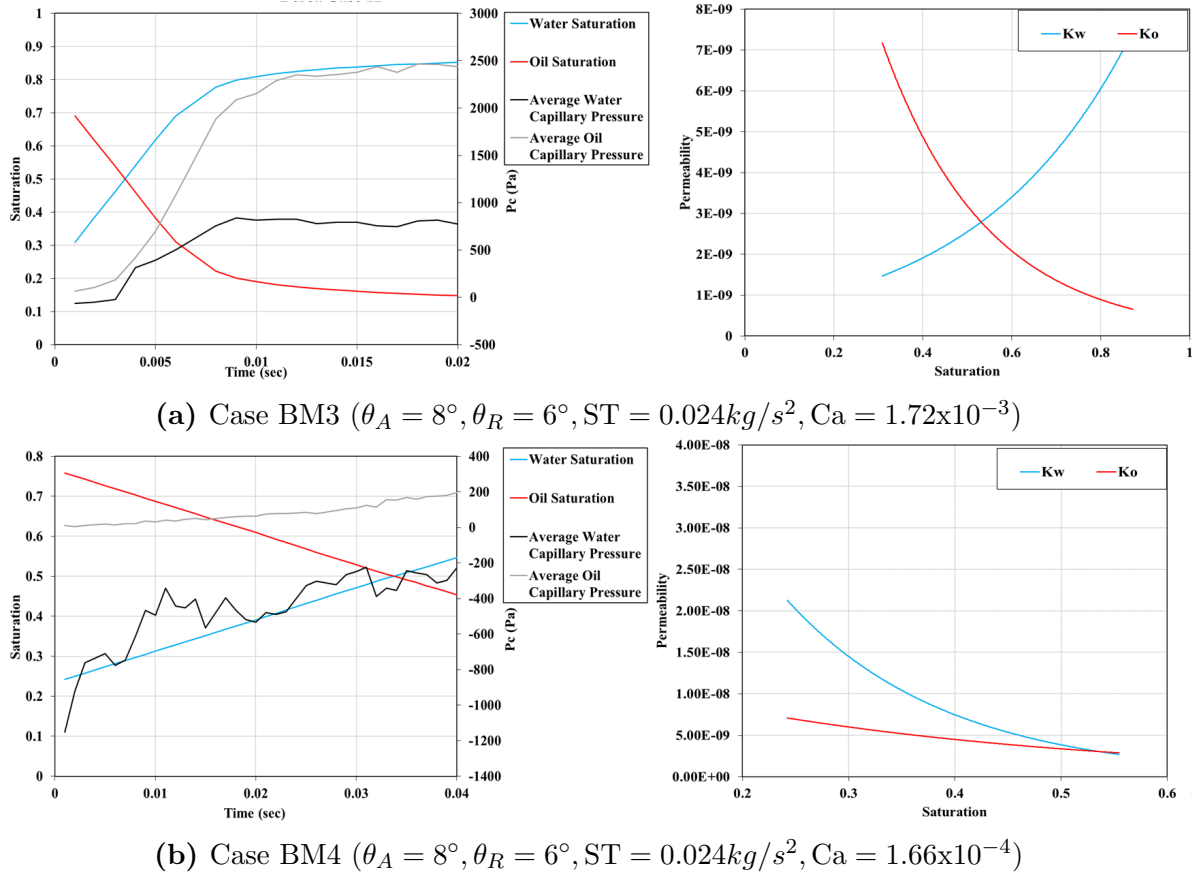
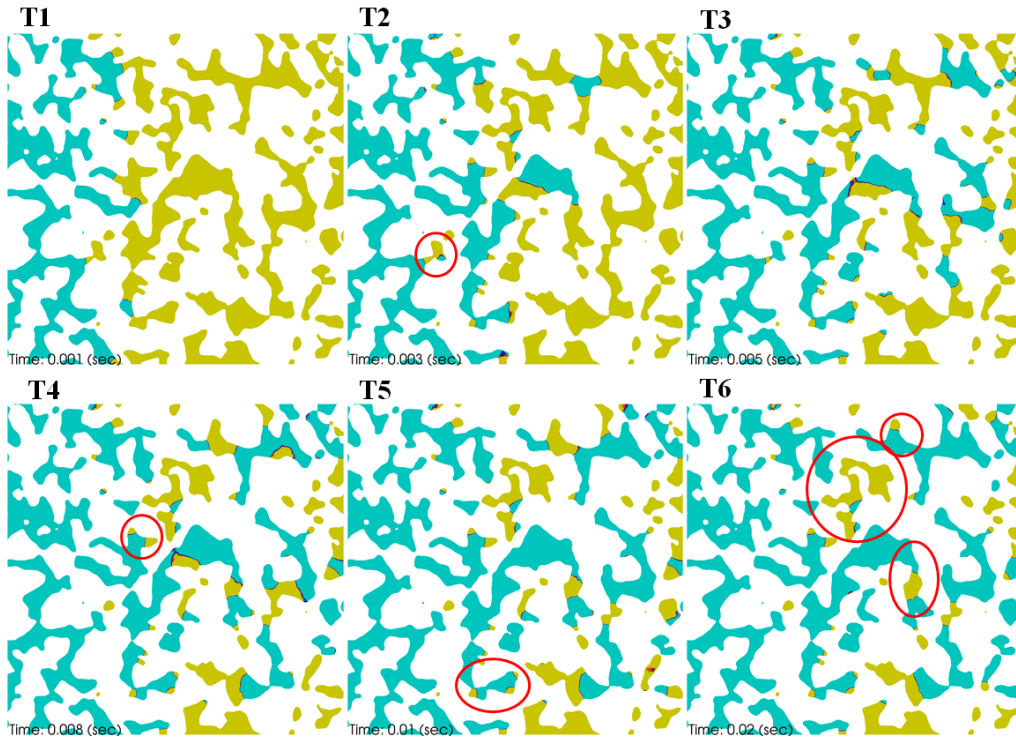


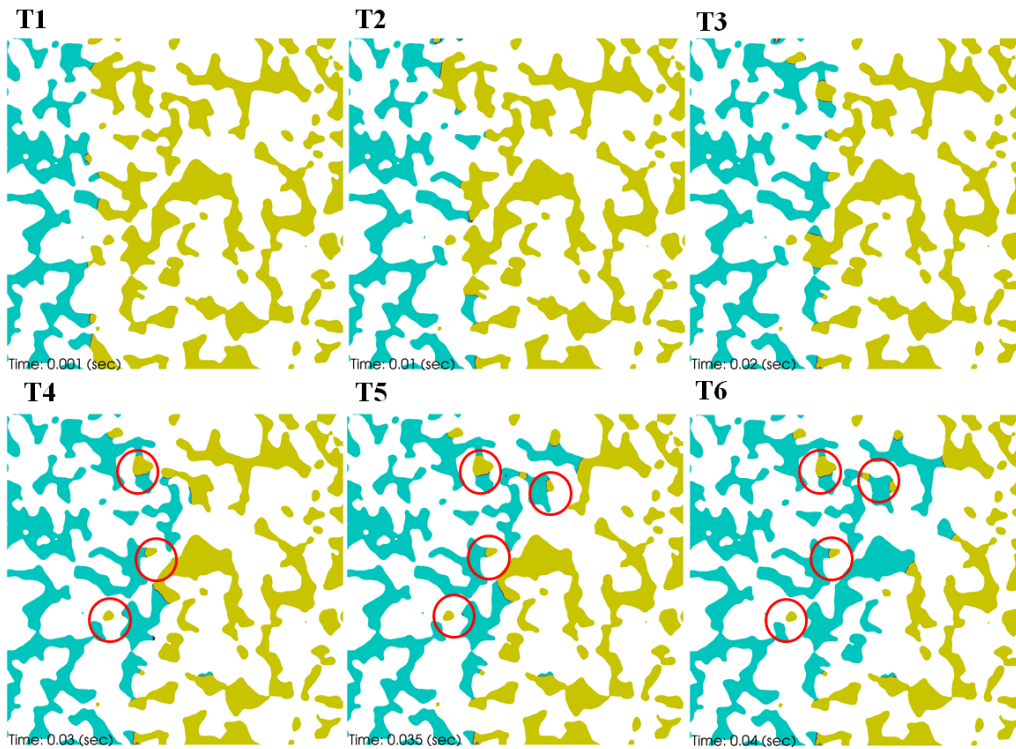
Figure 4.7: Plots of the capillary pressure in both phases (first row) and the computed effective permeability curves, showing the effect of the capillary number

shown in Fig. 4.9 allow to obtain the relation between the cluster size in the two models. It is important to mention that, some oil clusters close to the porous walls were found to be very similar in size, shape and location. This clusters are formed due to the effect of the wall boundary condition, whereby the imposed zero velocity at the walls increases the trapping at the walls. However, in an actual flow scenario, the porous (four) walls should not affect the flow behaviour, so it is recommended to use a cyclic boundary condition at the porous walls in order to increase the accuracy of the modelling process.

Similar to the model B1, the effect of the imposed contact angle on A1 was investigated. Due to the change in porous structure, a different oil behaviour was predicted using the developed solver. As shown in Fig. 4.10a, a low oil capillary pressure value was predicted in Case AM1, which was reflected in the slow oil saturation decrease in the time permeability curve. Also, when studying the saturation curve in Fig. 4.10a, it was observed that oil saturation reached a constant value of almost 25% towards the end of the simulation. While for Case AM2 a faster decrease rate was observed at the oil saturation curve Fig. 4.10b. The oil saturation in Case AM2 reaches almost 5% before equilibrium. The difference seen between Cases AM1 and AM2, shows the



(a) Case BM3 ($\theta_A = 8^\circ, \theta_R = 6^\circ, ST = 0.024kg/s^2, Ca = 1.72 \times 10^{-3}$)



(b) Case BM4 ($\theta_A = 8^\circ, \theta_R = 6^\circ, ST = 0.024kg/s^2, Ca = 1.66 \times 10^{-4}$)

Figure 4.8: Cross section showing the water phase in blue and the oil phase in yellow for comparison of Cases BM3 and BM4

direct link between the wetting condition and porous structure.

Nevertheless, comparing the permeability curves in Fig. 4.10a and Fig. 4.10b, a higher rate of decrease in oil permeability is observed in case AM2. It can also be

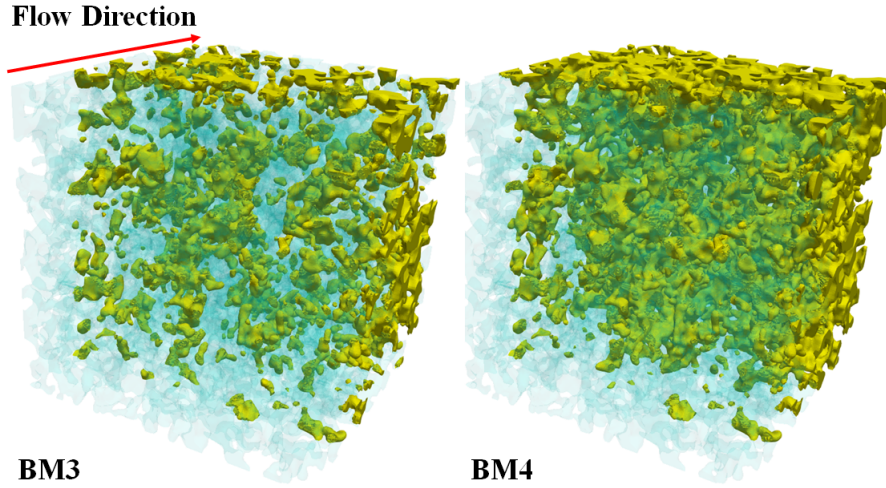
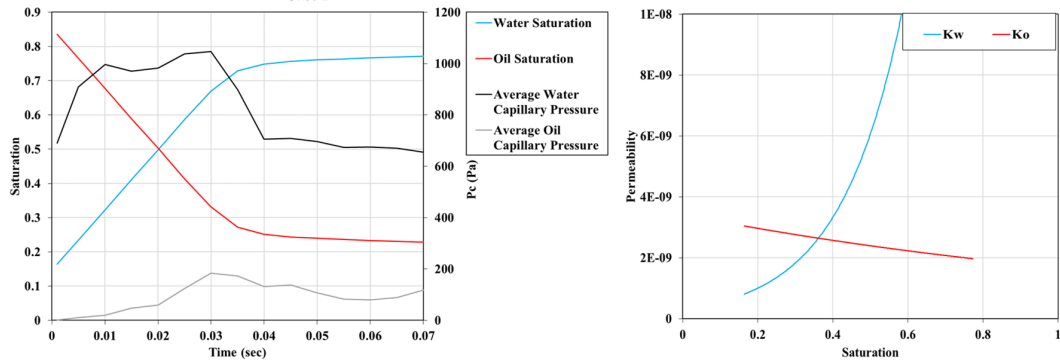
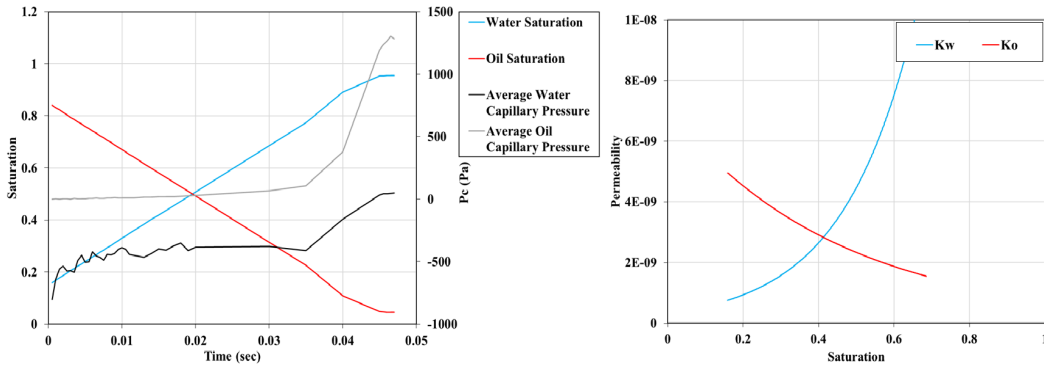


Figure 4.9: A 3D visualisation for the oil residuals for Cases BM3 at time = 0.0155s and Case BM4 at time = 0.041s

seen that the water permissibility in Case AM2 is shifted to the right (with respect to saturation), thereby showing the effect of a lower contact angle value on oil transport. Finally, inverse capillary pressure was seen between Case AM1 and Case AM2 for the imposed contact angle. The observed capillary pressure presented a direct link between the decrease in oil saturation and the wetting conditions. Also, a higher



(a) Case AM1 ($\theta_A = 120^\circ, \theta_R = 65^\circ, ST = 0.024kg/s^2, Ca = 1.5 \times 10^{-4}$)

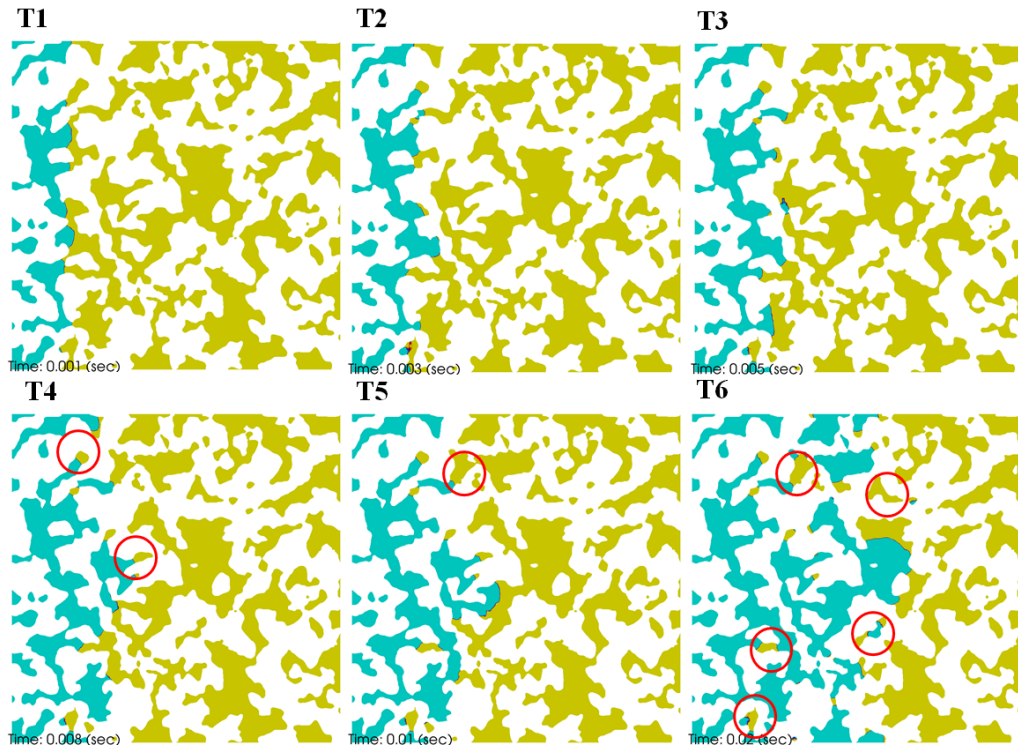


(b) Case AM2 ($\theta_A = 31^\circ, \theta_R = 31^\circ, ST = 0.024kg/s^2, Ca = 5.9 \times 10^{-4}$)

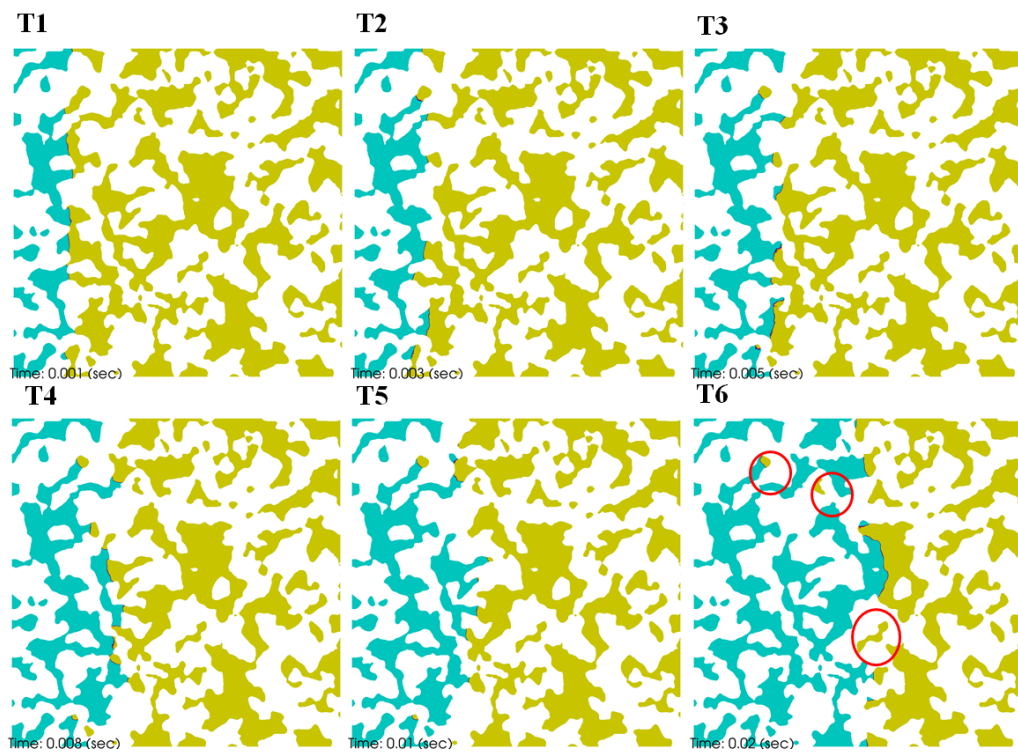
Figure 4.10: Plots of the capillary pressure in both phases and the computed effective permeability curves, showing the effect of varying the imposed contact angle

capillary pressure was seen in Fig. 4.10a, which was reflected in a longer duration of the oil removal process. Moreover, the saturation curve intersection for both cases in Fig. 4.10a and Fig. 4.10b at $t = 0.02\text{s}$ (for different saturation values) shows that regardless of the entry pressure effect, the overall saturation prediction can be achieved using the upscaled model from the pore scale simulation.

Reflecting on the observations of the permeability curves in Fig. 4.10 for the water/oil representation seen in Fig. 4.11, it can be that AM2 is found to have the least oil residual clusters in all the presented simulations. As predicted from the permeability curves, it emerges that the water interface front at a low contact angle value decreases the effect of the oil residual structure. As a result, the oil removal process has been very much affected in Case AM2. However, comparing AM2 to AM1, it noticed that a fingering pattern can be seen in Fig. 4.11a, which is responsible for decreases the number of trapped oil clusters as well as the oil removal rate during the drainage process.



(a) Case AM1 ($\theta_A = 120^\circ, \theta_R = 65^\circ, ST = 0.024 kg/s^2, Ca = 1.72 \times 10^{-3}$)



(b) Case AM2 ($\theta_A = 31^\circ, \theta_R = 31^\circ, ST = 0.024 kg/s^2, Ca = 1.66 \times 10^{-4}$)

Figure 4.11: Cross section showing the water phase in blue and oil phase in yellow when comparing Cases AM1 and AM2

4.4.3 Effect of Porosity During Primary Water Injection Using Dynamic Wetting Conditions

In order to understand the behaviour of oil phase transport through a porous structure, the effect of porosity and its relevance to the oil removal process needs to be examined. The porosity is considered to be an important factor in characterising the flow behaviour using the developed numerical simulation in a complex porous medium. This subsection is dedicated to comparing different porous structures and internal porosity values, whilst also predicting the permeability curves for different porous models. First, a comparison the previous two porous structures (B1 and A1) is presented in Fig. 4.12, showing the oil phase distributions at $t = 0.02$ secs. The water saturation at $t = 0.02$ s for BM1 Fig. 4.12-a is found to be around 75%, while for BM2 Fig. 4.12-b it is about 86% for the same injection flow rate. Regarding the visualisations of the water phase at $t = 0.02$ s in Fig. 4.12-a shows the presence of large clusters of the oil phase (yellow) partially connected to the outlet, while in BM2 Fig. 4.12-b, this illustrates how the oil phase clusters are trapped and surrounded by the water phase.

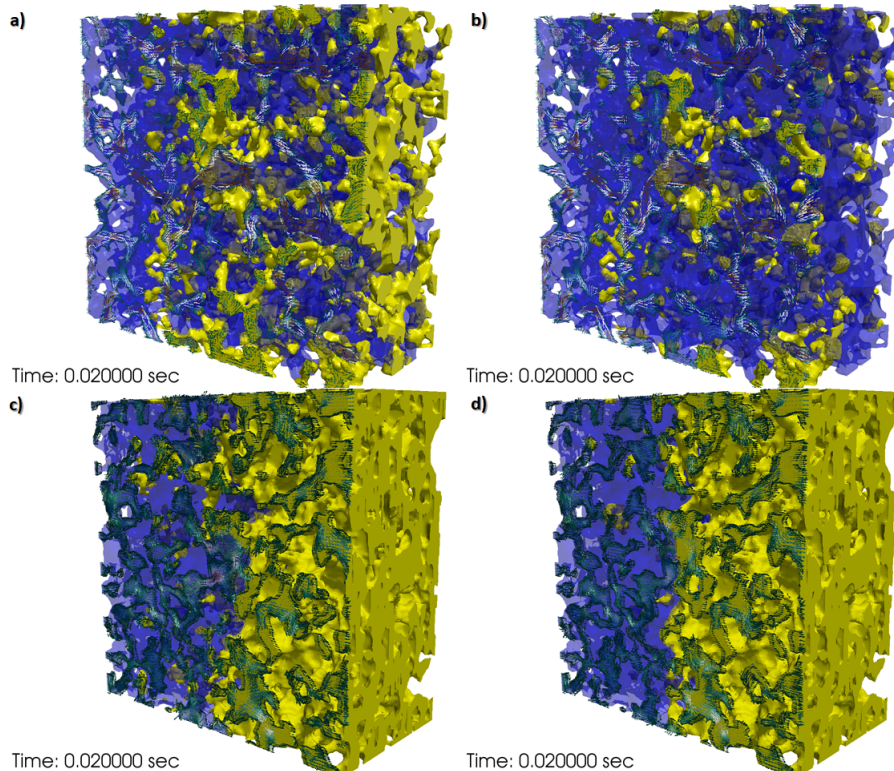


Figure 4.12: A visualisation of the indicator function (α_{Sh}): blue represents the water phase and yellow the oil phase, after 0.02 secs of water injection, for a capillary number of 8×10^{-5} ; a) presents BM1, b) presents BM2, c) presents AM1, and d) presents AM2

Comparing Case BM1 with Case AM1 (for which they share the same water injection flow rate and imposed wetting conditions), as seen in Fig. 4.12-c, it is found

that water saturation at $t = 0.02s$ is around 49%. The lower value of water saturation, as seen between the two models (BM1 and AM1), is due to the lack of unconnected paths in the A1 model. Also, similar behaviour was found in AM2 Fig. 4.12-d, where it emerged that only 50% of the water saturation invaded the porous media at the same time step. It is important to note that, the porosity value for the two models (B1 and A1) was found to be close (see Table 4.3); however, the link between porosity and liquid behaviour during oil drainage process found to be very important. Also, a small difference was noticed in oil saturation between Cases AM1 and AM2 at this particular time step compared to Cases BM1 and BM2 under the same boundary conditions, due to the permeability values shown in the previous section. Moreover, it is important to point out that the numerical model used does not consider layer flow through corners. So, if the layer thickness is smaller than the mesh size at the pore corners, the developed solver will not be able to capture its effect. This may increase the calculation error in some cases, although it has been reported by Dong [140] that the flow through such layers is slow and will not have a significant effect on the results.

To extend the porosity investigations, two more porous structures are considered in this section. Porous models B2 and S1 found in Table 4.3 present a tight porous structure effect on the fluid behaviour. In order to conduct an accurate comparison based on the porosity effect. Cases SM1 and B2M1 share the same imposed flow conditions as AM1. Similar to the previous section a comparison between the saturation curves and flow pattern using a cross section at the middle of each model was made.

Comparing Case AM1 (which presents a porosity of 41.9%), as seen in Fig. 4.13a and Case SM1 (which presents a porosity of 13.29%), as seen in Fig. 4.13b, the significant effect of porosity on capillary pressure behaviour can clearly be seen. This significant effect shows that both phases of capillary pressure are found to increase during the injection process with a tight SM1 porous structure. When comparing the capillary pressure behaviour between Cases SM1 and AM1, it is observed that in Case SM1 the values of the capillary pressure are higher than those for Case AM1. Also, it is clear that the capillary pressure value is not decreasing in Case SM1 compared to Case AM1. This can be a significant characteristic behaviour for capillary pressure when there is a tight porous structure, where the narrow or blocked paths induce a higher capillary pressure that increases over time for both phases. This blocked paths also reflect the tortuosity and the permeability effect of the porous structures.

Also, by looking closer at the saturation curves presented in Fig. 4.13a and Fig.

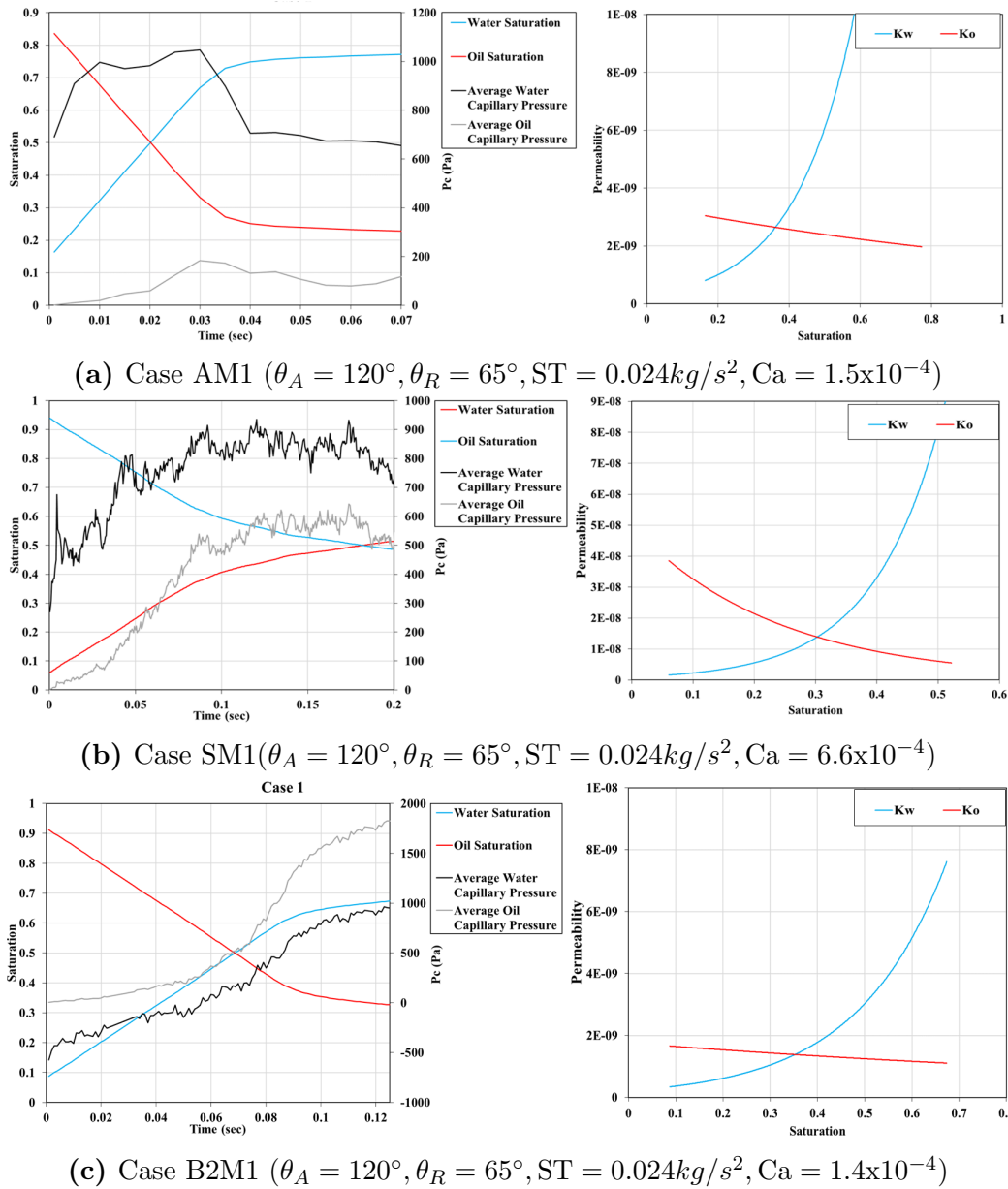


Figure 4.13: Plots of the capillary pressure and saturation curves for both phases and the computed effective permeability curves, showing the effect of varying porosity across Cases AM1, SM1 and B2M1

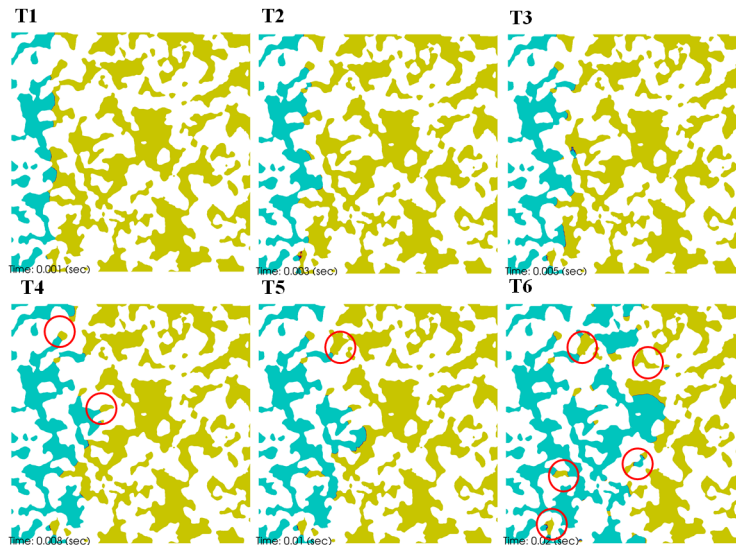
4.13b, a slow rate of oil removal is found in Case SM1. In addition, compared to Case AM1 the saturation curve intersection for SM1 has shifted to the right with respect to time, which signifies a difficulty during the injected phase in finding wide connected paths between the inlet and the outlet. As a consequence of the saturation curve represented in Fig. 4.13b, the oil permeability curve shown in the same figure is found to have a higher value compared to Case AM1. The permeability value indicates that (as seen in saturation curves) it will take a longer time to reach the oil saturation steady state, with a high possibility of larger clusters of trapped oil. It is also important to note that, by capturing the macroscopic behaviour for SM1 during drainage process,

one can reflect using the previous section (for the effect of different wetting) to change the imposed wetting condition to enhance oil recovery.

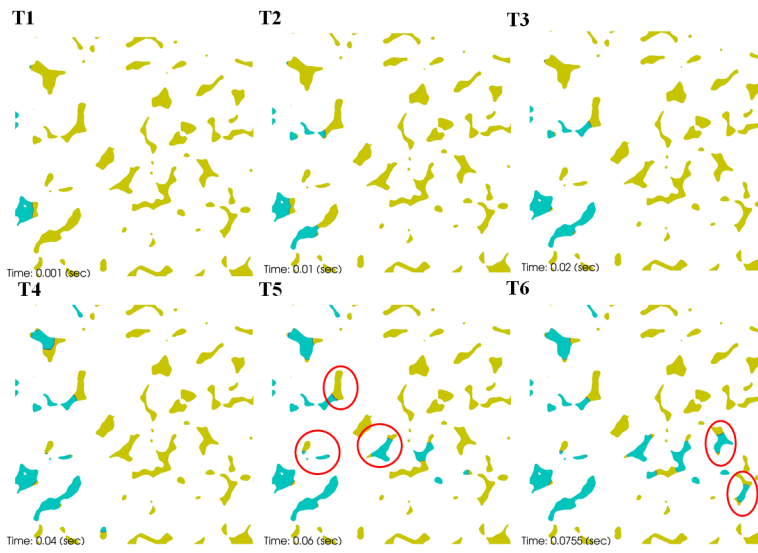
For a deep understanding of the effect of the permeability curve on the trapped oil cluster in a tight porous structure, S1, the patterns of water penetration, as shown in Fig. 4.14, can be compared. The tight porous media SM1 Fig. 4.14b shows a significant amount of trapped fluid compared to AM1 Fig. 4.14a. The high capillary pressure, as illustrated in the previous Fig. 4.13 in SM1, also represent importantly relation between porosity value and wetting condition. The trapped oil phase clusters are even bigger than with the B1 model. This observation can be explained by the fact that at low capillary numbers the viscous forces are lower, and the capillary pressure generated in the oil phase clusters can oppose the dynamic pressure gradient force as well as the viscous drag force between the two phases for bigger trapped oil droplets. Also, in the presence of low value porosity, the permeability effect increases the influence of trapping during water injection. Based on the results presented in the previous section, the maximum capillary field found in the oil phase droplet is inversely proportional to the oil droplet size. Hence, at a high capillary number, the size of the droplet should be smaller such that the magnitude of the capillary field in the droplet will be greater than the capillary pressure gradient. However, the droplet size has been shown to be also related to the porosity value. The size directly reflects in the capillary pressure, as it is observed that at low porosity models the induced capillary pressure is higher than A1 model.

Comparing the B2 tight porous structure seen in Fig. 4.13c to S1 and A1 at the same imposed contact angle, it can be seen that there is a higher capillary pressure compared to Case SM1 and AM1. The higher predicted capillary pressure is a result of the low porosity value with a complex porous structure between the inlet and the outlet. The higher oil capillary pressure was reflected in the oil permeability prediction compared to Case SM1, where oil saturation was shown to be faster under the same water injection rate. It should also be noted that, in Fig. 4.14c, the trapped oil phase was found to be less compared to Case SM1. The reason for this is due to the flow behaviour during the water injection, whereby the water front was accessed with a larger number of pores connected to the outlet of the porous media.

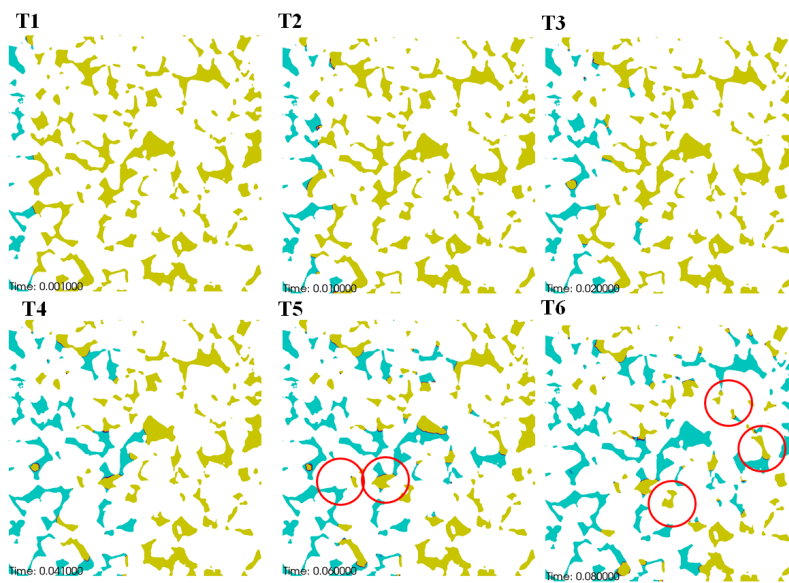
Visualisation of the oil phase presented in Fig. 4.15 shows that there are larger clusters of the water phase connected to the outlet in Case AM1 than for Cases SM1 and B2M1. This implies that not all of the oil phase at the end of the simulations is



(a) Case AM1



(b) Case SM1



(c) Case B2M1

Figure 4.14: Cross section showing the water phase in blue and oil phase in yellow, when comparing cases AM1, SM1 & B2M1

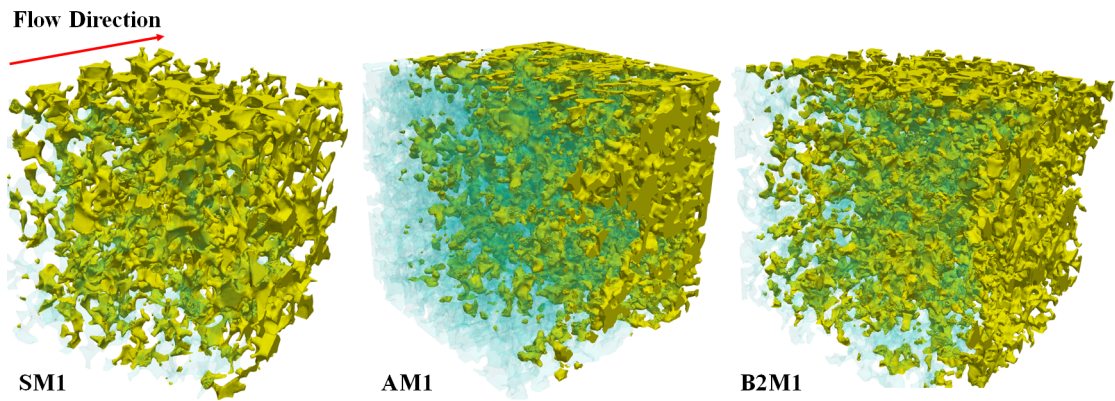


Figure 4.15: A 3D visualisation for the oil residuals for Cases SM1, AM1 and B2M1 at time = 0.05 secs

trapped. Moreover, the 3D representation in Fig. 4.15 captures a snapshot of the oil clusters at an early stage (time = 0.05 secs) and it is absolutely clear that for the S1 and B2 tight porous media, the water phase behaviour is quite different. This could be assumed to be because they share a similar porosity and hence, may behave the same during the oil drainage process.

The simulation results show that the (inlet/outlet Velocity) boundary condition for velocity at the outlet allows the connected clusters of the water phase to exit the domain. This implies that the residual water phase saturation will be decreased to a lower value given sufficient time. The results in Fig. 4.15 and Fig. 4.6 indicate that the flow is not dominated by capillary fingering as the capillary number decreases. The scan sizes used in this study have been found to be not big enough to sample a sufficient number of capillary fingers and thus, obtain representative results for cases of low capillary numbers. In fact, in all the presented cases the water front characteristics were obtained using the middle cross section slice. Using the cross section results, as seen in the previous section, a wide range of water and oil behaviour based on wetting conditions, porosity value and injection rate has been shown.

It is important to mention that using the link between the 3D representation and the saturation and permeability curves, provides a better understanding of the oil transportation behaviour during the drainage process. Moreover, using the 2D slices from the water and oil representation was found to be helpful for analysing trapped oil cluster behaviour. Further, the developed solver using the adaptive compression scheme was able to predict the microscopic transport behaviour for the oil clusters, as well as the injection water behaviour. The direct link made using the developed solver between the microscopic behaviour using the interface tracking method and the

macroscopic calculation for the permeability is a major contribution of the research. The results presented work in this chapter were extended to include two test cases for secondary oil drainage behaviour. Appendix A.4 touches very briefly on oil flow behaviour in the presence of water during the secondary water injection process.

4.4.4 Effect of Surface Tension on Oil Drainage Behaviour

This subsection considers very briefly the the effect of different surface tension on the oil drainage process. when comparing Case BM1 and Case BM5 (case setups provided in Table 4.3), Fig. 4.16 show the effect of varying the curve tension on the process saturation curves and the permeability calculations. As seen in the saturation curves in Fig. 4.16a and Fig. 4.16b, no major change was noticed between the two plots in terms of saturation or capillary pressure. However, looking at the permeability curves, it can be seen that there is a change in the water permeability curve for Case BM5. The calculated change in the permeability in Case BM5 compared to BM1, shows a change in the water phase behaviour during saturation process, which leads to less permeability in this case.

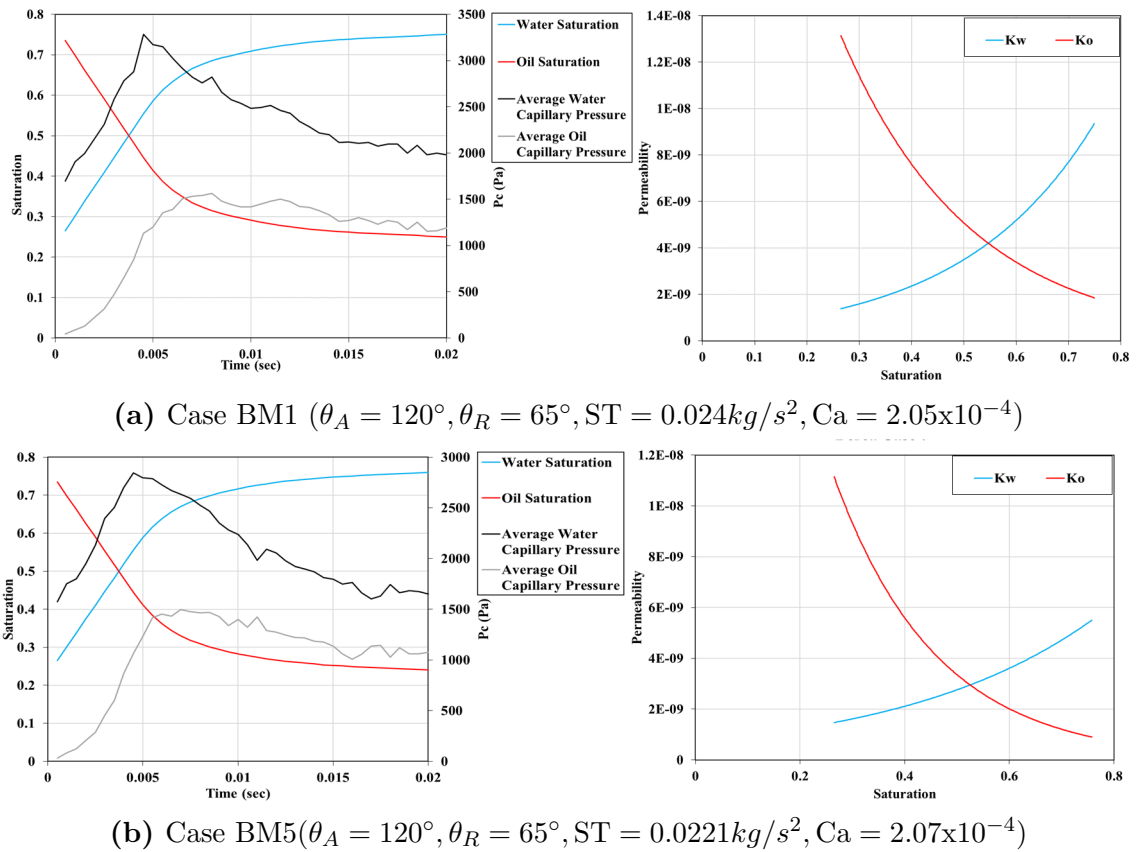
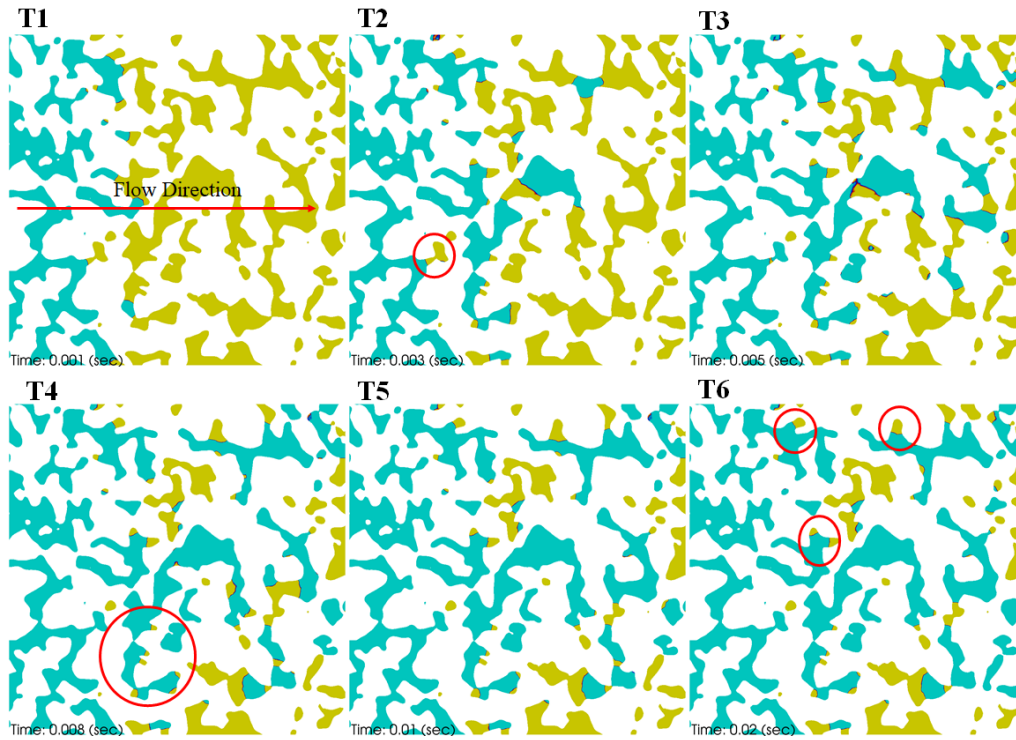


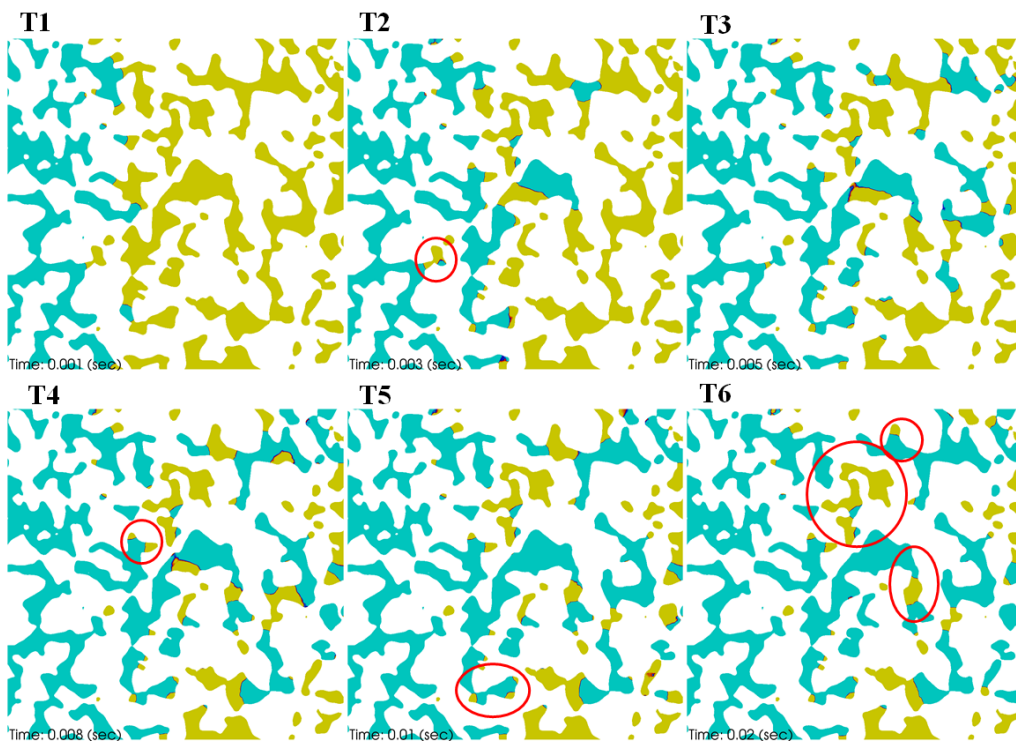
Figure 4.16: Plots of the capillary pressure and saturation curves for both phases and the computed effective permeability curves, showing the effect of varying porosity between Cases BM1 and BM5

Reflecting the permeability prediction on Fig. 4.17, it can be that in some locations the trapped clusters blocked the water paths to the outlet. Whilst it will be difficult to trace the exact location of the trapped clusters from the 2D slice by analysing the 3D images for the porous structure, it is noticed that some blockage is found in the Y-direction. This observation leads to the recognition of the importance of surface tension

forces when it comes to trapped oil cluster transport. As can be seen, by decreasing the surface tension value in case BM5, the overall percentage for the oil removal was not affective, whilst the water phase capillary pressure decreased due to a decrease in surface tension forces per unit area.



(a) Case BM1 ($\theta_A = 120^\circ, \theta_R = 65^\circ, ST = 0.024kg/s^2, Ca = 2.05 \times 10^{-3}$)



(b) Case BM2 ($\theta_A = 31^\circ, \theta_R = 31^\circ, ST = 0.0221kg/s^2, Ca = 2.07 \times 10^{-3}$)

Figure 4.17: Cross section showing the water phase in blue and oil phase in yellow, when comparing Cases BM1 and BM5

4.5 Concluding Remarks

In this chapter, two-phase flow simulations of micro-CT reconstructed porous media have been presented. A numerical framework relating the forces controlling the flow at the pore scale to obtain a better understanding of the Darcy-scale pressure drops in relation to different wetting conditions has been provided. Moreover, the effect of the capillary number was studied by comparing the simulation results for different inlet injection flow rates, which reflect different capillary numbers for each porous media. The pressure drop in each individual phase was computed to define the rate of viscous dissipation of energy in each phase. Using this framework, it was possible to characterize the permeability. Moreover, the effect of the capillary number on the trapped oil phase as well as that on wettability and porosity on oil cluster sizes have been elicited.

The numerical results presented in this chapter for modelling two-phase flow simulations on reconstructed porous media show that the trapping oil cluster can be characterised based on the imposed wetting conditions. Based on this approach, by imposing different wetting conditions, the trapped cluster illustrated various across the porous. When the size of the trapped droplet is large, the effect of imposed contact angle was illustrated showing the oil behaviour during drainage process. In some situations, the oil droplets are seen to decrease in size by going through the narrower throats and then breaking into smaller droplets due to an insufficient pressure gradient. In fact, the oil droplet size has emerged as decreasing until the capillary pressure field is able to oppose the dynamic pressure gradient force.

Further work is needed to quantify the role played by three phase flow in confined porous media. That is, future work could be directed at studying fluid tracking methods in more than two fluids, which will pose a big numerical challenge. However understanding the effect of a third phase on oil and gas transport is very important. Also, it is considered that illustrated results in this chapter can be used as a starting point to the next step research regarding two-phase flow transport under different thermal effects, which play important role in changing viscosity and wettability.

Chapter 5

Drop Impact on Micro-CT Porous Media

5.1 Introduction

Micro-scale fluid phenomena are involved in various applications and research areas [38]. Understanding the behaviour of droplet spreading on porous media is important for a variety of industrial applications, such as ink jet printing, raindrops on textiles, spray paint on wood, penetration of raindrops into building walls, needleless injections, the coating of porous materials, irrigation, among many others. Droplet spreading on solid flat surfaces has been the subject of numerous experimental and numerical studies over the last few decades [144, 145]. However, droplet impact on porous media is still far from being understood. Studies of such micro-scale fluid phenomena need careful and combined consideration of droplet dynamics and porous media characteristics.

Generally, this phenomenon is controlled by two main counter-acting processes: droplet spreading on porous surfaces and imbibition inside the porous media [10]. As the droplet spreads onto the surface it also fills the voids of the porous material due to capillary action. The spreading behaviour of the impinging droplet on the surface is known to depend on the liquid properties, i.e. density, viscosity and surface tension as well as impact conditions, such as droplet size, impact velocity, and surface wettability [146]. Absorption, on the other hand, is governed by both, the liquid and the porous medium properties, including porosity, pore size and pore wettability [37].

In recent studies, it had been identified that the spreading of impacting droplets on a porous medium is influenced by hydrophobic dynamic contact angles (i.e. hydrophobic wetting conditions), in particular the hydrophobicity of the porous surface limits the droplet in a maximum spreading condition [11]. Given the difficulty of visualising the status of a liquid within porous media, the absorption of impacting droplet has been rarely studied with regards to real complex porous media.

Different experimental methods have been used in visualising the absorption process inside porous media have been used to observe directly the liquid content redistribution within [10]. Absorption in porous media has been studied with several non-destructive techniques, including X-rays, neutron and gamma-ray radiography, magnetic resonance imaging (MRI) and nuclear magnetic resonance.

Most of the experimental studies have been focused on depleting droplets, as discussed by [147], where the contact radius variation during droplet absorption is modelled. Also, Clarke et al. [45] determined the absorption of deposited droplets into microporous filter membranes was determined by measuring the volume of deposited

droplet remaining on the surface. An analytical model based on the the Lucas-Washburn equation was proposed, assuming only vertical liquid uptake and using constant permeability. However, several experimental studies have shown that droplet absorption does not follow Washburns law for liquid uptake in granular media [148, 149]. The absorption process of an impinging droplet has been fully characterised in [10] from spreading to evaporation in terms of absorbed mass during droplet depletion and moisture for three different natural stones. Lee et al. [11] reported that the drop base reaches its maximum quickly in the first step and then shrinks in the second. Also, Lee et al. [11] stated that the contact line pins at maximum spreading on the porous stone, which determines the liquid contact area on the porous structure.

Droplet spreading on simplified shapes representing porous structures has been investigated using numerical methods in a limited number of studies [24, 150]. Moreover, a limited number of CFD studies have been published in the literature regarding the effect of porous media heterogeneity on imbibition using explicit porous geometry. In Davis and Hocking [151], models were developed to study the time evolution of drop spreading, the position of the contact line and liquid motion using a pore network model. In [152], three-dimensional simulations were carried out to study the effect of impact velocity and surface roughness. The spreading of droplets shown in [152] when deposited onto a substrate consisting of randomly placed and orientated freely penetrating disks using the lattice-Boltzmann method. The same methodology was used in [153] to simulate pore-level droplet spreading on a porous surface and to investigate the power law time evolution of the wetted zone radius.

The aim of this chapter is to study numerically the characteristics of a droplet interacting with a real porous surface, using the 3D porous media described in Chapter 4. A direct comparison of simulation versus experimental results found in [11] is presented. Finally, an investigation of the time evolution of impinging droplet shape as well as the velocity on two different porous media is presented. The effects of wettability and surface tension are probed, with the purpose of understanding the spreading and penetration behaviour for single and multiple droplets.

5.2 Case Setup

Three-dimensional simulations for droplet impacting and penetrating porous media are examined in this chapter. The computational domain and the grid are shown in Fig. 5.1, whilst the applied boundary conditions are shown in Fig. 5.3. The grid representation in Fig. 5.1 and 5.2 shows the complexity of the mesh refinement needed to capture the complex porous features. Moreover, Fig. 5.2 presents the hybrid mesh constructed to join the porous structure mesh and the box mesh regions together. The initial conditions for the simulated geometry are illustrated in Fig. 5.3, while the material properties and the initial conditions for the impacting liquid (water) are summarised in Table 5.1.

Different values for the wetting conditions are illustrated in Tables 5.1, 5.2 and 5.3, where different numerical simulations were performed to show the influence of wetting on spreading behaviour using two different porous media. The initial droplet radius has been varied between 0.5 and 1.6 mm. For the initialisation process, a set field was used at the first time step to set a spherical liquid drop inside the numerical domain to place the liquid phase on top of the porous surface.

Two different porous media were used to show the effect of porosity and porous structure influence on spreading and absorption, as mentioned in the previous section. Berea sandstone and carbonate porous media with porosity of 18.5% and 23.3 % were reconstructed using the same method described in Section 4.2. Each porous domain was linked to an upper box, as shown in Fig. 5.2, which contained the droplet set field at the middle of the domain.

5.2.1 Numerical Setup

The numerical setup for the two different porous domains is shown in Fig. 5.3 (a). For the porous structure and for the wall surface on top of the porous media, the dynamic Kistler boundary conditions (KBC) were used. The Kistler model, as explained in

Table 5.1: Properties of water droplets and impact conditions for the drop test

	$\rho(Kg/m^3)$	$\mu(Kg/ms)$	$\sigma(N/m)$	
Water Properties at 25 deg C	998	0.001	0.07 – 0.05	
	$R_0(mm)$	$V_i(m/s)$	We	Re
Impact conditions	0.5 – 1.6	0.5 – 1	10 – 20	498 – 1000

Chapter 1, can be used to determine the dynamic contact angle. The Hoffman function, f_{Hof} , as $\theta_{dyn} = f_{Hof}[Ca + f_{Hof}^{-1}(\theta_e)]$, where θ_e is the equilibrium contact angle and Ca the capillary number calculated based on an spreading velocity was utilised. For the interface that connects porous voids and the box domain, an interior conformal interface was used, as shown in the zoom in Fig. 5.2. A fixed value pressure and mixed type boundary condition (pressure-Inlet-Outlet) for the velocity was used as a boundary condition at the top of the domain box, as shown in Fig. 5.3 (b), to represent the open atmospheric conditions. While a zero-gradient boundary condition for the pressure for the rest of the porous media domain were used, as shown in Fig. 5.3 (c), representing a solid wall.

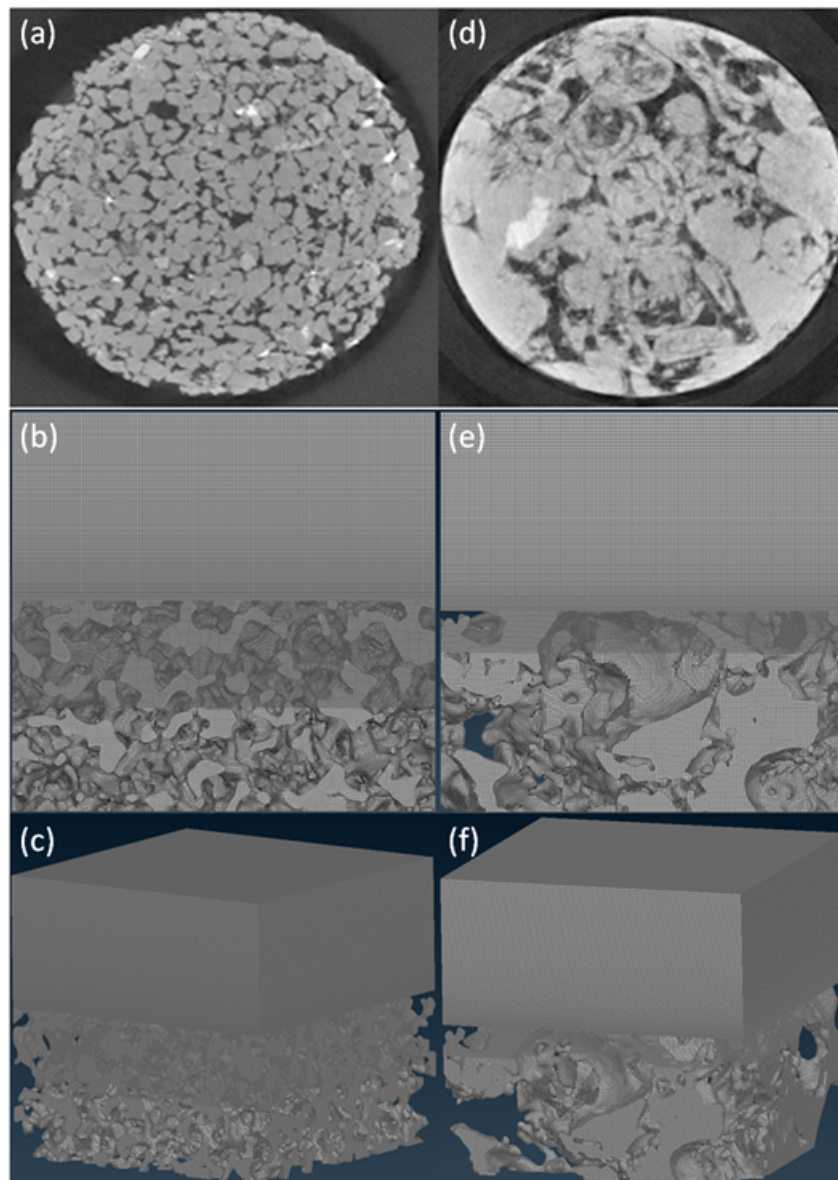


Figure 5.1: Numerical model for Berea and carbonate porous media. (a and d) represent the original Mico CT for the two different porous media [9]; (b and c) represent the computational mesh for the Berea sandstone; (e and f) represent the carbonate

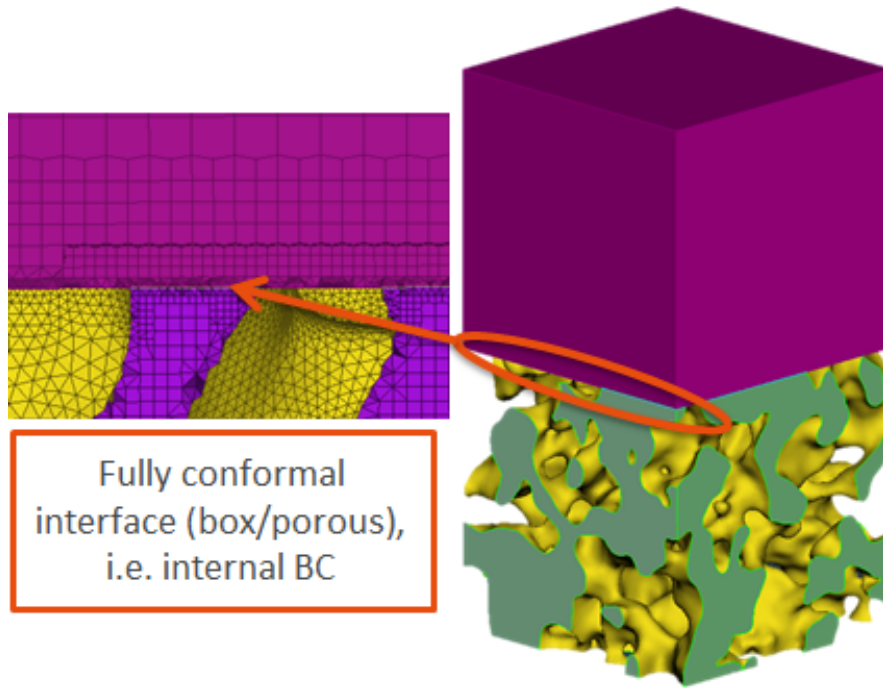


Figure 5.2: Representation of hybrid grid transformation from conformal mesh (at the box region) to conformal Hexa denominated mesh (at the porous region)

The developed solver *interPore* was used to track the droplet interface during the spreading and penetration event. All the numerical schemes setup is similar to T-junction test case presented in Chapter 3. Various wetting boundary conditions were used during this study to characterise the relation between spreading and penetration, with Table 5.3 summarising the conditions used, which contained two sets of dynamic contact angles imposed independently. The surface contact angle (SCA) was imposed on the solid surface of the porous medium, while the second set of contact angles was imposed inside the porous medium to the pores all namely (Pore contact angle (PCA)). The SCA was applied to two sets of dynamic wetting conditions to simulate hydrophilic and hydroponic surface spreading. While the PCA was allocated a range of

Table 5.2: Properties of porous stones and mesh quality

	Berea	carbonate
Average Porosity	18.5%	23.3%
Average Pore Size (microns)	45.9	73.1
Max aspect ratio	11.9796	7.54027
Number of cells	5689735	3777008
Max non-orthogonality (degrees)	78.2862	76.1127
Max Element length (meters)	$1e^{-4}$	$9e^{-5}$
Max skewness	11.024	11.4674

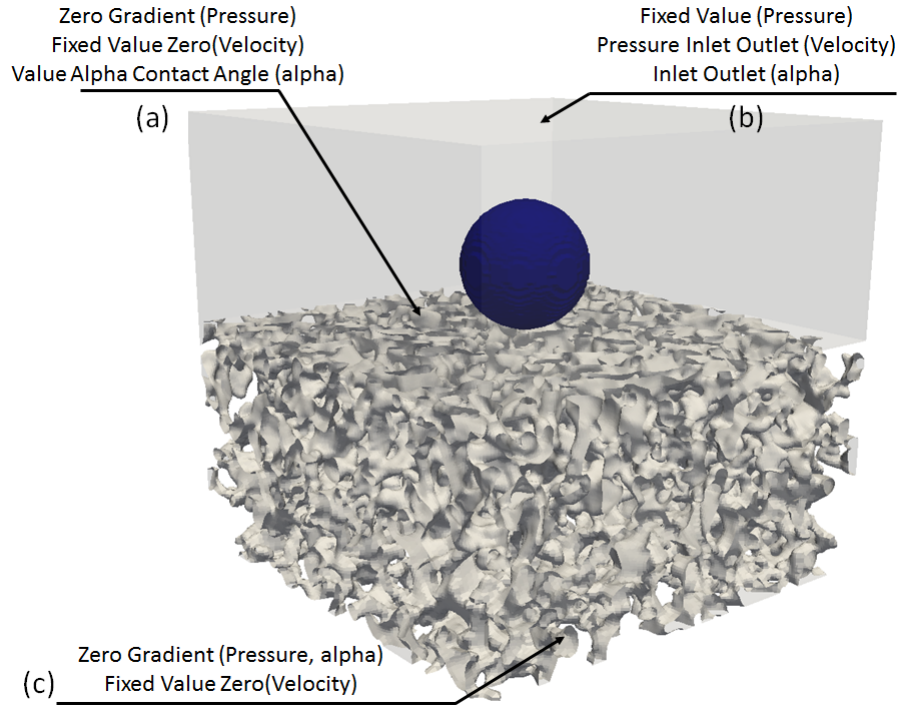


Figure 5.3: Three-dimensional computational domain, mesh and boundary conditions

values, as shown in Table 5.3, to simulate the wetting capillary effect due to constant and dynamic wetting conditions.

Table 5.3: Imposed contact angle for a porous media surface (using the Kistler dynamic contact angle model) with different assumptions concerning the contact angle of the pore surfaces (varying from fully hydrophilic to fully hydrophobic) at an impact velocity of 0.5 m/s and droplet radius of $R = 1$ mm

Case	Surface contact angle	Pore contact angle
Case 1	$\theta_A = 125^\circ, \theta_R = 25^\circ$	$\theta_A = 125^\circ, \theta_R = 25^\circ$
Case 2	$\theta_A = 125^\circ, \theta_R = 25^\circ$	$\theta_{eq} = 0^\circ$
Case 3	$\theta_A = 125^\circ, \theta_R = 25^\circ$	$\theta_{eq} = 180^\circ$
Case 4	$\theta_A = 60^\circ, \theta_R = 22^\circ$	$\theta_A = 60^\circ, \theta_R = 22^\circ$
Case 5	$\theta_A = 60^\circ, \theta_R = 22^\circ$	$\theta_{eq} = 0^\circ$
Case 6	$\theta_A = 60^\circ, \theta_R = 22^\circ$	$\theta_{eq} = 180^\circ$
Case 7	$\theta_A = 125^\circ, \theta_R = 25^\circ$	$\theta_A = 60^\circ, \theta_R = 22^\circ$

Water droplet properties are presented in Table 5.1, illustrating the different initial droplet radii and surface tensions being used in this study. Impact conditions are also listed in Table 5.1 showing the range of the impact velocity used as well as the Weber and Reynolds numbers. Later in this chapter, the research will be extended to include five more cases presenting different ranges of velocity and droplet sizes, as shown in Table 5.4.

In the next section, the described setup will be used for all the cases. First, the

numerical setup will be validated by comparing it to a similar experimental setup. Then, it will be used to test a wide range of wetting conditions, droplet sizes and the impacted velocity effect.

5.3 Results and Discussion

The following sections will present the numerical simulation results for a wide range of cases. First, a validation test case will be presented showing the characteristic trend of droplet spreading over porous media and this spreading trend will be compared to experimental data. Then, the influence of porous wettability on spreading dynamics using two different porous media is investigated. Also, the droplet penetration and the effect of wettability on the inertial spreading and viscous spreading stages are discussed. In the validation subsection, the code is compared with the standard VoF based solver of OpenFOAM *interFoam*.

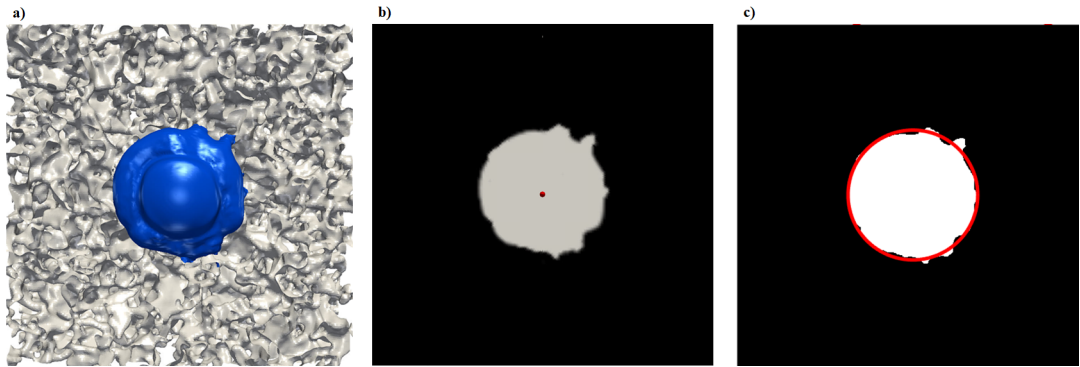


Figure 5.4: 3D simulated profile (a), 2D Top plan-view profile (b) and Calculated spreading radius (r) in red (c)

Due to the irregular spreading on the porous surface, the droplet radius at the time of impact was measured using the average radius based on the best fitted circle. The fitting circle was calculated based on the water wetting outside the porous structures during the spreading event using the water volume fraction (α). The topographical irregularity, this induce in an asymmetrical spreading and absorption profile. Rather than using the spreading diameter of the droplet, an interpretation of the plan view surface spreading was preferred. The interpreted spreading diameter was calculated at a planar located at the surface of the porous media. The locations were then closed by a series of third order polynomials and integration about the local axes of the discretised closed shape yielded the wetted area. Figure 5.4 summarise the stages required to calculate the spreading diameter. In Fig. 5.4-a, a representation of the droplet iso-surface can be seen, while in Fig. 5.4-b, the wetted area (in grey) just above the porous structures is presented. Finally, the approximated droplet diameter calculated using the average wetting surface profiles is presented in Fig. 5.4-c.

in order to study the relation between droplet spreading and penetration the volume

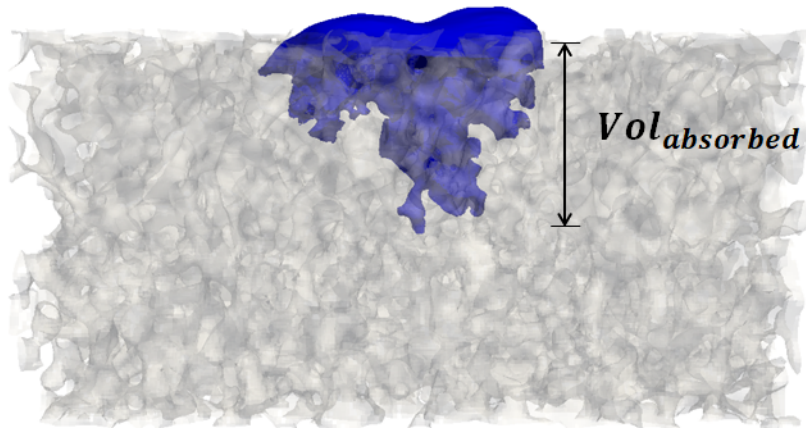


Figure 5.5: Droplet penetration Iso- surface

of fluid absorbed into the porous structure below the nominal surface was calculated, as seen in Fig. 5.5. Since the porous fluid paths found in the presented porous materials are not systematic, the droplet flow into this path will be difficult to trace. Moreover, based on the penetration, the droplet tend to spread in different ways based on the wetting conditions and the porous topology.

5.3.1 Validation of the Numerical Method

The test case used to validate the numerical model is of a droplet impacting on Berea sandstone with an impact velocity of $V_i = 1m/s$ ($We = 20$, $Re = 1000$). The porosity of the sandstone is 18.5%. The numerical simulation is compared against experiments reported in [10, 11]. To validate the numerical solver results, the experimental porous media, namely Meule [10], with an average porosity of 16.6% was used. Despite the numerical and the experimental porous material not sharing the same porous structures, they share similar average porosity. By comparing the droplet spreading trend to the experimental results, the numerical accuracy of the developed solver can be measured.

Depending on how close the numerical predictions are, conclusions can be extracted regarding the evolution of the relation between spreading and penetration. It should be noted that care must be taken when modelling the wetting conditions, as they may dominate the spreading behaviour. In order to guarantee that the numerical and experimental model has the same wetting behaviour, the reported contact angles by Lee et al. [11] were used. The reported advancing and receding contact angles are (125° and 25°), respectively, these being used as initial conditions for the imposed Kistler wetting model. Figure 5.6 shows the normalised time evolution (t/τ), where t is the time and τ is defined as the inertial time scale of the first stage of wetting, where $\tau = \left(\frac{\rho R^3}{\sigma}\right)^{0.5}$, as defined by Biance et al. [154].

Moreover, the droplet spreading normalised radius (r/R) was used in the same figure, where R is the initial droplet radius, and r is the calculated droplet radius over the porous media during spreading, based on the method shown in Fig. 5.4. As mentioned in the previous section, the spreading radius r over the porous media was found to be irregular compared to the normal droplet spreading over a flat surface (not a perfect circular shape). To determine the spreading radius r , the numerical results were used to calculate the wetted area of the irregular spreading shape, and the equivalent radius based on the centre of gravity was extracted, as mentioned in Fig. 5.4-c.

As shown in Fig. 5.6, the spreading behaviour between $t/\tau = 0$ to approximately 0.4 found to be increasing. It was reported by Lee et al. [155] that the droplet diameter will increase reaching to a maximum spreading value, known as the spreading phase and then, it stabilises. Whilst for the first phase the same increase is noticed for the droplet spreading over solid surfaces, the second phase is different when it comes to

porous media. For, when a droplet impacts on a porous medium, its diameter remains almost constant, thus implying that the imbibition phase has started (for this case at $(t/\tau)=0.6$) [155]. Compared to the droplet impacting on a solid surface (as shown in Appendix A.2) the spreading diameter usually decreases during the second phase, which is referred to as the recoiling phase. These phases were well captured by the newly developed solver, while the standard one failed to predict the correct transition to the imbibition phase. That is, it overpredicted the spreading, as seen in Fig. 5.6-a and Fig. 5.6-c. Also, it can be seen that for the imbibition phase the developed solver has a very close match with the experiments.

Finally, it was observed that, for the spreading phase there are some differences between the experimental and numerical curve, which indicates a slower spreading process of the droplet of the numerical model in comparison to the experimental one. This can potentially indicate that average pore size might not be enough to describe the spreading process and more information for the pore distribution is necessary. However, it was anticipated from the beginning that the numerical results and the experimental results would not be exactly the same due to the difference in the porous structures used. Using the Kistler boundary condition is a key element to capturing the correct physical behaviour for the droplet spreading. Nevertheless, when imposing this boundary condition to the standard solver *interFoam*, an overestimation for the spreading was noticed. The reason comes from the incorrectly calculated contact line velocity during the inertial phase caused by the parasitic currents. The overestimated spreading is not reflected in the simulation using the modified solver due to the parasitic current filter used, as presented in Chapter 2. Based on the [154] theoretical power-law (r/R) as $\frac{r}{R} = 0.8(\frac{t}{\tau})^{0.5}$ was plotted. However, it failed to estimate the correct spreading behaviour due to the unaccounted for influence of the porous structure and wettability effect.

According to the proposed experiment in Fig. 5.6-a the droplet diameter remained constant after reaching its maximum value, showing droplet pinning behaviour at the maximum spreading (or by the end of inertia phase). The same trend was achieved using the modified solver regardless of the different porous structure effects, while the standard solver *interFoam* failed to predict the pinning behaviour. Also, it is noticed that standard solver predicted much higher contact line velocities, which led to a substantial increase in the droplet size (around the rim), which not allow the surface tension to overcome inertia and this is why no pinning was seen. Figure 5.6-b

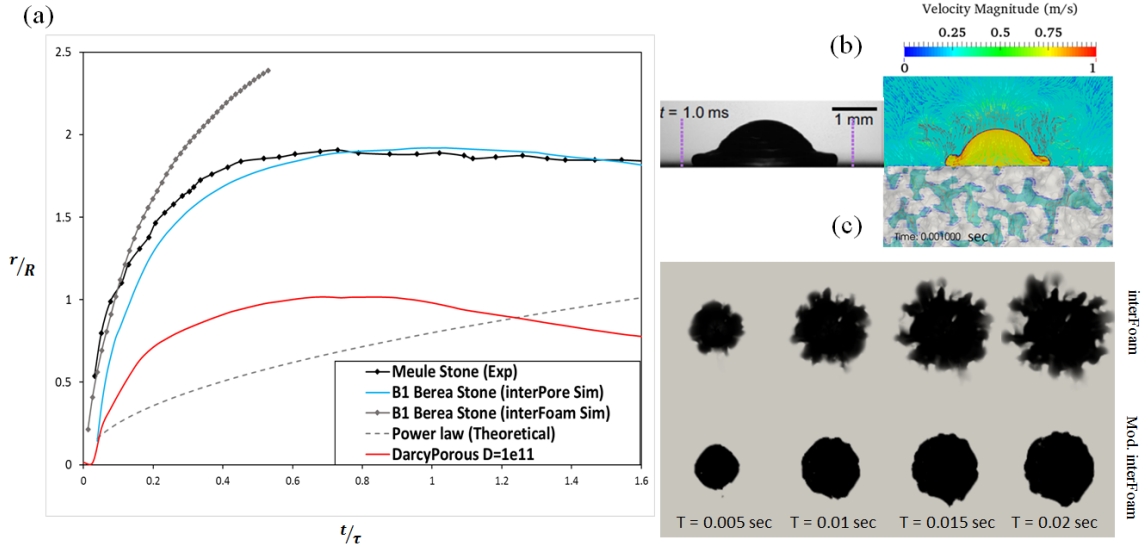


Figure 5.6: Comparison of droplet impacts for $D_0 = 2.0\text{mm}$ and $V_i = 1.0\text{m/s}$ on Berea stone (numerical) and Meule stone (experimental). (a) is a normalised wetted zone width r/R evolution for water droplets at $We = 28.5$. Developed solver at wetting conditions of $\theta_A = 125^\circ$ and $\theta_R = 25^\circ$ at the porous surface and porous media; standard solver *interFoam* at the same wetting conditions for the porous surface and porous media; the plot also includes the spreading predictions using the Darcy simulation and power law. (b) snapshots of droplet impact on porous materials at time = 1 ms. (c) droplet spreading using the developed and standard codes

illustrates a direct comparison between simulation and experiment for a given time step at 1 ms. It is evident that a good qualitative agreement has been achieved between the developed numerical model and experimental results.

Also, the numerical Darcy model using the two phase flow solver *interFoam* was compared, as shown in Fig. 5.6-a. As can be seen, the Darcy model under predicted the spreading behaviour during the droplet impacting on the implicit porous media. However, a similar spreading trend was achieved during the first spreading phase. Nevertheless, two major problems were found when modelling spreading using the Darcy models, first, the standard Darcy model implementation does not offer the the ability to impose a wettability effect on the porous domain. This means that the sink term in the Darcy model should include an extra amount of energy dissipation during spreading in order to model the effect of wettability. Second, the Darcy model does not offer a direct method for modelling the irregularity presented by actual porous structures, as for all the spreading behaviour is considered to be symmetrically distributed. Due to these two factors, the curve prediction using the Darcy model failed to describe accurately the spreading behaviour during the droplet impacting. Moreover, whilst Reis et al. [25] developed a method based on the Darcy model to predict spreading, it lacks the effect of dynamic wetting conditions in characterising the spreading behaviour.

5.3.2 Influence of Porous Wettability on Droplet Spreading

This subsection discusses the effect of changing the wetting conditions for a porous surface and the porous core using a constant droplet radius and a constant impact velocity. First, the wetting effect on spreading is examined. In Table 5.3, the wetting conditions imposed on the surface and porous media are reported in order to demonstrate the effect of droplet spreading while penetrating porous media at different conditions. The demonstrated conditions in Table 5.3 can predict a wide range of wetting behaviours, which can be used, for example, to understand the coating effect inside porous structures. In some applications, pore coating is very important, as it can be used to alter the spreading patterns. The numerical test was performed on two different porous media, which presented two different porosities and internal porous structures. Reis et al. [25] showed in his research that as the porosity of the porous media increases, the liquid tends to penetrate more, and the spread ratio outside of the porous media decreases. Increasing the porosity decreases the capillary pressure, lowering the force that pulls the liquid into the pores. However, in this subsection the relation between spreading and the dynamic contact angle imposed on the porous walls is investigated in order to establish a link between porosity, spreading and imposed wetting conditions. In this subsection, different wetting effects due to droplet properties or surface properties are not considered.

As listed in Table 5.3, three case setups (from 1 to 3) were used to demonstrate the effect of various types of wetting conditions inside the porous material on a non-wetting surface using the dynamic wetting condition. A second three case setups (from 4 to 6) were deployed to demonstrate the effect of various types of wetting conditions inside the porous material on a wetting surface using the dynamic wetting condition. For Case number 7, a hydrophobic dynamic contact angle was imposed on the porous surface, while a hydrophilic dynamic contact angle was imposed inside the porous media to demonstrate the effect of a mixed wetting condition on spreading and penetration behaviour. The aforementioned case setups were simulated in two different porous media, as presented in the previous section. In the rest of this subsection, 14 simulations results will be presented accordingly.

Focusing first on the low porosity value Berea Sandstone, Fig. 5.7 demonstrates the droplet profile at an early stage ($t=0.0025s$). As seen in Fig. 5.7 Cases 1 to 3, similar shapes have been formed mainly after the impact, yet Case 2 shows a higher penetration

compared to Cases 1 and 3. In Case 4 to 6, three different shapes were formed at the same time step with a higher fluid penetration except for Case number 6. Due to the case setup, the first three Cases (from 1 to 3) achieved less spreading compared to Cases 4 to 6. However, the similarity demonstrated between Cases 3 and 6 regarding the shape of the liquid portion going down the porous media was not expected, as more surface spreading should allow for an increase in liquid penetration. It can be seen that Cases 2 and 5 share similar a velocity vector field near the droplet cap outside the porous media, even though they do not share the same imposed surface wetting conditions, which demonstrates a direct influence of the porous side on the droplet outside the porous media.

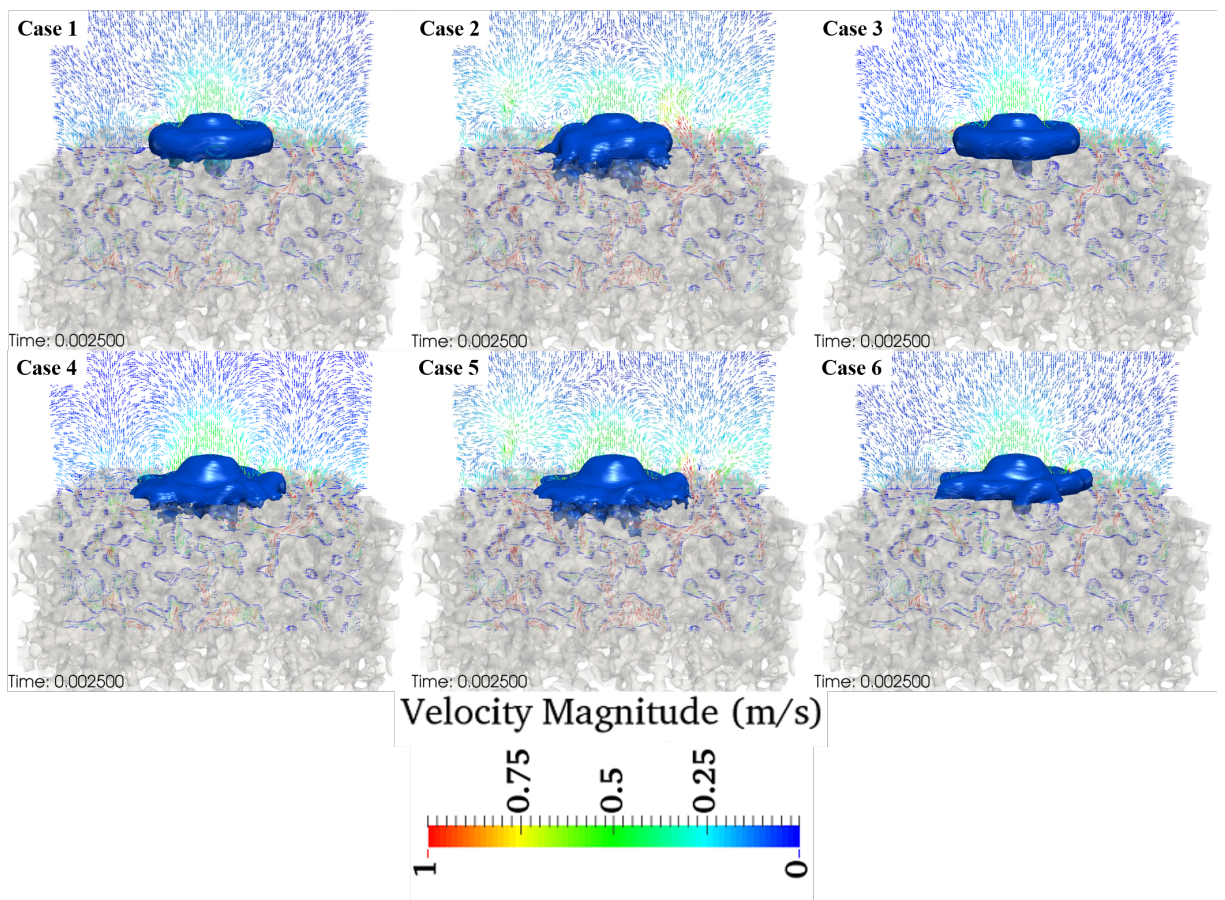


Figure 5.7: Early stage snapshot of the droplet spreading and penetration for Berea porous media at $T = 0.0025s$. A velocity vector field is plotted on a slice passing by the middle of the porous structure. A constant impact velocity of 0.5 m/s and an initial droplet radius of 1 mm was used to simulate the influence of the contact angle presented in Table 5.3

Reflecting the results from Fig. 5.7 on the droplet spreading presented in Fig. 5.8, which demonstrate the spreading behaviour on the porous media surface, it is clear that the imposed contact angle on the surface represented the primary influence on spreading. In Fig. 5.8 the spreading for the first three cases made a group showing the same low spreading factor (r/R), while the second set of three cases made a different

group with a higher spreading factor. Using the low porosity porous material, Fig. 5.8 reveals interesting behaviour: changing the wetting conditions of the porous media from a high hydrophilic surface to high hydrophobic one has a minimum influence on the spreading trend. However, some changes in the spreading behaviour can be seen for Cases (4 to 6), where the penetration at the early stage was instant, especially in Case 6. The high spreading for Cases (4 to 6) also shows+ an increase in spreading with time, which is due to the lack of a pinning effect, especially with Case 6, as the penetrating fluid helps in the spreading.

Considering Case 7, which combines the hydrophilic effect at the surface using the dynamic and hydrophilic wettings effect at the porous side, a higher spreading factor compared to Cases (1 to 3) can be observed. The reasons for this can be attributed to the influence of the imposed dynamic wetting condition, which introduces a lower capillary effect that helps spreading in the horizontal direction rather than vertically, as seen in Case 2.

One extra comparison was made between the experimental results from droplets impacting on Savonnieres rock [10, 11] and Berea Rock with the simulations in Fig. 5.8. Unfortunately, it was difficult to compare the Berea simulation results with similar porosity value rock to validate the spreading trend. However, by comparing the simulations with the Savonnieres rock (that carries porosity of 26.6%) it was found that the simulation results were able to predict the correct spreading trend. Nevertheless (as expected), the experimental results do not match any of the simulated impact scenarios. As seen in Fig. 5.8, the experimental spreading results were found to be in the middle between hydrophilic and hydrophobic spreading simulation ones. The experimental spreading behaviour shows that a higher porosity value porous structure may act in a similar way to a hydrophilic tight porous media.

To provide further insight into the local phenomena that drive the capillary imbibition of the droplet inside porous media, a top and a side view of the droplet when impacting on the porous structure is shown in Fig. 5.9. This figure represents the droplet behaviour (represented by the iso-surface of the droplet volume fraction at 0.5) inside and outside the porous material at different imposed dynamic contact angle, as described in the setup table. Some common features can be identified: firstly, the penetration in Cases 3 and 6 have the same trend, whereby fluid advances at the central pore and is retracted at the same time step. Secondly, a recoiling phase can be hardly observed in Cases (4 and 5), which is due to the lateral liquid penetration inside the

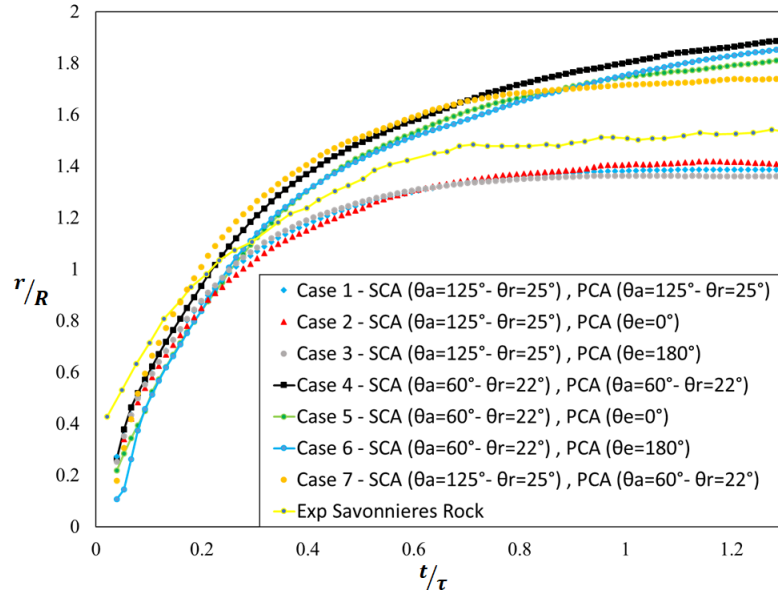


Figure 5.8: Normalised radius r/R with different surface and pore contact angles vs. normalised time t/τ Berea sandstone. A constant impact velocity of 0.5 m/s and an initial droplet radius of 1 (mm) was used to simulate the influence of the contact angle, as presented in Table 5.3. Experimental spreading curves for Savonnières rock (porosity of 26.6 %) can be found in [10, 11]

porous structures, with limited pinning behaviour at the droplet rim.

Hydrophobic conditions of the pore (i.e. Cases 1, 2 and 3) presents less liquid absorption, with a recoiling phase, yet still being characterised by pinning behaviour. Regarding the hydrophilic porous wetting, regardless of the imposed dynamic wetting conditions on the porous surface in the simulations, a limited recoiling phase is observed. However, the droplet edge is seen to undergo the same pinning with much more absorption, a behaviour that limits its spreading.

In contrast, the vertical penetration is seen in Case 7, which combines the pinning behaviour at the droplet edges and this limits the spreading while giving more liquid penetration due to the high capillary pressure for invading porous structures. In general, the hydrophobic cases (1, 2 and 3) show small liquid fingers in the initial spreading phase, which tends to recede from the pore space during the recoiling phase. While for the hydrophilic cases (4, 5, and 6), the fingering effect after the invasion and during the initial phase tends to increase over time. As a result, the droplet size decreases in the recoil phase and yet, a high average spreading factor is retained.

Moving on to the high value porosity structure (carbonate) presented in Table 5.2, the flow behaviour and penetration pattern will be investigated similar to the Berea sandstone. Comparing the high porosity model (carbonate) presented in Fig. 5.10 to the low porosity structure presented in Fig. 5.7, a high liquid penetration effect in the

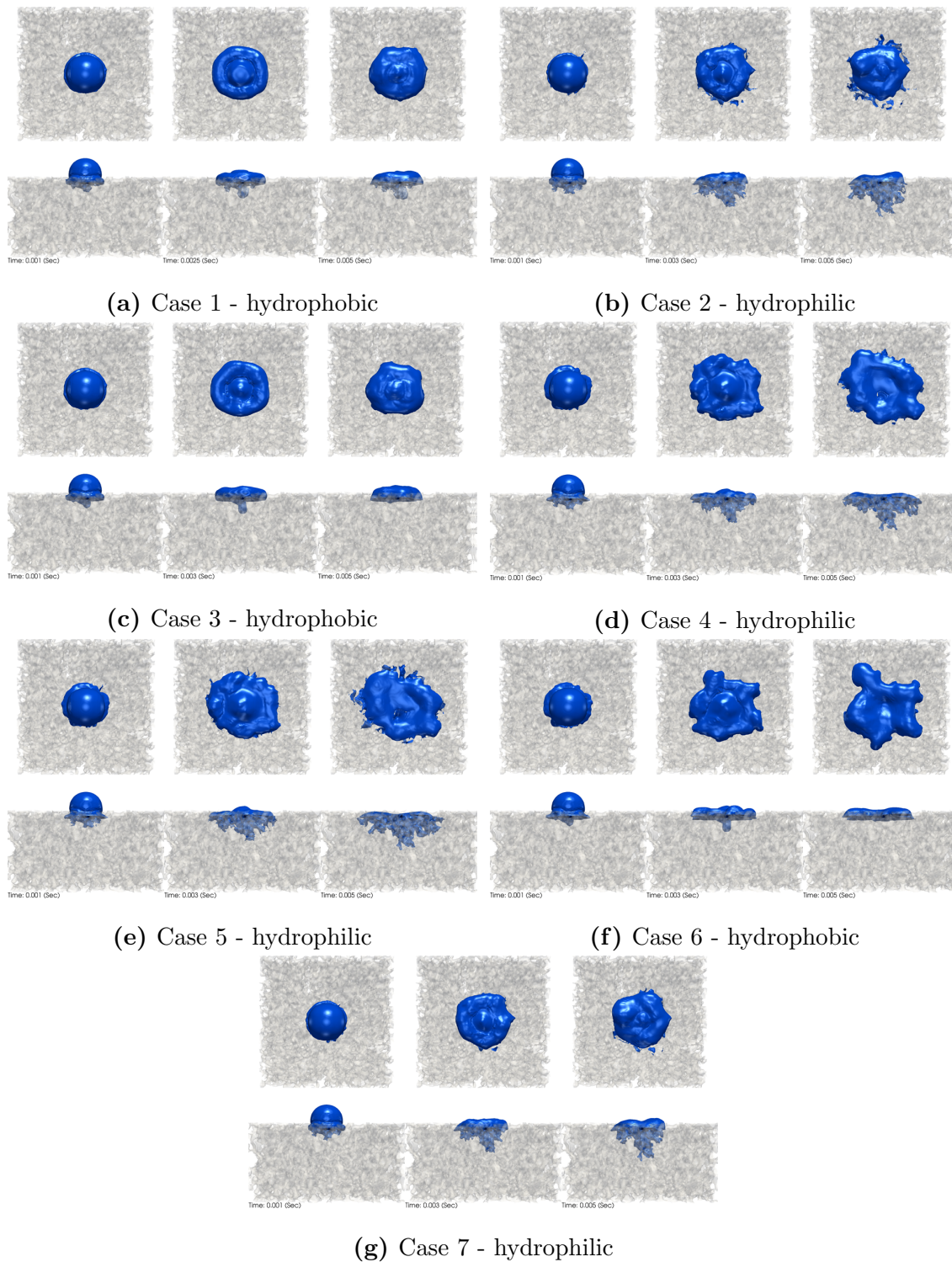


Figure 5.9: The early stage of capillary imbibition of pores after droplet impacting on solid surfaces for Berea sandstone. Seven cases are presented at different time steps using the top and side view. The figures show the wetting conditions ranges from fully hydrophobic to fully hydrophilic using alpha contour. A constant impact velocity of 0.5 m/s and an initial droplet radius of 1 mm was used to simulate the influence of the contact angle presented in Table 5.3

porous hydrophilic cases (2, 4 and 5) can be seen, while there is limited penetration in Cases 1, 3 and 6

As illustrated by the velocity field (see Fig. 5.10), a porous surface wetting condition in Cases 1, 2 and 3 limits the droplet spreading, with less velocity field around the

droplet outside the porous media limiting the penetration into the minimum. While in Cases 4 and 5 in Fig. 5.10, a higher velocity field is noticed around the droplet outside the porous media, thus indicating high capillary pressure and allowing for faster droplet penetration during spreading. In Case 6 in Fig. 5.10 the spreading is higher than in Cases 1 to 3, with there being no liquid penetration in the foremost case due to the imposed wetting condition, which happens to limit the penetration at the early impact stages. In Fig. 5.10 and 5.11, which demonstrate the spreading behaviour on the porous media surface, it is also clear that the imposed contact angle on the surface exhibits the primary influence on spreading. Yet, in contrast to the Berea sandstone the porous wetting condition is highly influential on the droplet spreading. In Fig. 5.11 the spreading for Cases 1 and 3 form a group showing the same low spreading factor (r/R). In Case 2 the lowest spreading with a retraction pattern was recorded by the end of the simulation time due to high liquid penetration. Regarding Cases 4 and 5 in Fig. 5.11, these show a higher spreading factor, due to the horizontal liquid penetration near to the porous structure. However, Case 6 shows the highest spreading due to the effect of a hydrophilic wetting condition imposed at the porous surface with the least penetration, due to the high hydrophobic wetting condition imposed at the porous media side.

It should be noted that a different behaviour is observed for Case 7 Fig. 5.11 compared to Case 7 in Fig. 5.8, where for the high porosity structure the spreading was less than expected. This behaviour is justified by looking at Fig. 5.12 Case 7 where a higher vertical penetration is limiting the spreading.

The higher porosity material shows the importance of the porous wetting condition that affects the droplet spreading dynamics at the impact early stages. Changing the wetting conditions of the porous media, from highly hydrophilic to highly hydrophobic, has a considerable influence on the spreading trend, which wasn't the case with the high porous media. Most importantly, Case 6 has limited absorption due to the imposed hydrophilic boundary condition at the pores side, which decreases the capillary pressure inside the porous media and has a direct impact on increasing the spreading. To understand the effect of penetration on spreading presented in Fig. 5.11, the penetration driven by capillary imbibition is illustrated in Fig. 5.12. Figure 5.12 show the droplet behaviour (represented by the iso-surface of a droplet volume fraction at 0.5) inside and outside the porous material using different wetting conditions as mentioned before.

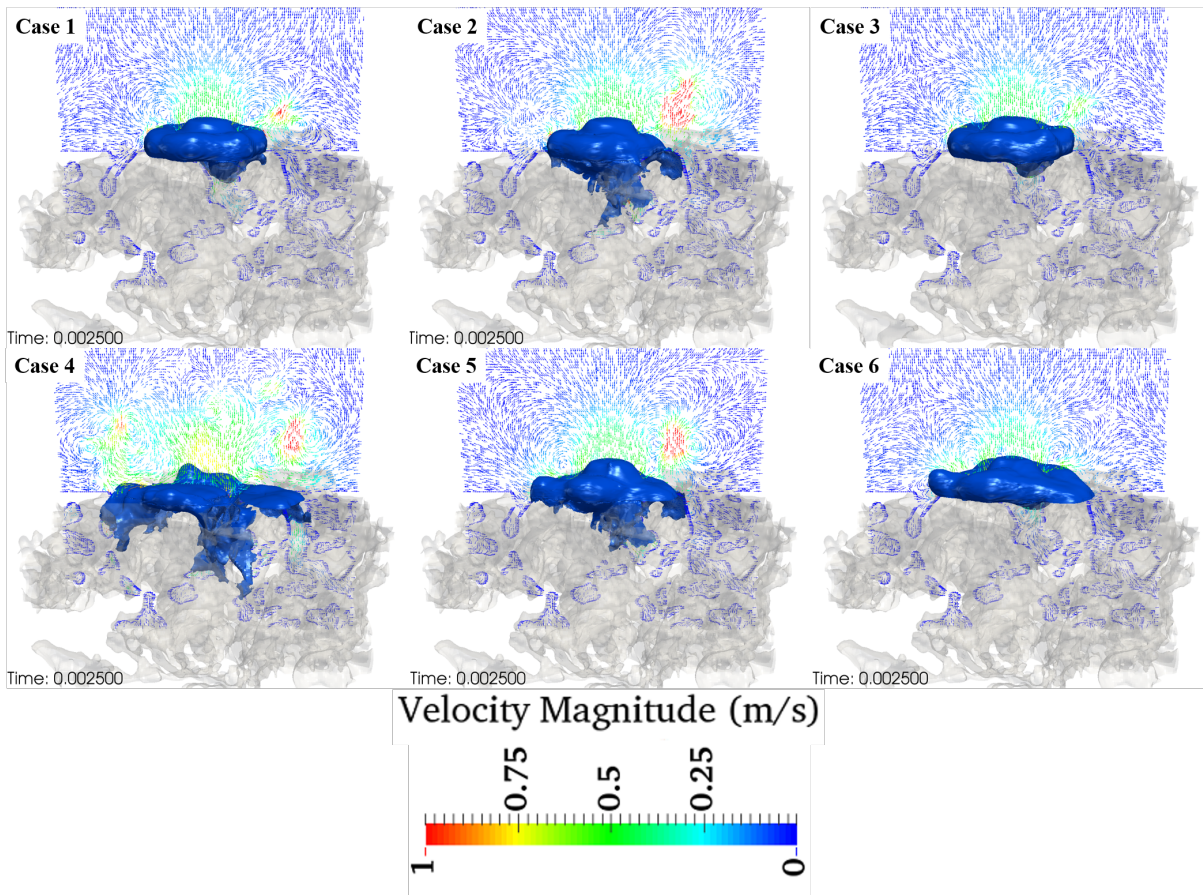


Figure 5.10: Early stage snapshot for droplet spreading and penetration for porous carbonate media at $T = 0.0025s$. A velocity vector field is plotted on a slice passing by the middle of the porous structure. A constant impact velocity of 0.5 m/s and an initial droplet radius of 1 mm were used to simulate the influence of the contact angle, as presented in Table 5.3

Comparing Fig. 5.12 to the previous representation of droplet impacting on Berea Sandstone, a general irregularity in droplet shape during spreading outside the porous structure can be seen. The irregularity is mainly influenced by liquid penetration. Focusing on Cases 1 and 3 in Fig. 5.11, a minimum penetration at the central pores due to the low capillary pressure imposed by the hydrophobic wetting boundary condition inside the porous structure is observed. The imposed wetting conditions in Cases 1 and 3 shows a recoiling behaviour combined with pinning, which helps the droplet to retract by the end of the spreading phase. The dynamic advancing behaviour in Case 1 also shows a vertical penetration while recoiling. Whilst in Case 2 a vertical penetration is noticed, which reduces the droplet spreading and also increases the vertical penetration compared to the horizontal penetration. Cases 4 and 5 in Fig. 5.12 illustrate irregular droplet shapes dependent on the penetration pattern due to the imposed wetting boundary condition.

In Case 4, a horizontal spreading pattern was achieved due to the low capillary pressure that also helped in faster horizontal imbibition compared to the vertical imbi-

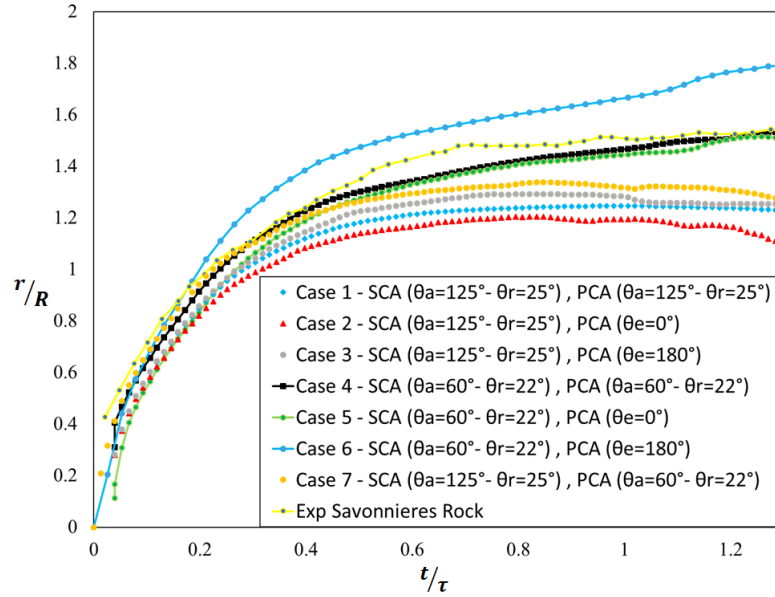


Figure 5.11: Normalised radius r/R with different surface and pore contact angles vs. normalised time t/τ for porous carbonate media . A constant impact velocity of 0.5 m/s and an initial droplet radius of 1 mm were used to simulate the influence of the contact angle, as presented in Table 5.3

bition. As a result, the droplets in Case 4 fragmentation into smaller droplets outside the porous structure, filling more pores while spreading. on the other hand, in Case 5 more vertical liquid penetration is seen by pinning at the droplet edges outside the porous structure during the recoiling phase. Case 6 Fig. 5.12 shows unexpected sliding, while spreading with minimum penetration due to the low capillary pressure. This behaviour allows for the longitudinal formation of the droplet edges while recoiling. The behaviour in Case 6 shows a strong link between the porous wetting condition (in this case highly hydrophilic) with the dynamics of spreading and the final droplet shapes, even when the droplet undergoes minimum liquid penetration. The highly vertical penetration achieved by Case 7 demonstrates the effect of limiting the spreading at the early stage of droplet impact, which is helped by the high capillary pressure to increase the liquid vertical penetration.

Comparing the numerical results with the experimental results for the Savonnières rock, as covered in the previous section, the spreading behaviour is very close to the predicted results from Cases 4 and Case 5. The hydrophilic behaviour predicted by the developed code represent the importance of the wetting model, whereby the different behaviours are predicted using the same porous topology under different wetting conditions. Also, comparison between two different rocks with similar porosity values (like the carbonate and the Savonnières rock) shows the relation between different porous rocks can be driven by two important factors: 1 - generic porosity value; and

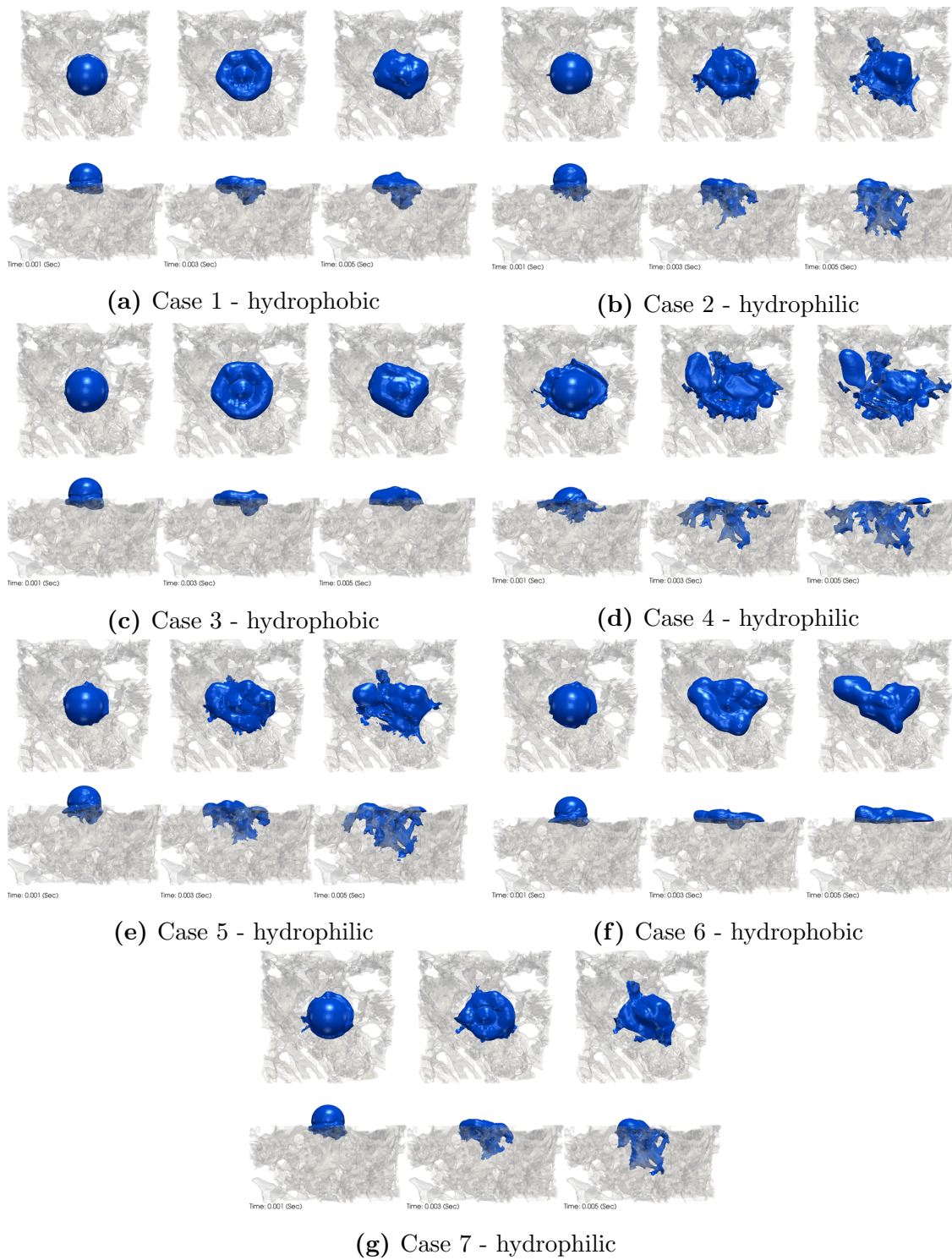


Figure 5.12: The early stage of capillary imbibition of pores after droplet impacting on solid surfaces. Four views are provided at each of five-time steps. The figures show two different wetting condition ranges from fully hydrophobic to fully hydrophilic. A constant impact velocity of 0.5 m/s and an initial droplet radius of 1 mm were used to simulate the influence of the contact angle, as presented in Table 5.3

2 - surface and porous wetting conditions. However, the spreading curve presented in Fig. 5.11 shows the spreading behaviour without showing the effect of penetration, yet penetration patterns are completely different for the three cases. It is also crucial to register the importance of using two-phase flow simulations to predict a number of

penetration scenarios for the same initial conditions. These predictions are problematic using the standard Darcy law as it lacks definition of the wettability and topology effects. Also, it will be challenging to predict this behaviour using experiments as this requires sophisticated ways to change the porous media wettability.

5.3.3 Influence of Porous Wettability on Droplet Penetration

While the previous subsection focused on the spreading behaviour with respect to porosity and porous wettability were considered, in this section the focus is on penetration. Figure 5.13 presents the penetration inside the porous media by analysing the amount of liquid volume that goes inside the porous media. Figure 5.13 shows the droplet relative height outside the porous medium, which reflects the droplet penetration behaviour with respect to porosity and wettability.

To provide a better understanding of the qualitative penetration pattern presented in Fig. 5.9 and Fig. 5.12, the relative volume of liquid penetrating $\frac{Vol_{absorbed}}{Vol_{total}}$ into the porous media was recorded during the impact time. Figure 5.13 shows the actual volume absorbed by the porous medium divided by the total volume of the droplet at the time of impact. Figure 5.12-(a) presents the penetration of the carbonate porous model, whilst Fig. 5.12-(b) illustrates the porous model for Berea sandstone. It is clear that the high carbonate porosity model has higher penetration compared to the low porosity of Berea sandstone and yet, various absorption dynamics were observed. In Fig. 5.13 (a), a very limited penetration is recorded by the end of the impact time in Case 6, which pertains to a hydrophilic surface and hydrophobic porous walls.

The penetration pattern can be seen as evidence of longitudinal spreading behaviour in Fig. 5.12 Case 6. In Figure 5.12, Cases 2 and 4 representing the high porosity carbonate model demonstrate the highest penetration values due to the hydrophilic boundary condition imposed. Also, in Fig. 5.12, regarding Cases 2 and 4, the penetration values look identical regardless of the surface wetting condition imposed. The behaviour of these two cases shows the influence of the porosity on the penetration pattern and value as well as the wetting conditions, where the capillary pressure in the tight porous media did not allow for a high liquid penetration, as observed by comparing figure (b) to figure (a).

Figure 5.13 shows the link between the porous wetting condition and porosity. For example, in Case 1, the similarity of the pattern can be seen, whereby the amount of volume penetrating into the porous medium is increasing in both porous stones. While in Cases 2 and 4 the behaviour is quite different to the carbonate porous model (high porosity), for its volume increases exponentially until it reaches a constant value, whereas in the Berea sandstone porous structure (low porosity) the penetration rate is less, but its penetration pattern is increasing over time. Looking at Case 3, the be-

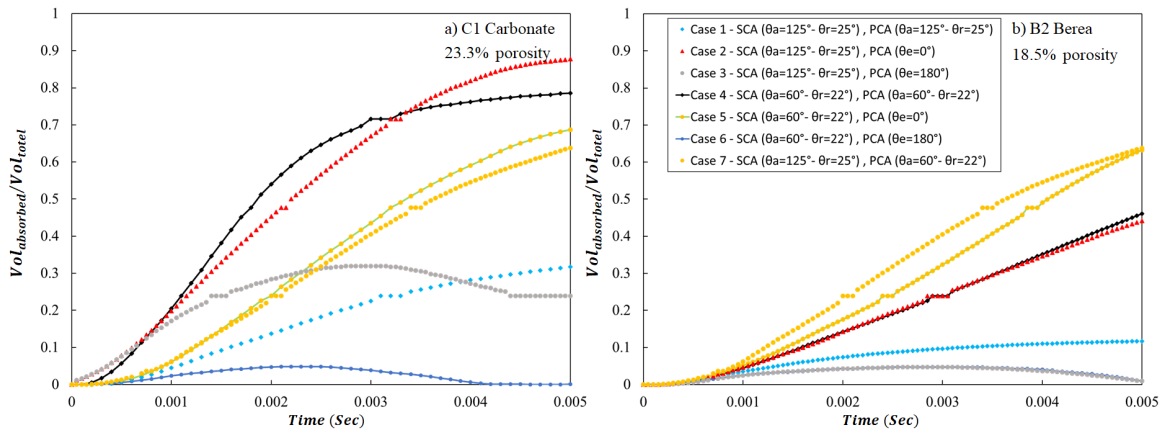


Figure 5.13: The volume of liquid penetration during droplet impacting on porous media. On the left-hand side, the carbonate model is presented, while on the right-hand side is the Berea model. A constant impact velocity of 0.5 m/s and an initial droplet radius of 1 mm were used to simulate the influence of the contact angle presented in Table 5.3

behaviour appears to be the same, due to the lesser effect of the porous wetting condition. Cases 5 and 7 present an increase in penetration for both porous media. It is also important to point out that regarding these two cases, the Berea sandstone porous media is considered to have the highest penetration effect seen in the tight porous media, due to the effect of its hydrophilic surface. Also, Case 6 for both porous material illustrate the lowest penetration as the inertia is not dominant due the imposed contact angles.

Finally, it was observed that smaller contact angle values promote surface wettability, i.e. in these cases there is greater penetration; the higher the wettability, the greater the liquid penetration. This is because the capillary pressure tends to pull the liquid more into the porous structure. Also, it is evident that the spreading ratio of the droplets decreases for smaller values of contact angles, which demonstrates the important link between the external and internal porous structure wetting conditions.

In order to relate the effect of droplet penetration behaviour inside the porous structure to the droplet height during spreading, a non-dimensional representation for this height is shown. Figure 5.14 illustrates the non-dimensional height (h/H), where h is the final droplet height at the time of impact, whilst H is the initial one. Also, Fig. 5.14 presents some inductive results for the actual droplet height using $\alpha = 0.5$, showing the shape of the droplet over time. In Fig. 5.14a, the droplet height on top of the Berea sandstone is presented, showing identical behaviour for the droplet height in the seven cases up to $t/\tau = 0.25$. This droplet behaviour outside the porous structure is very significant, where the effect penetration patterns shown in the previous figure is not detected. However, it is observed that after $t/\tau = 0.25$ a significant change

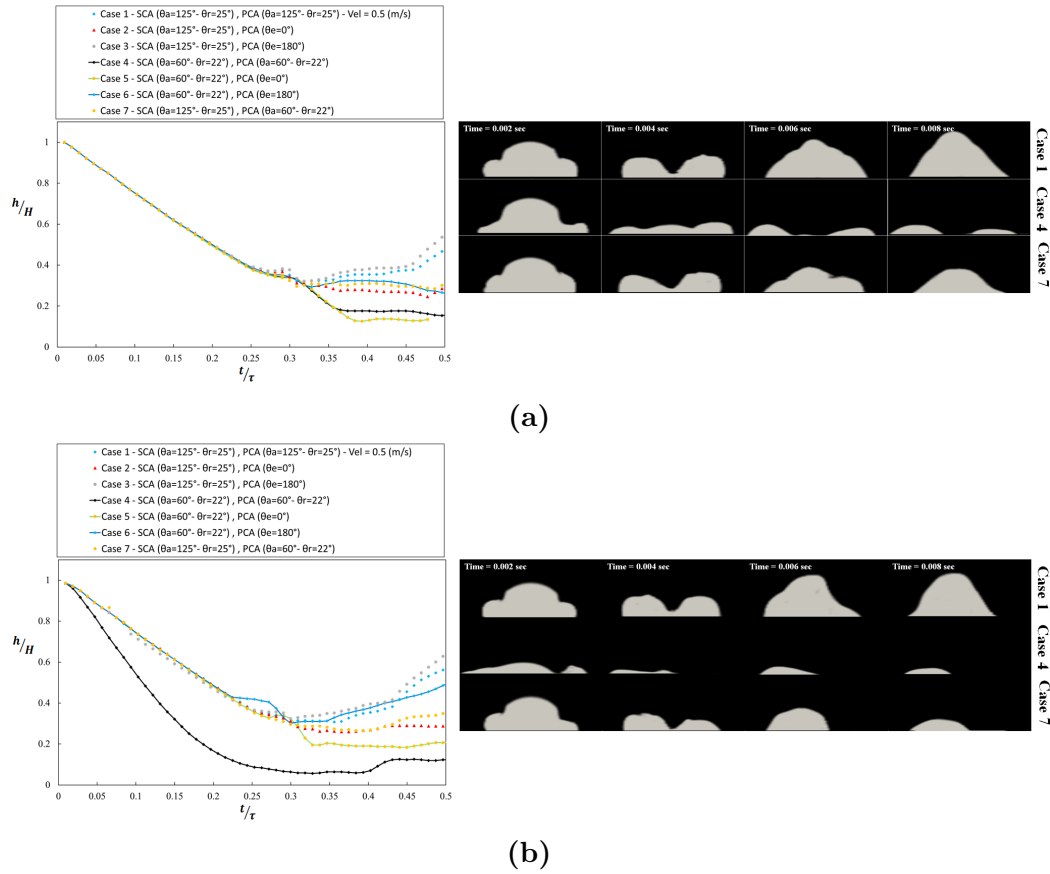


Figure 5.14: (a) droplet height with respect to time when penetrating the Berea porous structure; (b) and penetrating the carbonate porous structure. A constant impact velocity of 0.5 m/s and an initial droplet radius of 1 mm was used to simulate the influence of the contact angle, as presented in Table 5.3. On the left, the non-dimensional droplet height is plotted with respect to time, while on the right, some inductive results for the droplet shape are shown

in droplet height, for example, Case 4 shows a very low h/H value due to the high penetration and capillary number. While for Cases 1 and 7, a high value of h/H was predicted due to the low penetration pattern predicted in the previous section.

The comparison between the seven cases presented in Fig. 5.14a demonstrate a direct relation between droplet height, penetration and wetting condition after the first instance of impact (after $t/\tau = 0.25$). For instance, a linear decrease in droplet height reflects a balance between the spreading and the penetration behaviour. Also, it is observed that, based on the imposed wetting conditions, the amplitude of the droplet oscillation (presented by the h/H peaks) will be defined. In Fig. 5.14a, for Cases 1 and 3, the highest oscillations were predicted, due to the low capillary value imposed. These high h/H peaks represents a repulsive force added to the recoiling phase, where the droplets bounce outside the porous structure. Whilst Cases 2, 7 and 6 show a steady height development after $t/\tau = 0.25$ due to a balance between the penetration and spreading rates.

In Fig. 5.14b, a similar investigation for the droplet height of a porous carbonate structure is presented. Comparing the results presented in Fig. 5.14a to Fig. 5.14b, it is obvious that the height trend shown in the Berea sandstone is not achieved with this media. Looking at Case 4 in Fig. 5.14b, a very small height was predicted due to the high capillary pressure discussed in the previous section. In particular, a limited amount of height increase is registered during the recoiling phase, when the droplet viscous force tries to pull up the penetrated liquid. Apart from Case 4, it would appear that the rest of the six cases has a linear decrease in droplet height up to $t/\tau = 0.22$. Regardless of the difference in porosity, a similar oscillation trend has been observed in porous carbonate media compared to the Berea sandstone. For example, Cases 1 and 3 share the same characteristic high height oscillation in both Figs. 5.14a and 5.14b. Similarly, Cases 2 and 7 share the same stable height progression in porous carbonate media as seen in Berea sandstone. However, the simulation predicted an unexpected overshoot in Case 6, where the 3D presentation shows the droplets sliding during spreading, as mentioned in the previous section.

Comparing the 2D droplet representation shown in Figs. 5.14a and 5.14b (right hand side), a similarity between the droplet height and shape between Case 1 in the two porous models can be observed. This similarity was unpredicted as the penetration behaviour should control the amount of liquid on the surface, in which case the shape of the droplet will depend on the porous structure. However, comparing the droplet cross section representation for Cases 1 and 7 in both porous media, a similarity in droplet height was observed. These findings are crucial, as they show the importance of micro scale prediction for understanding the physical behaviour seen outside the porous media. As mentioned before, most of the similar results will focus on the spreading and its relation to height due to the challenging task of observing penetration and its link to contact angle dynamics

5.3.4 Effect of Varying the Reynolds Re and Weber We Numbers at Fixed Porosity

In this section, the effect of changing the Reynolds Re and Weber We numbers on droplet spreading and penetration behaviour is investigated. The Weber number is used to assess the relative importance of the droplet inertia compared with the surface tension and Reynolds number defines the relative importance of the droplet inertia and the viscous force. Incorporating these two dimensionless numbers, different types of droplet impact behaviour and postimpingement characteristics on porous media surfaces have been reported.

By varying the Re number using the impact velocity in the range 0.5, 1 and 2 m/s the resulting Re numbers range between 200 and 2000. Generally, as the impact Re number increases, the resulting spread diameters and retraction droplet heights are increased. At the same time, at higher Re numbers, more of the liquid penetrates into the pores at the first spreading instances. Hence, the droplet outside the porous medium loses more mass and it becomes smaller at the end of the first retraction period. These smaller droplets have less inertia, thus reducing their penetration action. Table 5.4 presents all the relevant cases for varying impact velocity, droplet size and surface tension. By changing the droplet size at constant impact velocity, it was possible to characterise the effect of inertia on liquid spreading and penetration. Regarding which, the We number was used to represent the changes for three different droplet sizes with radii of 0.5, 1 and 1.6 mm.

Table 5.4: Imposed conditions for Berea porous media surface (using Kistler, dynamic contact angle model) with assumptions of constant contact angle of $\theta_A = 125^\circ, \theta_R = 25^\circ$ at different impact velocity, droplet radius and surface tensions

Case	Velocity (m/s)	Droplet radius (mm)	Surface tension (N/m)	Re	We
Case 8	1	1	0.07	996	14.29
Case 9	2	1	0.07	1992	57.14
Case 10	0.5	0.5	0.07	249	1.79
Case 11	0.5	1.6	0.07	796.8	5.71
Case 12	0.5	1	0.05	498	5

The next subsection presents the effect of changing droplet properties on penetration and spreading at a fixed imposed dynamic contact angle. In fixing the imposed wetting conditions to $\theta_A = 125^\circ$ as well as $\theta_R = 25^\circ$ for both the surface and pores, the

next subsection presents the relation between the We number and porous structure. The test cases presented in Table 5.4 are performed on the Berea sandstone porous structure.

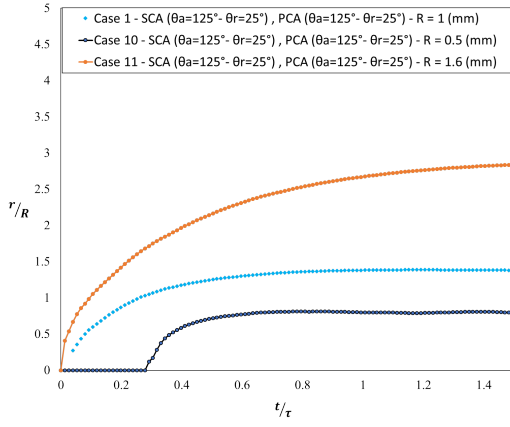
5.3.4.1 Penetration and Spreading Behaviour Under Various Conditions

This subsection will present a comparison between different imposed initial conditions and their relation to droplet behaviour at constant porosity. The proposed parametric study in this subsection will link between the capillary effect during the impact process and the droplet spreading behaviour. Using this link, it is possible to map the droplet behaviour under various conditions.

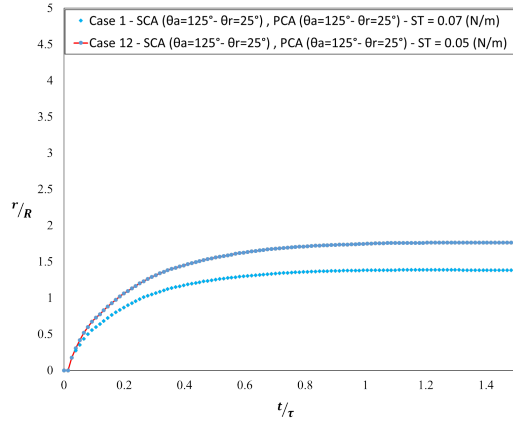
Figure 5.15 shows the time evolution of the water droplet spreading at variant droplet radii (see Fig. 5.15a), variant surface tensions (see Fig. 5.15b), variant impact velocities (see Fig. 5.15c, and finally, for Fig. 5.15d, which illustrates all the cases penetration behaviour. These parameters have been chosen to represent spreading and penetration at low capillary number application. The calculated Re and We numbers for the represented cases are based on the droplet diameter and its impact velocity.

Increasing Re increases the rate of droplet spread on the porous structure and reduces the time scale for penetration to occur. At the same time, increasing Re increases the inertia of the fluid penetrating the porous substrate. Figure 5.15d shows variation of dimensionless droplet volume with respect to time.

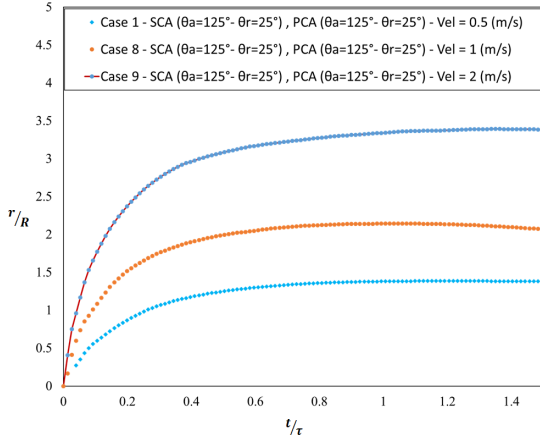
As seen in Fig. 5.16, capillary forces in the porous substrate increase, resulting in larger degrees of penetration for large droplet size and also, high impact velocity. Moreover, the spreading ratio of the droplets on the surface of the substrate decreases due to more volume of liquid penetrating into the substrate, as seen in Fig. 5.15. Figure 5.15a and 5.15b show that by increasing the impact velocity or reducing the droplet size, the spreading directly increases and this also enhances the wettability of the liquid into the porous substrate by increasing the penetration. Figure 5.17 maps the average liquid penetration rates at constant wetting condition for different Re and We numbers. For Cases 8 and 12 (where only surface tension is changing) the average liquid penetration over time was very similar at a value of 13 % of liquid penetration. Also, the average penetration effect for Cases 10 and 11 share a similar value of 20-25 % of liquid penetration, which illustrates the effect of size on penetration. Cases 10 and 11 share the same impact velocity of 0.5 m/s with two totally different droplet



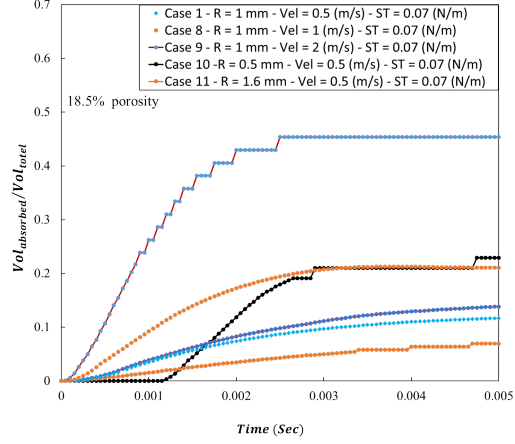
(a) Effect of droplet radius on spreading



(b) Effect of surface tension on spreading



(c) Effect of impact velocity on spreading



(d) Volume penetration for Cases 8, 9 and 10 and with comparison to Case 1

Figure 5.15: The early stage of droplet spreading on a Berea sandstone porous structure. a, b and c present different droplet conditions, while figure (d) summarises the effect of these conditions on penetration at constant imposed wettability

sizes of radii 0.5 and 1.6, respectively. The behaviour observed in Case 10 is due to the relatively small-sized droplet.

The penetration rate was high once it spread into porous voids at very low capillary pressure. The penetration behaviour for Case 11 was different as the penetration rate was lower, yet the penetration was affected by the high capillary pressure while the droplet was spreading. For Case 9, the average penetration was the highest because of the imposed impact velocity.

It can be seen in Fig 5.18 that as the surface tension value decreases the effect on spreading becomes more important. As was expected, less spreading is observed for Case 12, which is accompanied by a different penetration behaviour, as seen in Fig. 5.18. The effect of reducing the surface tension is clearly seen in the capillary pressure distribution, where an increase in penetration was seen at instant $t = 0.005s$. Whilst

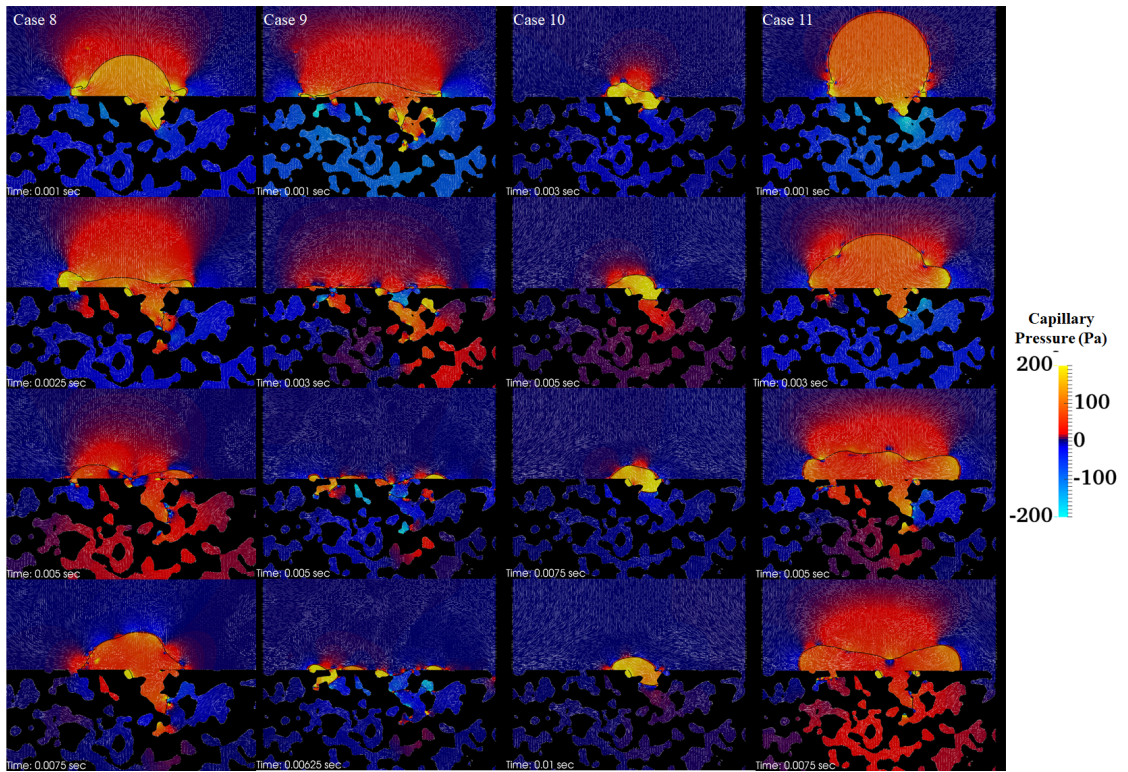


Figure 5.16: Effect of capillary pressure on droplet presentation behaviour for different droplet sizes or impact velocity by imposing constant wettability conditions

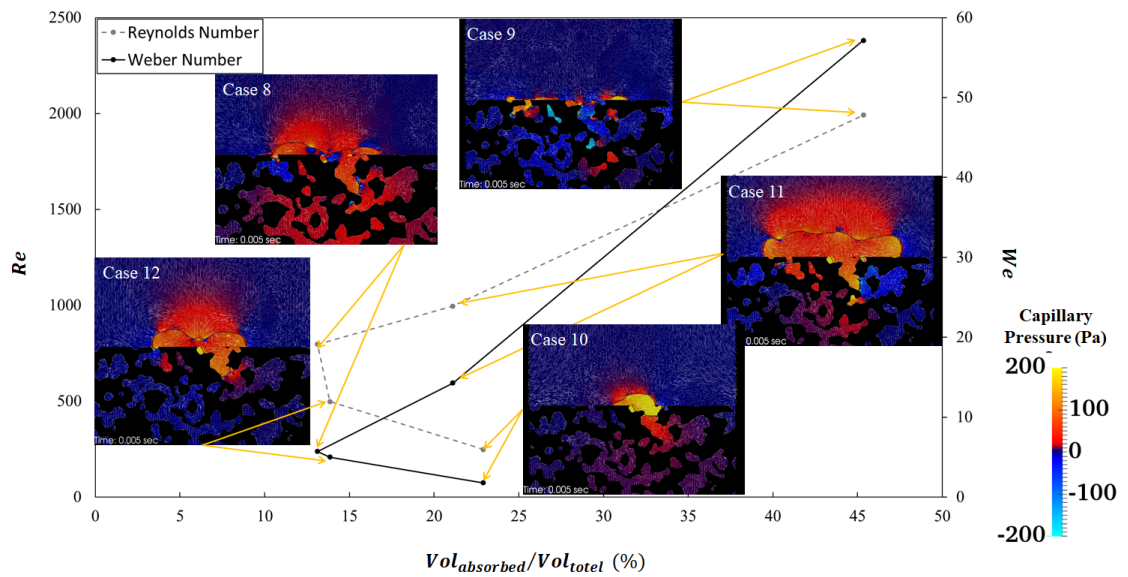


Figure 5.17: Mapping penetration with respect to Reynolds and Weber numbers; snapshots are presented for $T = 0.005s$

he penetration behaviour is found to affect the overall spreading behaviour, the overall pattern can be seen as being the same.

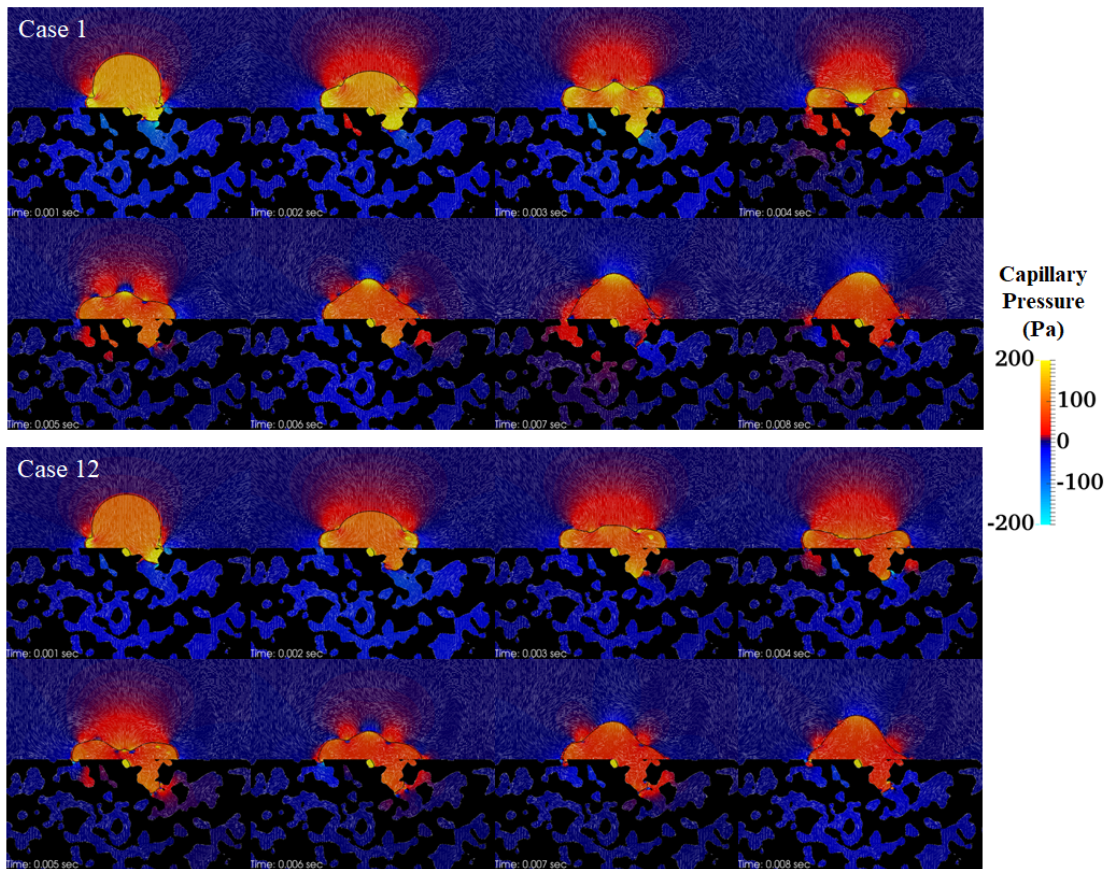


Figure 5.18: Effect of surface tension on droplet spreading and penetration, with an impact velocity of 0.5 m/s and a constant contact angle of $\theta_A = 125^\circ$, where $\theta_R = 25^\circ$

5.4 Multiple Droplet Impacting Porous Medium

Moving on to a realistic scenario, one may consider the effect of multiple droplets behaviour during the spreading and penetration process. In some real life applications, such as rain droplets impacting on porous surfaces, the droplet interaction during spreading and penetration presents a challenging phenomenon. Studying multiple droplet dynamics introduces two important challenges, first, the effect of droplet position on spreading and penetration behaviour, whilst second, there is the impact of multiple droplets interaction during the penetration event. Following the investigations presented in the previous section, this one will be focused on the interaction between more than one droplet during the impact event.

The objective is to determine the fluid dynamic processes that may occur when a number of droplets impact on a single porous structure. In particular, the droplet spreading and penetration into the porous medium are of concern. The interaction between droplets during spreading and penetration is of interest, because it explains the penetration dynamics during spreading and the capillary effect on the penetration. In order to perform the described simulation on multiple droplet impacting on the given porous structures, the Berea porous structure was used for investigations. As shown in Fig 5.19, five droplets were initially placed at the centre and the four corners of the domain. Depending on the droplet radii, the distances a , b and c were varied to make the droplet stay at the centre of each quarter for all the simulations.

Three different droplet sizes were investigated at the same impact velocity and surface tension, as shown in Table 5.5.

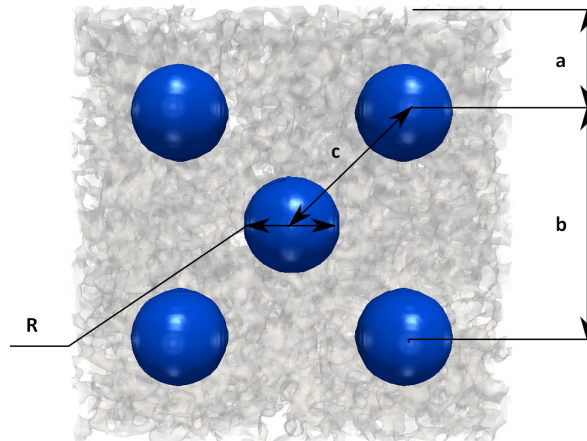


Figure 5.19: Schematic for multi droplets set-up: distance (a) represents the distance from porous edge; (b) is the distance between droplets; (c) is the distance from the centre; and R represents the droplet radius

Multiple droplet impact was investigated to uncover the capillary effect during spreading and penetration. Fig. 5.21 presents the capillary pressure distribution and the velocity vector field on a diagonal slice at the middle of the porous media. Also, Fig. 5.21 presents the 3D droplets during spreading using the liquid volume fraction at a value of ($\alpha = 0.5$).

Table 5.5: Imposed conditions for Berea porous media surface (using the Kistler dynamic contact angle model) with the assumption of a constant contact angle of $\theta_A = 125^\circ$ and $\theta_R = 25^\circ$ at different impact velocities and different droplet radii

Case	Velocity (m/s)	Droplet radius (mm)	Surface tension (N/m)
Case 13	0.5	0.5	0.07
Case 14	0.5	0.75	0.07
Case 15	0.5	1	0.07

Three different droplet sizes were considered to identify the effect of droplet interaction and the penetration patterns. Fig. 5.20 (a) presents the smallest droplet radius disposition on the porous structures. Fig. 5.20 (a) shows the effect of the droplet location with respect to the spreading behaviour. The mentioned spreading dynamics occurred due to the droplet size being very close to the porous surface holes, which affected the droplet spreading pattern based on the location. Regarding Fig. 5.20 (a), at time step 0.004s, shows the diagonal droplets show a recoiling behaviour, while the middle droplet is still. This behaviour defines the effect of the porous surface topology and the droplet size. This effect will not be captured using the standard Darcy model, as aforementioned, it does not carry any information about local porous changes. At $T = 0.01s$ in Fig. 5.20 (a), it is observed that the droplets spreading starts to decrease, with some changes in the initial droplet location being recorded. The change in location during the latest spreading phases is an indication of capillary penetration behaviour, where the inertia effect does not contribute to the droplet penetration at low impact velocity.

Figure 5.20 (b) presents a bigger droplet radius of 0.75 mm, which impacts at 0.5 m/s. For Case 14, it can be seen that the five droplets during the first three time steps (0.002s, 0.004s and 0.006s) behave in similar manner, producing the same spreading features regardless of the location. This behaviour shows the minimised effect of the droplet spreading behaviour when the droplet radius increases with respect to the porous surface. Nevertheless, after $T = 0.008s$ onwards a change in behaviour is observed, where the inertia effect starts to decrease and the capillary absorption starts

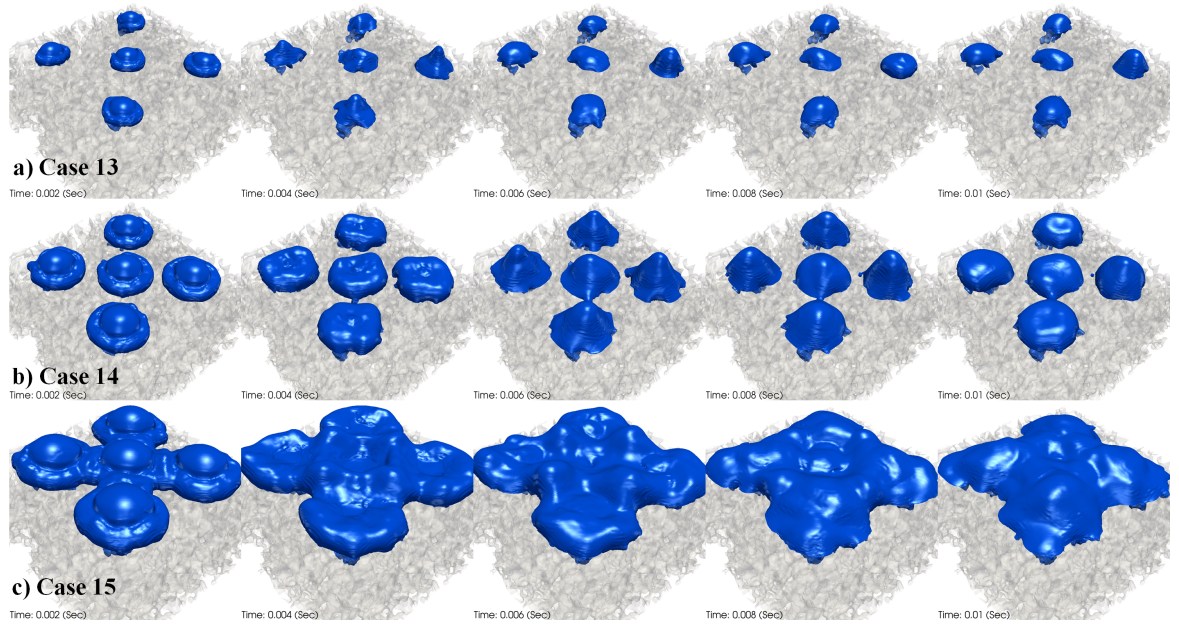


Figure 5.20: Alpha iso-surface for 3D droplet with constant impact velocity for the three cases of 0.5 m/s and constant contact angle of $\theta_A = 125^\circ$ and $\theta_R = 25^\circ$

to be more effective. Due to the imposed hydrophobic dynamic contact angle of the values ($\theta_A = 125^\circ$ and $\theta_R = 25^\circ$) the droplet recoils and stays in its position, where portions of the flow start to be absorbed by the porous media. However, as seen when $T = 0.01s$, the central droplet starts to merge with one of the diagonal droplets, which directly changes the two droplets spreading shape and increases the wetted surface area.

Figure 5.20 (c) presents different droplet behaviour, where the cloud of droplets merge during the spreading phase. The droplets interaction while spreading creates an interesting observation when the core of the droplets start to recoil. However, each individual droplet for the first two time steps 0.002s and 0.004s is seen to keep the spreading characteristic features. After $T = 0.006s$, the middle droplet starts to immerse into the porous structure, while the four outer droplets start to recoil from the outside. At $T = 0.008s$, the viscous force dominates the behaviour and the five droplets start to recoil together blowing the liquid outside the porous media. Also, it can be seen that by the last time, presented as $T = 0.01s$, the overall droplet behaviour is almost acting as one big droplet at the recoiling phase.

Figure 5.21 presents a diagonal cross-section showing the capillary pressure and the velocity vector for the impact instances. A numerical hydrophobic set-up for the three study cases was used to demonstrate the effect of capillary absorption. Figure 5.21a demonstrates a quick inertia dissipation around the droplets main volume, which is

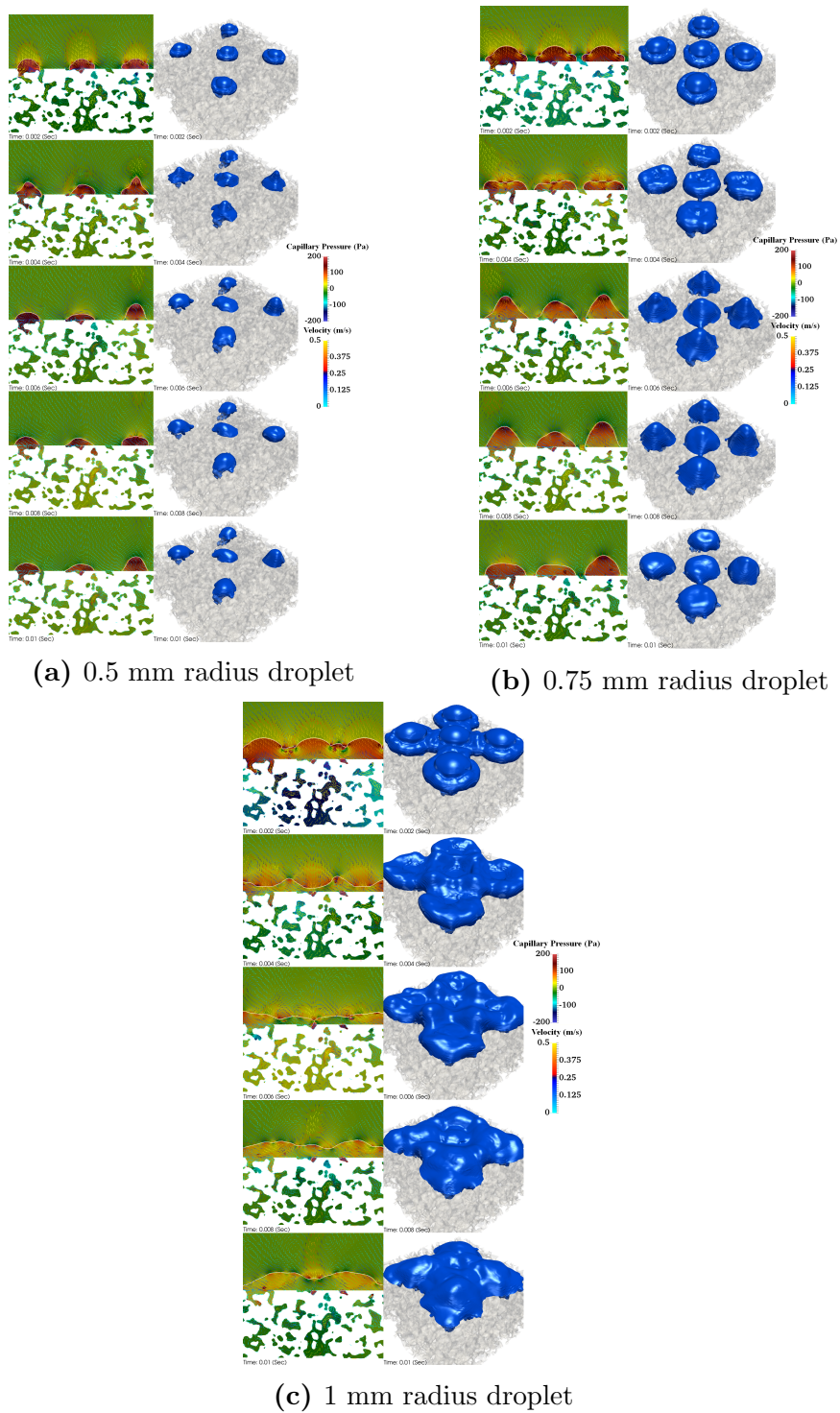


Figure 5.21: The early stage of droplet spreading on the Berea porous structure. On the left of each figure, is a diagonal cross-section presenting capillary pressure and the velocity vector, whilst on the right-hand side an alpha iso-surface for as 3D droplet is illustrated. There is a constant impact velocity for three cases of 0.5 m/s and constant contact angle of $\theta_A = 125^\circ$ and $\theta_R = 25^\circ$

accompanied by a low-pressure field at the pores zone. The lower pressure field helps some of the droplets to penetrate the porous structure due to the large pores size, while the middle droplet and the right-hand corner one behave as if they are setting on a solid surface with a minor change in position. Fig. 5.21a also shows the effect of capillary pressure on porous media, whereby the middle region demonstrates a higher

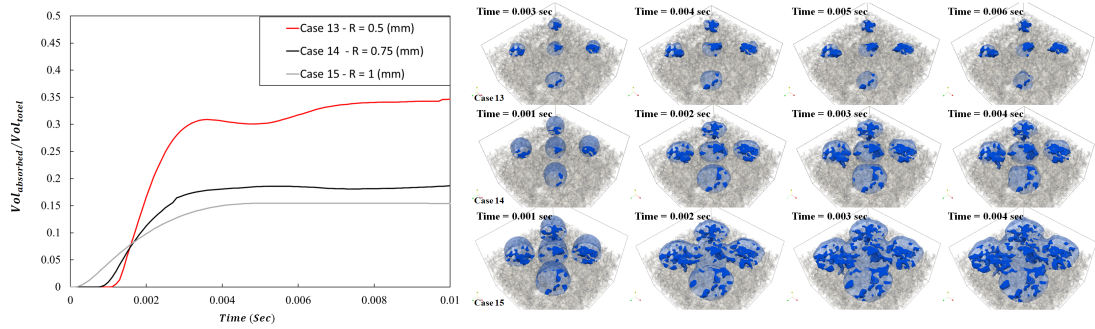


Figure 5.22: Multi-droplet presentation for porous media; on the left is the total volume penetration with respect to time; on the right is 3D VoF representation for the droplet penetration pattern

pressure value for the empty porous structure, which plays an important role in terms of the droplets lesser penetration behaviour during the inertia phase. Also, considering the cross-section area of the droplet, it can be seen that, based on the droplet position its height at the recoil phase varies. This effect is due to the surface topology and also, due to the porous media pressure reaction during the impact.

This significant prediction gives the presented simulation a strong edge to characterise the droplet behaviour based on deposition on porous media. Reflecting the important of droplet position on the Darcy method, it is found to be challenging to correlate such behaviour into the Darcy method where topology changes the effect of the predicted results. Figure 5.21b demonstrates a different behaviour, where the first two time steps exhibit almost the same droplet shape during the spreading phase. A low penetration behaviour is shown in Fig. 5.21b due to the fluid spreading phase in that it blocks the pores. The low capillary pressure induces a repulsive behaviour, where the droplet recoils fast, leaving the liquid volume penetrating only relatively large pores. Once the droplet settles a slow penetration starts to take place by the capillary effect, leaving the outer rim of the droplet attached to the porous surface. It is important to note that due to the low-pressure field created during the penetration some of the droplets start to rejoin together inside the porous media.

By predicting the capillary penetration for a hydrophilic porous media, it has proven possible to show the importance of effect of pore size distribution on a porous structure. Comparing Fig. 5.21c to Fig. 5.21b, it can be observed that the same capillary pressure drop behaviour at the porous structure during the first impact occurs. However, due to the fact of droplet merging the capillary penetration is seen to be less due to the high-pressure region found close to the porous surface. Also, due to the fact of droplet merging during the final time step, the five droplets were acting like a single droplet, as

mentioned before, which resulted in a recoil phase, which decreased the pressure under the droplet which help to droplets to overcome the capillary suction. This behaviour is quite unique, because liquid penetrating the porous structure, as seen in Fig. 5.21b, normally invariably occupies the biggest pores and starts moving down the porous structure. However, Fig. 5.21c shows the opposite, where the recoiling forces from the viscosity dominate the absorption.

In order to understand the penetration behaviour, the relative total liquid volume penetration for the three presented cases was computed, as seen in Fig. 5.22. The total volume absorbed by the porous structure during the time of impact was normalised by the total droplet volume as $\frac{Vol_{absorbed}}{Vol_{total}}$. Two different penetration behaviours are observed in Fig. 5.22, with the first one being observed before the three curve intersection, where a high rate of penetration was found in Case 15, followed by lower rates of penetration for Cases 14 and 13. While after the intersection, a second penetration can be seen, where a step rate of penetration was found at Case 13, 14 and 15 respectively. These two opposing behaviours show the effect of the impact of inertia and capillary pressure on the absorbed volume. For Case 13, the biggest amount of liquid penetration, as seen in Fig. 5.22, is found to be after the droplet settles down and capillary penetration takes place. While Cases 14 and 15 share the same behaviour of slow rate penetration, especially in Case 15, where the merging behaviour for the liquid droplets affects the rate of penetration. However, Case 14 presents a unique penetration behaviour in that it shares a similar sharp absorption rate before the curve intersection with Case 13, but then has a stabilised penetration rate after the curve intersection similar to Case 1. This idiosyncratic behaviour reflects the effect of droplet size with relation to the porous network and also, the wetting conditions, which give further evidence of the importance of microscopic effects on modelling droplet impact regarding porous structures.

Studying three different droplet sizes has shown the relation between liquid absorbed and porous structure wetting conditions. In particular, it has been found to be very important to study the hydrophilic effect on liquid penetration. The outcomes from the presented study, involving the deployment of three test cases, suggest that droplet spreading behaviour with respect to impact velocity and porosity are vital for understanding the penetration dynamics.

5.5 Concluding Remarks

In this chapter, a parametric numerical study was performed to obtain detailed information about the droplet dynamics of impact on and penetration into a non-homogeneous real porous structure. The numerical framework used in this study has shown its robustness in dealing with low capillary number flow at the microscale of the porous medium. Using a realistic porous structure in studying the effect of porous structures on spreading and penetration was found to provide deeper understanding of the effect of liquid imbibition and its relation to droplet spreading when compared to the Darcy model. The numerical investigations were carried out for a range of parametric factors, such as the effects of the Reynolds Number (Re), Weber number We , porous wetting conditions and porosity of the porous medium. Careful observation while changing wetting conditions and Re showed that the penetration could be differentiated into vertical suction, horizontal capillary penetration and high capillary resistance (minimum penetration).

The rate of horizontal and vertical penetration is highly dependent on the We number. Droplet oscillation during the spreading diameter and droplet height outside the porous structure highly influence the penetration of the liquid into the pore geometry. The droplet behaviour may follow a similar behaviour under the same imposed Re number, but the droplet height oscillates with larger amplitude at a higher dynamic contact angle. For a larger degree of penetration droplet spreading behaviour is unpredictable. Also, the damping effect is mainly due to the penetration pattern. That is, a solid-to-liquid area inside the pore network has been shown to have a significant role in surface energy dissipation and oscillation damping outside the pore network.

The effect of porosity using two different porous structures has shown that the penetration volume decreases due to smaller pore size in a lower porosity structure. Moreover, penetration depth itself is highly dependent on the wetting conditions on the porous surface as well as the porous. The effect of the We number has also been studied by changing the surface tension of the liquid droplets. The smaller the value of the Weber number, the larger the volume of penetration. The Reynolds number was varied to study the effect of droplet impact velocity and found to have a similar behaviour to the We number. However, surface tension studies showed a direct effect droplet behaviour inside and outside of the pore geometry.

Multiple droplet behaviour was studied during the spreading and penetration.

Based on the droplet diameter different oscillation behaviours were observed at different porous locations. Using the same impact velocity, the surface to porous relation was found to affect the droplet penetration process. At large droplet diameters, the droplets have shown a merging behaviour at the same level of spreading and oscillation pattern compared to the single droplet dynamics. Regarding merging droplets, more investigations are needed to study the effect of porous structures, impact velocity and wetting conditions on the merging and penetration levels.

Chapter 6

Conclusions and Future work

6.1 Conclusions

In this chapter, a summary of this thesis is presented, conclusions are provided, and recommendations for future studies are made. In this thesis, a complete framework for the simulation of two-phase flow within porous media reconstruction process from CT images has been presented. This was for simulating and predicting the macro-scale behaviour of flow inside porous media as well as for probing droplet impacting and impact. To track the interface flow in porous structures, a new two-phase numerical framework based the VoF method, which can be used to solve the mass and momentum balance equations in the porous structure was developed. The two-phase flow framework solver was constructed using the OpenFOAM platform as this provides open source capabilities for implementing new models with existing libraries.

In Chapter 2, the proposed framework was developed for modelling two-phase flow for micro-scale models at very low flow rates, where the capillary forces play an important role. To improve the numerical model stability and to decrease the computational requirements, a new adaptive compression scheme was introduced in Subsection 2.2.1. The latter allows for dynamic estimate of the compressive value only at the areas of interest (typically the diffused interface) and has the advantage of avoiding the use of a priori defined parameters for the areas where it is applied. The proposed adaptive method has been found to increase the numerical accuracy and to reduce the sensitivity of the methodology to tuning parameters, as shown in Sections 3.4, 3.5 and 3.6. The model was coupled with additional sharpening and smoothing algorithms for interface capturing, as presented in Subsections 2.2.2 and 2.2.3. Coupling the adaptive compression scheme with these sharpening and smoothing algorithms helps in minimising the parasitic currents present in low capillary number simulations when viscous forces and surface tension dominate inertial forces, as discussed in Section 3.6. Also in Section 3.6, it has been shown that a sharp surface force model could eliminate the problem of spurious currents. As a result of the numerical unbalance when modelling the movement of a closed interface, it is difficult to maintain a zero-net capillary force. By using the calculated forces from the mentioned models, it was possible to filter the capillary fluxes using a thresholding scheme, as explained in Subsection 2.2.5, to maintain a zero-net capillary force, while modelling the movement of the interface.

Coupling between the capillary pressure and the Navier-Stokes equations was added to improve the efficiency of the numerical method for low capillary number flows, as

covered in Subsection 2.2.4. The capillary pressure equation was solved separately from the dynamic pressure, which allowed for filtering the capillary forces to avoid numerical errors and instabilities. Chapter 2, also contain an implicit formulation for capillary forces, which alleviates the capillary time-step constraint and allows larger time-steps for long-term prediction of two-phase flow at low capillary numbers was presented. The new solver implementation is able to decrease accurately and efficiently the computational cost for this type of simulation by eliminating the spurious current problem present in the standard VoF formulation.

In Chapter 3, the numerical framework was verified by using it to model several two-phase benchmark cases. The static capillary pressure was predicted by solving the differential form of the Young-Laplace equation numerically for single and multiple droplets. Also, the developed solver was tested using the Rayleigh Taylor problem with homogeneous layers of a high-density fluid penetrating a low-density one under the influence of gravity. Moreover, in this chapter a comparison between the code developed for this thesis and the LS method using the Rayleigh Taylor problem was presented. This revealed the advantages and disadvantages when predicting droplet break-up under viscous effects. The solver performance was also validated using the vortex flow, as presented by [68], to verify the ability of the developed model in dealing with severe interface stretching.

In addition to the circle in a vortex field benchmark, the solver was tested using the rotation test of the slotted disk, which is known as the Zalesak problem [114] to determine the effect of the adaptive compression method on sharp interface diffusion. Finally, an experimental T junction test case to validate the developed solver in real complex flow was used. This test showed the importance of the dynamic compression scheme in droplet break-up prediction. By using the developed solver, it was possible to predict the sharp advancing interface during the break-up process for different operating conditions. To summarise, based on the numerical results presented in Chapter 3, the numerical method was considered as being a reliable and efficient method to solve the flow at low capillary numbers encountered in flow through porous media.

In Chapter 4, studies of the effect of oil residual saturation after water injection simulations at low capillary numbers were reported upon. The numerical results presented in this chapter for modelling two-phase flow simulations on geometries obtained from micro CT, showed that trapping and droplet transport can be predicted based on the capillary pressure and its relation to the contact angle. According to this approach,

by changing the imposed capillary contact angle, the trapped droplet behaviour will change resulting in a less trapped cluster of the oil droplets. This prediction shows the importance of added surfactants to the injection water where droplet clusters remain trapped. It was found that the trapped cluster will have a direct relation with the imposed dynamic pressure gradient, which affects the threshold capillary field when it resists the dynamic pressure gradient force and the viscous drag force between the two phases.

Using the developed solver, analysis was undertaken to obtain the relative permeability curves from the simulations data of four different porous structures reconstructed from CT scans. The relative permeability curves and the residual oil saturation obtained at low capillary numbers showed that the simulation results were representative. The solver was also used to predict the capillary fingering behaviour using various porous contact angles at low capillary numbers. Using the numerical method, it was possible to study the effect of different parameters, such as contact angle and capillary number, on the macroscopic properties (capillary pressure and relative permeability curves) and residual saturation. Overall, this thesis provides a new framework for a detailed pore-scale analysis of multiphase flow, which works along the lines of researching the foundation for large-scale modelling in porous media.

In Chapter 5, the developed solver was used to study a different application, where accurate prediction of flow behaviour is at technological importance and challenging. The fluid dynamics of the impact of a liquid droplet on a permeable porous structure was investigated numerically, with the results being compared to those of available experiments in the literature. The impact of water droplets were impacted on top different porous structures was analysed. Also, the dynamics of the water spreading on the top surface and its penetration into the porous structure were investigated. Different droplet diameters and impact velocities were tested to validate the results of the penetration, and selected results were presented and analysed. Two different penetration behaviours were observed by imposing different contact angles. Initially, there is a fast penetration period, which occurs immediately after droplet impact, referred to as the inertia driven penetration. This is followed by a slow penetration period, governed by capillary action, and referred to as the capillary driven penetration. Also, different impact velocities showed that the first phase of penetration occurs as the droplet spreads on the porous media.

It was also observed that the imposed contact angle at the pore level has a great

effect on the viscosity and surface tension, which can change the droplet spreading and penetration behaviour. At the end of the spreading stage, penetration halts and droplet retraction occurs on the surface of the porous media which, in some cases illustrate that water suction into porous structures. Parametric studies showed that impact velocity and dynamic contact angle effect are dominant over droplet diameter and pore size. Further, when using hydrophilic contact angles for both surface and pores, a significant increase in horizontal penetration was observed.

In Chapter 5 also illustrated the impact of liquid droplets on a porous structure at different sizes and impact velocities. The investigations was carried out by changing the value of the Re number, We number, porosity, and liquid viscosity. By increasing the value of Re number, it was possible to predict the increase in the penetrated volume at the dynamic imposed contact angle. It was observed that vertical penetration mainly happens within the inertia driven penetration regime. Moreover, the capillary regime mainly stabilises the penetrated liquid into the adjacent horizontal plane rather than pushing it lower along the vertical direction.

The effects of porosity using two different pore size studied in this chapter showed that penetration volume decreases due to smaller void volume in lower porosity substrates. However, the penetration depth itself increases in lower porosities due to the smaller voids. Changes in the Weber number showed a direct effect on the capillarity of the pore network geometry. Moreover, decreasing the value of the We number increases the effect of surface tension, which increases the capillarity of the pore network geometry. Increased surface tension stabilises the liquid in the horizontal plane that it wets and does not significantly affect the penetrated volume.

Chapter 5, also touched on the behaviour of multiple droplets impacting on porous media. Multiple droplet behaviour was studied during the spreading and penetration. Based on the droplets diameter different oscillation behaviour was seen at different porous locations. Using the same impact velocity, the surface to porous link was found to affect the droplet penetration process. At large droplet diameters, the droplets have shown a merging behaviour at the same level of spreading and oscillation pattern compared to the single droplet dynamics. Regarding merging droplets, more investigations are needed to study the effect of porous structures on the merging and penetration levels.

6.2 Recommendations and Future Work

In this section, the future work will be highlighted based on the conclusions and the literature previously presented, the future work and the recommendations are provided in two subsections as follows.

6.2.1 Numerical Aspects

Further optimisation of the numerical solver for modelling two-phase flow through porous structures should be considered. First, it is important that the dynamic mesh refinement be optimised with the proposed interface tracking methods, thereby solving the flow equations on a coarse mesh, while also being able to capture the flow of thin wetting layers. The computational time has emerged as being one of the biggest limitations when attempting to combine the dynamic mesh refinement algorithm with the adaptive compression scheme.

Also, it is important to focus on strategies to optimise the numerical constants introduced in Chapter 2, where an additional adaptive scheme for smoothing loops and a capillary filter is needed. The effect of heat transfer is very essential aspect that should be added to the numerical model. It is important with some applications to consider the effect of phase change during transport in the porous structure. As future work, the developed numerical should be extended to include evaporation model. Finally, it is essential for future research considering the (multiphase) flow solvers using the VoF in the case of more than two immiscible phases are simulated.

6.2.2 Application Aspect

In this thesis, two different types of application where the microscopic effects play an important role in fluid flow behaviour have been presented. Also, the developed numerical solver was used to relate flow rates to the forces, and then these were related to the pressure drops. This approach enables parametrising the effect of the geometry on the flow and force fields. It would be beneficial to extend the modelling presented in Chapter 4 to include: a) a lower capillary number for oil drainage for the fluid transport in porous structures; b) a wider range of imposed dynamic wetting conditions, where water/oil behaviour is highly unpredictable and c) a greater depth in the secondary injection behaviour at different injection rates in the same porous structure.

Moreover, using more computational power, larger porous samples should be used so as to have a better understanding of the relation between microscopic and macroscopic flow behaviour. Also, it is important to engage in experimental work for flow in porous media, where having extracted capillary pressure curves from the simulation results, the results could be compared with the experimental measurements.

Concerning the size of the porous matrix in Chapter 5, it represents a strong limitation on simulating of larger droplet. It is important to consider larger porous samples in order to understand the effect of droplet size on penetration.

Also, thermal studies of the impact and penetration that change the behaviour of the viscosity, surface tension, and contact angle are recommended as the next stage of the developed present numerical methodology. Solidification of liquid inside the pore network is expected to change the dynamic of penetration significantly. With such simulations, the dynamics of impact and penetration would make this research even more relevant to understanding liquid droplet impact and penetration on a paper substrate.

Appendix A

Complementary Simulations -

Appendix A

A.1 Introduction

In this appendix, we present some complementary simulation data that has been used either during code validation or during application investigations. It is important to mention that some of these simulations cannot be conclusive by their own. However, they played an important role in understanding the code performance or the simulation behaviour during the development period.

A.2 Droplet Impinging on a Porous Surface Using Darcy Model

Droplet spreading on a porous surface is somewhat different from droplet spreading on a solid surface. In the case of spreading on a porous surface, the liquid penetrates and spreads at the same time. Which of these two processes is faster than the other depends upon the porosity of the substrate, impact velocity of the droplet and the surface tension of the liquid. Fig A.1 shows the impact of the η – *heptane* droplet ($D_0=1.5$ mm, $U_0=0.93$, $We=6$) on the porous surface when the explicit porous zone model is used. The permeability of this model is $K=1.04 \times 10^{-12} \text{ m}^2$ and the porosity $\epsilon=0.25$. Four snapshots of the collision covering a time period of 0.4 ms are shown for the volume fraction (iso-surface of $\alpha=0.5$) and velocity and compared with experiments [12]. Experimental photographs present the image of the portion of the liquid droplet outside the porous substrate, while the numerical simulations display the liquid both inside and outside the porous region.

The mechanism driving this flow is mainly related to the pressure difference between the impact region outside the substrate and the capillary pressure acting in the fluid interface inside the porous medium. During the initial stages of impact, the stagnation pressure in the drop, which drives the outward jetting of the liquid, is much larger than the restraining forces due to surface tension and viscosity (i.e. shear stress). As the droplet spreads out into a thin film the kinetic energy is, however, dissipated; stopping further spreading of the liquid. In the first few instants of the impact, liquid projects radially from beneath the droplet away from the impact point. The numerical simulation accurately predicts this phenomenon. Although it can be seen that towards further time steps of the impact, a blob-like structure appears at the edges of the droplet implying the formation of a rim around the lamella, which is not visible in

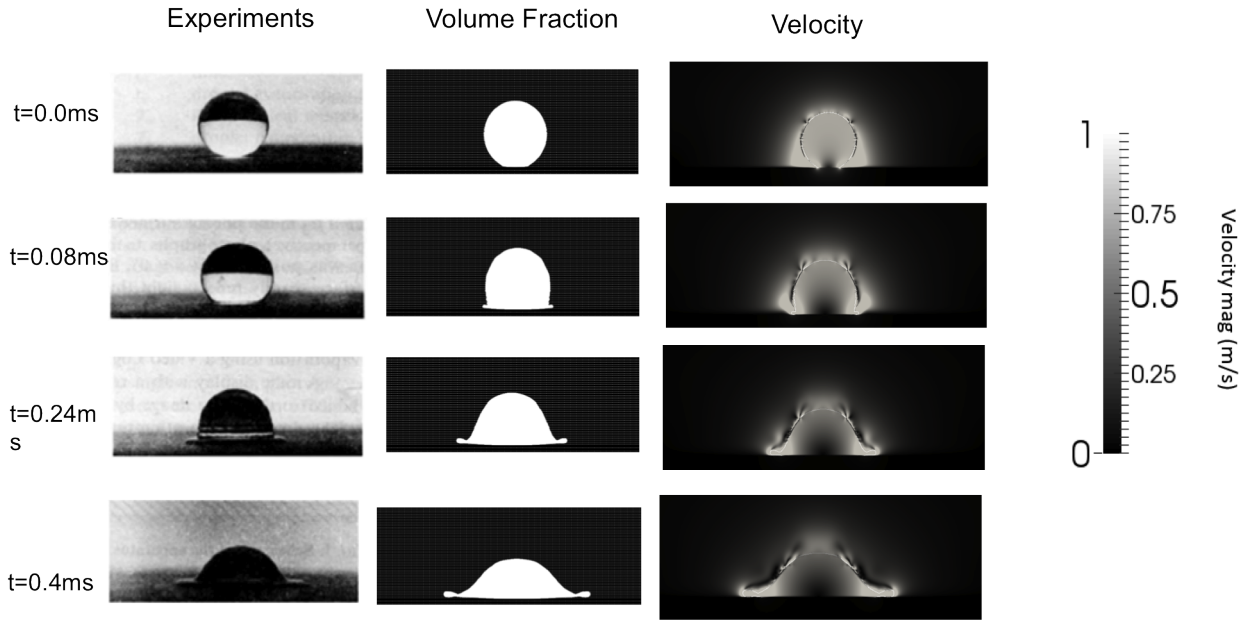


Figure A.1: Time evolution of the droplet shape when impacting on a ceramic porous medium ($K=1.04 \times 10^{-12}$,). Numerical simulations of the indicator function and velocity magnitude are compared with the photographs obtained by Chandra and Avedisian [12]

the experiments. This is mostly attributed to the explicit porous model that does not allow for an appropriate representation of the contact angle rather than the interface tracking method as such.

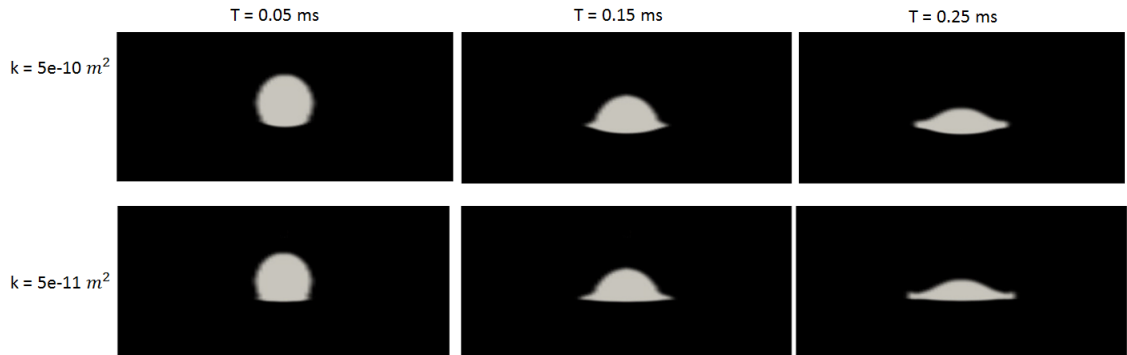


Figure A.2: Time evolution of the shape of the impinging droplet obtained by numerical simulation for different permeability values. The white colour shows the indicator function

Two additional sensitivity studies (Case 3) are included in Fig A.2 in order to demonstrate the effect of permeability ($K=5 \times 10^{-11} m^2$ and $5 \times 10^{-10} m^2$). When permeability is increased it is expected that the droplet will penetrate more while the spreading will be less if the We number is kept constant. Although previous attempts [25] correctly reproduced the effect of permeability on penetration using similar explicit models, the spreading effect was not accurately captured. In our simulations, we can see

the balance between spreading and penetration Moreover in contrast to the experimental observations of [12] that were presented in Fig. A.1 -where the resistance imposed by the porous substrate was large enough to prevent significant liquid absorption- in the case of $K=5 \times 10^{-10} m^2$ the droplet is partially absorbed by the substrate.

A.3 Droplet Impinging on a Porous Surface Using 2D Porous Media Geometry

Spreading on porous surfaces -as we saw in the previous section- is a combination of two phenomena. First is the spreading of the droplet over the substrate which results in an increase of the droplet base. Second is the movement of the droplet into the porous substrate which decreases the droplet base; however, it increases the depth of liquid wetted region inside the porous surface. This second process is the focus of this section where instead of treating the porous zone as a "black box" (explicit approach) we examine the penetration of a water droplet ($D_0 = 0.24mm$) inside a material (Sandstone) that its internal structure is represented through an implicit model. The porosity of the model is $\epsilon = 0.45$ while the permeability is $K= O(10^{-11})$. The Sandstone core sample is extracted from a porous rock of 0.6×0.5 mm presented by Sirivithayapakorn and Keller [14]. The range of the pores spaces is $3-15 \mu m$. In the current simulation, we simulate only a 2D axisymmetric slice of this sample as it can be seen in Fig. A.3 (a). Although the assumption of axisymmetry might not be valid for real porous materials, since the material used here is homogeneous it can be considered a reasonable approximation. Moreover, experiments in the literature [13, 155] show that droplets penetrating in porous materials exhibit a universal hemispherical shape which could also explain the axisymmetric assumption. Another important point is that although the rotation of this 2D slice would result in an artificial space filled with toroidal items (see Fig.A.3 (b)) while the real material is filled with discrete particles the porosity of both materials is the same (0.45). The meshing process is described in detail in [156]. A total number of 57342 cells have been used. The minimum cell size is $0.1 \mu m$ and the maximum is $17 \mu m$. The samples in Case 1-3 have bigger dimensions than in Case 4. This creates the need to downscale the droplet impinging the porous medium ($D_0 = 0.24mm$) of Case 4 in order to maintain a constant ratio between droplet and pore space and make it comparable to the previous cases. Two sensitivity tests are

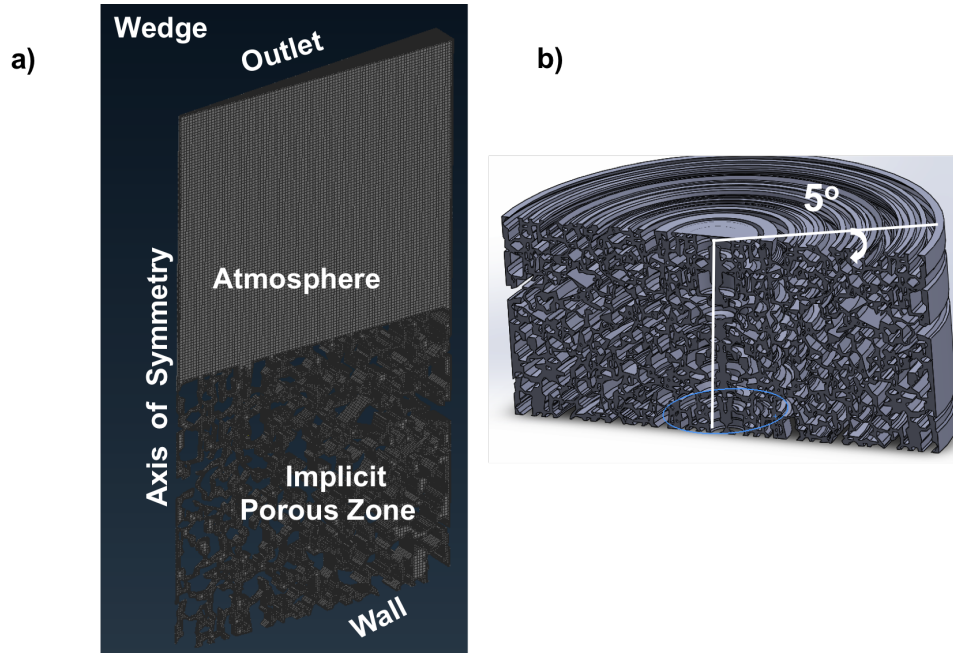


Figure A.3: Schematic of the numerical grid. Picture (a) corresponds to the 2D slice (wedge) used in the calculation and picture (b) shows a schematic of the 3D rotation of this slice that results in a domain filled with toroidal items.

run. One corresponds in the same We number as Case 3 ($We=6$) and one additional case is included for completeness that the We number is increased. Also our sample for Case 4 has the same porosity as the porosity and permeability that corresponds to the first row of Fig. A.2.

The value of the Weber number denotes the importance of inertia in relation to surface tension effects. When the We number is increased when the flow is much more inertia-dominated for the spreading phase although inside the porous medium capillary effects are equally important. In order to provide a better insight of the process Figs A.4 to A.6 are presented. Figure A.4 shows the time evolution of the shape of the impinging droplet for $We = 62$ and $We = 6$. With an increase of We number the spreading is increased. The penetration at the high We number is influenced by the higher impact velocity that then is redistributed at the radial direction as well and causes more spreading. The locally higher pressure at the impact point for higher We number also results in higher penetration at the first steps of the impact.

Looking through at the last snapshot we can see that the droplet inside the porous medium for $We=6$ has a more hemispherical shape while when the We is increased the shape is more uniformly distributed at the radial direction following the higher spreading outside the substrate. For $We = 6$ the radial momentum is less so the "weak rim" around the droplet has less inertia to penetrate. The penetration is higher in the

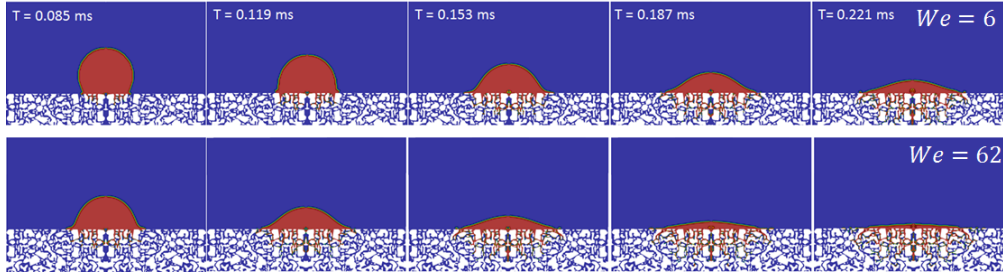


Figure A.4: Time evolution of the shape of the impinging droplet: (a) $We = 62$ and (b) $We = 6$.

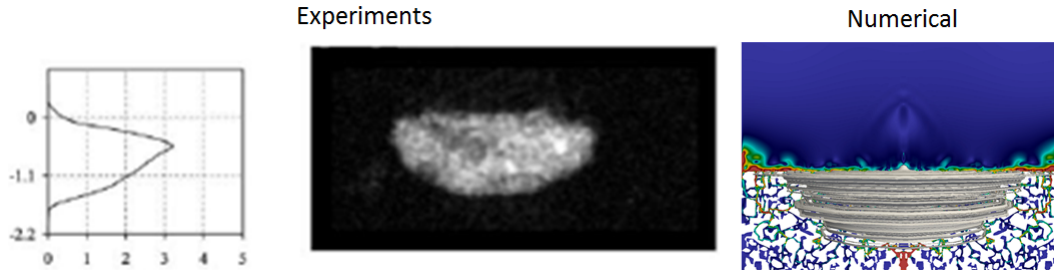


Figure A.5: Experimental picture of a water droplet impinging on $120 \mu m$ glass beads [13] (left) compared with numerical simulation of the Sandstone [14]. Both samples have the same porosity and permeability.

middle of the droplet that holds most of the impact velocity inertia. This is responsible for the hemispherical shape. For higher We that the inertia is higher at the radial direction as well, the droplet penetrates more uniformly (see Fig. A.4). This difference in the shape of the penetrating droplet for varying We numbers is also consistent with the experimental results from [155]. Although the porosity for this case was different.

Figures (A.5,A.6) present results for the case of $We=6$ since it is the same as in Case 3 ($K= O(10^{-11} m^2)$) of the previous section in terms of porosity, permeability and We number. The dimensions of the porous zone and the droplet are different. However, the same ratio of porous space and droplet size is maintained. Figure A.5 shows the comparison of the experimental picture of a water droplet impinging on $120 \mu m$ glass beads [13] (left) and the numerical simulation of the Sandstone [14] (right). Both samples have the same porosity and permeability while their dimensions are different. It can be seen that our simulations show the same almost hemispherical shape as the experiments. It appears that this shape is almost universal regardless of the size of the droplet/model used as soon as some parameters like porosity and permeability are maintained. This could, in reality, justify the use of the explicit model in the literature. However what we notice here if we compare the penetration at $T= 0.25$ ms of $K=5 \times 10^{-11} m^2$ case of Fig. A.2 (that corresponds to $\epsilon = 0.45$ and $We =6$)

and $T = 0.221$ from Fig. A.4 ($K = O(10^{-11} \text{ m}^2)$, $\epsilon = 0.45$ and $We = 6$) we see that the implicit model predicts much more penetration than the explicit model. Also, it is more consistent in terms of the shape of the penetrated liquid with the experiments. This is attributed to the better representation of the capillary pressure inside the sample as it can be seen from Fig. A.6.

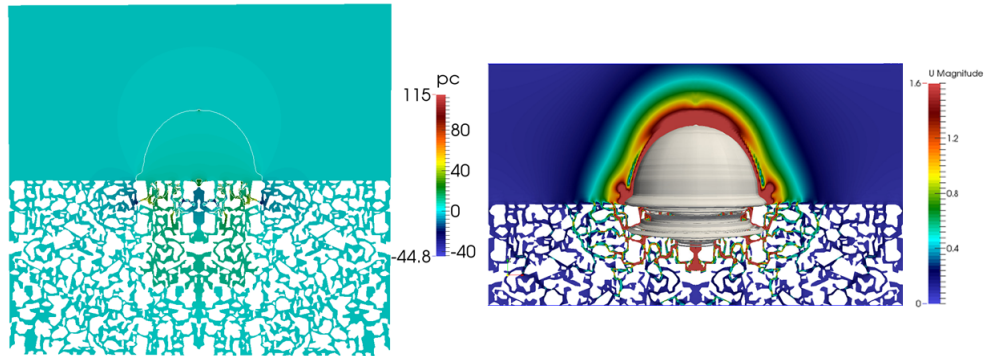


Figure A.6: Snapshot at $t = 73$ msec of drop with $We=6$ into a porous stones geometry: numerical simulations of the indicator function (iso-surface of $\alpha = 0.5$) (right) and capillary pressure field (left) are presented.

Although the suggested model might not represent a real porous medium but (the representation maintains some the realistic features from the porous material and thus allows to get some insight for the liquid penetration inside the material such as the preferential paths the liquid will flow, the changes in the velocity depending on the depth.

A.4 Flow and Transport in Porous media - Complimentary Studies

In this section, we present some complimentary simulations for the secondary injection scenario where porous media contain a mixture of water and oil. These simulations took longer to produce one conclusive results, and it was found to demand higher computational power than expected. We were aiming at studying the effect of porosity and porous structures on the oil saturation during secondary water injection. However, due to the high computational power needed and also due to time limitation we coded test more than one porous media. The presented results touch very briefly on our initial findings. Nevertheless, more work can be done using these exciting models to investigate the saturation behaviour during oil removal under different dynamic wetting conditions.

A.4.1 Secondary Water Injection for Water/Oil Mixed Porous Reservoir

This section presents the secondary water injection simulation results that contain a mixture of both oil and water phases. The simulation starts with injecting oil into the water phase until the saturation rate for oil stops increasing. Then we inject water (as a secondary injection process) using two different capillary numbers on the Berea Sandstone porous media. Similar to the previous sections presented in Chapter 4, we use a zero-gradient boundary condition for the indicator function and the velocity at the outlet. For the velocity at the inlet, we impose a constant injection rate for the water phase and the oil phase velocity is set to zero initially. The pressure boundary condition at the outlet is a fixed value. Similar to the previous simulations. Initially, all the mesh located in the first 5% of the porous media are refilled with the water phase, and the injection of the water phase is done through those parts of the inlet which are not invaded by the forward-moving oil phase. On the solid walls, a dynamic contact angle presented in table A.1 has been used in the two presented simulations. Table A.1 presents the simulation conditions for Berea Sandstone porous structure and the non dimensional numbers associated .

The results presented in Fig. A.7 confirm that for the case of higher capillary number the trapped oil clusters are smaller in size by the end of simulation. However,

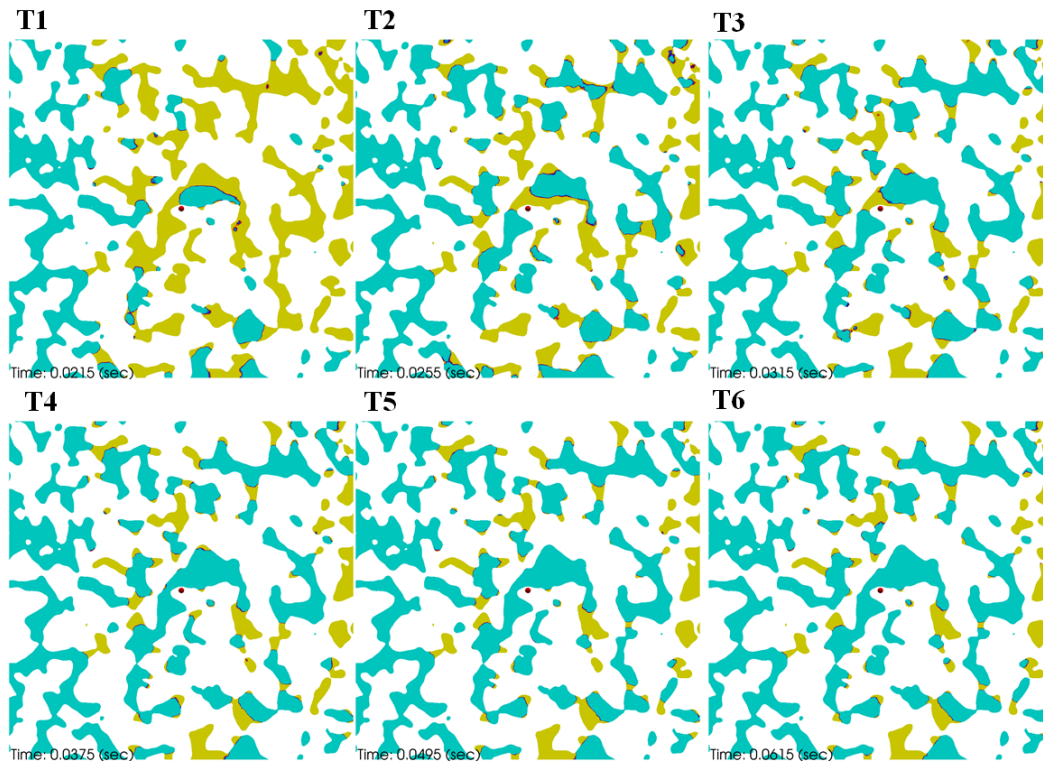
Model	Case	Injection flow rate (m^3/s)	Advancing Contact Angle	Receding Contact Angle	Average Capillary no.	Average Reynolds no.	Surface tension σ (kg/s^2)
B1	BM5	1×10^{-8}	8	6	2.05×10^{-3}	229	0.024
B1	BM6	1×10^{-9}	8	6	1.87×10^{-3}	208	0.024

Table A.1: Wetting Conditions for secondary water injection simulation

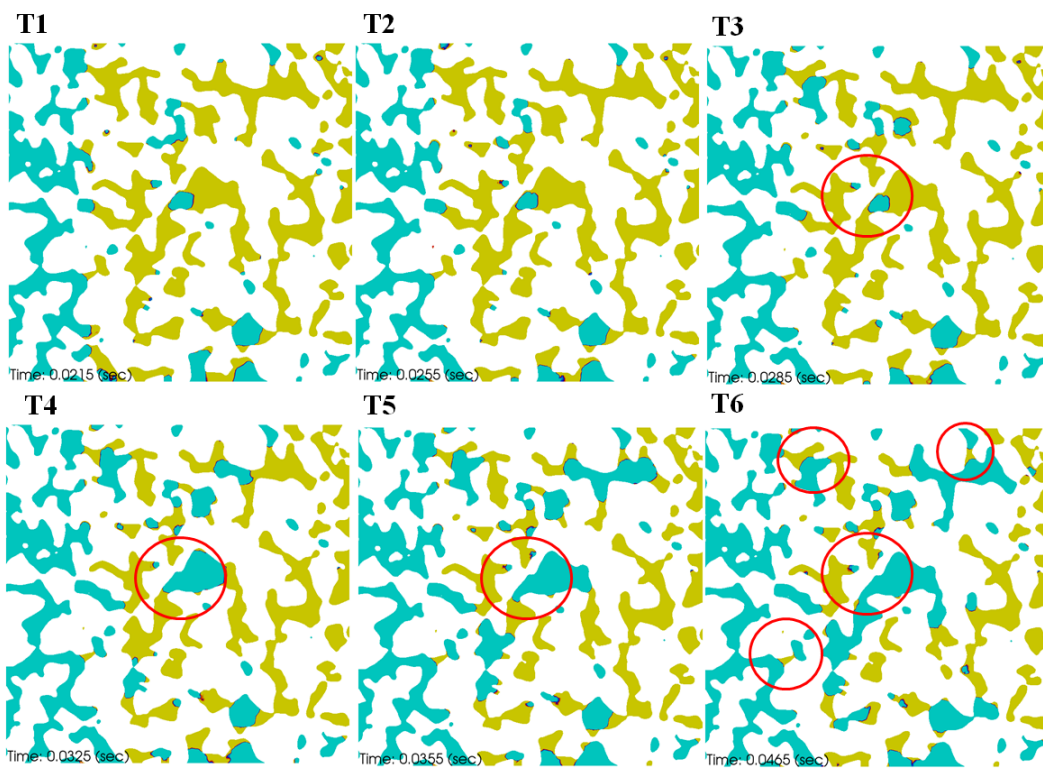
for the case of low capillary number the trapped oil phase blobs are bigger. This observation confirms that the sizes of the trapped droplets are related to the capillary number at which the water phase is injected. This observation could be explained by the criteria presented for blob mobilization shown by Raeini et al. [143]. The criteria states that for a fixed aspect ratio, the size of the blobs trapped should be small enough so that the maximum capillary field after snap-off can oppose the dynamic pressure gradient field and the viscous drag force between the two phases. The capillary field opposing force for the oil cluster mobilization is inversely proportional to the blob size, while the driving force dynamic pressure gradient and the viscous drag force between the two phases are proportional to the capillary number. Therefore, when the oil clusters are smaller, the capillary field will be higher and can resist the dynamic pressure gradient and the viscous drag force at higher capillary numbers.

Figure A.8 presents the saturation and permeability curves for the capillary numbers mentioned in Table A.1. As seen in Fig. A.8a oil saturation start decreasing at the early begin of the injection process, while in Fig. A.8b the oil saturation decreases at a very slow rate. Due to the high injection rate in BM5 compared to BM6, it is expected to predict a higher saturation rate at BM5. However, the long delay in the oil saturation in BM6 was also found to be not limited to the the water injection rate, but also linked to the very low developed capillary pressure seen by the water phase. The predicted oil saturation curve seen in Fig. A.8 represents an excellent example for the link between the trapped oil clusters and oil removal. As seen in Fig. A.7b large number of trapped oil cluster was found during the simulation period. This trapped oil cluster decrease the number of connected water paths between the the inlet and the outlet.

The previous observation is directly reflected on the permeability curves shown in Fig. A.8, where a higher permeability curves was found by BM6 compared to

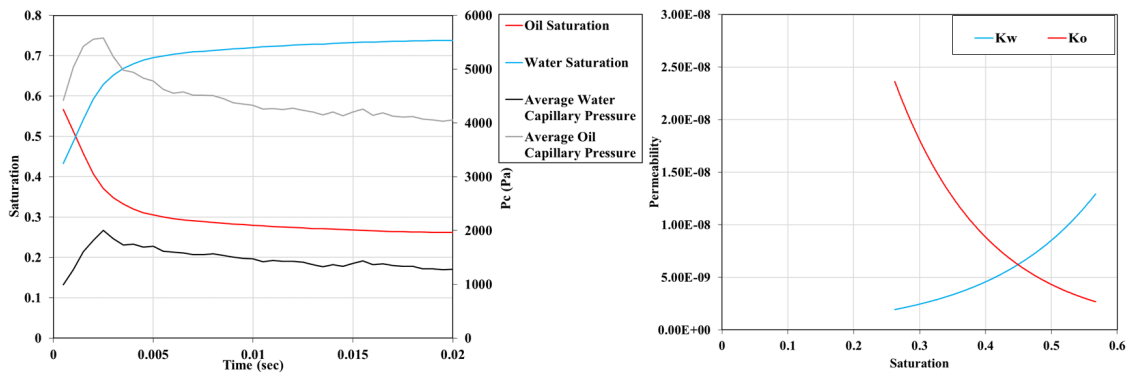


(a) Case BM5

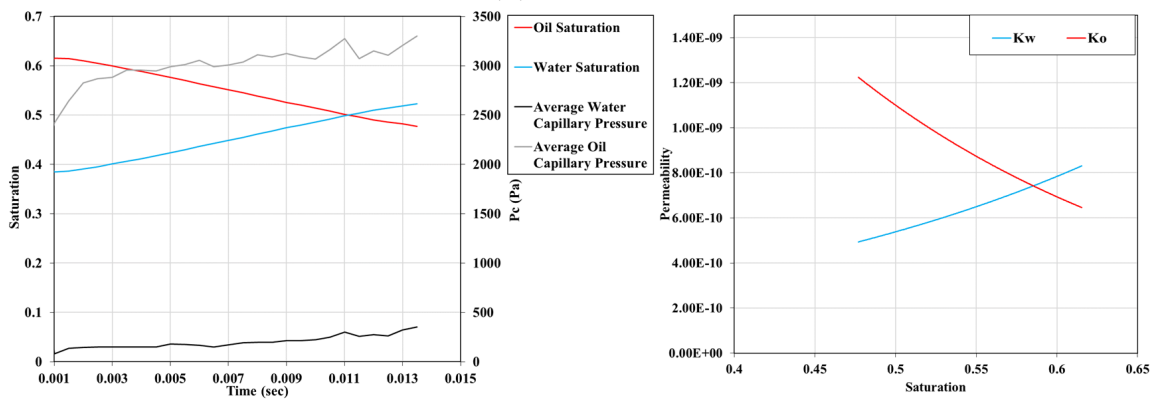


(b) Case BM6

Figure A.7: Cross section showing water phase in blue and oil phase in yellow comparing case BM5 & BM6, showing the effect of capillary number on oil saturation at secondary injection



(a) Case BM5



(b) Case BM6

Figure A.8: Plots of the capillary pressure and phase saturation (on the left), and also the computed effective permeability curves (on the right) for oil removal at secondary water injection process

BM5. Permeability curve as predicted in Fig. A.8a show a lower values compared to test case BM3 presented in Chapter 4. The lower predicted value indicate the importance and the effect of water/oil presented during oil removal process. Comparing the permeability results between BM5 and BM6, we found a higher permeability value achieved by BM6 due to the act of capillary pressure. We could not run the simulation for too long, however we were able to predicate the intersection of permeability curves at BM6. The High permeability value presents an important observation where the presence of oil and water phases blocked some of the fluid passages creating extra force of resistance to the flow field. Also due to the imposed dynamic contact angle the trapped oil clusters found to be harder to remove due to the difference of capillary pressure. This results show a much higher permeability value compared to the case BM4 presented in Chapter 4. Finally the presented difference between primary and secondary injection behaviour shows the importance of pore scale simulations where predicting permeability curves can be in some cases impossible using the conventional Darcy law.

A.5 Using Dynamic Grid Refinement

Due to recent progress in adaptive grid refinement (AGR) techniques, simulations for many applications such as atomization and many others start being feasible in the sense that the ratio of the largest to the finest scales becomes tractable with the present computing power. AGR methods have been introduced long time ago for Cartesian grids [157] and used since then for many types of flows. The usage of local grid refinement can be directed to the increase of mesh resolution at the interface, where modelling errors can be decreased. However, the AGR method found to increase the simulation time due to the computational cost specially at micro-scale flows.

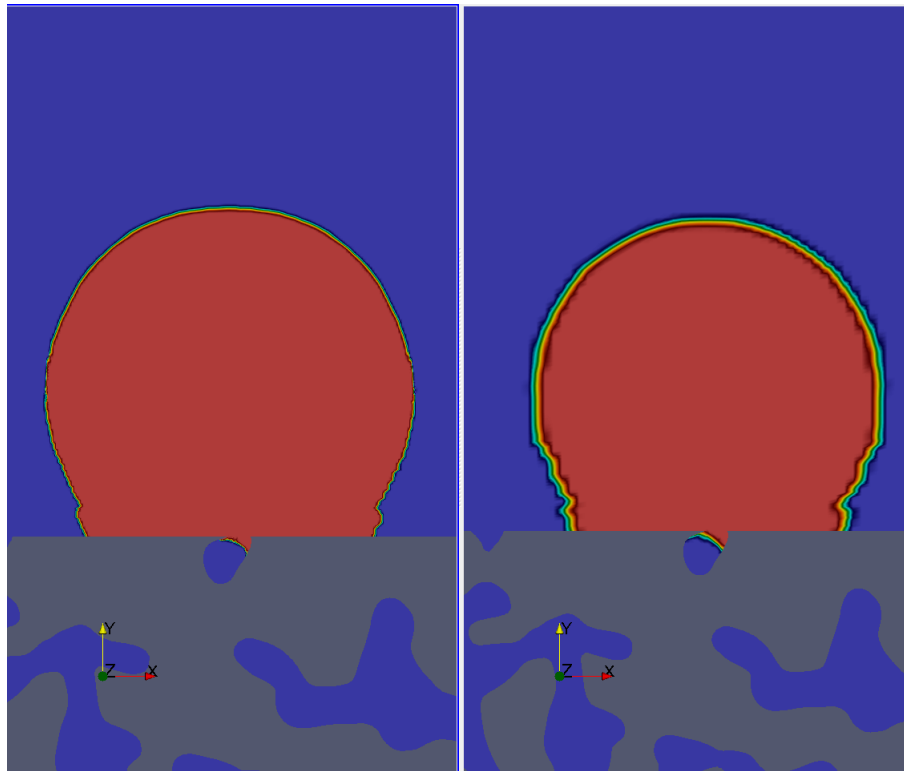


Figure A.9: Comparison between dynamic refinement effect (on the left) and no refinement method

During our research we implemented the numerical method mentioned in chapter 3 to the adaptive grid refinement method found in OpenFOAM. The aim of implementing the development numerical method to the extract grid refinement method was to increase the interface capturing accuracy and to predict efficiently the formation of bubbles or liquid snapping for example. As seen in Fig. A.9 by implementing our numerical framework to the local grid refinement solver, a very sharp droplet interface was captured. However, some disadvantages was found such as 1) the time taken to fil-

ter the numerical errors and to decrease the parasitic current increase due to the rapid change of grid and also the size of the grid, 2) due to the fine grid close to the interface and the solid boundary, we found a higher than expected parasitic current, which may need some alterations on the formulation proposed in chapter 2, 3) Each simulation using the adaptive method found to occupy a very large disk space compared to the non refining method

Nevertheless, we computed one simulation for the droplet impacting over porous media, to understand the effect of AGR on the spreading results. As seen in Fig. A.10 case 19 presents the simulation using our developed solver computed with the (AGR) solver and case 1 without the (AGR) solver. The vertical black lines presents 5% deviation between the two solver results.

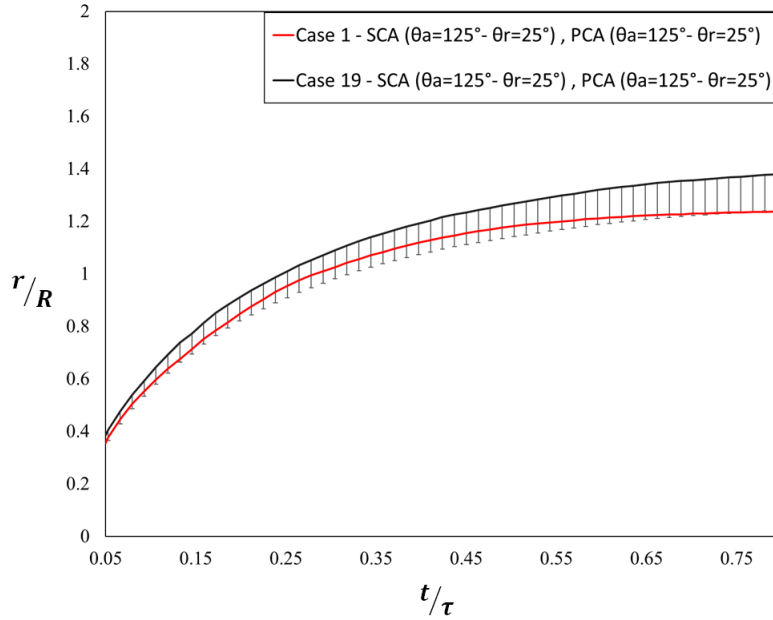


Figure A.10: Comparison between spreading on porous media (carbonated rock) using dynamic grid refinement Case 19 and without dynamic refinement Case 1 the graph showing 5% deviation while spreading. spreading conditions are impact velocity of 0.5 (m/s) and Droplet radius ($R = 1$ mm) with assumptions constant contact angle of $\theta_A = 125^\circ$, $\theta_R = 25^\circ$

By recording the time taken to perform the same simulation presented in Fig. A.10 we found that our method without the grid refinement is almost 1.75 times faster. So as conclusion, 5% is not a very big gain compared to the time taken to compute the same results. Also performing the adaptive mesh refinement was harder in terms of mesh set-up as the AGR solver demands very specific mesh quality to be able to split the volume cells during the refinement process. However, its very important to point out, using the AMR method we were able to predict the formation of air bubbles

trapped between the porous media and the droplet as seen in Fig. A.11.

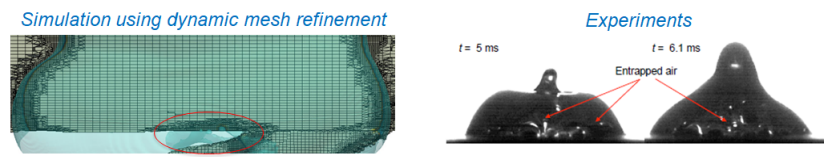


Figure A.11: Comparison between dynamic refinement effect (on the left) and experiments by [10] showing the bubble formation during impact.

Bibliography

- [1] Marco Marengo, Carlo Antonini, Ilia V Roisman, and Cameron Tropea. Drop collisions with simple and complex surfaces. *Current Opinion in Colloid & Interface Science*, 16(4):292–302, 2011.
- [2] Woo Shik Kim and Sang Yong Lee. Behavior of a water drop impinging on porous substrates- examination of contact-line drag effect. *Atomization and Sprays*, 26(3), 2016.
- [3] CFD Open. Openfoam programmer’s guide. *OpenFOAM Foundation*, 13(3.0.1), 2015.
- [4] Terence D Blake. The physics of moving wetting lines. *Journal of colloid and interface science*, 299(1):1–13, 2006.
- [5] R Scardovelli and S Zaleski. Direct numerical simulation of free-surface and interfacial flow. *Annual Review of Fluid Mechanics*, 31:567–603, 1999.
- [6] Vinay R Gopala and Berend GM van Wachem. Volume of fluid methods for immiscible-fluid and free-surface flows. *Chemical Engineering Journal*, 141(1): 204–221, 2008.
- [7] M Pasandideh-Fard, YM Qiao, Sanjeev Chandra, and Javad Mostaghimi. Capillary effects during droplet impact on a solid surface. *Physics of fluids*, 8(3): 650–659, 1996.
- [8] Ilias Malgarinos, Nikolaos Nikolopoulos, Marco Marengo, Carlo Antonini, and Manolis Gavaises. Vof simulations of the contact angle dynamics during the drop spreading: Standard models and a new wetting force model. *Advances in colloid and interface science*, 212:1–20, 2014.

- [9] Martin J Blunt, Branko Bijeljic, Hu Dong, Oussama Gharbi, Stefan Iglauer, Peyman Mostaghimi, Adriana Paluszny, and Christopher Pentland. Pore-scale imaging and modelling. *Advances in Water Resources*, 51:197–216, 2013.
- [10] JB Lee, AI Radu, P Vontobel, D Derome, and J Carmeliet. Absorption of impinging water droplet in porous stones. *Journal of colloid and interface science*, 471:59–70, 2016.
- [11] JB Lee, D Derome, and J Carmeliet. Drop impact on natural porous stones. *Journal of colloid and interface science*, 469:147–156, 2016.
- [12] S. Chandra and C.T. Avedisian. Observations of droplet impingement on a ceramic porous surface. *International Journal of Heat and Mass Transfer*, 35(10):2377 – 2388, 1992. doi: [http://dx.doi.org/10.1016/0017-9310\(92\)90080-C](http://dx.doi.org/10.1016/0017-9310(92)90080-C).
- [13] N.C Reis, R.F Griffiths, M.D Mantle, and L.F Gladden. Investigation of the evaporation of embedded liquid droplets from porous surfaces using magnetic resonance imaging. *International Journal of Heat and Mass Transfer*, 46(7):1279 – 1292, 2003. doi: [http://dx.doi.org/10.1016/S0017-9310\(02\)00395-2](http://dx.doi.org/10.1016/S0017-9310(02)00395-2).
- [14] S. Sirivithayapakorn and A. Keller. Transport of colloids in saturated porous media: A pore-scale observation of the size exclusion effect and colloid acceleration. *Water Resources Research*, 39(4):n/a–n/a, 2003. doi: 10.1029/2002WR001583.
- [15] Martin Wörner. Numerical modeling of multiphase flows in microfluidics and micro process engineering: a review of methods and applications. *Microfluidics and nanofluidics*, 12(6):841–886, 2012.
- [16] Raed Abed Mahdi, HA Mohammed, KM Munisamy, and NH Saeid. Review of convection heat transfer and fluid flow in porous media with nanofluid. *Renewable and Sustainable Energy Reviews*, 41:715–734, 2015.
- [17] Charles N Baroud, Francois Gallaire, and Rémi Dangla. Dynamics of microfluidic droplets. *Lab on a Chip*, 10(16):2032–2045, 2010.
- [18] Arvind Kumar Yadav, José Carlos de la Cal, and María Jesús Barandiaran. Feasibility of tubular microreactors for emulsion polymerization. *Macromolecular Reaction Engineering*, 5(1):69–77, 2011.

- [19] Matthew Andrew, Hannah Menke, Martin J Blunt, and Branko Bijeljic. The imaging of dynamic multiphase fluid flow using synchrotron-based x-ray microtomography at reservoir conditions. *Transport in Porous Media*, 110(1):1–24, 2015.
- [20] Isabelle Pezron, Guillaume Bourgain, and David Quéré. Imbibition of a fabric. *Journal of Colloid and Interface Science*, 173(2):319–327, 1995.
- [21] Norman R Morrow and Geoffrey Mason. Recovery of oil by spontaneous imbibition. *Current Opinion in Colloid & Interface Science*, 6(4):321–337, 2001.
- [22] Ugur Pasaogullari and Chao-Yang Wang. Two-phase transport and the role of micro-porous layer in polymer electrolyte fuel cells. *Electrochimica Acta*, 49(25):4359–4369, 2004.
- [23] Aline Delbos, Elise Lorenceau, and Olivier Pitois. Forced impregnation of a capillary tube with drop impact. *Journal of colloid and interface science*, 341(1):171–17 year=2010, publisher=Elsevier.
- [24] Neyval C Reis, Richard F Griffiths, and Jane Méri Santos. Parametric study of liquid droplets impinging on porous surfaces. *Applied Mathematical Modelling*, 32(3):341–361, 2008.
- [25] Neyval C Reis, Richard F Griffiths, and Jane M Santos. Numerical simulation of the impact of liquid droplets on porous surfaces. *Journal of Computational Physics*, 198(2):747–770, 2004.
- [26] Dganit Danino and Abraham Marmur. Radial capillary penetration into paper: limited and unlimited liquid reservoirs. *Journal of colloid and interface science*, 166(1):245–250, 1994.
- [27] JH Kim, SM You, and Stephen US Choi. Evaporative spray cooling of plain and microporous coated surfaces. *International Journal of Heat and Mass Transfer*, 47(14):3307–3315, 2004.
- [28] Christof Sodtke and Peter Stephan. Spray cooling on micro structured surfaces. *International Journal of Heat and Mass Transfer*, 50(19):4089–4097, 2007.

- [29] Eric A Silk, Jungho Kim, and Ken Kiger. Spray cooling of enhanced surfaces: impact of structured surface geometry and spray axis inclination. *International Journal of Heat and Mass Transfer*, 49(25):4910–4920, 2006.
- [30] RG Cox. The dynamics of the spreading of liquids on a solid surface. part 1. viscous flow. *Journal of Fluid Mechanics*, 168:169–194, 1986.
- [31] Gangtao Liang and Issam Mudawar. Review of drop impact on heated walls. *International Journal of Heat and Mass Transfer*, 106:103–126, 2017.
- [32] EB Dussan. On the spreading of liquids on solid surfaces: static and dynamic contact lines. *Annual Review of Fluid Mechanics*, 11(1):371–400, 1979.
- [33] Hasan N Oguz and Andrea Prosperetti. Bubble entrainment by the impact of drops on liquid surfaces. *Journal of Fluid Mechanics*, 219:143–179, 1990.
- [34] SF Kistler. Hydrodynamics of wetting. *Wettability*, 6:311–430, 1993.
- [35] Richard L Hoffman. A study of the advancing interface. i. interface shape in liquidgas systems. *Journal of colloid and interface science*, 50(2):228–241, 1975.
- [36] Pengtao Yue and Yuriko Renardy. Spontaneous penetration of a non-wetting drop into an exposed pore. *Physics of fluids*, 25(5):052104, 2013.
- [37] Karen P Hapgood, James D Litster, Simon R Biggs, and Tony Howes. Drop penetration into porous powder beds. *Journal of Colloid and Interface Science*, 253(2):353–366, 2002.
- [38] Tatiana Gambaryan-Roisman. Liquids on porous layers: wetting, imbibition and transport processes. *Current Opinion in Colloid & Interface Science*, 19(4):320–335, 2014.
- [39] JO Marston, Sigurdur T Thoroddsen, WK Ng, and RBH Tan. Experimental study of liquid drop impact onto a powder surface. *Powder technology*, 203(2):223–236, 2010.
- [40] Song-Chuan Zhao, Rianne de Jong, and Devaraj van der Meer. Raindrop impact on sand: a dynamic explanation of crater morphologies. *Soft matter*, 11(33):6562–6568, 2015.

- [41] Ahmed Hamraoui and Tommy Nylander. Analytical approach for the lucas–washburn equation. *Journal of colloid and interface science*, 250(2):415–421, 2002.
- [42] TD Blake and Joël De Coninck. The influence of pore wettability on the dynamics of imbibition and drainage. *Colloids and Surfaces A: Physicochemical and Engineering Aspects*, 250(1):395–402, 2004.
- [43] N Hsu and N Ashgriz. Nonlinear penetration of liquid drops into radial capillaries. *Journal of colloid and interface science*, 270(1):146–162, 2004.
- [44] SH Davis and LM Hocking. Spreading and imbibition of viscous liquid on a porous base. ii. *Physics of fluids*, 12(7):1646–1655, 2000.
- [45] A Clarke, TD Blake, K Carruthers, and A Woodward. Spreading and imbibition of liquid droplets on porous surfaces. *Langmuir*, 18(8):2980–2984, 2002.
- [46] B Markicevic and HK Navaz. Primary and secondary infiltration of wetting liquid sessile droplet into porous medium. *Transport in porous media*, 85(3):953–974, 2010.
- [47] NC Reis, RF Griffiths, MD Mantle, LF Gladden, and JM Santos. Mri investigation of the evaporation of embedded liquid droplets from porous surfaces under different drying regimes. *International journal of heat and mass transfer*, 49(5):951–961, 2006.
- [48] Larry W Lake. Enhanced oil recovery. 1989.
- [49] Marianne M Francois, Sharen J Cummins, Edward D Dendy, Douglas B Kothe, James M Sicilian, and Matthew W Williams. A balanced-force algorithm for continuous and sharp interfacial surface tension models within a volume tracking framework. *Journal of Computational Physics*, 213(1):141–173, 2006.
- [50] Gretar Tryggvason, Asghar Esmaeli, Jiakai Lu, and Souvik Biswas. Direct numerical simulations of gas/liquid multiphase flows. *Fluid Dynamics Research*, 38(9):660–681, 2006.
- [51] Yuriko Renardy and Michael Renardy. Prost: a parabolic reconstruction of surface tension for the volume-of-fluid method. *Journal of Computational Physics*, 183(2):400–421, 2002.

- [52] D H Sharp. An overview of rayleigh-taylor instability. *Physica D: Nonlinear Phenomena*, 12:3, 1984.
- [53] J Brackbill, D Kothe, and C Zemach. A continuum method for modeling surface tension. *Journal of Computational Physics*, 100:335–354, 1992.
- [54] S Popinet and S Zaleski. A front-tracking algorithm for accurate representation of surface tension. *International Journal for Numerical Methods in Fluids*, 30:775–793, 1999.
- [55] Grétar Tryggvason, Ruben Scardovelli, and Stéphane Zaleski. *Direct numerical simulations of gas–liquid multiphase flows*. Cambridge University Press, 2011.
- [56] H G Weller, G Tabor, H Jasak, and C Fureby. A tensorial approach to computational continuum mechanics using object-oriented techniques. *Journal of Computational Physics*, 12:620–631, 1998.
- [57] Stéphane Popinet. Gerris: a tree-based adaptive solver for the incompressible Euler equations in complex geometries. *Journal of Computational Physics*, 190(2):572–600, 2003.
- [58] J. A. Sethian and P Smereka. Level set methods for fluid interfaces. *Annual Review of Fluid Mechanics*, 25:341–372, 2003.
- [59] D. M. Anderson, G. B. McFadden, and A. A Wheeler. Diffuse-interface methods in fluid mechanics. *Annual Review of Fluid Mechanics*, 30:139–165, 1998.
- [60] Cyril W Hirt and Billy D Nichols. Volume of fluid (vof) method for the dynamics of free boundaries. *Journal of computational physics*, 39(1):201–225, 1981.
- [61] Bruno Lafaurie, Carlo Nardone, Ruben Scardovelli, Stéphane Zaleski, and Gianluigi Zanetti. Modelling merging and fragmentation in multiphase flows with surfer. *Journal of Computational Physics*, 113(1):134–147, 1994.
- [62] O Ubbink and RI Issa. A method for capturing sharp fluid interfaces on arbitrary meshes. *Journal of Computational Physics*, 153(1):26–50, 1999.
- [63] CS Wu, DL Young, and HC Wu. Simulations of multidimensional interfacial flows by an improved volume-of-fluid method. *International Journal of Heat and Mass Transfer*, 60:739–755, 2013.

- [64] Eugenio Aulisa, Sandro Manservigi, Ruben Scardovelli, and Stephane Zaleski. Interface reconstruction with least-squares fit and split advection in three-dimensional cartesian geometry. *Journal of Computational Physics*, 225(2):2301–2319, 2007.
- [65] Fabian Denner and Berend GM van Wachem. Compressive vof method with skewness correction to capture sharp interfaces on arbitrary meshes. *Journal of Computational Physics*, 279:127–144, 2014.
- [66] IR Park, KS Kim, J Kim, and SH Van. A volume-of-fluid method for incompressible free surface flows. *International Journal for Numerical Methods in Fluids*, 61(12):1331–1362, 2009.
- [67] BGM Van Wachem and Alf-Erik Almstedt. Methods for multiphase computational fluid dynamics. *Chemical Engineering Journal*, 96(1):81–98, 2003.
- [68] Johan Roenby, Henrik Bredmose, and Hrvoje Jasak. A computational method for sharp interface advection. *arXiv preprint arXiv:1601.05392*, 2016.
- [69] S Muzaferija and M Peric. Computation of free-surface flows using interface-tracking and interface-capturing methods. *Advanced Fluid Mechanics*, 24:59–100, 1999.
- [70] H Jasak and H. G. Weller. Interface-tracking capabilities of the InterGamma differencing scheme. Technical report, Imperial College London, 1995.
- [71] BP Leonard. The ultimate conservative difference scheme applied to unsteady one-dimensional advection. *Computer methods in applied mechanics and engineering*, 88(1):17–74, 1991.
- [72] Stéphane Popinet. An accurate adaptive solver for surface-tension-driven interfacial flows. *Journal of Computational Physics*, 228(16):5838–5866, 2009.
- [73] Fabian Denner and Berend GM van Wachem. Numerical time-step restrictions as a result of capillary waves. *Journal of Computational Physics*, 285:24–40, 2015.
- [74] Stanley Osher and James A Sethian. Fronts propagating with curvature-dependent speed: Algorithms based on Hamilton-Jacobi formulations. *Journal of Computational Physics*, 79:12–49, 1988.

- [75] Mark Sussman, Peter Smereka, and Stanley Osher. A level set approach for computing solutions to incompressible two-phase flow. *Journal of Computational physics*, 114(1):146–159, 1994.
- [76] Frank Losasso, Ronald Fedkiw, and Stanley Osher. Spatially adaptive techniques for level set methods and incompressible flow. *Computers & Fluids*, 35(10):995–1010, 2006.
- [77] David L Chopp. Computing minimal surfaces via level set curvature flow. *Journal of Computational Physics*, 106(1):77–91, 1993.
- [78] Giovanni Russo and Peter Smereka. A remark on computing distance functions. *Journal of Computational Physics*, 163(1):51–67, 2000.
- [79] Murray Rudman. Volume-tracking methods for interfacial flow calculations. *International journal for numerical methods in fluids*, 24(7):671–691, 1997.
- [80] Mehdi Raessi and Heinz Pitsch. Modeling interfacial flows characterized by large density ratios with the level set method. *Annual Research Brief*, 2009.
- [81] M Aboukhedr, M Gavaises, A Georgoulas, M Marengo, and K Vogiatzaki. Numerical investigation of droplet spreading on porous and non-porous surfaces. In *ILASS Europe – Proceedings of the 23rd Annual Conference on Liquid Atomization and Spray Systems*, Brighton, UK, 2016.
- [82] M. Sussman and E. G. Puckett. A coupled level set and volume-of-fluid method for computing 3d and axisymmetric incompressible two-phase flows. *Journal of Computational Physics*, 162:301–337, 2000.
- [83] T. Ménard, P. A. Beau, S. Tanguy, and A. Berlemont. Primary break-up: DNS of liquid jet to improve atomization modelling. *Computational Methods in Multiphase Flow*, 3:343–353, 2005.
- [84] T. Ménard, S. Tanguy, and A. Berlemont. Coupling Level Set/VOF/ghost fluid methods: Validation and application to 3D simulation of the primary break-up of a liquid jet. *International Journal of Multiphase Flow*, 33:510–524, 2007.
- [85] Kensuke Yokoi. A practical numerical framework for free surface flows based on CLSVOF method, multi-moment methods and density-scaled CSF model:

- Numerical simulations of droplet splashing. *Journal of Computational Physics*, 232(1):252–271, 2013.
- [86] M. Arienti and M. Sussman. An embedded level set method for sharp-interface multiphase simulations of diesel injectors. *International Journal of Multiphase Flow*, 59:1–14, 2014.
- [87] Andrea Ferrari, Mirco Magnini, and John R. Thome. A Flexible Coupled Level Set and Volume of Fluid (flexCLV) method to simulate microscale two-phase flow in non-uniform and unstructured meshes. *International Journal of Multiphase Flow*, 2017.
- [88] M. Dianat, M. Skarysz, and A. Garmory. A Coupled Level Set and Volume of Fluid method for automotive exterior water management applications. *International Journal of Multiphase Flow*, 91:19–38, 2017.
- [89] Stanley Osher and James A Sethian. Fronts propagating with curvature-dependent speed: algorithms based on hamilton-jacobi formulations. *Journal of computational physics*, 79(1):12–49, 1988.
- [90] Mark Sussman, Emad Fatemi, Peter Smereka, and Stanley Osher. An improved level set method for incompressible two-phase flows. *Computers & Fluids*, 27(5):663–680, 1998.
- [91] Thibault Pringuey and R Stewart Cant. Robust conservative level set method for 3d mixed-element meshesapplication to les of primary liquid-sheet breakup. *Communications in Computational Physics*, 16(02):403–439, 2014.
- [92] Thibault Pringuey and R Stewart Cant. High order schemes on three-dimensional general polyhedral meshesapplication to the level set method. *Communications in Computational Physics*, 12(01):1–41, 2012.
- [93] Paul Meakin and Alexandre M Tartakovsky. Modeling and simulation of pore-scale multiphase fluid flow and reactive transport in fractured and porous media. *Reviews of Geophysics*, 47(3), 2009.
- [94] J Willard GiBBS. *The Collected Works of J. Willard Gibbs, Ph. D., LLD [Vol 1-2]*. London, England, Yale University Press, 1957.

- [95] Gene Whyman, Edward Bormashenko, and Tamir Stein. The rigorous derivation of Young, Cassie - Baxter and wenzel equations and the analysis of the contact angle hysteresis phenomenon. *Chemical Physics Letters*, 450(4-6):355–359, 2008.
- [96] Thomas Young. *Phil. Trans Roy. Soc*, 95:65–75, 1805.
- [97] LM Hocking and AD Rivers. The spreading of a drop by capillary action. *Journal of Fluid Mechanics*, 121:425–442, 1982.
- [98] Auro Ashish Saha and Sushanta K Mitra. Effect of dynamic contact angle in a volume of fluid (vof) model for a microfluidic capillary flow. *Journal of colloid and interface science*, 339(2):461–480, 2009.
- [99] H Keith Moffatt. Viscous and resistive eddies near a sharp corner. *Journal of Fluid Mechanics*, 18(1):1–18, 1964.
- [100] OV Voinov. Hydrodynamics of wetting. *Fluid dynamics*, 11(5):714–721, 1976.
- [101] Jordan G Petrov, John Ralston, Matthew Schneemilch, and Robert A Hayes. Dynamics of partial wetting and dewetting in well-defined systems. *The Journal of Physical Chemistry B*, 107(7):1634–1645, 2003.
- [102] Tsung-Shann Jiang, OH Soo-Gun, and John C Slattery. Correlation for dynamic contact angle. *Journal of Colloid and Interface Science*, 69(1):74–77, 1979.
- [103] Yulii D Shikhmurzaev. *Capillary flows with forming interfaces*. CRC Press, 2007.
- [104] Yu D Shikhmurzaev. The moving contact line on a smooth solid surface. *International Journal of Multiphase Flow*, 19(4):589–610, 1993.
- [105] OpenFOAM OpenCFD. The open source cfd toolbox. *User Guide, OpenCFD Ltd*, 2009.
- [106] R. Issa. Solution of the implicitly discretised fluid flow equations by Operator-Splitting. *Journal of Computational Physics*, 62:40–65, 1985.
- [107] Joel H Ferziger, Milovan Peric, and Anthony Leonard. Computational methods for fluid dynamics, 1997.

- [108] A. Georgoulas, P. Koukouvinis, M. Gavaises, and M. Marengo. Numerical investigation of quasi-static bubble growth and detachment from submerged orifices in isothermal liquid pools: The effect of varying fluid properties and gravity levels. *International Journal of Multiphase Flow*, 74:59 – 78, 2015. doi: <http://dx.doi.org/10.1016/j.ijmultiphaseflow.2015.04.008>.
- [109] Ali Q Raeini, Martin J Blunt, and Branko Bijeljic. Modelling two-phase flow in porous media at the pore scale using the volume-of-fluid method. *Journal of Computational Physics*, 231(17):5653–5668, 2012.
- [110] M Aboukhedr, M Gavaises, A Georgoulas, M Marengo, and K Vogiatzaki. Numerical investigation of droplet spreading on porous and non-porous surfaces. *27th Annual Conference on Liquid Atomization and Spray Systems*, 2016.
- [111] John David Anderson and J Wendt. *Computational fluid dynamics*, volume 206. Springer, 1995.
- [112] Š Šikalo, H-D Wilhelm, IV Roisman, S Jakirlić, and C Tropea. Dynamic contact angle of spreading droplets: Experiments and simulations. *Physics of Fluids*, 17(6):062103, 2005.
- [113] HG Weller. Derivation, modelling and solution of the conditionally averaged two-phase flow equations. *Nabla Ltd, No Technical Report TR/HGW/02*, 2002.
- [114] Steven T Zalesak. Fully multidimensional flux-corrected transport algorithms for fluids. *Journal of computational physics*, 31(3):335–362, 1979.
- [115] William J Rider and Douglas B Kothe. Reconstructing volume tracking. *Journal of computational physics*, 141(2):112–152, 1998.
- [116] H Jasak and HG Weller. Interface tracking capabilities of the inter-gamma differencing scheme. *Department of Mechanical Engineering, Imperial College of Science, Technology and Medicine*, 1995.
- [117] MW Williams, DB Kothe, and EG Puckett. Accuracy and convergence of continuum surface tension models. *Fluid Dynamics at Interfaces, Cambridge University Press, Cambridge*, pages 294–305, 1998.

- [118] J W S Rayleigh. Investigation of the character of the equilibrium of an incompressible heavy fluid of variable density. *Proceedings of the Royal Society of London*, 14:170–177, 1883.
- [119] G I Taylor. The instability of liquid surfaces when accelerated in a direction perpendicular to their planes. *Proceedings of the Royal Society*, 201:192, 1950.
- [120] C Bilger, M Aboukhedr, K Vogiatzaki, and RS Cant. Evaluation of two-phase flow solvers using level set and volume of fluid methods. *Journal of Computational Physics*, 2017.
- [121] Kensuke Yokoi. A numerical method for free-surface flows and its application to droplet impact on a thin liquid layer. *Journal of Scientific Computing*, 35(2-3): 372–396, 2008.
- [122] STÉPHANE Popinet and STÉPHANE Zaleski. A front-tracking algorithm for accurate representation of surface tension. *International Journal for Numerical Methods in Fluids*, 30(6):775–793, 1999.
- [123] Elbridge Gerry Puckett, Ann S Almgren, John B Bell, Daniel L Marcus, and William J Rider. A high-order projection method for tracking fluid interfaces in variable density incompressible flows. *Journal of Computational Physics*, 130(2): 269–282, 1997.
- [124] Thibault Pringuey and R Stewart Cant. Robust Conservative Level Set method for 3D mixed-element meshes Application to LES of primary liquid-sheet breakup. *Communications in Computational Physics*, 16:403–439, 2014.
- [125] Elbridge Gerry Puckett, Ann S Almgren, John B Bell, Daniel L Marcus, and William J Rider. A High-Order Projection Method for Tracking Fluid Interfaces in Variable Density Incompressible Flows. *Journal of Computational Physics*, 130:269–282, 1997.
- [126] Vinay R Gopala and Berend G M van Wachem. Volume of fluid methods for immiscible-fluid and free-surface flows. *Chemical Engineering Journal*, 141:204–221, 2008.
- [127] Sir Horace Lamb. *Hydrodynamics*. Cambridge University Press, 1895.

- [128] Subrahmanyam Chandrasekhar. *Hydrodynamic and Hydromagnetic Stability*. Oxford University Press, 1961.
- [129] H J Kull. Theory of the Rayleigh–Taylor instability. *Physics Reports*, 206:197–325, 1991.
- [130] E. Fermi and J. von Neumann. Taylor instability of incompressible liquids. Part 1. Taylor instability of an incompressible liquid. Part 2. Taylor instability at the boundary of two incompressible liquids. Technical report, Los Alamos Scientific Laboratory, August 1953.
- [131] J. R. Ristorcelli and T. T. Clark. Rayleigh–Taylor turbulence: self-similar analysis and direct numerical simulations. *Journal of Fluid Mechanics*, 507:213–253, 2004.
- [132] Guy Dimonte, D. L. Youngs, A. Dimitis, S. Weber, M. Marinak, S. Wunsch, C. Garasi, A. Robinson, M. J. Andrews, P. Ramaprabhu, A. C. Calder, B. Fryxell, J. Biello, L. Dursi, P. MacNeice, K. Olson, P. Ricker, R. Rosner, F. Timmes, H. Tufo, Y. N. Young, and M. Zingale. Density ratio dependence of Rayleigh–Taylor mixing for sustained and impulsive acceleration histories. *Physics of Fluids*, 16(5):1668–1693, 2004.
- [133] Kai Kadau, Timothy C Germann, Nicolas G Hadjiconstantinou, Peter S Lomdahl, Guy Dimonte, Brad Lee Holian, and Berni J Alder. Nanohydrodynamics simulations: An atomistic view of the Rayleigh–Taylor instability. *Proceedings of the National Academy of Sciences of the United States of America*, 101(16):5851–5855, 2004.
- [134] Yohei Sato and Bojan Ničeno. A conservative local interface sharpening scheme for the constrained interpolation profile method. *International Journal for Numerical Methods in Fluids*, 70(4):441–467, 2012.
- [135] Ilias Malgarinos, Nikolaos Nikolopoulos, and Manolis Gavaises. Coupling a local adaptive grid refinement technique with an interface sharpening scheme for the simulation of two-phase flow and free-surface flows using vof methodology. *Journal of Computational Physics*, 300:732–753, 2015.

- [136] Gregor Černe, Stojan Petelin, and Iztok Tiselj. Numerical errors of the volume-of-fluid interface tracking algorithm. *International journal for numerical methods in fluids*, 38(4):329–350, 2002.
- [137] S Arias, Xavier Ruiz, Jaume Casademunt, Laureano Ramírez-Piscina, and Ricardo González-Cinca. Experimental study of a microchannel bubble injector for microgravity applications. *Microgravity Science and Technology*, 21(1-2):107–111, 2009.
- [138] Laure Ménérier-Deremble and Patrick Tabeling. Droplet breakup in microfluidic junctions of arbitrary angles. *Physical Review E*, 74(3):035303, 2006.
- [139] Volkert van Steijn, Chris R Kleijn, and Michiel T Kreutzer. Flows around confined bubbles and their importance in triggering pinch-off. *Physical review letters*, 103(21):214501, 2009.
- [140] Hu Dong. *Micro-CT imaging and pore network extraction*. PhD thesis, Department of Earth Science and Engineering, Imperial College London, 2008.
- [141] 3d-modelling from ct-data of physical objects. URL <https://www.beta-cae.com/retomo.html/>.
- [142] William E Lorensen and Harvey E Cline. Marching cubes: A high resolution 3d surface construction algorithm. In *ACM siggraph computer graphics*, volume 21, pages 163–169. ACM, 1987.
- [143] Ali Q Raeini, Martin J Blunt, and Branko Bijeljic. Direct simulations of two-phase flow on micro-ct images of porous media and upscaling of pore-scale forces. *Advances in Water Resources*, 74:116–126, 2014.
- [144] Kensuke Yokoi, Damien Vadillo, John Hinch, and Ian Hutchings. Numerical studies of the influence of the dynamic contact angle on a droplet impacting on a dry surface. *Physics of Fluids*, 21(7):072102, 2009.
- [145] R Rioboo, M Marengo, and C Tropea. Time evolution of liquid drop impact onto solid, dry surfaces. *Experiments in Fluids*, 33(1):112–124, 2002.
- [146] AL Yarin. Drop impact dynamics: splashing, spreading, receding, bouncing. *Annu. Rev. Fluid Mech.*, 38:159–192, 2006.

- [147] M Denesuk, GL Smith, BJJ Zelinski, NJ Kreidl, and Donald R Uhlmann. Capillary penetration of liquid droplets into porous materials. *Journal of colloid and interface science*, 158(1):114–120, 1993.
- [148] Terrence G DOnofrio, Homayun K Navaz, Bojan Markicevic, Brent A Mantooth, and Kenneth B Sumpter. Experimental and numerical study of spread and sorption of vx sessile droplets into medium grain-size sand. *Langmuir*, 26(5):3317–3322, 2009.
- [149] NC Reis, RF Griffiths, MD Mantle, and LF Gladden. Investigation of the evaporation of embedded liquid droplets from porous surfaces using magnetic resonance imaging. *International Journal of Heat and Mass Transfer*, 46(7):1279–1292, 2003.
- [150] Homayun K Navaz, Bojan Markicevic, Ali R Zand, Yuri Sikorski, Ewen Chan, Matthew Sanders, and Terrence G D’Onofrio. Sessile droplet spread into porous substratesdetermination of capillary pressure using a continuum approach. *Journal of colloid and interface science*, 325(2):440–446, 2008.
- [151] SH Davis and LM Hocking. Spreading and imbibition of viscous liquid on a porous base. *Physics of Fluids (1994-present)*, 11(1):48–57, 1999.
- [152] VM Starov, SA Zhdanov, and MG Velarde. Spreading of liquid drops over thick porous layers: complete wetting case. *Langmuir*, 18(25):9744–9750, 2002.
- [153] X Frank and Patrick Perre. Droplet spreading on a porous surface: A lattice boltzmann study. *Physics of Fluids (1994-present)*, 24(4):042101, 2012.
- [154] Anne-Laure Biance, Christophe Clanet, and David Quéré. First steps in the spreading of a liquid droplet. *Physical Review E*, 69(1):016301, 2004.
- [155] J.B. Lee, A.I. Radu, P. Vontobel, D. Derome, and J. Carmeliet. Absorption of impinging water droplet in porous stones. *Journal of Colloid and Interface Science*, 471:59 – 70, 2016. ISSN 0021-9797. doi: <http://dx.doi.org/10.1016/j.jcis.2016.03.002>.
- [156] M. Abokhedr, K. Vogiatzaki, N. Mitroglou, and E. Gavaises. A numerical simulation of single and two-phase flow in porous media: A pore scale observation of

effective microscopic forces. *6th BETA CAE International Conference*, 2, 2015.
doi: 10.13140/RG.2.1.5032.4643.

- [157] Mark Sussman, Ann S Almgren, John B Bell, Phillip Colella, Louis H Howell, and Michael L Welcome. An adaptive level set approach for incompressible two-phase flows. *Journal of Computational Physics*, 148(1):81–124, 1999.